

© 2017 by Spencer H. Bryngelson. All rights reserved.

STABILITY AND TRANSITION OF CAPSULE-FLOW SYSTEMS

BY

SPENCER H. BRYNGELSON

DISSERTATION

Submitted in partial fulfillment of the requirements
for the degree of Doctor of Philosophy in Theoretical and Applied Mechanics
in the Graduate College of the
University of Illinois at Urbana-Champaign, 2017

Urbana, Illinois

Doctoral Committee:

Professor Jonathan B. Freund, Chair and Director of Research
Associate Professor Randy H. Ewoldt
Professor Sascha Hilgenfeldt
Professor Luke N. Olson

Abstract

This work focuses on the mechanical stability of three different capsule-viscous-flow-systems. Red blood cells, which are often modeled as capsules, can form uniform “trains” when flowing in narrow confines; however, in less confined environments their flow appears disordered. This time-stationary system is analyzed through a nonmodal stability analysis which includes full coupling between the viscous fluid flow and elastic cell membranes. The linearization is constructed via a complex set of orthogonal small disturbances which are evaluated using boundary integral techniques. Transiently ($t \rightarrow 0^+$) and asymptotically ($t \rightarrow \infty$) unstable disturbances are identified, with their corresponding growth rates and perturbation conformations depending upon on the flow strength, viscosity ratio between the inner and exterior cell fluids, cell-cell spacing, cell at-rest shape, and vessel diameter. An ellipsoidal capsule subject to homogeneous shear flow is also considered. While this flow configuration is seemingly more simple, the base motion of the capsule is time-dependent, though periodic, rather than steady, requiring an extension of our methods. This capsule flow is known to display different kinematic behavior, depending on the flow strength, membrane material properties, and capsule shape. The stability of the capsule motion has been studied based on empirical observations of simulations; here we build upon these results though a direct stability analysis. Our analysis utilizes Floquet methods, which yields Floquet multipliers that classify the asymptotic stability of the capsule motion, and quantify how viscous dissipation will rapidly damp most disturbances. However, we also identify disturbances that decay slowly, over many periods of the capsules rotating motion, as well as neutrally stable perturbations. The last flow system considered here is a spherical capsule subject to large amplitude oscillatory extensional (LAOE) flow, which is often used to study the rheology and dynamics of complex fluids. Examining soft particles in LAOE is particularly challenging, partially due to the instability of the flow system. We again quantify this stability through linear analysis, here extending the aforementioned Floquet formulation to include nonmodal and intra-period effects. The analysis shows the asymptotic stability of the capsules for all flow descriptions, as defined by the relative flow strength and capsule time scale. Transiently unstable modes are found for all cases, though again their growth saturates quickly. We also identify an intra-period instability to capsule translations, which matches that of a rigid particle, though it does not have finite amplification from period-to-period.

To my parents.

Acknowledgments

Prima facie, I am most appreciative and thankful for the guidance provided by my advisor, Professor Freund, who was always prepared to intellectually challenge and stimulate me (if only after an extra cup of coffee). I also have great gratitude for the insightful and never banal discussions with Professor Ewoldt, fostering my interest in rheology. The past and current members of the Freund and Ewoldt research groups are also due grateful acknowledgement for propelling this work to its conclusion. I thank the other members of my dissertation committee, Professors Hilgenfeldt and Olson, who were ever eager to answer my seemingly endless stream of questions, during class or otherwise. Finally, my friends and family were instrumental in making this arduous process as painless as possible, for which there is likely no other therapy. I also acknowledge funding from the National Science Foundation under Grant No. CBET 13-36972.

Table of Contents

List of Figures	viii
Nomenclature	xiii
1 Introduction	1
1.1 Capsules	1
1.2 Capsule suspensions: kinematics and stability	2
1.2.1 Microcirculatory blood flow	2
1.2.2 Capsule suspensions of other types	4
1.3 Cell-train stability	4
1.4 Stability of capsules in homogeneous shear flow	7
1.5 Stability of capsules in large-amplitude oscillatory extensional flow	8
1.6 Linear stability analysis	10
1.6.1 Previous studies	10
1.7 Overview and key findings	11
1.7.1 Overview of dissertation	11
1.7.2 Key findings	12
2 Capsule model	13
2.1 Models of capsule mechanics	13
2.1.1 Discrete models	13
2.1.2 Continuum-based models	14
2.2 Skalak membrane constitutive model	15
2.3 Membrane shapes	15
3 Numerical methods and solution	17
3.1 Capsule surface representation	17
3.2 Governing equations and boundary integrals	18
3.3 No-slip wall representation	19
3.4 Time-integration	20
3.5 Volume constraint	20
4 Red-blood-cell-train stability	21
4.1 Simulation setup and details	21
4.1.1 Physical model system	21
4.1.2 Numerical flow solution	22
4.2 Stability analysis formulation	22
4.2.1 Measure of configurational stability	22
4.2.2 Linearization	23
4.2.3 Eigensystem analysis and verification	24
4.3 Results	26
4.3.1 Base cases	26
4.3.2 Matched viscosity ratio $\lambda = 1$	26
4.3.3 Effect of viscosity ratio λ	32

4.3.4	Effect of flow strength Ca	35
4.3.5	Effect of cell reduced volume v	37
4.3.6	Disturbance strain energy	38
4.4	Conclusions	40
5	Stability of capsules in homogeneous shear flow	41
5.1	Simulation setup and details	41
5.1.1	Physical model system	41
5.1.2	Numerical flow solution	41
5.2	Cycles of capsule motion	42
5.3	Floquet stability analysis formulation	46
5.4	Results	47
5.5	Conclusions	49
6	Stability of a capsule in large amplitude oscillatory extension	50
6.1	Simulation setup and details	50
6.1.1	Physical model system	50
6.1.2	Numerical flow solution	50
6.2	Base capsule motion	50
6.3	Stability analysis	52
6.4	Results	52
6.5	Discussion and conclusions	57
7	Concluding remarks	58
7.1	Research summary	58
7.1.1	Model systems and solution method	58
7.1.2	Stability analysis	58
7.1.3	Flow instabilities	59
7.2	Reduced-order flow descriptions	60
7.3	Future work	61
7.3.1	Extensions of our methods	61
7.3.2	Discriminating chaotic from stochastic behavior in blood flow	62
A	Particle-mesh Ewald method	65
B	Buckling and its effect on the confined flow of a model capsule suspension	67
B.1	Introduction	67
B.2	Physical model system	68
B.3	Numerical methods	70
B.4	Results	72
B.4.1	Equilibrium shapes	72
B.4.2	Flow visualizations	73
B.4.3	Macroscopic resistance: Effective viscosity	75
B.4.4	Capsule-free layer	78
B.4.5	Capsule orientation	78
B.4.6	Buckling	81
B.4.7	Influence of buckled capsules and their kinematics	84
B.4.8	Hydrodynamic interactions	86
B.5	Conclusions	88

C Stability of capsule trains flowing within channels: a two-dimensional study	89
C.1 Two-dimensional model system	89
C.2 Numerical methods	92
C.3 Stability analysis formulation	93
C.3.1 Measure of configurational stability	93
C.3.2 Linearization	94
C.3.3 Eigensystem	95
C.3.4 Non-modal analysis	97
C.3.5 Character and verification of the linear system	97
C.4 Results	99
C.4.1 Transient amplification	99
C.4.2 Asymptotic amplification	102
C.4.3 Disturbance regime boundaries	102
C.4.4 An empirically stable, narrow-channel configuration	102
C.4.5 Transition to disordered flow	107
C.4.6 Elastic stiffness	111
C.5 Summary and conclusions	114
D Continuum-based methods for cell-train behavior	117
D.1 Model system	117
D.2 Linear stability analysis	118
D.3 Chebyshev methods	120
D.3.1 Differentiation	120
D.3.2 A representative example: Orr-Sommerfeld equation	121
D.4 Results	121
D.5 Discussion	122
E A rigid-sphere model for capsule trains	124
E.1 Rigid-sphere flow systems	124
E.2 Flow and stability of uniformly spaced sphere trains	125
E.3 Extensions and discussion	126
F Discriminating chaotic dynamics from stochastic noise in microcirculatory flow	128
F.1 Simulations	128
F.2 Data	128
F.3 Fourier spectrum	128
F.4 Correlation dimension	130
F.5 Structure function	130
F.6 Lyapunov exponents	132
References	133

List of Figures

1.1	(a) Scanning electron microscope image of human blood at rest [1] and (b) model cell used in this work.	1
1.2	Experimental observations of red blood cells flowing in (a) channels [2] and (b) tubes [3].	5
1.3	Empirical stability example for red blood cells using methods of Zhao <i>et al.</i> [4]. Both configurations were equally perturbed, but the $N = 8$ cell train in (a) seems to persist indefinitely, whereas the more dense $N = 12$ case in (b) undergoes a rapid transition. This shows a sensitivity to packing fraction in addition to diameter sensitivity discussed in the text.	5
1.4	Schematic of the model homogeneous shear flow system and velocity field.	7
1.5	Schematic of the LAOE model flow system.	9
2.1	Example capsule reference shapes as labeled.	15
3.1	Schematic of a model flow configuration. \mathcal{S}_i are the surfaces of the $N = 8$ capsules and no-slip tube wall, μ is the suspending fluid viscosity, and $\lambda\mu$ is the interior capsule viscosity, which we take to be the same for all capsules.	18
3.2	Schematic of an example cylindrical vessel	19
4.1	The model system.	21
4.2	(a) Eigenvalues of \mathbf{A} for a two cell case with $D = 10r_o$, $\phi = 0.2$, and viscosity ratio $\lambda = 5$. (b) a magnification of (a) as indicated.	25
4.3	Verification of the example case with $D = 10$, $\phi = 0.2$, and viscosity ratio $\lambda = 5$ for initial disturbance amplitude $\hat{\varepsilon} = 10^{-3}$. Linear predictions of \mathbf{A} and DNS of the same initial conditions agree within plotting precision.	25
4.4	Example base configurations for $D = 6$ and 10 and $\phi = 0.2$ and $\phi = 0.7$	26
4.5	(a) Spectral abscissa α for a range of D and ϕ . The curves of constant α show a region of apparent marginal (or near-marginal, see text) stability. (b) Example \vec{v}_α for cases (i)–(iv) as labeled in (a), magnified for visualization as $\vec{s} + 10\vec{v}_\alpha$. The wrinkled appearance of (i) is due to the magnification of an otherwise small shape disturbance.	27
4.6	(a) Numerical abscissa η . Solid black lines denote an approximate curve of constant η , as labeled. (b) Example \vec{v}_η for cases (i)–(iv) visualized as $\vec{s} + 10\vec{v}_\eta$. Their kinky appearance is due to linear magnification of an otherwise small shape disturbance.	29
4.7	Time evolution of $\ \vec{\varepsilon}(t)\ $ for the most amplifying transient and asymptotic amplifying disturbances and their linear predictions are shown with relatively large $\hat{\varepsilon} = 0.1$ initial disturbance for cases (a) $D = 10r_o$, $\phi = 0.2$ and (b) $D = 10r_o$, $\phi = 0.7$. Linear predictions of \vec{v}_α remain good for long times as expected, though transient disturbances \vec{v}_η undergo rapid decay.	30
4.8	Cell-averaged deformation spectra for \vec{v}_α and \vec{v}_η for the case $D = 10r_o$ and $\phi = 0.7$	31
4.9	Time evolution of \vec{v}_α and an <i>ad hoc</i> disturbance $\vec{v}_{a.h.}$ with $\hat{\varepsilon} = 0.1$ and its associated DNS for cases with $D = 10r_o$ and $\phi = 0.2$ and 0.7	31

4.10	(a) Spectral and (b) numerical abscissa for $\lambda = 1$ and 5 and $D = 8r_o$ and $12r_o$ as labeled for various ϕ .	33
4.11	Spectral abscissa α for $0.1 \leq \lambda \leq 100$ for (a) $\phi = 0.2$ and (b) $\phi = 0.7$ for a range of λ .	34
4.12	Cell-averaged deformation spectra for \vec{v}_α for the case $D = 10r_o$, $\phi = 0.7$, and λ as labeled.	35
4.13	Cell trains with $D = 8r_o$ for the (a) smallest ($Ca = 0.4$) and (b) largest Ca ($Ca = 20.5$) we consider.	35
4.14	Spectral abscissa for cell trains of diameters $D = 8r_o$ and $10r_o$, packing fractions (a) $\phi = 0.2$ and (b) $\phi = 0.7$, and $\lambda = 1$ for a range of Ca . Vertical dashed lines indicate the $Ca = 0.66$ used previously.	36
4.15	Example red blood cell equilibrium shapes for various levels of inflation and deflation, given by their reduced volume v . The reference healthy red blood cell used in previous sections has $v = 0.64$.	37
4.16	Visualization of cell trains with $D = 8r_o$ and $\phi = 0.7$ for the (a) smallest and (b) largest v we consider in this case.	38
4.17	Spectral abscissa α for cell trains of various D and packing fractions (a) $\phi = 0.2$ and (b) $\phi = 0.7$ for a range of cell reduced volumes v with $\lambda = 1$. Vertical dashed lines indicate the healthy red blood cell geometry $v = 0.64$. In (b) the shaded regime $v > 0.86$ indicates states which do not fit in the train without self-intersecting.	39
5.1	Schematic of the homogeneous shear flow model system.	42
5.2	Verification of long-time (a) Taylor parameter, (b) inclination angle, and (c) rotation period (see text) with Lac <i>et al.</i> for $a/b = 1$ and indicated Ca and C .	43
5.3	Cases with $a/b = 0.5$, $C = 1$, $E_b = 0$, and $Ca = 0.3$: (a) $\zeta(0) = 30^\circ$ and 75° , (b) $\xi(0) = \zeta(0) = 30^\circ$.	44
5.4	Character of capsule motion for a range of Ca .	45
5.5	Visualization of capsule over one half-period for example cases as labeled. We introduce $p_{\hat{x}-\hat{y}}$ as a tracker point on the membrane in the shear-plane for illustration of its motion.	45
5.6	The spectrum of \mathbf{C} for $Ca = 1.4$. Neutrally (ρ_o) and modestly (ρ_-) stable modes are labeled.	47
5.7	(a) Linear prediction and DNS of example Floquet multipliers as labeled over several periods for the $Ca = 1.4$ case. (b) Associated eigenvectors (ii) \vec{v}_- and (iii) \vec{v}_b , magnified for visualization as $\vec{s}[0] + 5\vec{v}$.	48
5.8	Floquet multipliers for a range of Ca .	49
6.1	Schematic of model LAOE flow system and velocity field.	51
6.2	Base-flow motion for the case $Wi = 0.8$ and $De = 0.03$.	51
6.3	Floquet multipliers ρ_i , numerical abscissa $\eta_{1,i}$, and maximum intra-period growth Δ for the case $Wi = 0.8$ and $De = 0.03$.	53
6.4	Linear theory and DNS for \vec{v}_η and \vec{v}_Δ over one period for example cases as labeled.	54
6.5	(a) \vec{v}_η and (b) \vec{v}_Δ for the case $Wi = 0.8$ and $De = 0.03$, magnified for visualization as $\vec{s}[0] + 5\vec{v}$.	55
6.6	(a) Δ for various De and Wi . (b) Least-squares fitted α for $\Delta = \exp(\alpha/De)$ at select Wi .	56
6.7	Pipkin space showing isocontours of Δ and η_{100} as labeled.	56
7.1	Schematic of a proposed core-annular rheological flow. \mathbf{U} is the fluid velocity profile, the dotted curve is an example of a perturbation to the fluid-fluid interface, and the hashed lines indicate the no-slip wall boundary.	60
7.2	Schematic of a model rigid-sphere flow system.	61

7.3 Evolution (and magnification) of the radial cell position of the flow above, as quantified by the cell centroid distance from the vessel centerline for an example cell. The entire time series entails 3000 vessel diameters of streamwise cell travel. A visualization of the disordered flow is also shown, the mean velocity is from left to right.	63
B.1 Schematic of the two-dimensional streamwise-periodic model channel with capsules of area A and perimeter l_o	69
B.2 Example equilibrium shapes for different ξ_o	72
B.3 Flow visualizations for $H_c = 0.25$, $W = 14r_o$, cases are $Ca = 0.2$ and $Ca = 1.0$ and $\xi_o = 1.0, 1.7$ and 3.0 as labeled. For these visualizations $L = 30r_o$	74
B.4 Visualizations showing the onset of apparent buckling behavior for $H_c = 0.25$, $W = 14r_o$, $Ca = 1.0$ for ξ_o as labeled. The numbers indicate the buckling metric defined in section B.4.6.	75
B.5 Instantaneous μ_{eff} from (B.12) for $H_c = 0.25$, $W = 20r_o$ and $\xi_o = 2.4$. The nominally transient period is shaded, after which effective viscosity deviates by $< 2\%$	75
B.6 Effective viscosity μ_{eff} from (B.12): (a) as a function of hematocrit for fixed channel width and (b) as a function of W for $H_c = 0.20$. Note that the dashed lines represent empirical fits of experimental data from [5].	76
B.7 Effective viscosity for several different cases of H_c and ξ_o . $W/r_o = 20$, $Ca = 1$ for all cases.	77
B.8 Dependence of the capsule-free layer thickness on ξ_o and capillary number Ca , shown for cases with $W/r_o = 20$, $H_c = 0.25$	78
B.9 Schematic of model capsules (solid) and their respective fitted ellipsoids (dashed.)	79
B.10 Average orientation angle for varied ξ_o and flow strengths Ca . $H_c = 0.25$ and $W/r_o = 20$ for all cases.	80
B.11 Variance of orientation angle σ_α as a function of configuration aspect ratio and capillary number for $W/r_o = 20$ and $H_c = 0.25$. The vertical dashed lines represent approximate geometry and behavioral regimes as indicated.	81
B.12 Auxiliary flow configurations: capsules in (a) Taylor–Green stagnation point flow and (b) homogeneous shear.	82
B.13 Buckling parameter $\lambda \equiv \lambda_1/\lambda_2$ from (B.14) for representative biconcave $\xi_o = 1.6$ capsule and a dog-bone $\xi = 2.6$ capsule. Dashed lines show the equilibrium $\lambda = \lambda_r$ condition. In both cases, $H_c = 0.25$, $Ca = 1.0$ and $W = 20r_o$	83
B.14 Scaling of critical buckling aspect ratio due to forcing F^* due to the fluid. Visualizations show examples from the different flow fields for $\xi_o = 2.8$, $Ca = 1$. The channel has $W/r_o = 20$ and $H_c = 0.25$. The straight lines are power-law fits $F^* \sim l_c^{-b}$ with $b = 2.65$ for the channel, 1.82 for the stagnation flow, and 1.82 for the homogeneous shear.	84
B.15 Transverse position for five representative biconcave and dog-bone capsules with $H_c = 0.25$, $W/r_o = 14$ and $Ca = 1.0$. The orientation of a buckled (c, dotted) versus non-buckled dog-bone capsule (c, solid) are shown as defined (see text) and shown in figure B.13, as well as the orientation of a biconcave capsule (d).	85
B.16 The average transverse velocity of the capsules $\langle \dot{y}/U \rangle$ and transverse displacement Δ_y/r_o from (B.19). We also show Δ_y for capsules that have buckled at least once during the course of the simulation, $(\Delta_y/r_o)_b$	86
B.17 Stresslet G_{ij} and rotlet R_{ij} strengths for different ξ_o for $H_c = 0.20$, $Ca = 1$ and $W = 20r_o$	88

C.1	(a) The model channel flow with mean flow U containing N capsules of area $A = \pi r_o^2$ and perimeter $l_o = 1.6 \times 2\pi r_o$. (b) An empirically stable single-file train in a narrow $W = 4r_o$ channel, (b) an empirically unstable train in a $W = 10r_o$ channel, and (d) its transition into an apparently chaotic flow.	90
C.2	Base configurations.	91
C.3	Eigenvalues of \mathbf{A} for $W = 40r_o$ and $\phi = 0.7$ with $N = 20$ capsules.	96
C.4	Perturbation amplification in time: (A) The transient growth based on maximum time dependent amplification $\zeta(t)$ from (C.20) for initial perturbation $\hat{\varepsilon}\vec{v}_\eta$; (B) direct evaluation of the matrix exponential $\exp \mathbf{At}$ from (C.14) for $\hat{\varepsilon}\vec{v}_\eta$, which matches (C) from the corresponding DNS; and (D) $\exp a t$ for $\hat{\varepsilon}\vec{s}_\alpha$ from (C.16), which matches the large t behavior of (E) from the the corresponding DNS.	98
C.5	Evolving maximum growth rate $\zeta(t)$ analyzed in figure C.4.	99
C.6	Numerical abscissa η from (C.17) for different lengths L for the channels of figure C.2. The straight lines are power-law fits.	100
C.7	Most transiently amplifying (non-modal) disturbances for the baseline cases with $N = 30$ of figure C.2: — baseline \vec{x} and perturbations visualized as — $\vec{x} + a\hat{\varepsilon}\vec{v}_\eta$ with $a\hat{\varepsilon} = 3.5$. These relatively large amplitudes aid visualization, though some of the features appear exceptionally sharp due to geometric nonlinearity. The A and B labels indicate the specific magnified capsules.	101
C.8	Disturbance metrics (C.22) through (C.26) for all $j = 1, \dots, N$ capsules for $N = 30$ applied to the most amplifying transient disturbances visualized in figure C.7. All metrics are plotted for all cases, normalized by the largest value of any.	103
C.9	Spectral abscissa α from (C.15) for different for cases of figure C.2. The straight lines are power-law fits.	104
C.10	Most asymptotically ($t \rightarrow \infty$) amplifying modal disturbances for the baseline case with $N = 30$ visualized in figure C.2: — baseline \vec{x} and — perturbations visualized as $\vec{x} + a\hat{\varepsilon}\vec{s}_\alpha$ with $a\hat{\varepsilon} = 3.5$. The selected magnified in capsules are labeled accordingly.	104
C.11	Disturbance metrics (C.22) through (C.26) for all $j = 1, \dots, N$ capsules for $N = 30$ applied to the most amplifying transient disturbances visualized in figure C.10. All metrics are plotted for all cases, normalized by the largest value of any.	105
C.12	Character of the most amplifying disturbances for a range of channel widths and packing fractions as labeled.	106
C.13	(a) The baseline configuration for an empirically stable case with $W = 4r_o$, $\phi = 0.5$ and $N = 7$. (b) The $t \rightarrow 0^+$ most amplified transient, and (c) the asymptotically most amplified disturbances. (d-e) The corresponding disturbance metrics (C.22) through (C.26). The exaggerated displacements cause these to look unphysical, as discussed in section C.4.1 in regard to figure C.7.	108
C.14	Disturbance amplification for the empirically stable narrow channel case, visualized in figure C.13 (a). The DNS track (curves C and D) the corresponding linear amplifications (curves A and B) only for short times.	109
C.15	Disturbance amplitude evolution for the wide-dense configuration ($W = 40r_o$ and $\phi = 0.7$) with $\hat{\varepsilon} = 0.001r_o$ and $0.01r_o$ for initial conditions and predictions as labeled. The $\Delta t \approx 10^3 \mathcal{T}/r_o \mu$ labels the approximate difference in time for onset of nonlinear for transient versus eigenvalue estimates for $\hat{\varepsilon} = 0.01r_o$ (see text).	109

C.16 Transition to disordered flow for the $\hat{\varepsilon} = 10^{-2}r_o$ cases of figure C.15. For plotting the initial configuration, the exaggeration factor is $a\hat{\varepsilon} = 3.5$. The walls are not shown; they can be seen for the baseline configuration in figure C.2 (d). The times shown $t^* = t\mathcal{T}/r_o\mu$ were selected to illustrate the development qualitatively.	110
C.17 Disturbance amplitude evolution for the narrow–sparse configuration ($W = 10r_o$ and $\phi = 0.2$) with $\hat{\varepsilon} = 0.001r_o$ and $0.01r_o$ as labeled. The $\Delta t \approx 10^2\mathcal{T}/r_o\mu$ labels the approximate difference in time for onset of nonlinear for transient versus eigenvalue estimates for $\hat{\varepsilon} = 0.01$ (see text).	111
C.18 Transition to disordered flow for the $\hat{\varepsilon} = 0.01r_o$ cases of figure C.17. For plotting the initial configuration, the exaggeration factor is $a\hat{\varepsilon} = 3.5$. The walls are not shown; they can be seen for the baseline configuration in figure C.2 (a). The times shown $t^* = t\mathcal{T}/r_o\mu$ were selected to demonstrate nonlinear disruption.	112
C.19 Effect of capsule stiffness on α and η	113
C.20 The $W = 40r_o, \phi = 0.7$ case: (a) The predicted disturbance amplitude for different membrane stiffnesses based on: $\dots \eta, — \zeta(t)$, and $— \alpha$; and (b) the relative strain energy of the transiently most amplified mode $\vec{v}_\zeta(t)$ at time $t —$. For reference, also shown in (b) are the energy of the corresponding to $\dots \vec{v}_\eta$ and $— \vec{s}_\alpha$. Note, neither plot displays the evolution of the system in time. Rather, they show the maximum possible linear amplification amplitude and corresponding strain energy for an $\hat{\varepsilon} = 0.001r_o$ disturbance at that time. The strain energy can change abruptly as different disturbances become the nominally most dangerous at specific times.	115
D.1 Schematic of the model system: A cylindrical Newtonian jet issuing into quiescent fluid of zero density. As usual, the azimuthal direction θ is a rotation about the x -axis.	117
D.2 (a) Absolute error in the largest imaginary eigenvalue $c_{I,1}$ of (D.25) with $Re = 10^4$, $k = 1$ and (b) the associated condition number of \mathbf{A}	122
D.3 $Re[s]$ for both (a) $Re = 0$ and (b) $Re \rightarrow \infty$ at a range of k , where $M = 20$	123
E.1 Flow schematic of a uniform one-dimensional sphere train. All spheres have radius a and d is the consecutive sphere-sphere spacing.	125
E.2 Schematic of a more complex sphere flow system.	126
F.1 $r_j[t]$ for one cell and cases as labeled.	129
F.2 Fourier spectrum of \mathbf{r}_j for (a) $D = 6r_o$ and (b) $D = 8r_o$, and j as labeled.	129
F.3 (a) Correlation dimension $v(\varepsilon)$ and (b) correlation integral $C(\varepsilon)$ for the several m for the case $D = 6r_o$	131
F.4 Maximum $v(\varepsilon)$ in the scaling region $0.03 < \varepsilon < 1$ (as shown in figure F.3).	131
F.5 Structure function for varying n and m , and (a) $k = 1$ and (b) $k = 2$	132
F.6 Four largest Lyapunov exponents $\mathcal{L}(\mathbf{r}_j)$ for $j = 1, \dots, N$	132

Nomenclature

μ_{eff}	Effective viscosity
p	Fluid pressure
D	Tube or vessel diameter
U	Streamwise flow velocity
N	Number of capsules
$\hat{\mathbf{x}}, \hat{\mathbf{y}}, \hat{\mathbf{z}}$	Cartesian coordinate directions
r_o	Nominal capsule radius
\mathbf{x}	Capsule shape
a, b	Principal radii of ellipsoidal capsules
μ	Exterior fluid viscosity
λ	Ratio between interior and exterior fluid viscosity
E_s	Membrane shear modulus
E_d	Membrane dilatation modulus
E_b	Membrane bending modulus
$I_{1,2}$	Strain invariants
$\lambda_{1,2}$	Eigenvalues of the left Cauchy–Green tensor
\mathbf{V}	Left Cauchy–Green tensor
\mathbf{F}	Surface deformation tensor
\mathbf{a}, \mathbf{b}	Coefficients of the spherical harmonic expansion
\tilde{P}	Normalized Legendre polynomials
M	Size of spherical harmonic expansion
\vec{s}	Column vector of spherical harmonic coefficients
\vec{x}	Column vector of collocation points
\mathbf{B}	Discrete forward spherical harmonic transformation matrix
$\tilde{\mathbf{B}}$	Discrete backward spherical harmonic transformation matrix
S_i	Surfaces within the computation domain

\mathbf{u}	Surface velocity
\mathbf{u}^∞	Mean velocity within the computation domain
Ω	Union of all surfaces
$\Delta\sigma$	Surface tractions acting on the fluid
\mathbf{n}	Unit surface normal vector
\mathbf{G}	Stokeslet
\mathbf{T}	Stresslet
δ_{ij}	Kronecker symbol
$\vec{\mathbf{u}}$	Column vector of the velocity of the collocation points
t	Time
Δt	Discrete time step
L	Length of computational domain
ϕ	Capsule packing fraction
Ca	Capillary number
ε	Disturbance to a base flow
$\vec{\varepsilon}$	Column vector of disturbance displacement
$\hat{\varepsilon}$	Magnitude of initial disturbance
\mathbf{x}_b	Base flow surface position
$\vec{\delta}$	Set of disturbances for constructing linear stability analysis
\mathbf{A}	Matrix containing first order coupling of a disturbance to base flow
α, \vec{v}_α	Spectral abscissa and associated eigenvector
η, \vec{v}_η	Numerical abscissa and associated eigenvector
Δz	Traveled streamwise distance
\tilde{N}	Number of capsules in one wavelength of a disturbance
E_n	Distribution of the spherical harmonic spectrum
$\vec{v}_{a.h.}$	<i>Ad hoc</i> disturbance
v	Reduced volume
w	Strain energy
kT	Thermal energy
p_ζ	Point initially at the tip of the shortest capsule principal axis
p_ξ	Point at the tip of the shortest capsule principal axis
ζ	Angle between p_ζ and the flow vorticity axis
ξ	Angle between p_ξ and the flow vorticity axis

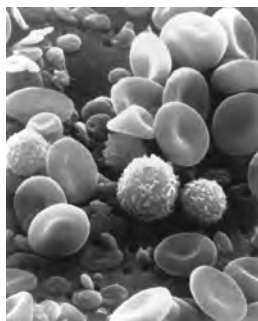
C	Ratio of membrane dilatation and shear moduli
T	Temporal period
L_i	Length of capsule principal radii
D_{ij}	Taylor parameter
Φ	Capsule inclination angle
\mathbf{X}	Fundamental matrix
\mathbf{C}	Monodromy matrix
μ_i	Floquet exponents
ρ_i	Floquet multipliers
De	Deborah number
Δ, \vec{v}_Δ	Maximum intra-period amplification and associated eigenvector

1 Introduction

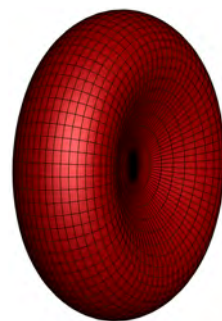
1.1 Capsules

Capsule is a term popularized by Barthès-Biesel for an elastic membrane enclosing a drop of incompressible fluid [6–8]. Examples of natural capsules include cells, vesicles, viruses, and eggs. Red blood cells, a focus of this work, are a common example of a natural capsule. As seen in figure 1.1, a distinct biconcave shape is formed by the membrane. The membrane itself is complex: formed by a lipid bilayer, decorated by molecular components such as proteins [9, 10], buttressed by a spectrin filament network [11], and filled with an approximately homogeneous and Newtonian fluid called the cytosol [12–14]. This membrane is approximately 8 μm in diameter and 100 nm in thickness [15–17]. Indeed capsule membranes, in general, are thin, approximately 100 times smaller in thickness than diameter. Thus, a thin-shell model is justified to describe the capsule-scale mechanics. While the molecular details of the capsule membrane can be important for the properties of any particular capsule system, we will focus on the finite-deformation dynamics of their highly deformable membranes.

Inspired by biological membranes, artificial capsules have been manufactured efficiently in large quantities with suspension cross-linking [18, 19], coacervation/phase-separation [20, 21], inkjet printing [22–24], and solvent evaporation techniques [25, 26], though these capsules typically have nearly spherical shapes, as more complex geometries are difficult to manufacture reliably [27–29]. Methods have also been developed for manufacturing capsules-within-capsules, (so-called compound capsules) [30–32]. Artificial capsules are typically manufactured using synthetic polymers, such as alginate, poly-L-lysine, or polyacrylates [33–35], or biopolymers



(a) Red and white blood cells



(b) Model red blood cell

Figure 1.1: (a) Scanning electron microscope image of human blood at rest [1] and (b) model cell used in this work.

such as cellulose derivatives [36, 37].

These advancements in manufacturing have increased interest in the applications for such capsules. For example, artificial capsules have been utilized for inkjet printing [38], cosmetics [39, 40], gums [41, 42], textiles [43, 44], repellents [45, 46], flame retardation [47, 48], release of aromas and flavors [49–51], absorption of CO₂ in gas plumes [52], and for biomedical purposes including targeted drug delivery [53–56] and screening [57, 58], contrast-enhanced ultrasound techniques [59], and the development of artificial blood [60, 61] and organs [62–64]. In certain applications, such as those involving selective membrane transport, artificial capsules can even outperform their biological counterparts [65, 66]. In most settings, the capsules are immersed in a flowing suspending liquid, called a capsule suspension. As a result, the flow of the suspension can depend on the capsules themselves, which we consider next.

1.2 Capsule suspensions: kinematics and stability

The dynamics and rheology of particulate suspensions depend upon the mechanics of the suspended elements, especially when they are highly confined. In these cases, the particle deformation is strongly coupled with the overall flow dynamics [8, 67–70], making it difficult to analyze. While suspension of other types share this property (e.g. rigid-particle [71, 72] and colloidal suspensions [73, 74]), we focus on elastic capsules due to their versatility, as described in section 1.1, and physiological relevance (discussed next). Herein, we investigate a variety of capsule flow systems, particularly in regard to their stability, beginning with cellular blood flow.

1.2.1 Microcirculatory blood flow

Capsule suspensions have been studied for a long time, blood flow perhaps being the first of such efforts. Whole blood is a suspension primarily composed of red blood cells (erythrocytes), which makeup approximately 45% of blood by volume [75], though the exact proportion depends upon the vessel size [76–78]. Other prominent constituents are white blood cells (leukocytes) and platelets, though these make up less than 2% of whole blood by volume [79], so the mechanics of blood flow are generally dominated by red blood cells [80]. These components are suspended in plasma, which is an aqueous solution of organic molecules and proteins that is often modeled as a homogeneous Newtonian fluid [12, 14, 81], and is considered in this approximation here.

Poiseuille was the first to study the mechanics of circulatory blood flow [82]. He defined an *effective viscosity*, the viscosity as deduced based on pressure drop were it a homogeneous Newtonian fluid,

$$\mu_{\text{eff}} = \frac{\langle \partial_x p \rangle D^2}{32U}, \quad (1.1)$$

where $\langle \partial_x p \rangle$ is the pressure drop in the streamwise direction, U is the mean flow velocity, and D is the vessel diameter. This measure, useful for defining viscous flow resistance,

combined with typical length scales and flow velocities of microcirculatory flow [78, 83], give a small Reynolds number, typically $Re < 0.01$. Thus, flow inertia is negligible and Stokes flow typically assumed [84, 85], which we utilize here. *In vitro* blood flow studies then became more common, motivated by medical therapies, such as those of blood pressure [86], metabolism [87], and inflammatory response [88]. Ultimately, these efforts led to the discovery of a complex scale-dependent behavior of effective viscosity [78, 89–91], a particularly famous example of which is the non-monotonicity of effective viscosity with vessel diameter. Known as the Fåhræus–Lindqvist effect [92, 93], the root mechanism of this behavior is the formation of a cell-free (or cell-depleted) layer, or simply a layer near the vessel wall where cells are typically not found. A direct result of red-blood-cell-membrane mechanics [94–99], the cell-free layer acts as an effective lubricant for a red-blood-cell-rich core flow, and is thought to be an important factor in microcirculatory dynamics [5, 100]. A marginating phenomenon has also been observed: white blood cells and platelets typically flow more near the vessel wall than red blood cells [101–105]. This behavior is, again, thought to be due to the mechanics of the red blood cells, particularly in regard to their relative stiffness [106–108]. Margination is known to be important for the rolling [80, 109] and attachment [109] of white blood cells to the vessel wall [110], and thus the inflammatory response that occurs due to disease, such as that of Alzheimers [111–113], cancer [114–116], and osteoarthritis [117, 118].

These flow phenomena are examples of the complex behavior often observed in non-Newtonian flows. The bulk rheological characteristic of whole blood is evidenced by its scale-dependent effective viscosity [84] and blunted velocity profile [119], leading it to be classified as non-Newtonian in these contexts. Further, the effective viscosity of blood is also a function of shear-rate for sufficiently narrow confinement or small shear-rates, and is thus *viscoelastic* in these conditions [120, 121]. This property is primarily due to the elastic energy stored in red blood cells as they deform, then dissipated via viscosity [121, 122], and is suspected to be affected by red blood cell aggregation and alignment in flow [122]. Further, at sufficiently small shear-rates, this aggregation leads to a yield stress [123, 124]. That is, for sufficiently small shear stresses whole blood effectively behaves as an elastic solid. These observations have challenged the use of continuum models for blood flowing in narrow confines. However, continuum modes have been useful when the blood vessels are many cell diameters across, and the specific dynamics of any single cell are not suspected to be important [78, 95, 125]. For example, the Maxwell model (and its nonlinear extensions), which quantifies the shear stress–strain-rate relationship by a spring and dash-pot in series, has been used to model whole blood viscoelasticity [126, 127]; and the Bingham model, which defines the strain rate as a step-function of shear stress, has been used to model the yield stress behavior [128, 129]. More complex models, and combinations of models, have been developed in pursuit of predicting microcirculatory flow phenomena [78, 130, 131], though they necessarily do not account for the finite deformation and dynamics of individual cells, which are known to be important in sufficiently narrow confines. Thus, we will model individual red blood cells as finite-deformation thin-shell membranes suspended in and encasing Newtonian fluids, and not attempt such a continuum flow description.

1.2.2 Capsule suspensions of other types

Development of artificial capsules has encouraged the study and design of other capsule suspensions. Simulation-based efforts have identified the roles of the confining geometry [132–135], capsule shape [104, 132] and stiffness [104, 133, 136], and flow strength [135, 136] on the flow and its rheological character. For example, the present author found that varying the capsule geometry from round to a more slender shape affects the suspension rheology through a buckling mechanism [132]. In this case, more slender capsules trigger a rotational-type response, as quantified through multipole analysis, which is concomitant with a disappearance of the capsule-free layer observed in suspensions of more round capsules, and a stark increase in the effective viscosity. The article which describes this behavior in detail is included in appendix B for completeness.

The importance of capsule-scale kinematic behavior for determining rheological and bulk-flow properties then motivates study of the mechanical stability of the capsule flow motion itself. Studying the stability of such a fluid–structure flow system directly is difficult due to its spatial complexity and intrinsic nonlinearity of the governing equations, so highly accurate numerical simulations are often required. Herein, we present a series of analyses based upon common capsule flows.

1.3 Cell-train stability

We first consider the stability of red-blood-cell trains [137]. Red blood cells flowing in vessels of diameter smaller than $D \approx 8 \mu\text{m}$ are observed to take in an axisymmetric bullet-like formation along the vessel center-line [70, 138–142], which is often referred to as a cell train. However, as D increases such trains are not observed [138, 143], as seen in figure 1.2, presumably because it is unstable, and the cellular flow appears far more complex [139, 144–148]. This empirical behavior has been reproduced in detailed numerical simulations [4, 136, 149]; an example in figure 1.3 shows sensitivity of the apparent stability to packing fraction. In this case, the more packed flow appears chaotic, and it is known that Stokes flow can display chaos in two-dimensional mixing [150, 151], some three-dimensional flows [152–155], and N -body systems such as a viscous suspension of spheres in a rotating cylinder [156, 157], so it is not surprising that such a transition can occur.

Here, we follow a previous study the stability of a two-dimensional model of such trains flowing in a narrow channel [158], which exhibited both transiently and asymptotically amplifying disturbances. Depending on the packing fraction and channel width, these disturbances showed an array of conformations: rigid-body-like tilts, lateral translations, and compressive “waves” of streamwise inter-cell spacing. This study is included in appendix C for completeness. Although this study of two-dimensional capsule trains was motivated, in part, by observations of red-blood-cell trains, given the well-known limitations of two-dimensional as model for phenomenology in three dimensions (especially in the viscous limit), we extend these methods to study the stability of geometrically and mechanically realistic red-blood cell trains. This has required an extension of the formulation and significantly more involved simulations.

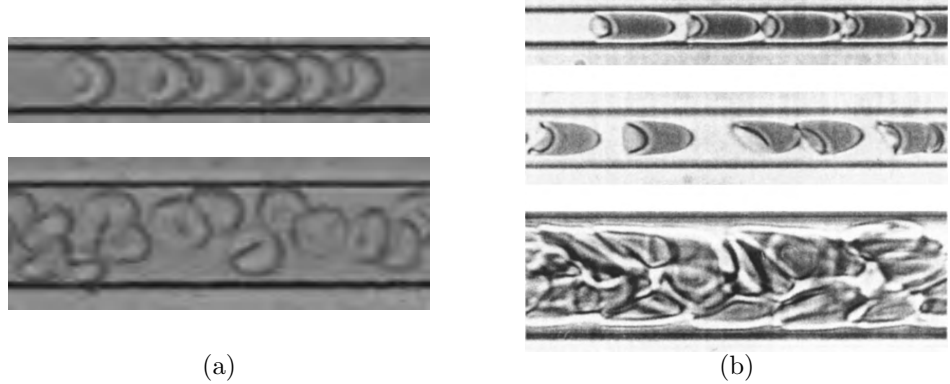


Figure 1.2: Experimental observations of red blood cells flowing in (a) channels [2] and (b) tubes [3].

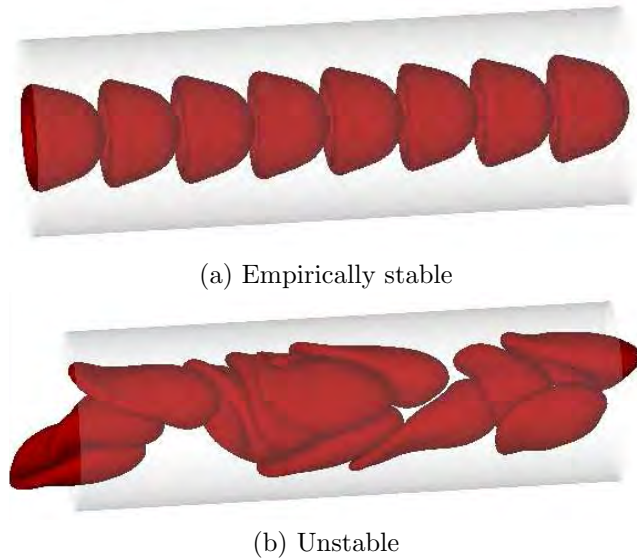


Figure 1.3: Empirical stability example for red blood cells using methods of Zhao *et al.* [4]. Both configurations were equally perturbed, but the $N = 8$ cell train in (a) seems to persist indefinitely, whereas the more dense $N = 12$ case in (b) undergoes a rapid transition. This shows a sensitivity to packing fraction in addition to diameter sensitivity discussed in the text.

At the outset, we can anticipate potential differences from our two-dimensional capsule-train study. The more rapid decay of the Stokeslet Green's function in three dimensions [159] can be anticipated to lead to more localized (or shorter) streamwise wavelengths of the most amplifying disturbances. The elastic resistance of the membrane is also fundamentally different. Like the two-dimensional capsule model, a red blood cell has a strong resistance to membrane dilatation. However, a shear modulus, without a direct analog in the two-dimensional model, is most important, while there is only weak bending resistance. Red blood cells are also known to have an interior viscosity that exceeds that of the suspending plasma; we consider this here, though it was not studied in the two-dimensional model.

The source of this instability is unknown, particularly in how it might be affected by cell properties or flow configurations, which can be altered, for example, by disease in red blood cells. In addition to the basic role of blood cells in transport through the microcirculation [81,160,161], many important microcirculatory flows are potentially sensitive to this change in character: the cell-free layers that form near vessel walls [162–164], the margination of leukocytes or platelets [102–105,165], intravenous drug-delivery of particles and capsules for which both cross-stream transport and the thickness of the near-wall cell-free layer can be important [166], the hemodynamic forces that mediate angiogenesis [167] and development [166,168,169], and tumor growth in cancer [170]. Cell-train stability is potentially even more important for microfluidic devices designed to manipulate the flow of cells or engineered capsules in order to perform sorting or other processing [171–176]. In such devices, it is seemingly easiest to develop processing procedures that operate on ordered trains rather than chaotic and disperse arrangements.

Thus, we focus on the character of the transition between the orderly flow, typically seen in the narrowest tubes or vessels [138,143], and its apparently chaotic counterpart, typically seen in less confined configurations [144,145]. Our goal is to identify factors mediating its transition, the rate at which disturbances amplify, and the character of the most amplifying disturbances. A three-dimensional flow of uniformly spaced red blood cells, which empirically displays this threshold behavior, is analyzed as a model system.

Our analysis is similar in spirit to stability analyses of settling rows or columns of rigid spheres in free space [177–179] or near a wall [180], which is analytically tractable in the limit of infinitesimal spheres, though often by neglecting interactions beyond nearest neighbors. The stability of one-dimensional droplet arrays has also been studied [181–186], though the simplicity of the droplet flow system enabled an illuminating analytic linearization of the governing equations. We have been unable to find a usefully simplified analytical description for elastic membranes. While similar in character to these simpler configurations, our study includes all viscous-flow interactions, including the coupled elastic stresses in the deformable capsule membranes. This complexity necessitates some reliance upon numerical methods, though the stability behavior itself is relatively clear.

While this many-cell confined flow system is complex, it is time-stationary in the cell velocity. More challenging is capsule motion in homogeneous shear flow, which requires a stability formulation that accounts for the time dependency and is considered next.

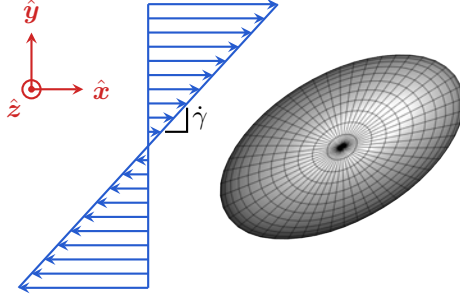


Figure 1.4: Schematic of the model homogeneous shear flow system and velocity field.

1.4 Stability of capsules in homogeneous shear flow

Determining the terminal dynamics of capsules in simple flows is a long standing problem. In particular, the stability of capsule motion when subject to homogeneous shear flow is thought to be important. If capsules undergo steady or periodic motion for particular flow conditions, we anticipate less collective viscous resistance. However, if the motion of a capsule in shear flow is fundamentally unstable, we can anticipate this to cause greater resistance to flow. Unsteady capsule motion can also be expected to cause additional stress on the capsule membranes, which can be often be fragile [187–189]. Studies of capsule stability in this respect have been based upon simulations, with the stability characterized by empirical observations of the flow system. We introduce direct stability analysis of this system. Like the empirical studies that guide it, our analysis relies upon numerical simulations. These are used to construct a linearized system for analysis, which is advantageous as it predicts the linear evolution, and thus the stability, of perturbations spanning the entire space of possible membrane disruption according to our description of its surface.

We focus our investigation on spherical and ellipsoidal capsules in simple shear flow, as shown in figure 1.4. This flow is known to produce a rich set of capsule kinematics, which depend upon the capsule shape and flow strength [190]. Computational studies have considered flow in both the Stokes limit [190] and with finite inertia [191, 192]; here, we only consider the viscous limit. The first efforts found that capsules with their revolution axis placed in the shear plane (\hat{x} – \hat{y} plane, here) were bound to remain in it [193–199]. For prolate capsules, weak flow strength, and long times, capsules have been observed undergoing a rolling motion, where the membrane rotates around the deformed capsule shape. For larger flow strength, the capsule precesses around the flow vorticity axis (\hat{z} , here), and for still larger flow strengths a swinging motion is observed, where the membrane rotates and undergoes oscillatory deformation [190, 192]. Oblate capsules have been observed undergoing similar motions at long times [191, 192, 200]. For weak flow strength, the capsule displays a swinging motion. A wobbling motion has been observed for intermediate flow strength, where the capsule oscillates about an intermediate angle from the shear-plane (\hat{x} – \hat{y} plane, here), and for sufficiently strong flow the capsule undergoes a rolling motion.

Experiments of artificial capsules significantly deviating from spherical shapes do not exist, as reliable techniques to fabricate them have not been developed (see section 1.1).

However, manufactured ellipsoidal capsules of shape slightly deviating from spherical have been observed undergoing significantly different behavior than spherical capsules [201, 202]. For small shear-rates, a tumbling regime exists, and a swinging regime has been observed at larger shear rates. Red blood cells are ubiquitous examples of oblate capsules and have been observed experimentally for a long time. While red blood cells are more complex than artificial capsules, they can still serve as a reference for computational efforts. Red blood cells in homogeneous shear flow have been observed undergoing a tumbling motion at small shear-rates and a swinging motion at larger shear rates [203–205]. However, the tumbling behavior was later found to be unstable, subsequently undergoing a rolling, then tank-treading motion [206–208].

Previous simulation-based studies have observed the long-time motion of ellipsoidal capsules to be independent of the initial capsule orientations they test, as quantified by the inclination of the capsule out of the shear-plane [190, 200], except for an instance of conflicting results [191], previously hypothesized to be due to too short of computation times [200]. However, this empirical result does not necessarily fully classify the stability, as it does not consider perturbations beyond the initial tilt of the capsule, such as those involving membrane deformations. It is known that particular membrane deformations can be unstable in other capsule flows, such as those found for slender capsules in sufficiently strong extensional flow [209] and capsule-trains flowing within channels [158] and tubes [137], so we anticipate this type of instability is possible for a capsule in simple shear flow. Our goal is then to classify the stability of these long-time capsule motions according to an accurate representation of its surface. This is done through a detailed linear stability analysis which spans all possible capsule disturbances as deduced from a spectral description of the membrane, and determines the rate at which perturbations grow or decay.

Our analysis is most closely related to the Floquet stability analysis of axisymmetric rigid particles in shear flow with weak inertia [210], though the simplicity of the rigid particle dynamics allowed for an analytic linearization of the governing equations about the periodic particle motion, and thus the stability. The deformable membrane introduced here presents additional complexity, and seems to preclude a direct extension of this previous method.

We next discuss another time-dependent capsule flow system, namely that of large amplitude oscillatory extension. This system introduces important nonmodal and time-global instabilities [211], requiring an extension of the stability analysis, and is discussed next.

1.5 Stability of capsules in large-amplitude oscillatory extensional flow

Oscillatory rheometry is often used to measure the rheological properties of polymer solutions and blends [212, 213], melts [214], and colloidal [215] and capsule suspensions [216, 217]. We focus on the large-amplitude oscillatory extensional flow (LAOE) shown in figure 1.5, which is used to quantify nonlinear viscoelastic and extensional flow phenomena, such as the unraveling and alignment of flexible bio-filaments [218]. While bulk properties of complex fluids, such

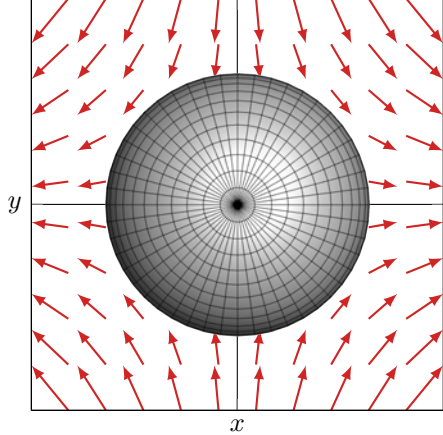


Figure 1.5: Schematic of the LAOE model flow system.

as melts and cross-linked polymer networks [219, 220], have been successfully examined using LAOE for a long time, micro-scale single particle studies are more challenging. A cross-slot flow is useful for examining such particles in extensional flow [221–224], and a sophisticated control mechanism seems necessary to maintain the particles position. Though complex, these techniques have enabled examination of polymer strands, including DNA [225, 226]. Quantifying the instabilities of such flow configurations, especially when the particles of interest are themselves complex, is potentially informative for the design of such microfluidic traps and devices. Here, we investigate this stability directly through a linear Floquet analysis of a model flow system.

Here we consider elastic capsules as canonical soft particles (visualized in figure 1.5). A steady flow version of a similar system has been studied; these efforts used numerical simulation [209, 227, 228] and experimental observation [229, 230] to identify shape instabilities of elongated axisymmetric vesicles in uniaxial axisymmetric extensional flow. The conformation and growth rate of the instabilities were found to depend upon the strength of the flow and the shape of the vesicle, with sufficiently round shapes being stable for all flow strengths. Capsules and vesicles in oscillatory flow can exhibit qualitatively different motion and stability than the steady-flow version of the same system, such as ellipsoidal or biconcave capsules in oscillatory [231–233] versus steady homogeneous shear flow [190, 198, 200, 207], so we anticipate capsules in oscillatory extension could share this behavior. Further, the shear resistance of a typical capsule membrane, often absent in models of vesicles, can be expected to qualitatively influence the stability of its motion as it does for capsules-trains flowing in tubes [137].

While this flow system is time-periodic, the capsule undergoes large deformation over the course of the period, and so we anticipate that intra-period effects can be important to its stability. Thus, a nonmodal and time-global linear Floquet stability analysis is appropriate for this system, which we discuss in the next section.

1.6 Linear stability analysis

The aforementioned capsule flow systems are analyzed through a linear stability formulation, which includes both eigensystem and singular-value analyses for predicting long-time and transient behavior of perturbations, respectively. Here, these methods are adapted to the fluid–structure coupled system in the viscous-flow limit, which includes full coupling between the capsule membrane and the interior and suspending fluid using a boundary integral method.

Beginning with the capsule-train system of chapter 4, we introduce a linearization about the axisymmetric and steadily-advection train is constructed via a full-rank set of orthogonal small disturbances based upon the capsule membrane description. This gives a matrix that describes the coupling between any small disturbance and the unperturbed base flow, which can be analyzed through traditional methods [234, 235].

We then extend this formulation to time-periodic flows, beginning with capsules in homogeneous shear in chapter 5. The periodicity of this system enables the use of traditional Floquet methods. In these cases, the system is linearized about the evolving configuration, which is represented by a discrete set of temporal realizations representing one period of the flow. This representation facilitates the time-integration necessary to determine the stability.

Finally, capsules in LAOE flow, as discussed in chapter 6 undergo large deformation over the course of one period. As a result, we anticipate that nonmodal and intra-period effects might be important. Thus, the previous asymptotic Floquet formulation is extended to consider this through singular value analysis. In all cases, direct numerical simulations are used to verify the predicted amplification rates.

1.6.1 Previous studies

Our formulation follows a similar approach to that used to analyze shear-flow instability at larger Reynolds numbers [234–240]. Similar non-modal stability analyses have also been used to study rheologically complex flows [241–243], but do not appear to have been used to analyze the behavior of confined particle suspensions, such as we consider here for flexible capsules.

The Floquet methods introduced for the time-periodic flows we consider have also been useful in understanding other complex flow phenomena: Flow in driven cavities [244–246] and oscillating channels [247] and pipes [248–250]; vortex streets of flow past rings [251, 252] and objects of square [253] and circular [254–256] cross-sections; pulsatile channel flow [257–260]; and Stokes layers which arises over an oscillating boundary [261–265] have all relied on Floquet methods to classify their stability. Given the complexity of these problems, an analytic Floquet formulation is rarely available and there is reliance on numerical methods. Such computations are often prohibitively expensive when the fluid itself is discretized, given the size of the discrete system in space, combined with the periodic time-dependence. This motivated proper orthogonal decomposition (POD) [266, 267], dynamic mode decomposition (DMD) [268, 269], and Koopman operator methods [269, 270] for constructing data driven reduced systems. However, there is little previous work on Floquet problems that include

fluid-structure interaction, such as we consider here with a fully coupled elastic membrane-viscous flow system.

1.7 Overview and key findings

1.7.1 Overview of dissertation

The physical capsule model is introduced in chapter 2, which is extended for the specific flow configuration in subsequent chapters. The numerical methods used to solve for the flow have been developed previously [4], are described for completeness in chapter 3, including the capsule surface description in section 3.1, the boundary integral formulation in section 3.2, the enforcement of a no-slip wall surface in section 3.3, and the capsule volume constraint in section 3.5.

Red-blood-cell-train stability is found in chapter 4. In section 4.1, the model blood vessel system and numerical implementation are detailed. The time-stationary linear stability analysis is described in section 4.2. Results in section 4.3.2 show transiently and asymptotically unstable disturbances and their amplification rates for different vessel diameters and packing densities. The long-time evolution of these disturbances, along with randomized *ad hoc* disturbances for comparison, are tracked into a nonlinear and disordered regime through direct numerical simulations (DNS) in subsection 4.3.2. Sensitivity of the train stability to cell-interior viscosity, membrane flexibility, and cell volume is also assessed, using a long-established nominal physiologic red-blood-cell model as a baseline case. The strain energy required to form the most amplifying disturbances is quantified in section 4.3.6.

Ellipsoidal capsules in homogeneous shear flow are then considered in chapter 5. Details of the specific physical model system and numerical implementation are discussed in section 5.1. We verify that our simulations reproduce particular results of previous studies in section 5.2; these also serve as the time-periodic base flows for the subsequent Floquet analysis. Our stability analysis is then extended from the time stationary formulation in section 5.3. The stability of the capsule motion, as deduced by our Floquet analysis, is presented in section 5.4 for a range of flow strengths.

The stability of spherical capsules in LAOE flow is investigated in chapter 6. The specific physical model and details of the numerical method are in section 6.1. In section 6.2 we present our construction of the time-periodic base-flows for analysis. The asymptotic Floquet analysis used to study capsules in homogeneous shear is extended to a global and non-modal effects in section 6.3. We verify our analysis and assess the capsule stability for cases of varying flow strengths and oscillatory time scales in section 6.4.

We present a cohesive set of conclusions and possible directions for future work in chapter 7. This includes a discussion of reduced models for anticipating red-blood-cell-train behavior, including continuum-based and rigid-sphere systems. Further detail on these hypotheses are found in the appendix.

1.7.2 Key findings

Red-blood-cell-trains

- The stability of flowing trains of red blood cells is quantified for varying vessel size, cell-cell spacing, cell shape, viscosity ratio between the interior and exterior fluids, and flow strength.
- Cell trains of moderate cell-cell spacing are asymptotically marginally stable for sufficiently small vessel diameters.
- All trains are transiently unstable, though this growth saturates quickly. Further, transiently unstable perturbations cannot form spontaneously due to thermal fluctuations as they entail large strain energy.

Capsules in homogeneous shear flow

- Swinging and rolling oblate capsules in homogeneous shear flow are asymptotically stable.
- Nearly all capsule perturbations dissipate completely before one period of the flow has elapsed.

Capsules in large-amplitude oscillatory extensional flow

- Spherical capsules in LAOE are asymptotically stable for all flow strengths and flow periods.
- All cases are transiently unstable, though this instability saturates quickly, and is thus expected to be unimportant for most applications.
- Spherical capsules exhibit an intra-period instability associated with a translational disturbance, which is able to amplify many orders of magnitude in some cases. This instability matches that of a rigid infinitesimal particle in the same flow.

2 Capsule model

2.1 Models of capsule mechanics

Herein, we develop a model for red blood cells flowing in the microcirculation, which will also serve as a model of artificial capsules that are often more simple in character. As discussed in section 1.1, red blood cells are natural capsules that encapsulate a very nearly Newtonian hemoglobin solution, though its rheological properties have not been thoroughly studied. We assume this fluid to be Newtonian, which is known to be a good assumption in the microcirculatory flows we will consider.

The elastic membrane of the red cell is highly deformable and can undergo large deformation in response to shearing and bending forces, allowing them to flow through capillaries even smaller than the nominal cell diameter. However, the membrane is nearly incompressible; that is, it maintains a nearly constant surface area due to a strong resistance to dilatation, a characteristic of its lipid bilayer structure.

The mechanics of red blood cell membranes have been modeled at varying levels of detail, from discrete representations of its molecular structure to purely continuum-based approaches, which are utilized as appropriate for the flow they are suspended in. We consider these in turn.

2.1.1 Discrete models

Discrete representations of red blood cells membranes attempt to faithfully model its molecular detail. Efforts to this end have described the membrane spectrin network down to the level of individual junctions using, for example, bead chain mechanics [271–273]. However, these models entail a very fine surface resolution, and have thus been computationally prohibitive for long simulations of many-cell flows. To this end, coarse-grained methods have been developed at varying levels of granularity, describing the microstructure more efficiently and reducing the degrees of freedom required [274–277]. This has facilitated larger simulations of models that represent the membrane microstructure, and in some cases yields simulations even more efficient than continuum-based representations [278].

These models have proved invaluable in simulations involving very large deformation or finite-temperature cell deformation, such as those involving micropipette aspiration [276, 279, 280] or deformation with simulated optical tweezers [271, 281, 282]; flows where the molecular structure itself is anticipated to be important, such as those involving diseases processes [283, 284] or cell aging [285, 286]; or flows involving cell lysis (membrane destruction), where a continuum model is clearly inappropriate [174, 287], or plastic deformation for which a purely elastic representation cannot model the mechanics [288, 289].

2.1.2 Continuum-based models

Thin-shell elastic continuum models have been developed as simplistic representations of complex capsule membranes, such as that of the red blood cell. These efforts have modeled the shear, dilatation, and bending resistance of actual membranes. As a result, continuum-based approaches have been successful in reproducing important properties of complex capsule suspensions. For example, these thin-shell models have reproduced the effective viscosity [4], Fåhræus effect [143], blunted velocity profile [144], specific membrane deformation [143, 290], and wall shear stress footprint [75] of microcirculatory flow. Thus, explicitly modeling the microstructural detail of red cell membranes is not required to reproduce these important properties of the flow. Commensurate with the goals of this work, which only require an accurate representation of these complex flow properties, we will utilize a thin-shell elastic model and do not consider the molecular makeup of any specific capsule.

We note that red blood cells also have a surface viscosity due to their lipid bilayer structure, estimated by extensional creep test simulations and experimental observations to be about 0.04 Pa·s [291, 292]. Mesoscale models that incorporate a finite membrane viscosity have found this contribution to only be important in extreme flow conditions, such as for the membrane loss modulus as computed from twisting torque cytometry simulations, which are utilized as simplifications of optical magnetic twisting cytometry experiments [291, 293]. However, the properties of microcirculatory flow simulations under physiologic conditions, such as those listed above, are known to be independent of the inclusion of such a membrane viscosity [70, 294, 295], and so we will ignore it.

While a thin-shell continuous elastic model is appropriate for our purposes, there are still many choices for modeling finite-deformation capsule mechanics, agnostic of the molecular makeup or origin of any particular membrane. Neo-Hookean membrane models have been used [296–299] and could be easily implemented. While they display a strain stiffening behavior (with a linear dependence of membrane tension on its deformation), this law only includes a shear modulus and, thus, its resistance to dilatation is not adjustable. As such, the neo-Hookean model is not considered to be appropriate for modeling nearly incompressible red blood cell bilayer membranes, or other capsules that strongly resist dilatation. The Mooney–Rivlin constitutive law has also been used to model capsule membranes [201, 296, 300]: it behaves as a rubber-like three-dimensional incompressible material, though its variation in thickness is often assumed to be negligible in these instances. However, the Mooney–Rivlin model is strain-softening, and is thus inappropriate for most capsule membranes, except those manufactured using interfacial polymerization techniques [301, 302].

Most appropriate for our purposes is the Skalak constitutive law, developed specifically for modeling red blood cells [143, 303] and has the ability to reproduce important microcirculatory flow characteristics, such as the effective viscosity behavior and blunted velocity profile discussed previously. Further, the Skalak law is highly versatile: its independent shear and dilatation moduli have proven useful for modeling artificial capsules generally [296, 304]. For nearly incompressible membranes, such as those of red blood cells, the dilatation modulus is simply set to be very large. The Skalak model also displays a strain stiffening behavior, which is considered typical for actual capsules [296, 305]. Thus, we choose the Skalak constitutive

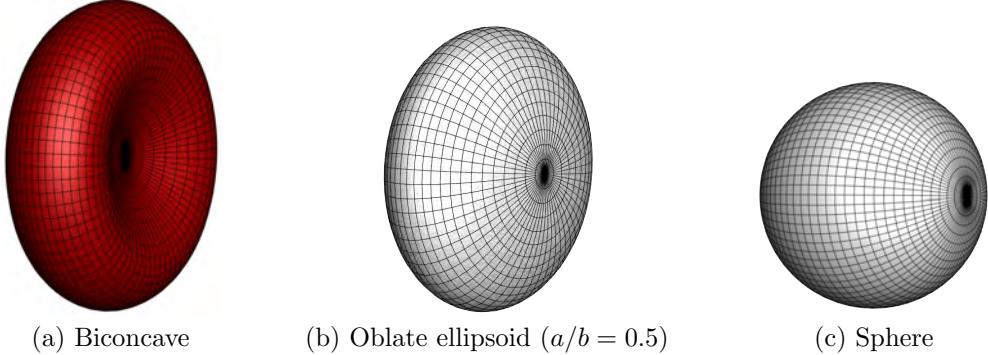


Figure 2.1: Example capsule reference shapes as labeled.

model for our purposes. However, we note that our numerical scheme is only loosely tied to this particular constitutive model, and this choice can be changed as necessary.

2.2 Skalak membrane constitutive model

The Skalak membrane model is given by its strain energy functional:

$$w = \frac{E_s}{8} (I_1^2 + 2I_1 - 2I_2) + \frac{E_d}{8} I_2^2, \quad (2.1)$$

where E_s and E_d are the independent shear and dilatation moduli, respectively,

$$I_1 = \lambda_1^2 + \lambda_2^2 - 2 \quad \text{and} \quad I_2 = \lambda_1^2 \lambda_2^2 - 1, \quad (2.2)$$

are the usual strain invariants [4, 303] and $\lambda_{1,2}$ are the eigenvalues of the left Cauchy–Green tensor $\mathbf{V} = \mathbf{F} \cdot \mathbf{F}^T$, where \mathbf{F} is the surface deformation tensor. We enforce bending resistance through a linear isotropic material model with modulus E_b [4, 306].

2.3 Membrane shapes

Herein, we will consider capsules of different reference shapes, including a biconcave disc for the red blood cells of chapter 4, ellipsoidal for the capsules of chapter 5, and spherical for the capsules of chapter 6; these are visualized in figure 2.1. Following Pozrikidis (2005), the biconcave shape typical of a healthy red blood cell (discocyte) can be expressed in cylindrical coordinates as

$$\begin{aligned} x &= r_o \frac{\beta}{2} (0.207 + 2.003 \sin^2 \phi - 1.123 \sin^4 \phi) \cos \phi, \\ r &= r_o \beta \sin \phi, \end{aligned} \quad (2.3)$$

which is based upon microscopic holographic measurements of actual red blood cells [307]. In (2.3), x and r are the axial and radial positions of the membrane, $\phi \in [0, \pi]$, $\beta = 1.385$, and r_o is the radius for a sphere of the same volume. The ellipsoidal reference shape we will

use is expressed in Cartesian coordinates $\mathbf{x} = \{x, y, z\}$ as

$$\left(\frac{x}{a}\right)^2 + \left(\frac{y}{a}\right)^2 + \left(\frac{z}{b}\right)^2 = 1, \quad (2.4)$$

where a/b is the aspect ratio; this gives $r_o = (ab^2)^{1/3}$. For $a/b < 1$ the ellipsoid is called oblate and for $a/b > 1$ it is prolate. Of course for $a/b = 1$ it is simply spherical. Both the exterior and interior fluids are Newtonian and incompressible, with viscosity μ and $\lambda\mu$, respectively.

3 Numerical methods and solution

Details of the numerical methods used to solve for the flow of a model capsule system are described herein. The most complex flow we will consider is shown in figure 3.1 and serves as an example system for describing our methods.

3.1 Capsule surface representation

Capsule membranes are represented by spherical harmonics according to

$$\mathbf{x}(\theta, \phi) = \sum_{n=0}^{M-1} \sum_{m=0}^n \tilde{P}_n^m(\sin \theta)(\mathbf{a}_{nm} \cos m\phi + \mathbf{b}_{nm} \sin m\phi), \quad (3.1)$$

where \mathbf{x} is the capsule membrane, \tilde{P}_n^m are normalized Legendre polynomials,

$$\tilde{P}_n^m(x) = \frac{1}{2^n n!} \sqrt{\frac{(2n+1)(n-m)!}{2(n+m)!}} (1-x^2)^{m/2} \frac{d^{n+m}}{dx^{n+m}} (x^2 - 1)^n, \quad (3.2)$$

and \mathbf{a}_{nm} and \mathbf{b}_{nm} are the coefficients of the expansion. The spectral description is advantageous as a relatively small number of modes are required to accurately describe the capsule shape and its derivatives, as well as for facilitating a nondissipative dealiasing method (for which $3M$ spherical harmonic modes are carried) for nonlinear stability [4]. The orthogonality of the spherical harmonic basis functions is particularly important for our linear stability formulation (see section 4.2).

The spherical harmonic coefficients are represented compactly as $\vec{s} = \{a_{nm}^{(i,j)}, b_{nm}^{(i,j)}\}$, where $i = 1, 2, 3$ is the vector coordinate direction index, $j = 1, \dots, N$ is the capsule index, and $n \geq m$ spectral expansion coefficient indices from (3.1), which together give a combined \vec{s} vector of length $3NM^2$. The corresponding discrete surface points are $\vec{x} = \{x^{(i,j)}(\theta_k, \phi_l)\}$ for coordinate direction i and capsule index j as computed by (3.1) over the unit sphere, where $\theta_l \in (0, \pi)$ for $l = 1, \dots, M$ are the colatitudinal Gauss points, and $\phi_m \in [0, 2\pi]$ for $m = 1, \dots, 2M$ are the equally spaced longitudinal points. The forward and reverse discrete spherical harmonic transforms can be expressed as

$$\vec{x} = \mathbf{B}\vec{s} \quad \text{and} \quad \vec{s} = \tilde{\mathbf{B}}\vec{x}, \quad (3.3)$$

where \mathbf{B} and $\tilde{\mathbf{B}}$ are $6NM^2 \times 3NM^2$ and $3NM^2 \times 6NM^2$ matrices representing (3.1) applied at the collocation points. All transforms are computed using the SPHEREPACK library [308, 309].

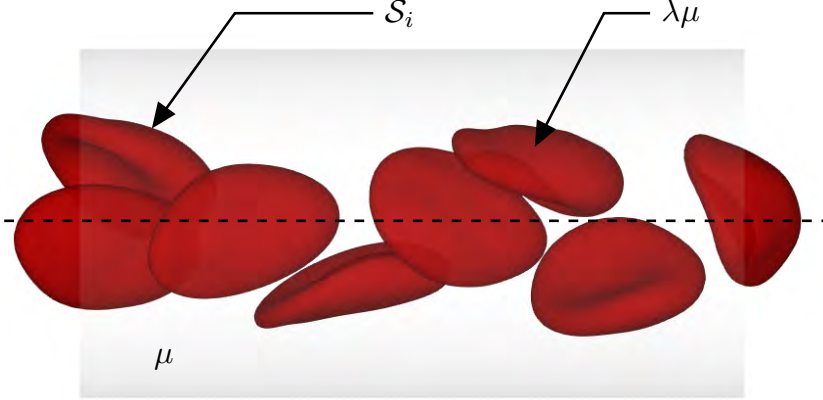


Figure 3.1: Schematic of a model flow configuration. \mathcal{S}_i are the surfaces of the $N = 8$ capsules and μ is the suspending fluid viscosity, and $\lambda\mu$ is the interior capsule viscosity, which we take to be the same for all capsules.

3.2 Governing equations and boundary integrals

The Reynolds number for capsule flows is generally small compared to unity, so inertia is assumed negligible in our formulation that is built upon the solution of the Stokes equations with point force inhomogeneity,

$$0 = -\nabla p + \mu \nabla^2 \mathbf{u} + \mathbf{g} \delta(\mathbf{x} - \mathbf{x}_o), \quad 0 = \nabla \cdot \mathbf{u}, \quad (3.4)$$

where p is the pressure and \mathbf{u} is the velocity. A standard boundary integral method is used to express (3.4) in terms of boundary integrals for the velocity [4, 159, 310–312],

$$\begin{aligned} u_i(\mathbf{x}_o) = & \frac{2}{1+\lambda} u_i^\infty(\mathbf{x}_o) - \frac{1}{1+\lambda} \frac{1}{2\pi\mu} \int_{\Omega} G_{ij}(\mathbf{x} - \mathbf{x}_o) \Delta\sigma_j(\mathbf{x}) dS(\mathbf{x}) \\ & - \frac{1-\lambda}{1+\lambda} \frac{1}{2\pi} \int_{\Omega} T_{ijk}(\mathbf{x} - \mathbf{x}_o) u_j(\mathbf{x}) n_k(\mathbf{x}) dS(\mathbf{x}), \end{aligned} \quad (3.5)$$

for coordinate direction $i = \{1, 2, 3\}$. In (3.5), \mathbf{x}_o is a point on a surface, \mathbf{u}^∞ is the mean flow in the $[0, L_1] \times [0, L_2] \times [0, L_3]$ rectangular computational domain, $\Omega = \cup_i \mathcal{S}_i$ is the union of all surfaces, $\Delta\sigma$ is the surface traction vector acting on the fluid, and \mathbf{n} is the normal vector to the surface. Note that when $\lambda = 1$, the last term of (3.5) vanishes and the equation becomes explicit in \mathbf{u} . Here, \mathbf{G} and \mathbf{T} are the so-called Stokeslet and stresslet Green's functions of the viscous-flow equations, the free-space representations of which are [159],

$$G_{ij}(\mathbf{x}_o) = \frac{\delta_{ij}}{\tilde{r}} + \frac{\tilde{x}_i \tilde{x}_j}{r^3} \quad \text{and} \quad T_{ijk}(\mathbf{x}_o) = -6 \frac{\tilde{x}_i \tilde{x}_j \tilde{x}_k}{\tilde{r}^5}, \quad (3.6)$$

where δ_{ij} is the Kronecker symbol, $\tilde{\mathbf{x}} \equiv \mathbf{x} - \mathbf{x}_o$, and $\tilde{r} \equiv \|\tilde{\mathbf{x}}\|$.

Direct computation of the Green's functions is expensive, scaling as $\mathcal{O}(N^2)$. For simulations with many capsules, such as the example system of figure 3.1, this computation can be prohibitively expensive. In these cases, fast summation methods are often used to improve the computational efficiency. In our simulations we use the particle-mesh Ewald (PME)

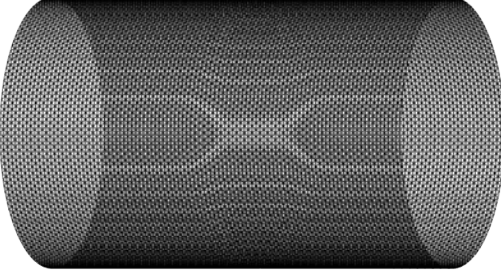


Figure 3.2: Schematic of an example cylindrical vessel

method, which splits the Green’s functions into short- and long-range components for more efficient computation [4, 313], yielding an $\mathcal{O}(N \log N)$ method (details of this method are available in appendix A). The fast multipole method has also been used for this objective, which groups long-range interactions for more efficient evaluation [314]. However, these formulations are typically built upon the free-space Green’s functions, and are thus not appropriate for the periodic many-capsule flows we will consider here.

The boundary integrals of (3.5) are then evaluated using a quadrature scheme for the collocation points \vec{x} [4], except for close interactions where a nearly-singular formulation of the integrands is used [4, 315].

3.3 No-slip wall representation

In some flow configurations, such as that of figure 3.1, we model a microvessel as a no-slip cylindrical surface. We represent this surface here by 6588 triangular mesh elements, as shown in figure 3.2), with force density represented with second-order linear elements as determined by a 7-point Gauss quadrature [159]. This mesh resolution has been shown to be sufficiently dense for the capsule dynamics to be insensitive to it in similar simulations [4, 110, 144]. When a capsule surface collocation point and wall point are very close, their interaction is singular or nearly singular and computed through a Duffy quadrature rule [316]. A single-layer potential, based on \mathbf{G} , is used to enforce the no-slip condition by solving for the required surface traction on the wall with a GMRES algorithm [4, 317].

We note this representation of the wall surface traction is ill-conditioned, with the condition number of the corresponding linear system increasing with the wall mesh refinement [4]. This conditioning can likely be improved through preconditioning [318], though this is not attempted here. For all reported simulations the maximum residual velocity is less than 10^{-4} within 100 GMRES iterations, which is sufficiently accurate for our purposes.

3.4 Time-integration

Once the velocity \vec{u} on the capsules is computed, the capsule surfaces are time advanced according to

$$\frac{d\vec{x}}{dt} = \vec{u}(\vec{x}), \quad (3.7)$$

or, in list form,

$$\frac{dx_i^{(\alpha)}}{dt} = u_i^{(\alpha)}(\vec{x}) \quad \text{for } i = 1, 2, 3; \alpha = 1, \dots, 2NM^2. \quad (3.8)$$

This is integrated using a first-order explicit method with time step Δt .

3.5 Volume constraint

Since both the interior and exterior fluids are modeled as incompressible, there should be no change in capsule volume. However, small numerical errors can accumulate in long-time simulations and pollute the solution. Our solution scheme addresses this through a variational formulation as a constraint, which adjusts the membrane surface in its normal direction [4]. This formulation is an extension of that used by Freund (2007) [165], and nearly preserves the capsule volume at every time step. Herein, reported simulations keep this adjustment below 0.001% of r_o per time step, though the stability analyses we conduct are wholly independent of this constraint.

4 Red-blood-cell-train stability

The first capsule flow configuration considered is that of flowing red blood cell trains, as introduced in chapter 1. For a study of a two-dimensional analog of this study, see appendix C. The simulation setup and specific details of the numerical methods relevant for this system are discussed in section 4.1. The time-stationary nonmodal linear stability formulation is in section 4.2 and its application to red-blood-cell-trains in different flow configurations is in section 4.3.

4.1 Simulation setup and details

4.1.1 Physical model system

The flow system is shown schematically in figure 4.1. It is a streamwise-periodic model microvessel of diameter varying from $D = 14$ to $34\text{ }\mu\text{m}$. This range includes cases for which cells are observed to flow in both ordered and apparently chaotic fashion. Red blood cells, modeled here as capsules, are initiated in their at-rest equilibrium biconcave geometry with size $r_o = 2.82\text{ }\mu\text{m}$, as described in chapter 2, with uniform spacing along the vessel center-line. Cells are advected due to a flow of mean velocity U until they reach a steadily flowing train of deformed cells. The stability of the cell train is expected to be sensitive to cell-cell spacing (as seen in figure 1.3), which we quantify with $\phi \equiv r_o N/L$, where N is the number of cells and L is the periodic length of the vessel. We vary ϕ between 0.2 and 0.7. Most cases have plasma viscosity $\mu_p = 0.0012\text{ Pa s}$ with matched cytosol viscosity $\mu_c = \mu_p$ for convenience and computation speed, however we also consider $\lambda \equiv \mu_c/\mu_p \neq 1$ in section 4.3.3.

The red blood cell model was described in chapter 2. Shear and bending moduli of the membrane are taken as $E_s = 4.2 \times 10^{-6}\text{ N m}^{-1}$ and $E_b = 1.8 \times 10^{-19}\text{ N m}$ respectively,

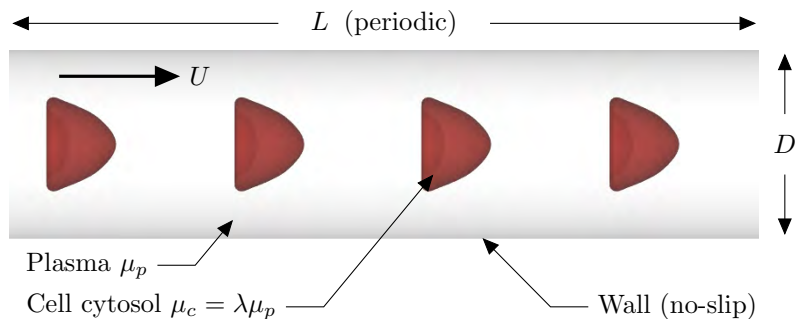


Figure 4.1: The model system.

which are based on experimental measurements, as discussed previously [3]. Red-blood-cell-membranes are known to be nearly incompressible, which is enforced here by a relatively large dilatation modulus $E_d = 67.7 \times 10^{-6} \text{ N m}^{-1}$, and we confirm the growth rates of section 4.3.2 are insensitive to this choice. Together, these parameters give a capillary number $Ca = \mu_p U/E_s$, which can be interpreted as a ratio of advection to relaxation times and is used as a measure of relative flow strength. The effect of changing Ca is studied in section 4.3.4. Though this model includes significant simplifications relative to an actual physiological blood flow, it is able to quantitatively reproduce the effective viscosity of microcirculatory flow [4, 144].

4.1.2 Numerical flow solution

The numerical methods used to solve for the flow were discussed in chapter 3; here, we present the details specific to the red-blood-cell-train simulations.

The total mean flow velocity in the $L_d \times L_d \times L$ rectangular computational domain is $\mathbf{u}^\infty = \{0, 0, \hat{U}\}$, where we use $L_d = D + 0.5$, and \hat{U} is useful for setting the flow strength [4]. However, \hat{U} does not exactly match U , since there is also flow outside the cylindrical vessel. Thus, U is determined by subtracting the flow rate outside the vessel from the total flow rate $L_d^2 \hat{U}$ and dividing by the cross-sectional area of the vessel [4]. U is then dependent on \hat{U} and the effective viscosity of the suspension within the vessel, though for the cases we consider ($U/D > 50 \text{ s}^{-1}$) the effective viscosity of microcirculatory flow is known to be shear-rate (U/D) insensitive [5]. In our computations we use $\hat{U} = 2.3 \times 10^{-3} \text{ m s}^{-1}$, and U/\hat{U} varies from only 1.244 to 1.256. Further, in section 4.3.4 we demonstrate that the growth rates we compute are only logarithmically sensitive to changes in Ca , and thus U . So, for our purposes, we will use a nominal $U = 1.25\hat{U} = 2.875 \times 10^{-3} \text{ m s}^{-1}$ for non-dimensionalization.

Herein, the spatial resolution is given by $M = 12$, as defined in (3.1), though we verify that the amplification rates of section 4.3 vary by only 1% for larger M . We use time-step $\Delta t = 0.0014 r_o/U$ for constructing the base-flows of section 4.3.1, though our stability analysis is wholly independent of time-integration and thus this choice. The no-slip condition on the vessel-wall is enforced using the method of section 3.3; we ensure that the maximum residual velocity of any cell collocation point when solving for the required wall surface traction is less than $10^{-4}U$, typically requiring less than 100 GMRES iterations. We again verify that the results of section 4.3 are independent of this choice.

4.2 Stability analysis formulation

4.2.1 Measure of configurational stability

To describe disturbances, we use a geometric displacement from the undisturbed uniformly advecting base state,

$$\boldsymbol{\varepsilon}(t) \equiv \mathbf{x}(t) - \mathbf{x}_b(t), \quad (4.1)$$

where the base state denoted by subscript b is further described in section 4.3.1. A similar strategy was used to study two-dimensional capsule trains, where displacements in the membrane surface in physical space \vec{x} quantified ε , though surfaces were represented using Fourier methods [158]. Fourier methods are unitary, so describing ε with either physical points or coefficients of the expansion are equally valid choices. However, the spherical harmonic methods we use here do not share this property. Indeed only the harmonic-to-physical space transformation can be computed unambiguously, as the physical-to-wave space transformation is overdetermined. Since our construction is built upon disturbances to $\vec{\varepsilon}$, we instead base our formulation upon the spherical harmonic coefficients \vec{s} :

$$\vec{\varepsilon}(t) \equiv \vec{s}(t) - \vec{s}_b(t). \quad (4.2)$$

By a generalization of Parseval's theorem, the norm of \vec{x} and \vec{s} are equivalent up to a constant [319], which is about 2.2 here, so we are ensured this is a proper measure for the disruption of the cell train. Specifically, this magnitude is quantified by the L_2 norm,

$$\|\vec{\varepsilon}\|^2 = \sum_{i=1}^{3NM^2} (\varepsilon_i)^2. \quad (4.3)$$

This metric is still not unique, however, and is not expected to be for such a complex system [234]. We note that an energy based metric, such as those often used for finite Re flows, is not implemented here since zero-strain-energy disturbances can drive the system to disorder through rigid-body-like tilts and translations [158].

4.2.2 Linearization

We linearize the fully-coupled flow system through direct evaluation of \vec{u} according to (3.8) for a disturbance to the spherical harmonic coefficients $\vec{\delta}$, which can be expressed

$$\vec{u}(\vec{x} + \mathbf{B}\vec{\delta}) = \vec{u}(\vec{x}) + \mathbf{C}\mathbf{B}\vec{\delta} + \mathcal{O}(\|\mathbf{B}\vec{\delta}\|^2), \quad (4.4)$$

where \mathbf{C} is unknown. Recasting (4.4) in terms of spherical harmonic coefficients and retaining only linear contributions,

$$\mathbf{A}\vec{\delta} = \tilde{\mathbf{B}}\vec{u}(\vec{x} + \mathbf{B}\vec{\delta}) - \tilde{\mathbf{B}}\vec{u}(\vec{x}), \quad (4.5)$$

where \mathbf{A} is a square matrix that contains the first-order coupling of the base state to the disturbance. We infer \mathbf{A} by systematically perturbing the system, computing the velocity, and performing the inverse spherical harmonic transform. Each column of \mathbf{A} is computed by disturbing one of the spherical harmonic modes $\alpha \in \{1, \dots, NM^2\}$ in one of the coordinate directions $i \in \{1, 2, 3\}$ and calculating $\tilde{\mathbf{B}}\vec{u}(\vec{x} + \mathbf{B}\vec{\delta})$. For each calculation, only the (i, α)

component of $\vec{\delta}$ is perturbed by δ , such that

$$\delta_j^\beta = \begin{cases} \delta & \text{for } j = i, \beta = \alpha \\ 0 & \text{otherwise,} \end{cases} \quad (4.6)$$

following the list notation of (3.8), which gives the (i, α) column of \mathbf{A} as

$$A_{ij}^{(\alpha\beta)} = \frac{\tilde{\mathbf{B}}\vec{\mathbf{u}}(\vec{x} + \mathbf{B}\vec{\delta})_j^\beta - \tilde{\mathbf{B}}\vec{\mathbf{u}}(\vec{x})_j^\beta}{\delta} \quad \text{for } j = 1, 2, 3 \quad \text{and } \beta = 1, \dots, NM^2. \quad (4.7)$$

Repeating this for each spherical harmonic coefficients and coordinate directions constructs the full $3NM^2 \times 3NM^2$ matrix \mathbf{A} . Since the spherical harmonic modes are mutually orthogonal, even in this formulation which exactly reflects the numerical discretization of the cell shapes, we are ensured that this \mathbf{A} describes the full linear dynamics of the system, which is confirmed in section 4.3 for $\delta = 10^{-3}$, which is used in most of the calculations. Once \mathbf{A} is constructed, any sufficiently small disturbance $\vec{\varepsilon}$ is governed by

$$\frac{d\vec{\varepsilon}}{dt} = \mathbf{A}\vec{\varepsilon}, \quad (4.8)$$

which has exact solution $\vec{\varepsilon}(t) = [\exp \mathbf{A}t]\vec{\varepsilon}_o$ for initial condition $\vec{\varepsilon}(0) = \vec{\varepsilon}_o$.

4.2.3 Eigensystem analysis and verification

Matrix \mathbf{A} is non-normal, as can be anticipated by the character of the vector Green's function of the Stokes operator, so in general it will not have a full set of orthogonal eigenvectors. As a result, transient growth is possible and the largest real eigenvalue of \mathbf{A} does not necessarily correspond to the maximum growth rate at all times [234, 320]. However, the eigensystem of \mathbf{A} nevertheless indicates the long-time asymptotic growth of small perturbations [235]. For $\vec{\lambda}(\mathbf{A})$ eigenvalues of \mathbf{A} , the spectral abscissa of the system is its largest real component, which bounds asymptotic growth,

$$\alpha \equiv \max \left\{ \operatorname{Re} \left[\vec{\lambda}(\mathbf{A}) \right] \right\}. \quad (4.9)$$

The corresponding eigenvector \vec{v}_α will amplify as $e^{\lambda_\alpha t}$ for $t \rightarrow \infty$. Similarly, the transient amplification rate for $t \rightarrow 0^+$ is bounded by the nominal numerical abscissa [234, 320],

$$\eta \equiv \max \left\{ \operatorname{Re} \left[\vec{\lambda} \left(\frac{\mathbf{A} + \mathbf{A}^T}{2} \right) \right] \right\}, \quad (4.10)$$

with corresponding eigenvector \vec{v}_η .

Example eigenvalues of \mathbf{A} are shown in figure 4.2. Similar to previous studies of two-dimensional capsule trains, most have $\operatorname{Re}[\vec{\lambda}(\mathbf{A})] < 0$ [158], and thus are asymptotically stable, which is perhaps expected for this viscous system. However, three eigenvalues do have positive real part, so the system is asymptotically unstable.

A comparison of the linear predictions of \mathbf{A} and corresponding direct numerical simulations

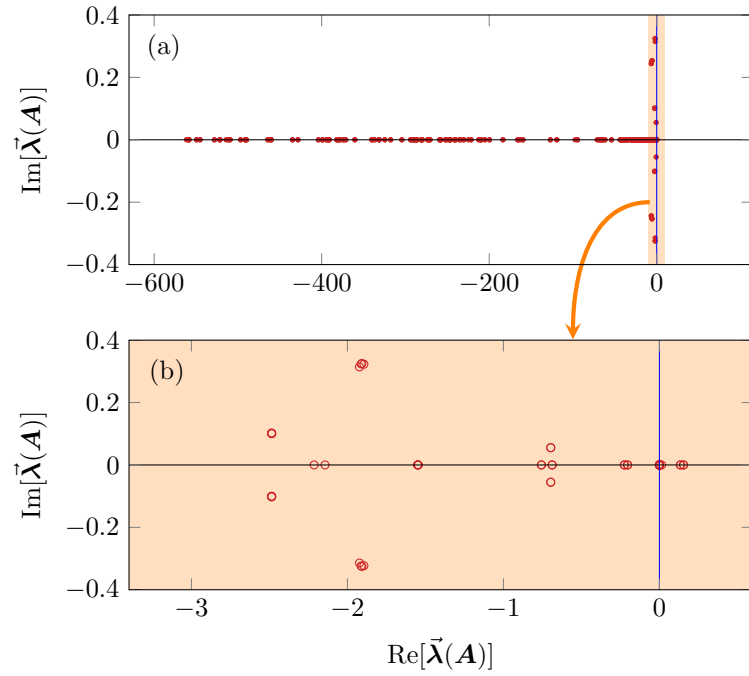


Figure 4.2: (a) Eigenvalues of \mathbf{A} for a two cell case with $D = 10r_o$, $\phi = 0.2$, and viscosity ratio $\lambda = 5$. (b) a magnification of (a) as indicated.

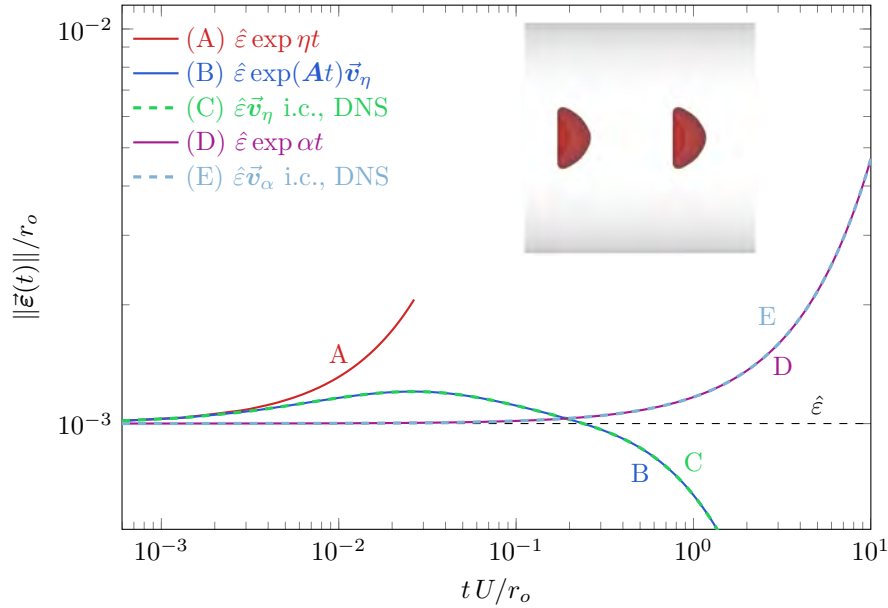


Figure 4.3: Verification of the example case with $D = 10$, $\phi = 0.2$, and viscosity ratio $\lambda = 5$ for initial disturbance amplitude $\hat{\varepsilon} = 10^{-3}$. Linear predictions of \mathbf{A} and DNS of the same initial conditions agree within plotting precision.

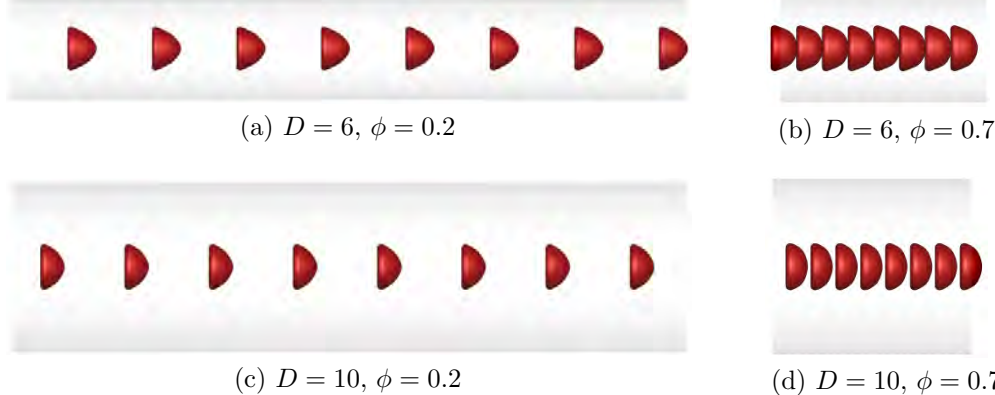


Figure 4.4: Example base configurations for $D = 6$ and 10 and $\phi = 0.2$ and $\phi = 0.7$.

(DNS) are shown in figure 4.3. While the growth determined by the numerical abscissa $\hat{\varepsilon} \exp \alpha t$ bounds transient growth for $t \rightarrow 0^+$, it is clear from figure 4.3 that the growth of this disturbance reverses after a relatively short time and decays below the most asymptotically amplifying disturbance \vec{v}_α by $t = 0.2U/r_o$. This non-monotonic behavior matches the matrix exponential $\hat{\varepsilon}[\exp At]\vec{v}_\eta$, which serves as a verification of its behavior at later times, as shown in figure 4.3. The growth of \vec{v}_α and its linear prediction match within plotting precision of all times.

4.3 Results

4.3.1 Base cases

Flows in different tube diameters D and packing ϕ are simulated to obtain a base state. These simulations are run until the maximum wall-normal velocity of any cell collocation point is less than $10^{-4}U$. Example steady base configurations are shown in figure 4.4. We focus on trains as shown with $N = 8$ cells; doubling N affects the unstable eigenvalues we identify by less than 1%, consistent with the short streamwise wavelengths on these maximally amplifying perturbations.

4.3.2 Matched viscosity ratio $\lambda = 1$

Extensive cases with $\lambda = 1$ are discussed in this section. The effect of $\lambda \neq 1$ is investigated for select cases in section 4.3.3.

Asymptotic behavior

As discussed in section 4.2, the long-time most amplifying growth of a disturbance to the cell train is given by the spectral abscissa. In the context of a cell train flowing through a microfluidic device, this growth gives a lower bound for the distance the train must travel before a small perturbation becomes large, and thus is valuable in these applications.

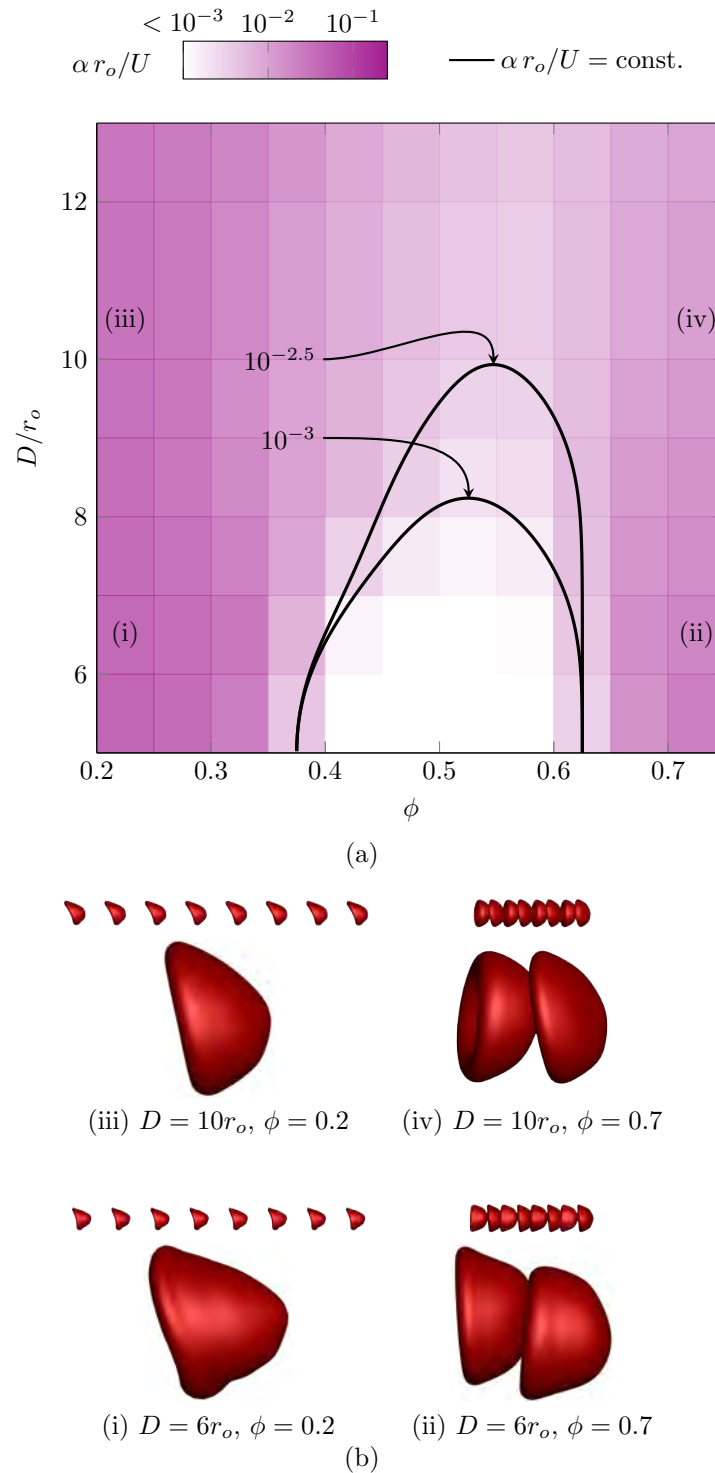


Figure 4.5: (a) Spectral abscissa α for a range of D and ϕ . The curves of constant α show a region of apparent marginal (or near-marginal, see text) stability. (b) Example \vec{v}_α for cases (i)–(iv) as labeled in (a), magnified for visualization as $\vec{s} + 10\vec{v}_\alpha$. The wrinkled appearance of (i) is due to the magnification of an otherwise small shape disturbance.

The dependence of α on D and ϕ is visualized in figure 4.5 (a). For $\phi = 0.2$ the system is unstable with $\alpha \approx 10^{-1}U/r_o$ for all tested diameters D , though the modestly smaller α for larger D suggest that increased cell–wall interaction is destabilizing. For this α and flow rate, a disturbance would amplify by a factor of 10 after flowing distance $30r_o$. The more packed cases with $\phi = 0.7$ also have $\alpha \approx 10^{-1}U/r_o$ for all D . However, for intermediate ϕ , growth is suppressed. That is, α increases with ϕ when $\phi > 0.55$ for any D , suggesting that cell–cell interactions themselves are most important in these cases. For $D \lesssim 10r_o$ and $0.4 \lesssim \phi \lesssim 0.55$ we find $\alpha < 10^{-3}$. Unfortunately, this is inconclusive, limited by the $\delta = 10^{-3}$ used to construct \mathbf{A} (as formulated in section 4.2). Smaller δ , better converged base states, and high resolutions would all likely be necessary to determine these α more precisely, though this would be challenging and likely unimportant in terms of the general conclusions. For $\alpha = 10^{-3}U/r_o$, the corresponding streamwise distance required for a disturbance to grow from $\hat{\epsilon} = 10^{-3}r_o$ to r_o is $\Delta z \gtrsim U \log(\hat{\epsilon}^{-1})/\alpha \approx 138\,000r_o$. Thus, it is sufficient to designate these cases to be marginally stable for our purposes. Their exponential amplification is markedly slower than the more obviously unstable cases we identify.

The corresponding disturbances are visualized in figure 4.5 (b) for select cases. Both the $\phi = 0.2$ cases have a uniform rotational disturbance, also seen for some two-dimensional capsule trains [158]. In contrast, disturbances associated with the $\phi = 0.7$ are wave-like, thought with only two cells per wave length. These seem to involve a combination of capsule translations and rotations.

Transient behavior

The numerical abscissa η is shown in figure 4.6 (a) for the same range of D and ϕ , for which it varies by about a factor of four, generally increasing with larger D and ϕ . This general behavior is similar to that for short, two-dimensional capsule trains, though it is insensitive to the periodic streamwise length of the tube, unlike in two dimensions.

The disturbances themselves shown in figure 4.6 (b) for select cases, and all are wave-like. In both the sparse $\phi = 0.2$ cases, a wave length has $\tilde{N} = 2$ and the disturbances are asymmetric in this case. Both of the more packed $\phi = 0.7$ cases have $\tilde{N} = 4$, and in contrast are asymmetric for $D = 6r_o$ and symmetric for $D = 10r_o$. These disturbances are similar in character to some of the (more extensively mapped) disturbances found for two-dimensional capsule trains [158], though without the apparent dependence on domain length found in that model configuration.

Although the transient growth rates of figure 4.6 are large, such that the disturbance would increase by a factor of 10 after traveling distance $0.4D$, this growth does not necessarily persist for small perturbations. Figure 4.7 shows the time evolution of example most-amplifying transient and asymptotic disturbances with $\hat{\epsilon} = 0.1r_o$. Transient growth is consistent with the linear prediction for short times, although it quickly decays with $\|\tilde{\epsilon}\| < \hat{\epsilon}$ by the time the cells have advected distance $\approx D$. These cases were selected because of their relatively large η , as seen in figure 4.6 (a), and the failure of such disturbances to trigger nonlinear interactions suggests a subservient role of the transient mechanism for small perturbations. In the analogous two-dimensional configuration, many transiently growing disturbances were

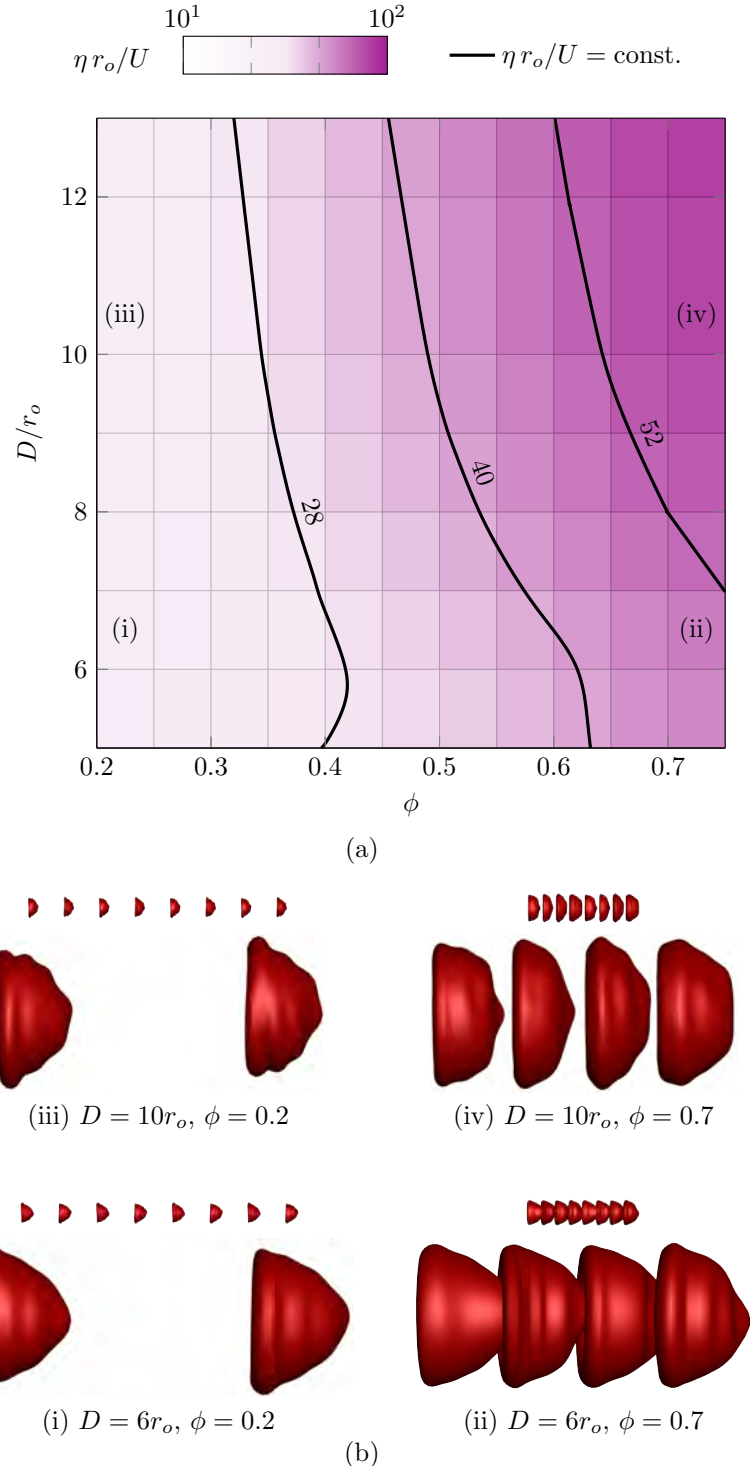
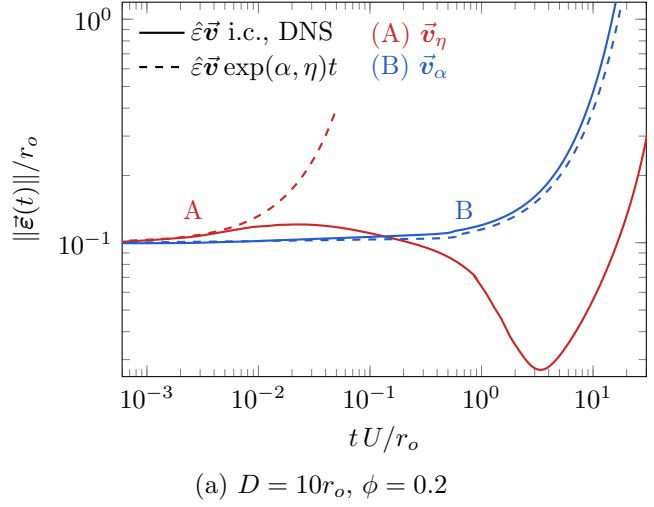
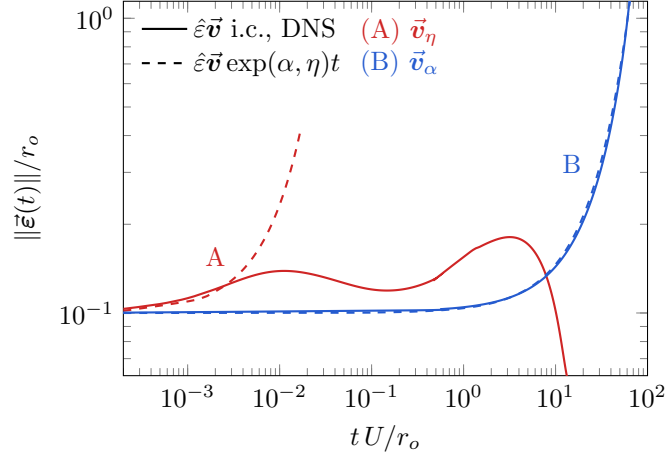


Figure 4.6: (a) Numerical abscissa η . Solid black lines denote an approximate curve of constant η , as labeled. (b) Example \vec{v}_η for cases (i)–(iv) visualized as $\vec{s} + 10\vec{v}_\eta$. Their kinky appearance is due to linear magnification of an otherwise small shape disturbance.



(a) $D = 10r_o, \phi = 0.2$



(b) $D = 10r_o, \phi = 0.7$

Figure 4.7: Time evolution of $\|\vec{\epsilon}(t)\|$ for the most amplifying transient and asymptotic amplifying disturbances and their linear predictions are shown with relatively large $\hat{\epsilon} = 0.1$ initial disturbance for cases (a) $D = 10r_o, \phi = 0.2$ and (b) $D = 10r_o, \phi = 0.7$. Linear predictions of \vec{v}_α remain good for long times as expected, though transient disturbances \vec{v}_η undergo rapid decay.

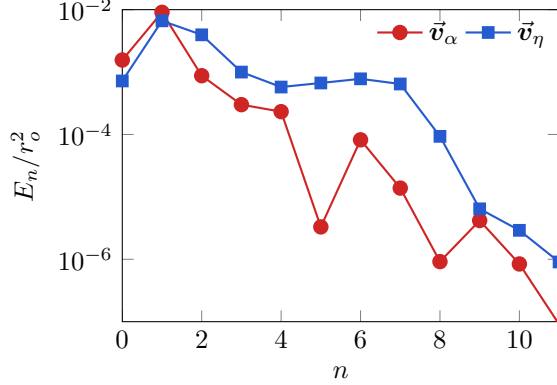


Figure 4.8: Cell-averaged deformation spectra for \vec{v}_α and \vec{v}_η for the case $D = 10r_o$ and $\phi = 0.7$.

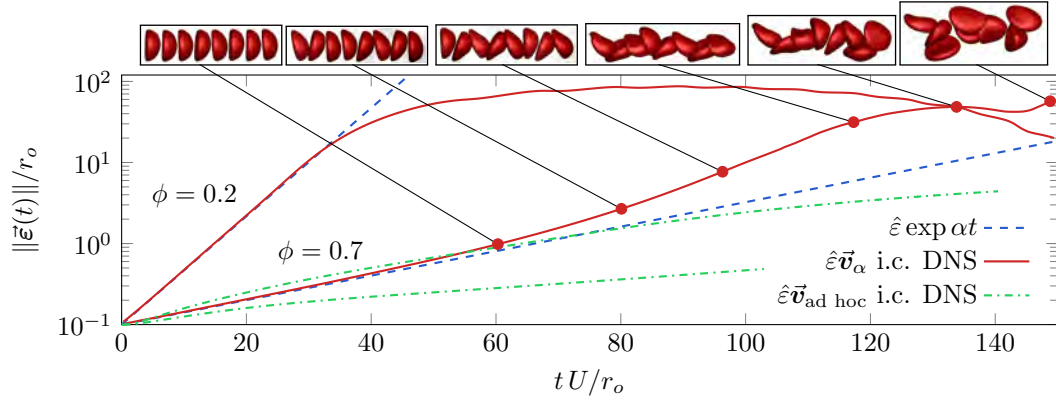


Figure 4.9: Time evolution of \vec{v}_α and an *ad hoc* disturbance $\vec{v}_{a.h.}$ with $\hat{\varepsilon} = 0.1$ and its associated DNS for cases with $D = 10r_o$ and $\phi = 0.2$ and 0.7 .

found to amplify to the point of nonlinear saturation [158]. DNS of such two-dimensional cases, disturbances amplified by a factor of 10 in less than two channel-widths of streamwise travel. In contrast, no such persistent transient growth was found here for blood cells.

Differences in the character of the disturbances for the most asymptotically and transiently amplifying disturbance can be quantified by their spherical harmonic spectrum:

$$E_n = \frac{1}{N} \sum_{j=1}^N \sum_{m=0}^n (|\mathbf{a}_{nm}^{(j)}|^2 + |\mathbf{b}_{nm}^{(j)}|^2), \quad (4.11)$$

where $\mathbf{a}_{nm}^{(j)}$ and $\mathbf{b}_{nm}^{(j)}$ are the spherical harmonic coefficients of the disturbance to cell j for the disturbance \vec{v} . In figure 4.8 we see that the \vec{v}_α are significantly smoother by this measure. The corresponding low-order moment contributions to the hydrodynamics away from any particular cell, might therefore be expected to be longer range, than the relatively broader spectrum of the \vec{v}_η modes. These are anticipated to be more hydrodynamically local, and we will also see that they carry significant strain energy.

Nonlinear saturation

Direct numerical simulation (DNS) shows the nonlinear development of these linear perturbation, leading to a disordered flow. Examples results are shown in figure 4.9, where they are compared with the their respective linear growth rates α . We see that the initial perturbations displace cells such that they are closer to the tube wall, where the flow is retarded. The relative slowing of these cells both affects the cell-cell spacing and seems to rotate them out of the train. Once this rotation becomes sufficiently large, they overturn and an apparently random long-time behavior is observed.

For comparison, the time evolution of an *ad hoc* translational disturbance $\vec{v}_{a.h.}$ is shown. This is manufactured by a randomly displacing the cells, without deformation, in each coordinate direction. This amplifies slower than \vec{v}_α by a factor of 4.3 for $\phi = 0.2$ and 2.7 for $\phi = 0.7$.

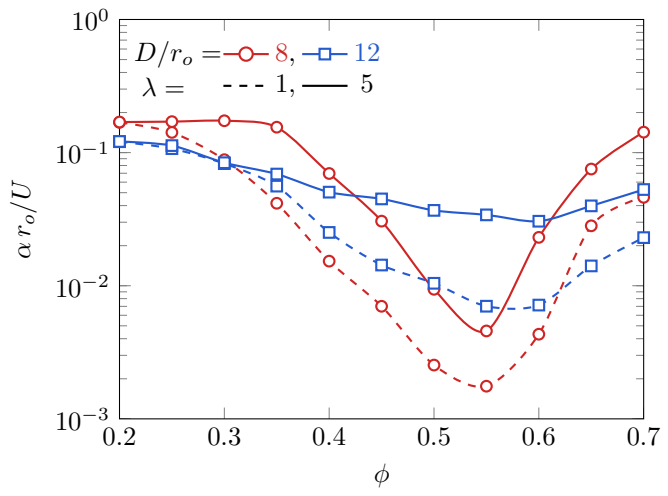
4.3.3 Effect of viscosity ratio λ

A healthy, newly-formed red blood cell is thought to have a cytosol viscosity $\lambda \approx 5$ times that of blood plasma [14], and this might increase as the cell ages [321–323]. Here, we consider both a $\lambda = 5$ nominally physiological case, as well as more extreme variations, including some unphysiological reduced cytosol viscosities. The base states of figure 4.4 still apply.

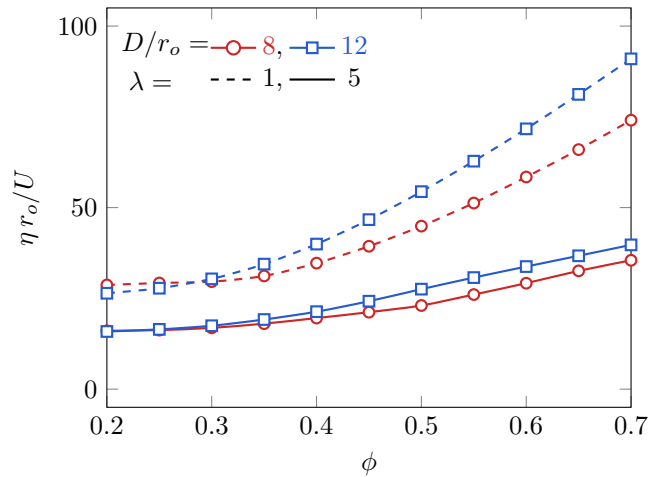
The asymptotic growth is increased for $\lambda = 5$, as seen in figure 4.10, except for the relatively sparsely spaced cases with $\phi \lesssim 0.3$. For larger ϕ , elevated $\lambda = 5$ increasing α by about a factor of 4 over the corresponding $\lambda = 1$ case. In contrast to the asymptotic behavior, η is suppressed by a factor of about 2 for $\lambda = 5$. We will see in section 4.3.6 that the shape-deformations associated with transient growth involve significant elastic strain energy, and speculate here that such disturbances decay more rapidly for larger λ due to larger viscous dissipation within the cell, and thus a smaller disturbance to the exterior flow.

Disease can alter the cell interior viscosity through deoxygenation [324, 325], and the exterior viscosity can be readily changed by altering the suspending fluids. Thus, we also consider $\lambda = 0.1$ up to 100 here. Spectral abscissa α is shown in figure 4.11 for these cases. For $\phi = 0.2$, increasing λ from 1 to 100 only increases α by about 10% for the cases shown. Once λ is sufficiently large, $\lambda \approx 20$ for the cases considered, α plateaus and it would seem that the cells effectively behave as rigid-bodies, as far as their stability is concerned. Interestingly, when λ is decreased from unity, the train is also more unstable. While this non-monotonic change in α is striking, the relative change is small for $\phi = 0.2$, likely due to the large distances between the cells. However, when the cell train becomes more densely packed, as for $\phi = 0.7$ in figure 4.11 (b), α is more sensitive to λ . Again, a non-monotonic behavior is observed, with $\lambda \approx 1$ seemingly the most stable. An approximate plateau in α is also observed in this case for $\lambda \gtrsim 20$.

The deformation spectrum E_n of \vec{v}_α for cases of various λ is shown in figure 4.12. For larger λ , E_n decreases more rapidly with n . This is expected as the more viscous interiors cause the cells behave more like rigid objects in the low-viscosity suspending fluid, and likewise the associated disturbances are more like rigid-body motions, with energy more confined to lower-order modes.

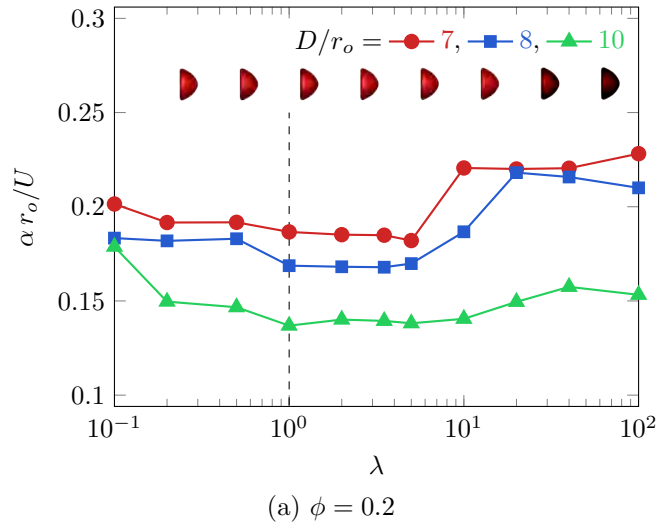


(a) Spectral abscissa

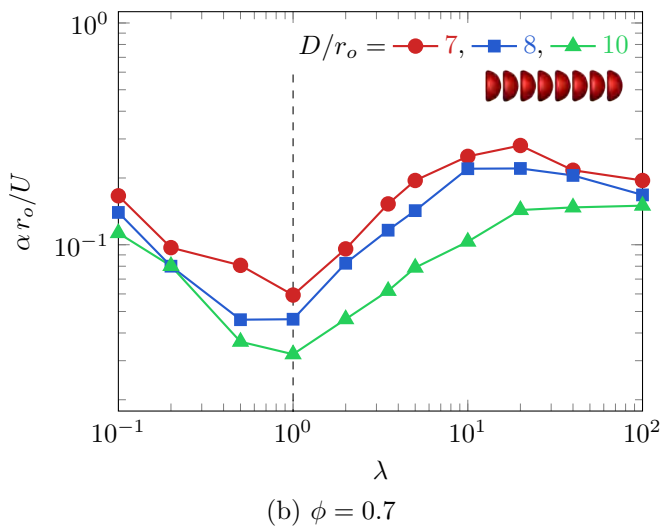


(b) Numerical abscissa

Figure 4.10: (a) Spectral and (b) numerical abscissa for $\lambda = 1$ and 5 and $D = 8r_o$ and $12r_o$ as labeled for various ϕ .



(a) $\phi = 0.2$



(b) $\phi = 0.7$

Figure 4.11: Spectral abscissa α for $0.1 \leq \lambda \leq 100$ for (a) $\phi = 0.2$ and (b) $\phi = 0.7$ for a range of λ .

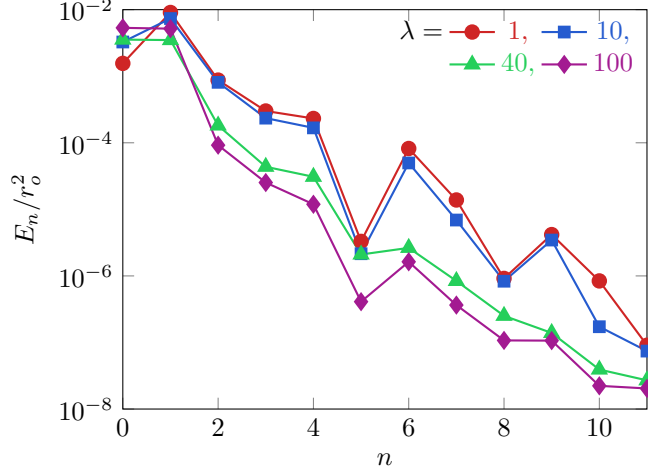


Figure 4.12: Cell-averaged deformation spectra for \vec{v}_α for the case $D = 10r_o$, $\phi = 0.7$, and λ as labeled.

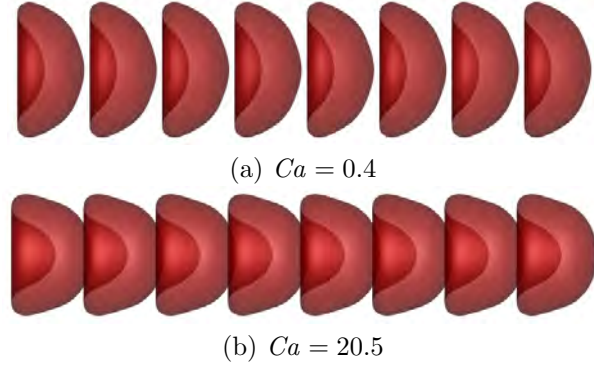


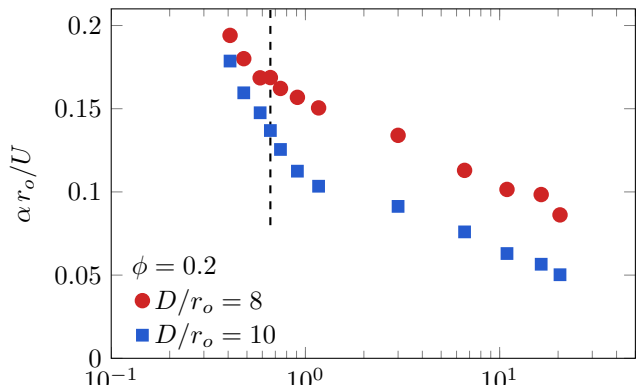
Figure 4.13: Cell trains with $D = 8r_o$ for the (a) smallest ($Ca = 0.4$) and (b) largest Ca ($Ca = 20.5$) we consider.

4.3.4 Effect of flow strength Ca

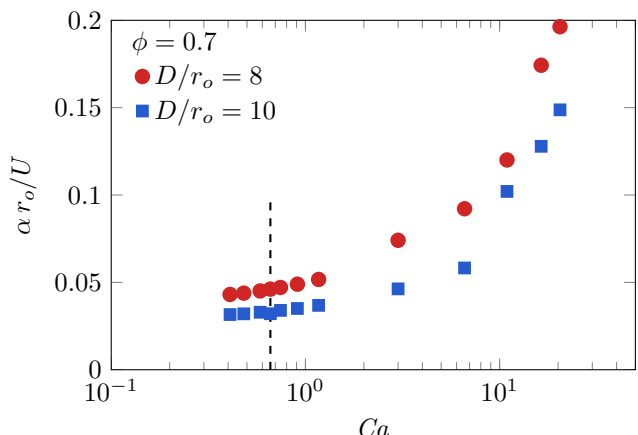
Flow strength $Ca \equiv \mu U/E_s$ is adjusted from 0.4 to 20.5, to understand its affect away from the $Ca = 0.66$ of the previous sections. The baseline configurations for the Ca extremes are visualized in figure 4.13..

The results are shown in figure 4.14. For $\phi = 0.2$, α decreases significant with Ca . Larger Ca results in more deformed cells, and thus a larger distance between the cells and the vessel wall, and comparatively smaller cell–wall interaction. Larger D , and thus smaller cell–wall interaction, was shown to have smaller α for $\phi = 0.2$ in section 4.3.2, which is consistent with this result.

In contrast, $\phi = 0.7$ are more unstable with increasing Ca , consistent with the results for two-dimensional capsule trains [158]. Larger Ca results in a smaller cell–cell spacing, which resulted in larger α (when increasing ϕ) in section 4.3.2 and is thus consistent with our result here.



(a) $\phi = 0.2$



(b) $\phi = 0.7$

Figure 4.14: Spectral abscissa for cell trains of diameters $D = 8r_o$ and $10r_o$, packing fractions (a) $\phi = 0.2$ and (b) $\phi = 0.7$, and $\lambda = 1$ for a range of Ca . Vertical dashed lines indicate the $Ca = 0.66$ used previously.

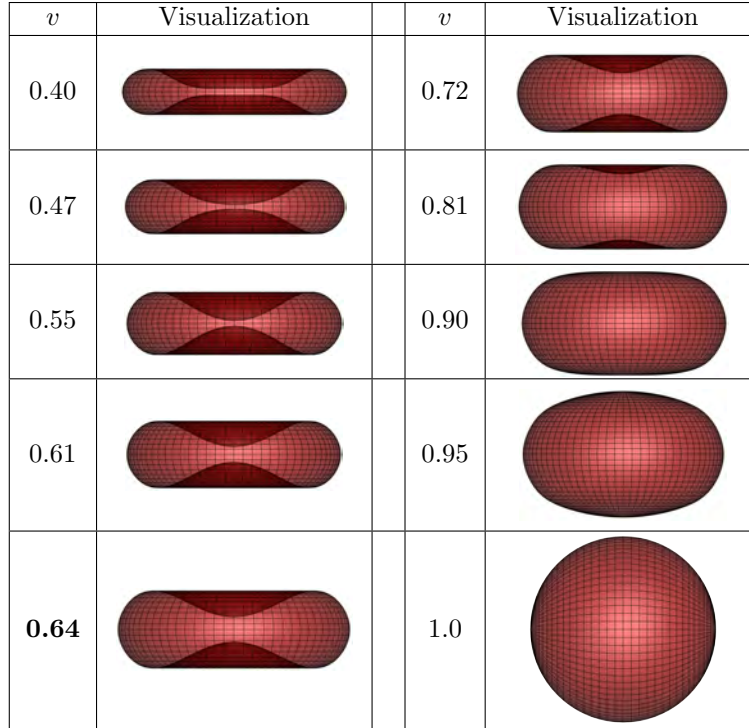


Figure 4.15: Example red blood cell equilibrium shapes for various levels of inflation and deflation, given by their reduced volume v . The reference healthy red blood cell used in previous sections has $v = 0.64$.

4.3.5 Effect of cell reduced volume v

Diseased or infected red blood cells often have modified shapes. Sickle or anemic cells are deflated [326], while elliptocytes and spherocytes are inflated examples of red blood cells [327, 328], so their stability in the context of a cell train is potentially important in the design of microfluidic devices used to operate on them. More generally, artificial capsules can be manufactured with a wide range of volumes [33]. Further, previous studies have shown the important effects such diseased or transformed cells can have on such flows in confinement [132, 329]. Here, we investigate the role of the cell geometry in the stability of the cell train by artificially inflating and deflating the biconcave reference configuration, otherwise matching the mechanical description of section 4.1.1.

In our simulations, we initiate a biconcave cell of increased (inflated) or decreased (deflated) volume V but the same membrane surface area as a healthy red blood cell. Healthy red blood cells have a reduced volume $v \equiv V/V_o \approx 0.64$ [330], as used in the previous sections.

We vary v from 0.4 to 1, with the resulting basic shapes visualized in figure 4.15. Though they retain their biconcave structure, deflated cells $v < 0.64$ are increasingly flat, while cells of $v > 0.64$ have increasingly round shapes and lose their biconcavity for $v \approx 0.9$. Base-flow configurations for extreme cases are visualized in figure 4.16.

Figure 4.17 shows the spectral abscissa α for a range of parameters. It is not obvious how to compare cases, since the more inflated cells, at the same centroid-to-centroid spacing have closer membrane-to-membrane spacing. Since their shapes depend in complex fashion upon

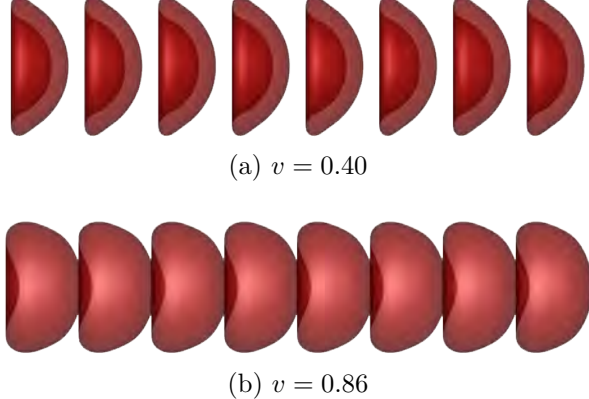


Figure 4.16: Visualization of cell trains with $D = 8r_o$ and $\phi = 0.7$ for the (a) smallest and (b) largest v we consider in this case.

v and Ca , we choose to retain the definition $\phi \equiv r_o N/L$ for making comparisons, though aware that membrane-to-membrane generally decreases with increasing v .

The widely spaced cases with $\phi = 0.2$ are maximally unstable for $v \approx 0.55$ for $D = 8r_o$ and $v \approx 0.52$ for $D = 12r_o$, with increasing stability for larger and smaller v . For $\phi = 0.7$, α monotonically increases with v , which can be anticipated by the decrease in cell-cell spacing and thus increase in importance of cell-cell interactions for increasing v , which was shown to be asymptotically destabilizing in sections 4.3.2 and 4.3.3 for healthy red blood cell shapes.

4.3.6 Disturbance strain energy

Our stability measure of section 4.2 is based on geometric displacement. However, it does not afford a direct assessment of the perturbation strain energy, which for cell j is [4, 306]

$$W_j = \int_{C_j} \left[\frac{E_s}{8} (I_1^2 + 2I_1 - 2I_2) + \frac{E_d}{8} I_2^2 + \frac{E_b}{2} (b - b^R)_i^2 \right] dS, \quad (4.12)$$

where C_j is the surface of the cell, $I_{1,2}$ are the usual strain invariants, b are the principal curvatures as discussed in section 4.1.1, and superscript R denotes the reference shape. The contributions of shear, dilatation, and bending resistance to W are denoted as W_s , W_d , and W_b , respectively. We report the cell-averaged strain-energy perturbation as

$$W' = \frac{1}{\hat{\varepsilon}N} \sum_{i=1}^N (W_i - W_i^B), \quad (4.13)$$

where W_i^B is the strain energy of a cell in the base state. Example numerical results are listed in table 4.1.

The most amplifying transient disturbances carry markedly more strain energy than asymptotic ones [158]. Further, we note that for the cases of table 4.1 all transiently unstable disturbances, not just the most amplifying, have $W' > 0.6$. This suggests that the transient mechanism entails membrane deformation. In contrast, the asymptotic modes have strain energy comparable to the linearization approximation made in our stability formulation. In

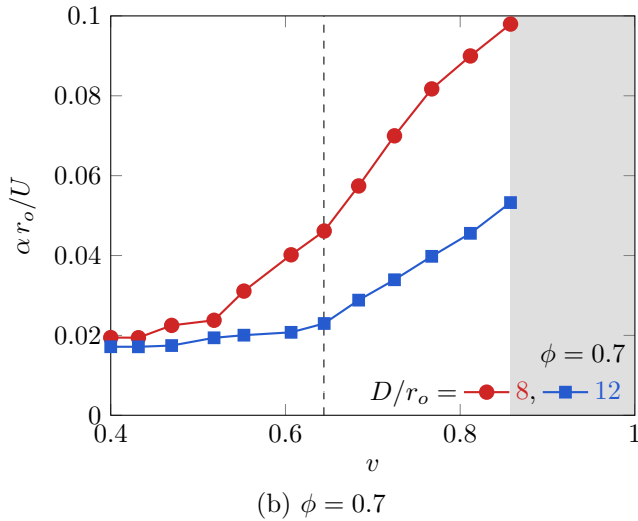
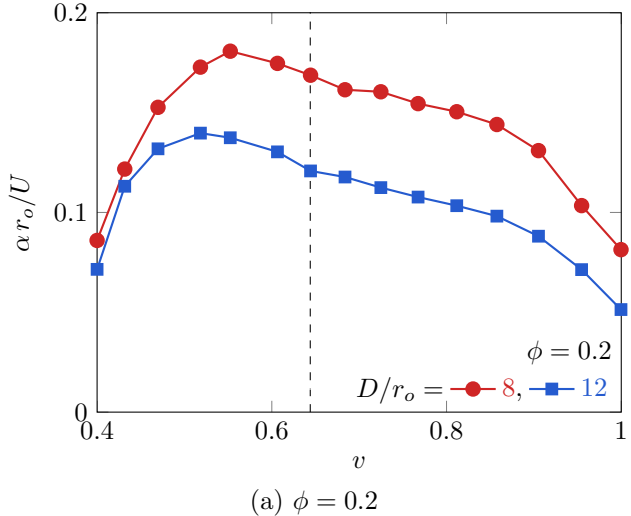


Figure 4.17: Spectral abscissa α for cell trains of various D and packing fractions (a) $\phi = 0.2$ and (b) $\phi = 0.7$ for a range of cell reduced volumes v with $\lambda = 1$. Vertical dashed lines indicate the healthy red blood cell geometry $v = 0.64$. In (b) the shaded regime $v > 0.86$ indicates states which do not fit in the train without self-intersecting.

D/r_o	ϕ	W'_α	$W'_\eta = W'_{\eta,s} + W'_{\eta,d} + W'_{\eta,b}$			
6	0.2	1.13×10^{-2}	2.48	0.43	2.01	0.04
6	0.7	4.29×10^{-3}	2.42	0.74	1.52	0.16
10	0.2	9.16×10^{-3}	1.95	0.59	1.31	0.05
10	0.7	3.95×10^{-3}	4.91	0.43	4.25	0.23

Table 4.1: Strain energy for most amplifying transient, W'_η , and asymptotic W'_α disturbances for a $\lambda = 1$ cell train of select vessel diameters D/r_o and packing fractions ϕ . All W' are nondimensionalized by r_o , U , and μ . All are computed for a $\hat{\varepsilon} = 10^{-3}$ perturbation.

all cases, the dilatation part $W'_{\eta,d}$ of the transient strain energy disturbance is largest and the bending part $W'_{\eta,b}$ is smallest, perhaps owing to their relatively large and small moduli, E_d and E_b , respectively. We confirm that the results of section 4.3.2 vary $< 2\%$ when doubling E_d , so we are ensured that the stability is insensitive to the relatively large E_d chosen in section 4.1.1. The smallest W'_η in table 4.1 provides as an estimate of the strain energy required to form the most amplifying transient disturbances. The quoted value corresponds to $\widehat{W}'_\eta \gtrsim 6 \times 10^{-18} \text{ J}$, which is more than 10^3 times larger than $kT = 4.3 \times 10^{-21} \text{ J}$ for $T = 37^\circ \text{ C}$, and so only disturbances with $\hat{\varepsilon} < 10^{-3} r_o$ are expected to arise via thermal fluctuations. This is consequential, since the results of section 4.3.2 suggest that even $\hat{\varepsilon} = 0.1$ is insufficient to trigger a nonlinear transition. Thus, it seems that transiently amplifying disturbances are unlikely to form spontaneously, and they are thus unable to trigger nonlinear dynamics. The most amplifying asymptotic modes do not share this constraint.

4.4 Conclusions

We see that the cell-train stability landscape is complex. For some parameters, the train is found to be $t \rightarrow \infty$ marginally stable, at least to within the precision of our calculations, which would correspond to vary long flow length. For larger tube diameters or sparse or dense cell-cell spacing in narrow tubes, many cases are found to be asymptotically unstable with qualitatively different forms of the most amplifying disturbances, including cell rotations and translations.

Transiently amplifying disturbances were identified for all cases in our parameter study. Many of these amplify thousands (or more) times faster than the corresponding asymptotically amplifying modes. However, they are unlikely to occur spontaneously as they require significant strain energy to form, and the subsequent growth is for to be so transitory that they are not expected to grow to the point of significantly nonlinearity. This is in contrast to the two-dimensional capsule trains of a previous study [158], for which the corresponding transient modes were able to trigger a nonlinear mechanism for small perturbations.

Larger cell-interior viscosity was found to increase the amplification rate until $\lambda \approx 20$ where the rate of amplification appears to saturate, seeming to reach a rigid-body-like behavior in this high-viscosity limit. Changing the reduced volume of the cells leads to a similarly rich behavior on the train stability; deflating the cells resulted in a less unstable cell train for the nearly jammed $\phi = 0.7$ cases we considered, and a more unstable train for the more sparse $\phi = 0.2$ cases. Transient instabilities we identified took the form of cell membrane deformations, which corresponded to finite strain energy disturbances, compared to the nearly zero strain energy disturbance of the asymptotically amplifying modes.

These results suggest that the train packing fraction, tube diameter, and cell interior viscosity and volume can be selected to mediate instability of the train, and thus provide a route to the improved design of microdevices used to process cells or capsules sequentially.

5 Stability of capsules in homogeneous shear flow

We next turn our attention to a time-dependent capsule flow system and consider an ellipsoidal or spherical capsule as it periodically swings or rolls in a homogeneous shear flow. The specific model system and simulation details are discussed in section 5.1.1. We verify that our simulations reproduce particular results of previous studies in section 5.2; these also provide the time-periodic base flows for subsequent Floquet analysis. The stability analysis is extended from that of section 4.2 to include a time-periodic base flow in section 5.3. Results for a range of flow strengths are shown in section 5.4

5.1 Simulation setup and details

5.1.1 Physical model system

The model flow system is shown in figure 5.1. The capsule is initiated as an ellipsoid with principal-axis half-lengths $\{a, a, b\}$ in the $\{x, y, z\}$ directions, as detailed in chapter 2. The capsule length scale is given by $r_o = (ab^2)^{1/3}$, which is the radius of a sphere of the same volume. The capsule perturbs a homogeneous shear flow,

$$\mathbf{u}^\infty(\mathbf{x}) = \dot{\gamma} y \hat{\mathbf{x}}, \quad (5.1)$$

where $\dot{\gamma}$ is the shear rate. Following Dupont *et al.*, we define ξ and ζ as the angles the shortest capsule principal axis and the point initially located at tip of the shortest principal axis make with the $\hat{\mathbf{z}}$ axis, respectively; corresponding points on the capsule are labeled as p_ζ and p_ξ in figure 5.1. Both the interior and exterior fluid are Newtonian and incompressible with the same viscosity μ . We take the membrane shear, dilatation, and bending moduli as E_s , $E_d = CE_s$, and $E_b = 5 \times 10^{-3} E_s r_o^2$, respectively, except for select cases in section 5.2, where $E_b = 0$ is used for comparison with other studies. These parameters are used to define an elastic capillary number $Ca = 2\dot{\gamma}\mu r_o/E_s$, which serves as a measure of flow strength. The factor of 2 is included so that our definition matches previous studies [200, 297].

5.1.2 Numerical flow solution

The numerical methods used to solve for the flow were described in chapter 3. We note that here, the free-space Green's functions are used since there is the flow is not spatially periodic and there is only one capsule; thus, all interactions are computed directly. The spatial resolution is given by $M = 6$, though we confirm the growth rates of section 5.4 are independent of this choice. The time step used when constructing the base-flow motions of

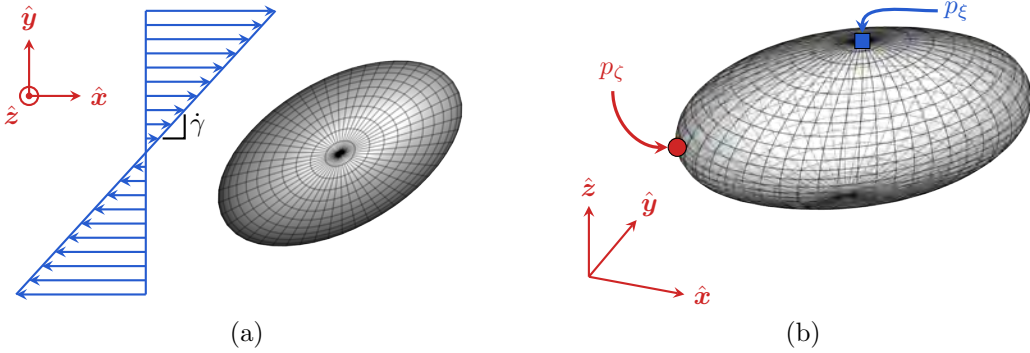


Figure 5.1: Schematic of the homogeneous shear flow model system.

section 5.2 is $\Delta t = 10^{-3}T$, where T is the period of the capsule motion as defined in that section.

5.2 Cycles of capsule motion

We simulate time-periodic cycles of the physical capsule membrane motion for cases with Ca , C , and a/b values selected to match commonly studied configurations, which also serves to facilitate verification of our numerical method and stability formulation. First, we simulate a spherical capsule ($a/b = 1$) and compare with Lac *et al.* The capsule motion and deformation are quantified by the Taylor parameter,

$$D_{ij}(t) \equiv \frac{|L_i(t) - L_j(t)|}{L_i(t) + L_j(t)} \quad \text{for } i, j = 1, 2, 3, \quad (5.2)$$

where L_i are the (decreasing with i) principal axes of the linear least-squares fitted ellipsoid of the capsule, the inclination angle Φ of the long-axis L_1 with respect to the flow direction \hat{x} , and the period of the capsule rotation T . The period is quantified by determining the smallest T such that $\|\vec{s}[t] - \vec{s}[t + T]\| < 10^{-3}$, where $\|\cdot\|$ is the L_2 norm. Steady values are denoted by D_{ij}^∞ and Φ^∞ , and are determined when their value varies $< 0.1\%$.

Figure 5.2 shows that these values match closely with those of Lac *et al.* [297]. In these cases we do not include membrane bending resistance ($E_b = 0$), consistent with their study [297]. As a result, the capsule membrane buckles [201, 297, 331, 332]. This buckling appears with short wavelength, often at the scale of the numerical discretization, and as such can pose resolution difficulty and sensitivity to the chosen numerical method and discretization [200, 331]. However, this sensitivity is not seen in figure 5.2 for a spherical capsule, where our results match those found through a finite element description of the membrane [297]. Oblate capsules ($a/b < 1$) are known to be particularly sensitive to buckling, as large compressive zones can form on the membrane [331]. We next consider such oblate capsules, which will also serve as our reference configuration for stability analysis.

We verify different base configurations, comparing with Dupont *et al.*, as shown in figure 5.3 [200]. Here, the principal axis angles $\xi(t)$ and $\zeta(t)$ are only similar to their reported

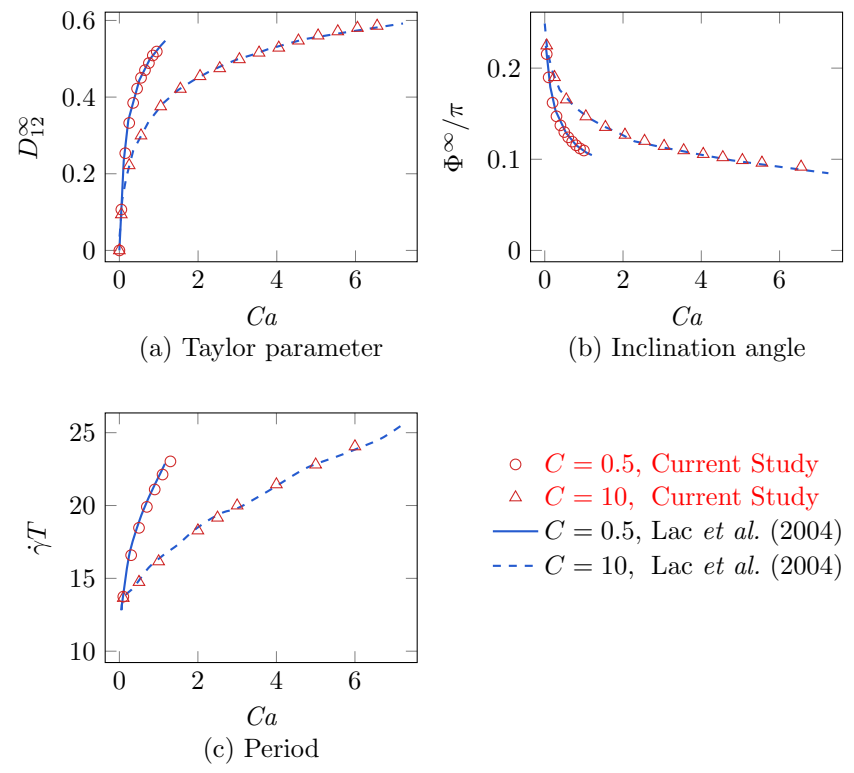


Figure 5.2: Verification of long-time (a) Taylor parameter, (b) inclination angle, and (c) rotation period (see text) with Lac et al. for $a/b = 1$ and indicated Ca and C .

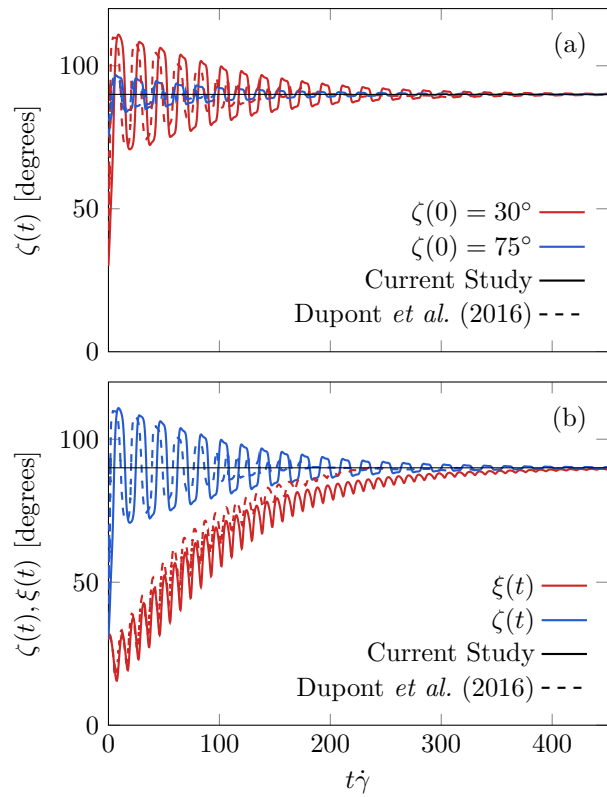


Figure 5.3: Cases with $a/b = 0.5$, $C = 1$, $E_b = 0$, and $Ca = 0.3$: (a) $\zeta(0) = 30^\circ$ and 75° , (b) $\xi(0) = \zeta(0) = 30^\circ$.

results, especially when $t\dot{\gamma} \lesssim 300$. However, for $t \gtrsim 400$ our results approach the same values, $\zeta = \xi = 90^\circ$. We hypothesize the small differences for $t\dot{\gamma} \lesssim 300$ are due to differences in the numerical methods. Particularly relevant for oblate capsules which do not resist bending and buckle at the wavelength of the spatial discretization, the finite element methods of Dupont *et al.* have intrinsic numerical dissipation and artificial membrane stiffness at the length scales of the discretization [198], of which our methods do not. However, the exact role of membrane buckling on the capsule motion, and thus $\zeta(t)$ and $\xi(t)$, is unknown. We confirm that our results for $t\dot{\gamma} \lesssim 300$ are insensitive to our choice of N to within 3%, and we note that the agreement for long times is most important for the primary objectives of our stability analysis.

With this verification against previous studies, we focus on cases with $a/b = 0.5$, $C = 1$, and Ca ranging from 0.05 to 5, commensurate with previous empirical studies of capsule stability [200]. We use a relatively small $E_b = 5 \times 10^{-3} E_s r_o^2$, which suppresses any obvious short-wavelength buckling discussed previously, and is thus consistent with the lack of such buckling in experimental observations [331]. It also facilitates a well resolved linear stability analysis, as discussed in section 5.3. Capsules are initiated with $\zeta(0) = \xi(0) = 30^\circ$, and advanced according to (3.8) until $\|\vec{s}[t] - \vec{s}[t + T]\| < 10^{-3}$ for some period T .

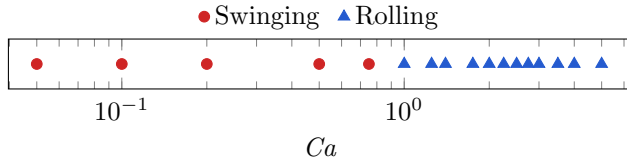


Figure 5.4: Character of capsule motion for a range of Ca .

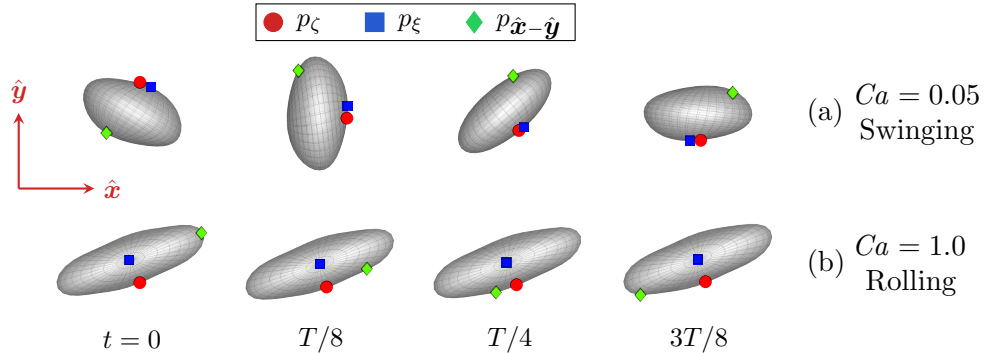


Figure 5.5: Visualization of capsule over one half-period for example cases as labeled. We introduce $p_{\hat{x}-\hat{y}}$ as a tracker point on the membrane in the shear-plane for illustration of its motion.

Figure 5.4 shows the swinging ($Ca < 1.0$) and rolling regimes ($Ca \geq 1.0$) of the base periodic capsule, example cases of which are visualized in figure 5.5. Note that no “wobbling” motion is observed here. Wobbling has been observed in certain cases [200], but is known to be sensitive to the flow description, particularly the initial capsule shape and the viscosity ratio between the interior and exterior fluids. Some reports of \hat{z} -axis wobbling have proved to be only transient, with the apparent actual long-time behavior being a swinging motion [191].

The present analysis is, in part, motivated by more direct analysis of these long time scales. We confirm the behaviors identified in figure 5.4 are insensitive to both the length of our simulations, which are more than five times longer than those of Dupont *et al.* ($t\dot{\gamma} \approx 8000$), and N . These time-periodic base flows are analyzed with Floquet analysis in the next section.

5.3 Floquet stability analysis formulation

Our stability formulation extends that developed to analyze steadily flowing red-blood-cell-trains [137] as discussed in section 4.2, to include the time-periodic base flow. Thus, we do not repeat this description in full detail, though we emphasize that our method depends upon the orthogonality of the spherical harmonic coefficients \vec{s} . The linearization proceeds by introducing $\vec{\delta}[t]$ as a small perturbation to $\vec{s}[t]$. Expanding (3.8) and retaining linear terms in $\vec{\delta}[t]$ yields:

$$\mathbf{A}[t]\vec{\delta}[t] = \tilde{\mathbf{B}}\{\vec{u}(\mathbf{B}\vec{s}[t] + \vec{\delta}[t]) - \vec{u}(\mathbf{B}\vec{s}[t])\}. \quad (5.3)$$

A full-rank orthogonal set of disturbances $\vec{\delta}_i$ gives each column i of matrix $\mathbf{A}[t_j]$ at time t_j , the details of which have been discussed elsewhere [137, 158]. We use $\|\vec{\delta}[t]\| = \delta = 10^{-3}$, and confirm insensitivity to this numerical parameter. We evaluate $\mathbf{A}[t_j]$ at 10^4 uniformly spaced times $t_j \in [0, T)$, and confirm that the results are also insensitive to this choice. Note that this is a 10 times finer temporal discretization than the corresponding simulations that provide the base state. The evolution of any small disturbance to the spherical harmonic coefficients $\vec{\epsilon}[t]$ is then governed by

$$\frac{d\vec{\epsilon}[t]}{dt} = \mathbf{A}[t]\vec{\epsilon}[t] \quad (5.4)$$

where $\mathbf{A}[t]$ has period T , and thus (5.4) is a canonical Floquet problem. The solution to (5.4) can be expressed as

$$\vec{\epsilon}[t] = \mathbf{X}[t]\vec{\epsilon}_o, \quad (5.5)$$

where $\mathbf{X}[t]$ is the fundamental solution operator, which can rarely be determined analytically, even for simple problems. Following usual procedures, we assume that $\vec{\epsilon}[t]$ has the form

$$\vec{\epsilon}[t] = \sum_{i=1}^n c_i \vec{p}_i[t] \exp \mu_i t, \quad (5.6)$$

where c_i are constants, μ_i are exponential growth rates, and $\vec{p}_i[t]$ are unknown periodic functions. Periodicity requires

$$\mathbf{X}[t+T] = \mathbf{X}[t]\mathbf{X}^{-1}[0]\mathbf{X}[T] = \mathbf{X}[t]\mathbf{C}, \quad (5.7)$$

where \mathbf{C} is the monodromy operator. Substitution of (5.7) into (5.5) provides the propagation of $\mathbf{X}[t]$,

$$\frac{d\mathbf{X}[t]}{dt} = \mathbf{A}[t] \mathbf{X}[t]. \quad (5.8)$$

It is established that the properties of the linear system can be determined independently of the initial condition $\mathbf{X}[0]$; we follow the usual practice of selecting $\mathbf{X}[0] = \mathbf{I}$, in which case $\mathbf{C} = \mathbf{X}[T]$ is the principal fundamental matrix. In our calculations $\mathbf{X}[T]$, and thus \mathbf{C} , is found by integrating (5.8) using the trapezoidal rule, which is chosen to exactly preserve time reversibility and avoid numerical dissipation. The eigenvalues ρ_i of \mathbf{C} are the Floquet multipliers and can be interpreted as the factor of growth or decay of $\|\vec{\epsilon}[t]\|$ over a period; $|\rho_i| > 1$ indicates unstable modes.

5.4 Results

The monodromy matrix \mathbf{C} and its eigenvalues are computed for the periodic flow of the $a/b = 0.5$ and $C = 1$ capsules of section 5.2, which identifies nominal Floquet modes and quantifies their stability.

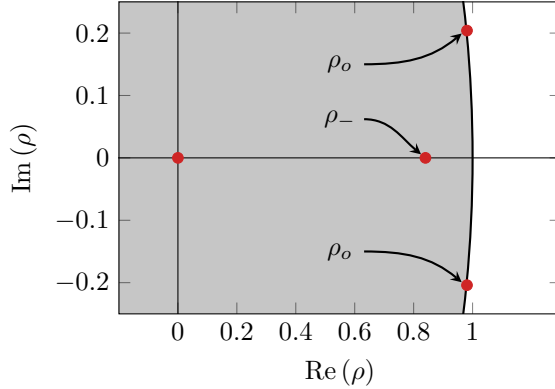


Figure 5.6: The spectrum of \mathbf{C} for $Ca = 1.4$. Neutrally (ρ_o) and modestly (ρ_-) stable modes are labeled.

The Floquet multipliers of an example case are shown in figure 5.6. These indicate a complex conjugate pair of neutrally stable multipliers $|\rho_o| \approx 1$ and a modestly decaying multiplier $\rho_- \approx 0.84$, which have associated eigenvectors \vec{v}_o and \vec{v}_- , respectively. Neutrally stable multipliers are only determined within the accuracy of our methods, which for this case is within $\rho_o = 1 \pm 10^{-2}$. This is a result of the approximations introduced by the finite δ used when constructing \mathbf{A} , the finite number of $\mathbf{A}[t]$ used to discretize the temporal period T for determining \mathbf{C} , and the precision of the periodic base flow motion. With this constraint, were a truly unstable mode to exist within our tolerance, it would require at least $t > 700T$ to amplify from an initial disturbance amplitude $\hat{\epsilon} = 10^{-3}$ to unity, so we refer to them as neutrally stable in our discussion. All other Floquet multipliers of figure 5.6 have $|\rho| \approx 0$, with their associated disturbances vanishing (within the accuracy of our methods)

well before a single period T . We select one of these $|\rho| \approx 0$ modes and labeled it as \vec{v}_b to illustrate its behavior subsequently.

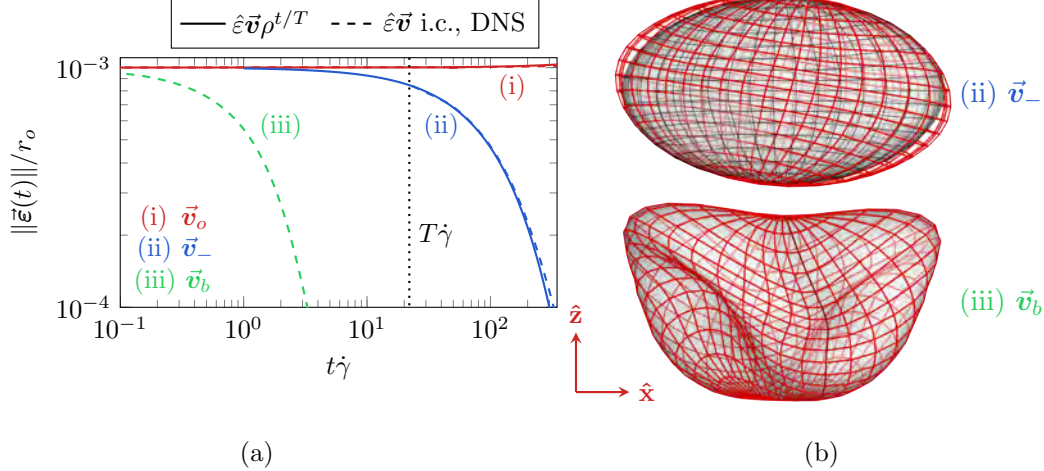


Figure 5.7: (a) Linear prediction and DNS of example Floquet multipliers as labeled over several periods for the $Ca = 1.4$ case. (b) Associated eigenvectors (ii) \vec{v}_- and (iii) \vec{v}_b , magnified for visualization as $\vec{s}[0] + 5\vec{v}$.

Figure 5.7 (a) shows agreement between the linear theory and DNS for the \vec{v}_o and \vec{v}_- modes, which serves as a verification of our analysis. Note that our analysis only attempts to predict the behavior of $\|\tilde{\epsilon}(t)\|$ at integer multiples of the period, so we only include the DNS evolution at these time intervals for clarity. The DNS of the \vec{v}_b mode shows a quick decay before the first period has elapsed, seemingly prohibiting a prediction of its behavior with our analysis. However, this is unimportant for stability purposes as it is an obviously stable mode.

The eigenvectors \vec{v}_- and \vec{v}_b , shown in figure 5.7 (b), appear as a tilt of the capsule about the \hat{y} axis and an unstructured deformation of the capsule, respectively. The quick decay of \vec{v}_b is then expected, as the disturbance dissipates primarily due to elastic, not hydrodynamic, effects. Eigenvector \vec{v}_o is simply a rotation of the capsule in the shear-plane ($\hat{x}-\hat{y}$, here), and so its neutral stability is unsurprising and not revealing of any particular behavior.

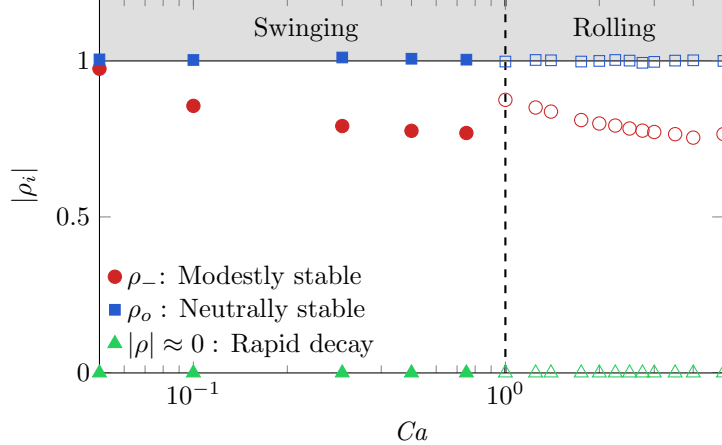


Figure 5.8: Floquet multipliers for a range of Ca .

We identify neutrally and modestly stable Floquet multipliers for all Ca considered, as shown in figure 5.8. Again, all other multipliers have $|\rho| \approx 0$, dissipating before a period has elapsed. Thus, we conclude that the flow is neutrally stable within the accuracy of our methods for all cases. The associated eigenvectors for each case have the same character as those described previously. For the weakly damped disturbances, ρ_- decreases with increasing Ca within each of the flow regimes (swinging or rolling), which can be anticipated as it has been observed that as flow strength increases, perturbations to the stable flow decay more quickly [200]. An apparent discontinuity in ρ_- appears at $Ca = 1$, which is expected as the flow qualitatively from swinging to rolling at this value.

5.5 Conclusions

We formulated a Floquet stability analysis for the swinging and rolling motions (for varying Ca) of oblate capsules in homogeneous shear flow. This was undertaken to clarify their long-time behavior given the challenges of actually performing long-time simulations. For each case, a set of rapidly decaying modes with $|\rho| \approx 0$ were identified, which dissipated before one period elapsed. A modestly stable mode that decayed over several periods was also identified in each case; its behavior was reproduced through direct numerical simulations and served as a verification of our methods. Finally, an approximately neutrally stable mode, within the accuracy of our methods, was identified. The absence of an unstable mode in any of the cases we considered confirms that the capsule flow motions are indeed stable.

6 Stability of a capsule in large amplitude oscillatory extension

The model system we investigate is introduced in section 6.1.1 and the numerical methods used to solve for the flow are described in section 6.1.2. In section 6.2 we present our construction of the time-periodic base-flows for analysis. We verify our stability analysis through direct numerical simulations (DNS) and assess the capsule stability for cases of varying flow strengths and oscillatory time scales in section 6.4.

6.1 Simulation setup and details

6.1.1 Physical model system

The model system is shown in figure 6.1, and the capsule model was discussed in chapter 2. An initially spherical elastic capsule of radius r_o is subject to oscillatory planar extensional flow, which has velocity field

$$\mathbf{u}^\infty(\mathbf{x}) = \dot{\gamma} \sin(2\pi t/T) [x \hat{\mathbf{x}} - y \hat{\mathbf{y}} + 0 \hat{\mathbf{z}}] \quad (6.1)$$

where $\dot{\gamma}$ is the shear rate and T is the period. Both the capsule interior and exterior fluids have viscosity μ . The Skalak membrane dilatation and bending moduli are $E_d = 10E_s$ and $E_b = 5 \times 10^{-3} E_s r_o^2$, which are considered typical of capsules. Together these parameters give a characteristic capsule relaxation time $\tau = \mu r_o / E_s$, Weissenberg number $Wi = \tau \dot{\gamma}$, which serves as a measure of relative flow strength, and Deborah number $De = \tau / T$, which is a ratio of capsule to flow time scales.

6.1.2 Numerical flow solution

The numerical methods used to solve for the flow were described in chapter 3. As in chapter 5, the free-space Green's functions are used and all interactions are computed directly. The spatial resolution of the capsule membrane is given by $M = 6$, and the capsule position is updated with time step $\Delta t = 10^{-3}T$.

6.2 Base capsule motion

Capsules are initiated with their centroid at the stagnation point $\mathbf{x} = 0$ and subject to (6.1), as determined for varying Wi and De . We first simulate up to $t = 10T$, then select the approximately periodic capsule motion once $\|\vec{\mathbf{x}}[t] - \vec{\mathbf{x}}[t + \tilde{T}]\|_2 < 10^{-5}$ for some period \tilde{T} .

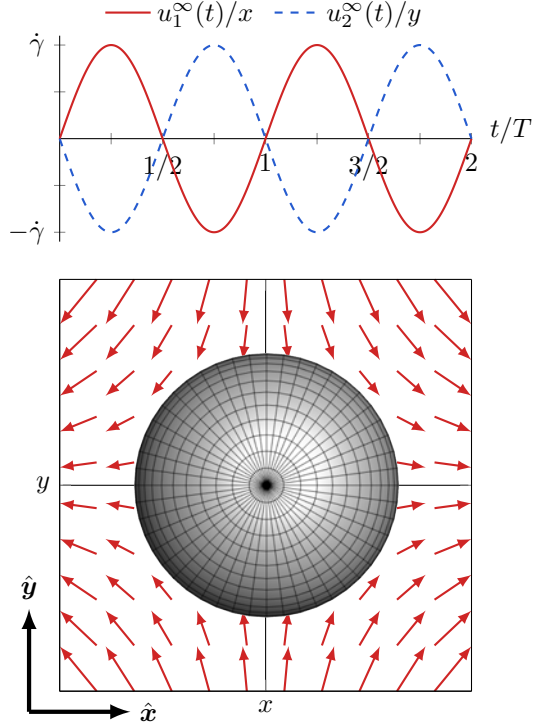


Figure 6.1: Schematic of model LAOE flow system and velocity field.

We have $|\tilde{T} - T| < 10^{-5}$, which is expected in the viscous limit as the capsule interacts instantaneously with the velocity field, so we simply quote T throughout.

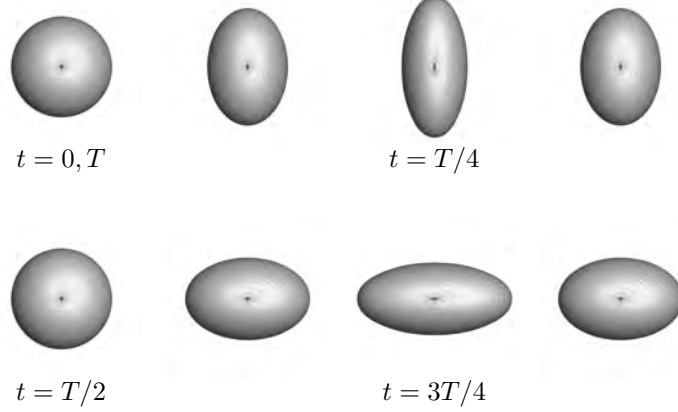


Figure 6.2: Base-flow motion for the case $Wi = 0.8$ and $De = 0.03$.

A single period of the capsule motion for an example case is shown in figure 6.2. The capsule at an integer multiple of T is spherical, then stretches in the \hat{y} -direction and compresses in the \hat{x} -direction. At the end of a half-period the capsule returns to a spherical shape and begins to stretch in the \hat{x} -direction and compress in the \hat{y} -direction. We construct this periodic base-flow for a range of Wi and De , and analyze its stability through a stability analysis as discussed in the next section.

6.3 Stability analysis

The periodic flows identified in section 6.2 are analyzed with an extension of the Floquet methods discussed in section 5.3 that includes non-modal and time-global effects. That is, In general, \mathbf{C} is real and non-normal ($\mathbf{C}^T \mathbf{C} \neq \mathbf{C} \mathbf{C}^T$), so it will not have a full set of orthogonal eigenvectors. Though not diagonalizable, the eigenvalues of \mathbf{C} , or Floquet multipliers, do dictate the $t \rightarrow \infty$ behavior of small disturbances, so long as they do not trigger significant nonlinear interactions before this behavior is realized [234]. We consider Floquet multipliers for this reason, and next present a non-modal analysis for predicting the behavior of $\|\vec{\varepsilon}[t]\|$ at shorter times.

The behavior of $\vec{\varepsilon}$ at any integer multiple (j) of the period is simply

$$\vec{\varepsilon}_j \equiv \vec{\varepsilon}(jT) = \mathbf{C}^j \vec{\varepsilon}_o, \quad (6.2)$$

and the maximum factor of growth G_j of $\|\vec{\varepsilon}\|$ from period j to $j+1$ is,

$$\eta_j^2 = \max_{\vec{\varepsilon}_o} \frac{\|\vec{\varepsilon}_j\|^2}{\|\vec{\varepsilon}_o\|^2} = \max_{\vec{\varepsilon}_o} \frac{\|\mathbf{C}^j \vec{\varepsilon}_o\|^2}{\|\vec{\varepsilon}_o\|^2} = \|\mathbf{C}^j\|^2, \quad (6.3)$$

where $\|\cdot\|$ is the L_2 norm as given by the maximum singular value. From (6.3) we see that the eigenvalues of \mathbf{C} only describe $\|\vec{\varepsilon}_j\|$ for all j if \mathbf{C} is normal. Thus, transient growth can occur if $\|\mathbf{C}^j\| > 1$ for any j , though this growth is bounded by $\max |\rho_i|$ for $t \rightarrow \infty$. The maximum growth after a single period is associated with the numerical abscissa [234], for which we denote $\eta_{1,i}$ as the i -th largest singular value of \mathbf{C} . When the subscript is omitted it is assumed $\eta \equiv \eta_{1,1}$; the associated singular vector \vec{v}_η is the disturbance that gives this growth.

Further, we bound the growth of $\|\vec{\varepsilon}[t]\|$ at any t , not just an integer multiple of the period, through $\mathbf{X}[t]$. The largest possible growth within the first period is,

$$\Delta \equiv \max_{t_j \in [0, T)} \|\mathbf{X}[t_j]\|. \quad (6.4)$$

This measure is particularly important if intra-period transient effects are sufficiently large to trigger a nonlinear effects, which are discussed in section 6.4. We emphasize that Δ will not necessarily grow from period-to-period. The singular vector associated with Δ , \vec{v}_Δ , gives this growth.

6.4 Results

We consider cases with Wi ranging from 0.1 to 4, which corresponds to a ratio of the longest and shortest capsule principal axes, as defined by the best-fit ellipsoid to the membrane shape, between about 1.2 and 5. We vary De between 0.006 and 0.2. The stability of each case is given by ρ , η , and Δ , as discussed in section 6.3.

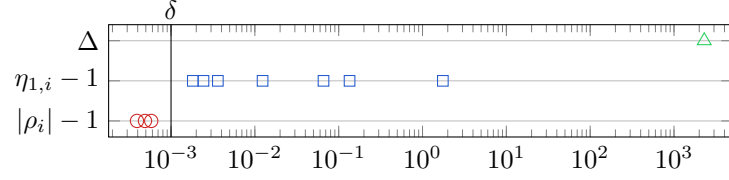


Figure 6.3: Floquet multipliers ρ_i , numerical abscissa $\eta_{1,i}$, and maximum intra-period growth Δ for the case $Wi = 0.8$ and $De = 0.03$.

Results are shown for an example case in figure 6.3. We see our formulation can only establish asymptotic neutral stability ($|\rho_i| - 1 \lesssim 10^{-3}$). That is, \mathbf{C} , and thus its eigenvalues, are only accurate within the $\delta = 10^{-3}$ used to construct each $\mathbf{A}[t]$. Of course smaller δ , even more precisely determined base-flow cycles, and smaller time steps could determine these values more accurately. However, this is challenging and likely unimportant as, were such an instability to exist within this limit, it would require at least 2000 periods to amplify by a factor of 10. Further, the three $|\rho_i| \approx 1$ multipliers in this case are associated with rigid-body-like rotations of the capsule, which this system is formally invariant to, and so their approximately neutral stability is unsurprising. More evident is the $\eta_i > 1$ we see, indicating transient instability. Here, 8 modes have $\eta_i > 1$, with the largest being $\eta = 2.74$, and all of which being associated with membrane deformations. Lastly, the $\Delta \approx 2000$ is strikingly large, which we will show to be associated with a purely translational instability.

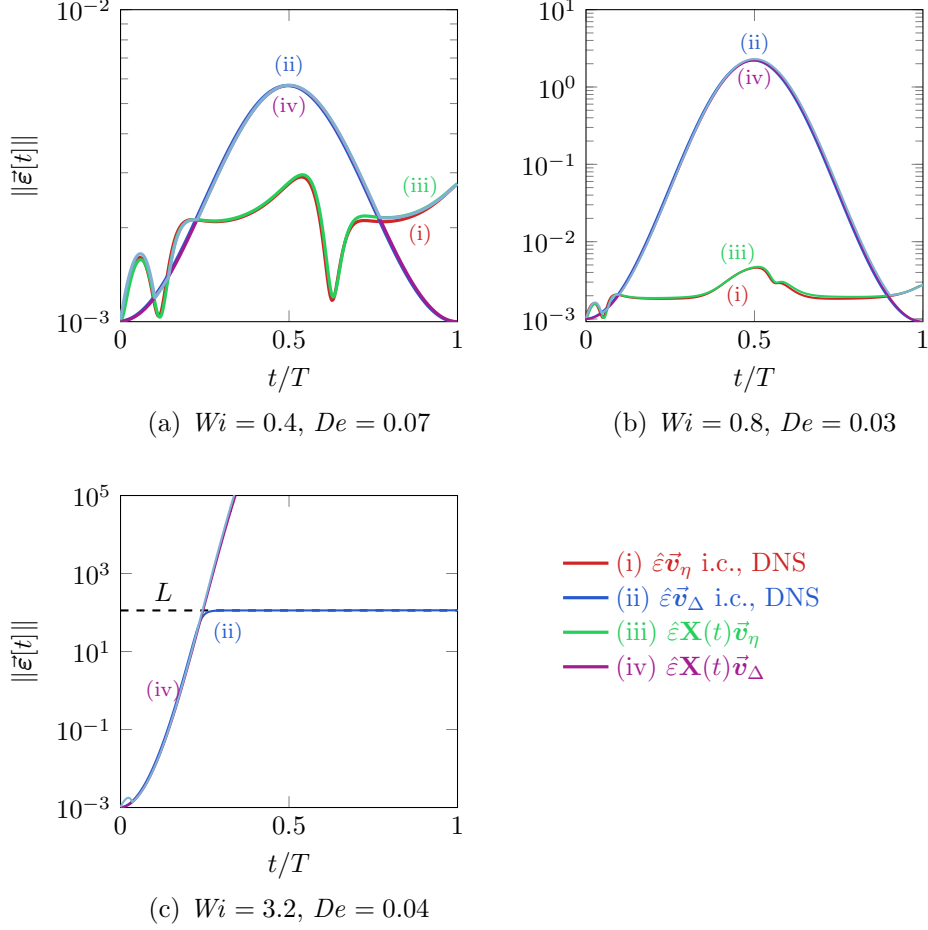


Figure 6.4: Linear theory and DNS for \vec{v}_η and \vec{v}_Δ over one period for example cases as labeled.

We show a verification of our methods in figure 6.4, with the linear theory and associated DNS closely matching for all cases and initial conditions. A relatively large intra-period amplification Δ is observed in each case, though this behavior is neutral from period-to-period. Thus, it is only important if it triggers nonlinear growth, which would not be or is sufficiently large to disrupt examination of the capsule for, for instance, experimental purposes. An example of very large Δ is shown in figure 6.4 (c), with \vec{v}_Δ amplifying about 5 orders of magnitude before ejecting the capsule from the computational domain (which has size L). Also shown is the evolution of \vec{v}_η , which does have finite amplification after one period, though this growth is transient in nature and must saturate at the rate given by the largest Floquet multiplier. However, we have $\max_i |\rho_i| = 1$ (within the accuracy of our methods) for each case, and thus asymptotically neutral stability.

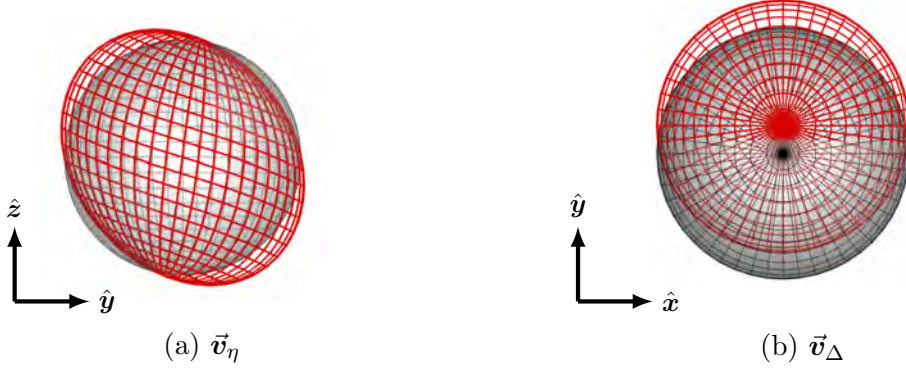


Figure 6.5: (a) \vec{v}_η and (b) \vec{v}_Δ for the case $Wi = 0.8$ and $De = 0.03$, magnified for visualization as $\vec{s}[0] + 5\vec{v}$.

Singular vectors \vec{v}_η and \vec{v}_Δ are shown for an example case in figure 6.2. Here, \vec{v}_η appears as a shearing-like deformation in the \hat{x} - \hat{y} plane and \vec{v}_Δ appears as a pure translation in the \hat{x} - or \hat{y} -direction. The appearance of the transiently amplifying disturbance \vec{v}_η as a shape deformation of the membrane is consistent with previous studies of transiently unstable capsule flows [137, 158]. The translational character of \vec{v}_Δ can be anticipated as the capsule is obviously unstable to such a disturbance in one of the coordinate flow directions at any time, though the direction of this instability switches at every integer multiple of the half-period, resulting in the neutral stability observed in figure 6.4.

Example Δ for several cases are shown in figure 6.6. We see Δ increases with Wi and $1/De$, which is expected as the strength and duration of the intra-period instability increases, respectively. The increase of Δ with $1/De$ is clearly exponential for constant Wi , which we describe with rate α . Further, α increases linearly with Wi (with slope $1/\pi$), as shown in figure 6.6 (b). Together, this gives,

$$\Delta(Wi, De) = \exp\left(\frac{Wi}{\pi De}\right). \quad (6.5)$$

Interestingly, this result is consistent with the displacement of a rigid, infinitesimal, particle perturbed in an analogous one-dimensional oscillatory extensional flow. This can be deduced from the governing equation of such a particle,

$$\frac{dx}{dt} = \dot{\gamma}x \sin\left(\frac{2\pi t}{T}\right), \quad (6.6)$$

where x is the particle position. This has solution

$$x(t) = \delta \exp\left(\frac{\dot{\gamma} T}{2\pi} \left[1 - \cos\left(\frac{2\pi t}{T}\right)\right]\right), \quad (6.7)$$

where δ sets the initial size of a translational disturbance to the particle. It is evident that the largest disturbance occurs when $t = T/2$ or $3T/2$, giving $\Delta = \exp(\dot{\gamma}T/\pi)$, consistent with (6.5). Thus, we deduce that the a spherical capsule behaves very nearly as a rigid, infinitesimal, particle when subject to a translational perturbation in LAOE flow.

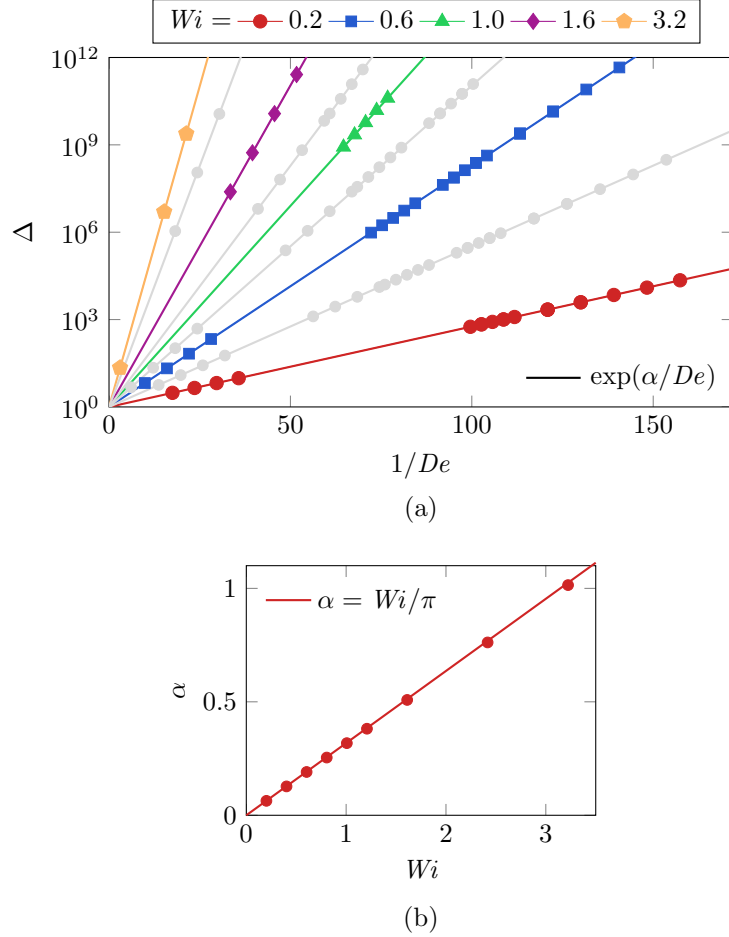


Figure 6.6: (a) Δ for various De and Wi . (b) Least-squares fitted α for $\Delta = \exp(\alpha/De)$ at select Wi .

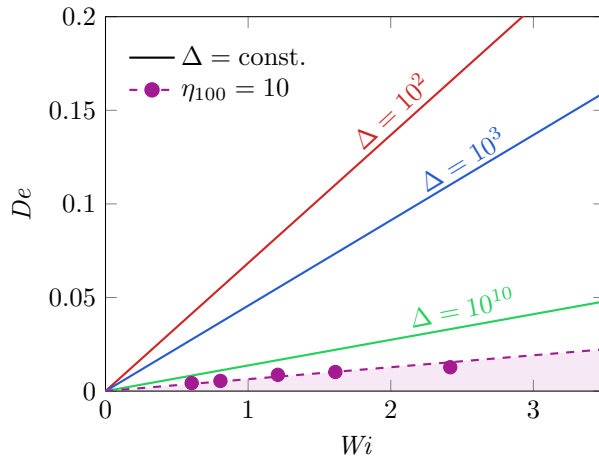


Figure 6.7: Pipkin space showing isocontours of Δ and η_{100} as labeled.

We use (6.5) to cast isocontours of Δ onto a Pipkin space (Wi versus De), as shown in figure 6.7. We also show the locus of cases with $\eta_{100} = 10$; that is, cases that could amplify a disturbance by a factor of ten over 100 periods through a transient mechanism. It's apparent that $\eta_{100} \gtrsim 10$ for only large Wi and small De , especially when compared to isocontours of Δ , which are very large for the same cases. Thus, we conclude that the transient instability we identify is subservient to the translational intra-period instability.

6.5 Discussion and conclusions

We formulated a non-modal Floquet stability analysis for fully-coupled capsule-viscous-flow systems, extending previous studies of time-stationary capsule flows. This analysis was applied to the motion of spherical capsules subject to LAOE flow of varying flow strength and time scales. All flow descriptions were found to be asymptotically stable, a result shared with the time-stationary version of the same system [333]. A set of transiently unstable disturbances, however, were identified for each case. These disturbances took the form of a shape distortion of the capsule membrane, consistent with other transient stability analyses of capsule flows [137, 158]. Here, transient disturbances amplified slowly over many periods, as demonstrated by the only small fraction of cases that satisfied $\eta_{100} > 10$. Further, their growth necessarily saturates at long times as a result of their asymptotic stability. Thus, this instability is unlikely to be important in most applications. Also identified in each case was an intra-period instability, associated with a translation of the capsule. This disturbance was able to amplify many orders of magnitude in certain cases, depending on the flow strength and period, and matched the behavior of a rigid infinitesimal particle in the same flow. However, the intra-period instability was neutrally stable from period-to-period, again precluded by the asymptotic stability of each case. As such, it is only expected to be important if it is not controlled for, as has been done previously for DNA [225, 226], and De is sufficiently small and Wi sufficiently large for the application of interest.

7 Concluding remarks

7.1 Research summary

7.1.1 Model systems and solution method

We investigated the mechanical stability of three capsule-viscous-flow systems, including red-blood-cell-trains flowing in a model microvessel and capsules in homogeneous shear flow and planar large-amplitude oscillatory extensional flow. In each case the capsules were modeled as thin-shell elastic membranes encasing and surrounded by incompressible and Newtonian fluids. Capsules were represented with spherical harmonics, which provided a highly accurate description of their membrane geometry, and the flow was discretized using boundary integral methods generalized for Stokes flow. This scheme was used to construct base flows for each flow system, which were then analyzed with respect to their stability.

7.1.2 Stability analysis

The main contribution of this dissertation was the establishment of a new approach to the linear stability analysis of coupled capsule-fluid flow systems, such as those of cellular blood flow or flowing capsule suspensions. A nonmodal time-stationary stability analysis was developed for studying red blood cells flowing in a microvessel, as the base flow advected at uniform velocity. This was extended with Floquet methods to formulate a stability analysis for time-periodic base flows; specifically, the rolling or tumbling motions of capsules in homogeneous shear flow. Finally, this Floquet formulation was extended to include nonmodal effects. This analysis was applied to spherical capsules in LAOE flow, as transient instabilities were anticipated important due to the large capsule deformation exhibited within one period of its motion.

In each case, the linearization was constructed via a full-rank orthogonal set of small disturbances to the capsule shapes, as constructed by the set of spherical harmonic modes that described them, and computed directly for the full nonlinear equations. This resulted in a linear system that described the first-order coupling of the base state to the set of disturbances, which was analyzed through eigenvalue and singular value analyses to determine its asymptotic and transient behavior, respectively.

The spectral description of capsule membranes employed here was able resolve capsule shapes with relatively few modes, preventing the linear system that arises from the stability analysis from becoming large. This was particularly important for our Floquet analysis formulation, which required a large discrete set of realizations of the time-stationary analysis about the flow period in order to construct the linear system. A less accurate membrane

description, such as those utilizing finite-element methods [7, 67], would require a finer surface discretization to obtain the same accuracy, and thus lead to larger linear systems. Further, the boundary integral methods used here were advantageous as the flow solution was described entirely by the position of the surfaces, so there was no need to evaluate the velocity of the fluid itself. Methods that requiring evaluation of the velocity of the surrounding fluid, such as those utilizing immersed boundary [334–336], homogeneous continuum models [337, 338], or lattice–Boltzmann techniques [339, 340], can thus be expected to generate large linear stability systems.

While our stability formulation was perturbation-based and included coupling between a full-rank set of disturbances and the base flow, its construction can be expensive. Data-driven methods, such as the dynamic mode decomposition (DMD) [266–269], or Koopman operator techniques [269, 270], have proved useful if a highly accurate base flow is unavailable or full construction of the linear stability analysis is prohibitively expensive. These methods determine the most unstable growth rate through a series of temporal realizations of the evolution to disordered flow. Often only a relatively small number of such realizations are required, making such analysis computationally efficient. Further, direct computation of disturbances to the flow, or construction of an accurate base flow, are not required. However, such analyses cannot quantify the rate at which a full-rank set of disturbances to the system decay, as the dynamics are dominated by the most unstable flow behavior, nor do they anticipate transient instabilities. We anticipate such methods can be applied to capsule flow systems such as the ones considered here, and would be particularly useful for very large systems, such as those derived from lower accuracy numerical methods or many-capsule flows. Of course advancement in computational capabilities will also facilitate these large-scale analyses.

7.1.3 Flow instabilities

While the flows considered were relatively diverse, including both confined and unconfined flow, and pure shear and extensional flow, they do share stability properties.

The character of the matrices deduced from our linear stability analyses was important for the type of instabilities that could be expected. For all flows this matrix was non-normal; that is, they were real and non-symmetric, a property which can anticipated from the flow equations (see chapter 4). As a result, the associated set of eigenvectors are not necessarily orthogonal, and transient instabilities were anticipated.

Transiently unstable disturbances were identified for all flows. In each case, the most transiently amplifying disturbance appeared as a shape deformation of the capsule membrane(s). For the cell trains of chapter 4, these disturbances even appeared kinky in character (though, as discussed in section 4.3.2, this was in part due to magnification of an otherwise small disturbance). Indeed all transiently unstable disturbances for all flows we considered shared this property, and we expect the non-normality of the stability analysis as computed from the governing flow equations of similar capsule systems to result in similar transient instabilities.

The shape distortion of the capsules membranes were quantified by the finite strain

energy associated with the disturbance. However, no asymptotically unstable disturbances carried finite strain energy, as they appeared as rigid-body-rotations and translations of the capsules. This has consequence: disturbances that carry large strain energy, such as the transiently unstable ones identified here, are unlikely to occur spontaneously due to thermal fluctuations. In section 4.3.6 we saw that transiently unstable disturbances to red blood cell trains were only able to form with magnitude less than one part in 1000 of the nominal cell radius due to such thermal effects, a size too small to result in asymptotic growth through a nonlinear mechanism, as shown in section 4.3.2.

We emphasize that the transient growth in each case saturated after a relatively short time, amplifying at most a factor of ten before decaying. As such, the transient mechanism was subservient to the asymptotic instabilities identified through eigenvalue analysis. This behavior can then be expected for other capsule flows, and transient growth analysis might not be necessary for cases where only small disturbances of the actual system are expected.

7.2 Reduced-order flow descriptions

One of the goals of the presented stability analyses was to identify the nominal stability behavior of the complex capsule flows. We expect this behavior to be important for the design of reduced-order flow systems, for which we consider two approaches here. Further, accurate computation of many-capsule flows, such as that required to determine the capsule-train base-states described in chapter 4 and appendix C, can be relatively expensive and relies upon a full description of the capsule membranes and viscous-flow system. We anticipate that a reduced description of this complex flows can expedite the analysis and lead to a direct understanding of the physical mechanism that amplifies the identified unstable disturbances. In this vein, we introduce two possible paths for developing such models; the first focuses on a continuum model, appropriate for the highly-packed red blood cell trains, and the other a discrete sphere system, focused on the motion of individual cells.

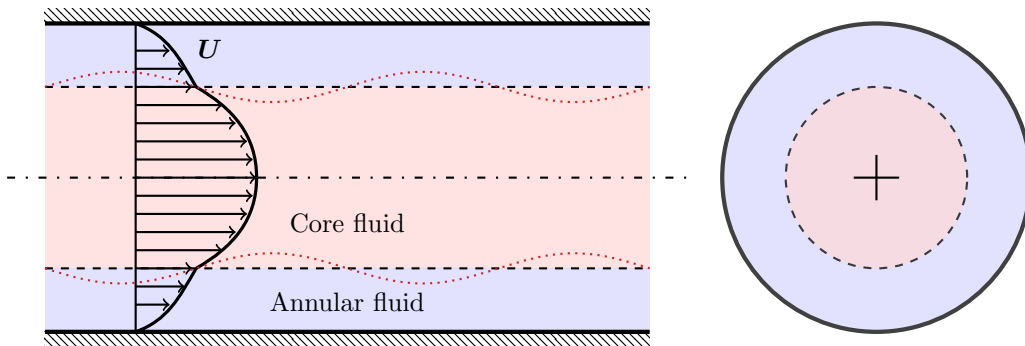


Figure 7.1: Schematic of a proposed core-annular rheological flow. U is the fluid velocity profile, the dotted curve is an example of a perturbation to the fluid–fluid interface, and the hashed lines indicate the no-slip wall boundary.

The continuous rheological flow is shown in figure 7.1. It is a core-annular flow of incompressible and immiscible fluids within a rigid tube. We anticipate this flow to be an appropriate model of capsule trains with relatively small capsule–capsule spacing (or

relatively large ϕ , in the notation of chapter 4). The core fluid should be capable of displaying the rheological properties of whole blood [341, 342]; examples of which are the Casson or Carreau–Yasuda models, both often used to model whole blood flow generally [343–345]. The annular fluid should model the behavior of blood plasma, and so a Newtonian fluid model is likely to be appropriate.

The continuous fluid–fluid interface interface can then be studied with regard to its stability. Assuming Stokes flow, the governing equations should be linearized about the base-flow shown in figure 7.1, then analyzed using the eigenvalue and singular value methods of section 4.2. Preliminary analysis of a further simplified system; that is, a jet of incompressible Newtonian fluid, is presented in appendix D and serves as a formulation and verification of the methods required to solve the more complex problem shown schematically in figure 7.1. Also included are further extensions of the proposed model flows and expected difficulties.

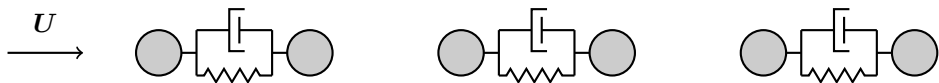


Figure 7.2: Schematic of a model rigid-sphere flow system.

When the train capsule–capsule spacing is relatively large, the continuum-based approach discussed above is surely not a good approximation of the actual flow behavior. For this flow configuration, we anticipate that a rigid-sphere flow system can model the the stability behavior of the capsule train. Indeed complex particulate flows have been modeled as rigid-sphere systems for a long time. A candidate model flow is shown in figure 7.2. It is a train of spheres flowing in a Newtonian fluid with constant velocity U . Each successive pair of spheres are connected with purely viscous and elastic elements, which are proposed as models for the viscous and elastic behaviors of actual capsules. The hydrodynamic interactions between the spheres, and thus their velocity, can be readily computed using Faxen’s law and the method of reflections [346]. This leads to a set of governing differential equations that can be studied with a normal mode stability analysis. In appendix E, an even simpler model sphere flow system, that is, one where all spheres are uniformly spaced with no elastic or viscous connections, is presented and analyzed. While this system is again simpler, it contains the core methods required to analyze more complex flows, such as that of figure 7.2. The challenges of analyzing these more complex systems are also discussed.

7.3 Future work

7.3.1 Extensions of our methods

While only capsule flows were considered here, the presented analysis provides a route to understanding soft particle motion and stability generally. Indeed this formulation would be applicable to the flow of droplets, colloids, vesicles, or other fluid–structure interaction problems whose velocity can be computed directly and accurately with numerical methods. Spectral boundary integral methods are particularly attractive in this respect, since they only rely upon an accurate representation of the particle surface, as discussed above.

The presented analyses proved particularly useful when the base flow is known or can be readily computed, but its stability is unknown. That is, for the capsule-trains of chapter 4 and the capsule in LAOE flow of chapter 6, the base flow could be anticipated based on flow symmetry or stagnation points, and for the oblate capsules in homogeneous shear of chapter 5 the base flow was computed directly. Indeed other rheometric flows share this property. For example, Stokes traps designed for multiplexed particle manipulation attempt to control the flow and stability of several flow stagnation points [347]. In this case, particles, such as polymers, are placed at the stagnation points and oscillated with respect to each other, resulting in an approximately periodic base flow. Such hydrodynamic flow traps are often used for determining the material properties and kinematic behavior of soft particles, motivating an understanding of their stability.

While the formulations presented here were limited to time-periodic base flows, methods for relaxing this restriction exist. Known as generalized Floquet methods, these techniques predict the stability of any time-dependent flow. Such analysis is expected to be more expensive than an analogous time-stationary or time-periodic flow, though is potentially tractable with the highly accurate methods presented here. Extending our formulation in this respect would then be appropriate for any non-time-periodic capsule flow, such as that of biconcave capsules in sufficiently strong steady [348] or oscillatory shear-flow [231], or single-vesicle dynamics in narrow confines [349].

Our stability formulation was strictly limited to linear terms in the disturbance of the base flow. This was not prohibitive for our analysis, as our methods were sufficiently accurate that very small perturbations (one part in 1000 of the nominal capsule radius, or smaller) could be analyzed, making the linearization a good approximation of the actual flow. However, disturbances in actual physical systems are not always this small. In such cases, nonlinear contributions of the disturbance to the base flow could be important. Fortunately, our formulation can be extended to consider weak nonlinearities with traditional methods [350–352]. This requires higher-order tensors for describing the higher-order couplings between the disturbances and base flow, which could be computed directly for sufficiently small disturbances with our highly accurate methods. However, this entails additional computational complexity as the tensors become much larger, and as such, only single- or few-capsule systems would likely be computationally tractable with our current methods.

7.3.2 Discriminating chaotic from stochastic behavior in blood flow

In section 4.3.2, we observed the breakup of uniform red blood cell trains into a disordered flow. Similar disordered flow has also been observed in microcirculation (see section 1.2.1), and previous efforts have reproduced details of the cell-scale kinematic behavior with the same numerical flow solver [144].

While this disordered flow is familiar, a predictive model of the cellular motion has yet to be found. Underpinning such a prediction is the origin of the dynamics themselves. The behavior of such dynamical system can be classified as stochastic or fractal noise, or

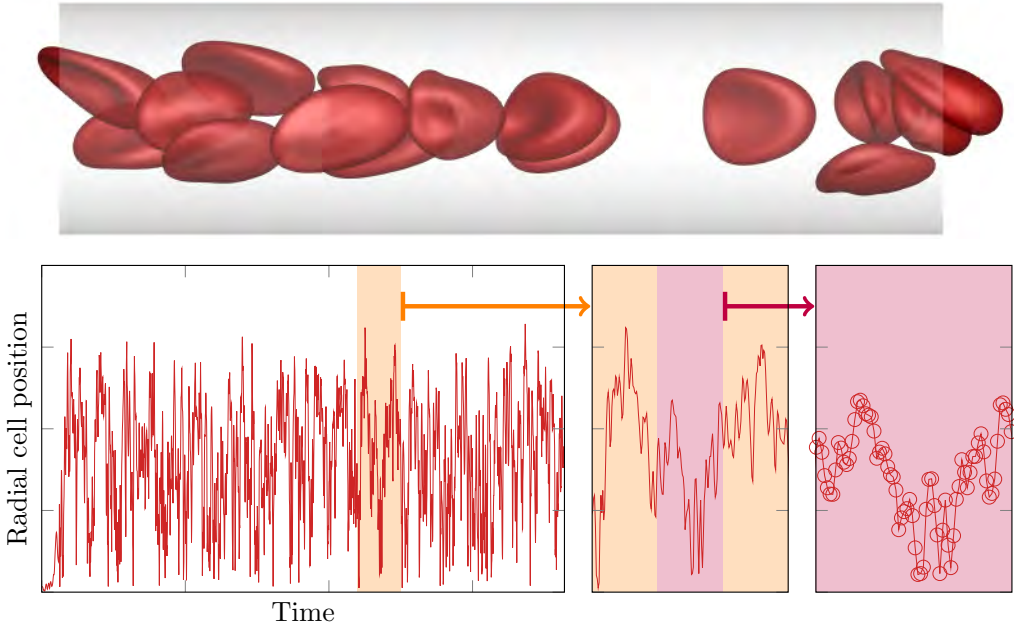


Figure 7.3: Evolution (and magnification) of the radial cell position of the flow above, as quantified by the cell centroid distance from the vessel centerline for an example cell. The entire time series entails 3000 vessel diameters of streamwise cell travel. A visualization of the disordered flow is also shown, the mean velocity is from left to right.

belonging to a chaotic attractor, often of much lower dimension than the full system. This has consequence: if the kinematics are chaotic, we can construct a low-dimension dynamical system that reproduces the flow behavior. However, if the disordered flow appears stochastic in nature; that is, appearing to derive from a random or nondeterministic process, such as that of turbulence [353, 354], then such a system cannot be found. We present a preliminary analysis based upon well-known tools for discriminating between these behaviors.

Figure 7.3 shows time series data for the cell kinematics of an example flow, which was solved using the methods of section 3. The radial location of a cell within the vessel is known to be an important quantity when analyzing cellular blood flow, as it is useful for quantifying margination (see section 1.2.1), and is expected to be important in microfluidic devices used to operate on cells individually. This time series then serves as example data for subsequent analysis.

Discriminating between chaotic and stochastic behavior is not trivial, and misuse of any specific metric used to quantify the difference can lead to erroneous conclusions [355, 356]. To this end, a combination of common measures are typically used to ensure the validity of the conclusions. The time series of figure 7.3 serves as an example data set that we analyze it with these measures; however, we confirm that the reported preliminary results hold for other measures describing the same flow, including the Euclidean distance between any two capsule centroids, and the magnitude of the velocity of any capsule centroid.

Fourier spectrum [357–359]	Utility: Identifying dominant frequencies. Chaotic systems often have a repeated structure in phase space, leading to “spikes” in the Fourier spectrum. Result: The spectrum has no dominant frequency. For small wavenumbers, the spectrum is flat. A power-law decay in the spectrum is observed for high wavenumbers, similar to that of turbulence. Conclusion: Stochastic behavior
Correlation dimension [360–362]	Utility: Given by the mean probability that states at two different times are within a threshold distance. Serves as a measure of spatial correlation of any pair of nearby points. Result: Correlation dimension is the same as the embedding dimension of the data for dimensions up to 100. Conclusion: Stochastic behavior
Structure function [363, 364]	Utility: Gives the stationary space-time correlations of the local cell position. Chaotic systems have the same structure function behavior as a function of space under time-differentiation, while stochastic noise does not. Result: Taking time derivatives of the data result in a flattening of the structure function. Conclusion: Stochastic behavior
Lyapunov exponent [365–367]	Utility: Gives the rate of divergence of nearby spatial trajectories. Result: The maximum exponent is extremely large, > 5 for all time series. This is much larger than is considered normal for chaotic systems. Conclusion: Stochastic behavior

Table 7.1: Tools for discriminating between chaotic and stochastic behavior and their results. Visualization of these metrics are not shown for brevity.

Table 7.1 shows a set of methods used to examine the behavior of the time series shown in figure 7.3. All methods point to the same conclusion: the data appear stochastic in nature and do not come from an underlying low-dimensional dynamics. Of course further analysis of these data is required to fully substantiate this claim, though this the subject of future work. Details of our simulations, data, and analyses around found in appendix F.

A Particle-mesh Ewald method

The periodic boundary conditions of chapter 4 require suited Green's functions. Following a common practice, these are computed using an Ewald summation [313, 368]. This is done by decomposing \mathbf{G} and \mathbf{T} into short-range (sr) and long-range (lr) components,

$$G_{ij} = G_{ij}^{\text{sr}} + G_{ij}^{\text{lr}} \quad \text{and} \quad T_{ijk} = -\frac{8\pi}{V}x_j\delta_{ik} + T_{ijk}^{\text{sr}} + T_{ijk}^{\text{lr}}, \quad (\text{A.1})$$

where $V = L_1L_2L_3$ is the volume of the computational domain. These have been previously calculated [290]. The short-range parts are

$$G_{ij}^{\text{sr}} = \sum_s \text{erfc}(\hat{r}) \left(\frac{\delta_{ij}}{r} + \frac{r_i r_j}{r^3} \right) + \frac{2}{\sqrt{\alpha}} \sum_s \exp(-\hat{r}^2) \left(\frac{r_i r_j}{r^2} - \delta_{ij} \right), \quad (\text{A.2})$$

and

$$T_{lmn}^{\text{sr}} = -\frac{8\sqrt{\pi}}{\alpha} \sum_s \Phi_{3/2}(\hat{r}^2) \hat{r}_l \hat{r}_m \hat{r}_n, \quad (\text{A.3})$$

where $\mathbf{s} = (n_1L_1, n_2L_2, n_3L_3)$ is the periodic shift, $\mathbf{r} = \mathbf{x} - \mathbf{x}_o + \mathbf{s}$ is the displacement vector, $\hat{\mathbf{r}} = \sqrt{\pi/\alpha}\mathbf{r}$ is its dimensionless form, α is the Ewald splitting parameter and gives the length scale of the decomposition, and Φ_β is an incomplete γ -function for order β . We compute (A.2) and (A.3) directly using a sufficient number of close interactions within the neighborhood of \mathbf{x}_o . This calculation converges quickly for expansion of the number of included neighbor points, as the short-range Green's functions decay exponentially with \hat{r} [369]. Thus, a near-neighbor list is used to efficiently track these interactions, giving a computational complexity of $\mathcal{O}(NM)$ [4, 290].

The long-range (or smooth) parts are

$$G_{ij}^{\text{lr}} = \frac{2\alpha}{V} \sum_{\mathbf{k} \neq 0} \Phi_1(\hat{k}^2) (\hat{k}^2 \delta_{ij} - \hat{k}_i \hat{k}_j) \exp[i2\pi \mathbf{k} \cdot (\mathbf{x} - \mathbf{x}_o)], \quad (\text{A.4})$$

and,

$$T_{lmn}^{\text{lr}} = \frac{2\alpha}{V} \sum_{\mathbf{k} \neq 0} (i2\pi)(k_l \delta_{mn} + k_j \delta_{ln} + k_n \delta_{lm}) \Phi_0(\hat{k}^2) \exp[i2\pi \mathbf{k} \cdot (\mathbf{x} - \mathbf{x}_o)] \quad (\text{A.5})$$

$$+ \frac{\alpha^2}{\pi V} \sum_{\mathbf{k} \neq 0} (i2\pi)^3 k_l k_m k_n \Phi_1(\hat{k}^2) \exp[i2\pi \mathbf{k} \cdot (\mathbf{x} - \mathbf{x}_o)]. \quad (\text{A.6})$$

where $\mathbf{k} = (n_1/L_1, n_2/L_2, n_3/L_3)$ is the local wavenumber and $\hat{\mathbf{k}} = \sqrt{\pi\alpha}\mathbf{k}$. The smooth part

is computed through usual smooth PME methods [313, 370, 371]. That is, the Ewald sum of (A.4) and (A.6) are calculated on a uniform mesh spanning the computational domain, for which each surface singularity is distributed to through B-splines, using fast Fourier transforms. The computed velocities are then interpolated back to the surfaces. This gives a total arithmetic operation scaling of $\mathcal{O}(NM \log NM)$ for the long-range component of the Green's functions, and thus of the overall PME method.

B Buckling and its effect on the confined flow of a model capsule suspension

B.1 Introduction

Rheology of suspensions depends upon the mechanics of the suspended elements, which can be particular complex for elastic capsules, especially when flowing in narrow confines. In such cases, the membrane deformations can be strongly coupled with the overall flow dynamics [67, 70, 372], making it difficult to analyze. We consider a simple model suspensions of such capsules, each an incompressible liquid filled elastic membrane. These can be considered models of natural capsules, such as vesicles, biological cells, or viruses, or artificial capsules such as those used for targeted drug delivery or time releasing aromas or flavors [49, 50, 53, 54]. Natural capsules typically are formed by a lipid bi-layer membrane, which is buttressed in many cases with additional molecular components such as proteins. Common artificial membrane are manufactured using polymers such as alginate, poly-L-lysine, or polyacrylates [33]. While these molecular details are important for the dynamics of any particular capsule system, we focus our study specifically on the finite-deformation dynamics of highly deformable membranes, and do not further consider their molecular make-up.

Blood is a particularly important suspension of this type, and though we only consider a two-dimensional model configuration, it does reproduce important phenomenology, quantitatively in cases, and potential implications for the flow of blood cells in tight confines are discussed throughout. The baseline configuration we considered displays a biconcave shape equilibrium similar to red blood cells [373–376]. We also consider capsules with increased and decreased relative surface area, which correspond to certain pathological conditions in blood. Both surface area and volume are approximately constant for healthy red blood cells, but some disease conditions cause relative volume to disproportionately increase forming spherocytes [327, 377, 378], or decrease forming sickle-shaped cells [326]. Similarly, shape and mechanical properties are potentially important design parameters for artificial capsules to be suspended in blood or used otherwise [379–382], and the development of artificial blood remains a long-term goal [60]. In our model, we consider a range of equilibrium shapes, loosely based upon these observed and potential variations, which lead to phenomenological changes in the capsule dynamics and thus the confined-suspension rheology.

The rheological behavior of such a suspension flowing in a narrow channel is most obviously manifested in its effective viscosity, as would be deduced based on pressure drop were it a homogeneous Newtonian fluid. For blood, complex scale-dependent behavior of effective viscosity has been observed for a long time [89, 90], the root mechanism of which seems to be the formation of a cell-free layer at adjacent walls. Their formation decreases

flow resistance and is thought to be an important factor in microcirculatory dynamics [5]. The thickness of this cell-free layer has been shown to decrease with increasing hematocrit, increase with increasing flow rate, and decrease with increasing cell stiffness [94–98]. We show a fundamental change in this layer for increasing membrane surface area: the overall viscous resistance increases abruptly with a concomitant disappearance of any significant cell-free layer. The implications of this potentially extend beyond the overall rheology since the properties of red blood cells are also known to mediate the margination process of leukocytes and platelets [101–105], which are important for inflammation and thrombosis.

Our goal is to quantify the effective viscosity, as it depends upon the membrane surface area, and understand how this rheological behavior relates to the dynamics of the suspended elastic capsules. In particular, we investigate changes that occur as capsule equilibrium shapes are varied from relatively circular to highly elongated, and how the microstructural dynamics of these capsules manifest in the macroscopic suspension dynamics. This is done with a detailed, though two-dimensional, flow configuration, which serves as model for blood and its flow, either in the microcirculation or in a microfluidic device. While this two-dimensional model will not necessarily be quantitatively precise for blood, or indeed any genuinely three-dimensional suspension, such a model has been used extensively to study capsule dynamics in homogeneous shear [67], and to reproduce key phenomena of the microcirculation [165, 383]. Its advantage is that it facilitates simulation of many cases and more extensive averaging to collect important flow statistics, which is helpful for discovering and mapping out flow mechanisms and regimes.

The specific flow configuration studied is introduced in section B.2, and the spectral boundary integral method used to solve the fully-coupled fluid-structure capsule dynamics is outlined in section B.3. The results are discussed in section B.4, which includes the rheological changes in the suspension effective viscosity and the microstructural changes in the suspended capsules. This section also includes auxiliary simulations to quantify a capsule buckling behavior that is linked to the overall suspension dynamics and is reflected in a rapid increase in the role of capsule rotation in the overall dynamics, as quantified by a multipole expansion analysis. Section B.5 summarizes the principal conclusions and provides some additional discussion regarding their implications.

B.2 Physical model system

We consider a streamwise periodic channel as a model for fully developed flow in a long section of a microvessel or microfluidic device as shown in figure B.1. The mean flow velocity is U , the channel width is W , its periodic length is L , and in it are N suspended capsules, each of area $A = \pi r_o^2$. For all quantitative results, $L = 40r_o$, which is sufficiently large that the reported results are insensitive to it. This was confirmed by doubling L and N for selected cases and confirming that effective viscosity statistics were unchanged. Channel widths vary from $W = 14r_o$ to $40r_o$. The area-fraction of the channel occupied by the

capsules, a nominal hematocrit were this blood, is

$$H_c = \frac{N\pi r_o^2}{WL}, \quad (\text{B.1})$$

which is varied $H_c = 0.01$ to 0.4 , covering a wide range from dilute to approximately that of whole blood.

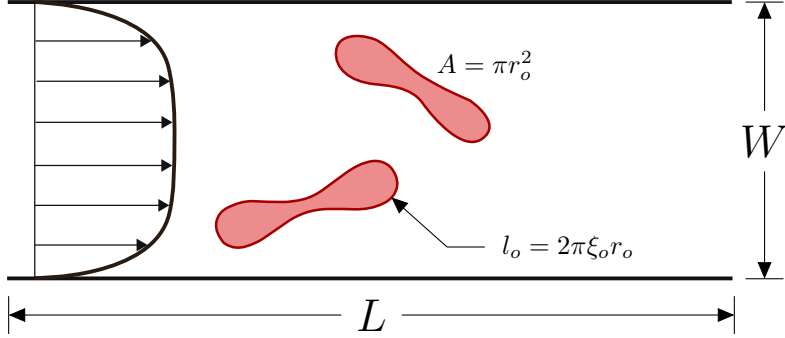


Figure B.1: Schematic of the two-dimensional streamwise-periodic model channel with capsules of area A and perimeter l_o .

The capsules are encased by elastic membranes with linear finite-deformation tension and bending moduli, \mathcal{T} and \mathcal{M} respectively. This linearization is derived from the full nonlinear Helfrich energy [384] and has been employed previously for thin elastic membranes [165, 385]. We also verify that key reported observables changed by at most 4% upon using the full nonlinear Helfrich energy. In terms of an arc length coordinate $s(s_o)$ and reference arc length s_o , the membrane tension τ and bending moment b are,

$$\tau = \mathcal{T} \left(\frac{ds}{ds_o} - 1 \right) \quad \text{and} \quad b = \mathcal{M}(\kappa - \kappa_o), \quad (\text{B.2})$$

where C is the curvature with reference curvature $C_o = 0$. With these, the net traction exerted by the cells on the fluid is

$$\Delta\sigma = \frac{\partial t\tau}{\partial s} + \frac{\partial}{\partial s} \left(\frac{\partial b}{\partial s} \mathbf{n} \right), \quad (\text{B.3})$$

where \mathbf{t} is the membrane unit tangent and \mathbf{n} is its outward unit normal. Of particular interest is the membrane reference length l_o relative to its minimum (that of a circle), which is parameterized by ξ_o : $l_o = 2\pi \xi_o r_o$. As such, ξ_o is the squared inverse of what might be considered a reduced area,

$$A_r = \frac{4\pi [\text{area}]}{[\text{perimeter}]^2} = \frac{1}{\xi_o^2}, \quad (\text{B.4})$$

though we will generally quote ξ_o because of its clear connection with the capsule reference perimeter and therefore buckling criteria (see section 4.6).

The fluid both inside and outside the capsules is Newtonian with viscosity μ . Actual

red blood cells are thought to have an elevated interior viscosity [12, 386], by about a factor of 5 [14], though matched viscosity has been shown to provide qualitatively realistic blood flow phenomena in two dimensions [165] and quantitative accuracy for many quantities in three dimensions [144]. Taking values appropriate for blood under physiological conditions, the Reynolds number based upon the mean flow $U \lesssim 1$ mm/s, mass density $\rho = 10^3$ kg/m³, $\mu \approx 3 \cdot 10^{-3}$ Pa·s, and $W = 30\ \mu\text{m}$ is $Re \approx 0.01$, which supports neglect of inertia in the governing equations. We assume that any corresponding manufactured capsules or microfluidic devices operate under similarly low-Reynolds-number conditions. For convenience we form the parameters into a capillary number

$$Ca \equiv \frac{\mu U}{\mathcal{T}}, \quad (\text{B.5})$$

which we vary from $Ca = 0.2$ to 1 and can be interpreted as a ratio of a relaxation time to an advection time. Similarly, we define a relative stiffness parameter,

$$\frac{r_0^2 \mathcal{T}}{\mathcal{M}} = 50, \quad (\text{B.6})$$

which we hold fixed at this relatively large value as a model for the near incompressibility of typical capsule membranes.

B.3 Numerical methods

The discretization is based upon a boundary integral representation for the velocity u_i in terms of the surface tractions from (B.3) [159, 311]:

$$u_i(\mathbf{x}) = U_i(\mathbf{x}) + \frac{1}{4\pi\mu} \int_{\Omega} S_{ij}(\mathbf{y} - \mathbf{x}) \Delta\sigma_j(\mathbf{y}) ds(\mathbf{y}), \quad (\text{B.7})$$

where $\mathbf{U}(\mathbf{x}) = (U, 0, 0)$ is the mean velocity and Ω represent all the membranes and the vessel walls with outward unit normal \mathbf{n} . The kernel S_{ij} in (B.7) is the Green's function of the Stokes equation (the so-named Stokeslet),

$$S_{ij}(\mathbf{x}) = \frac{\hat{x}_i \hat{x}_j}{r^2} - \delta_{ij} \ln r, \quad (\text{B.8})$$

evaluated at \mathbf{x} for a singular unit-strength Stokeslet force at \mathbf{x}' , with $\hat{\mathbf{x}} \equiv \mathbf{x} - \mathbf{x}'$ and $r \equiv |\hat{\mathbf{x}}|$.

Each membrane is discretized by N_p points distributed uniformly over its (periodic) reference arc length, parameterized by s_o . Derivatives and integrals on the membranes are computed via an interpolating Fourier series [4, 310]. Though the Stokes flow (B.7) and the constitutive model (B.2) are linear, the geometric factors (normals, tangents, and curvatures) introduce nonlinearity, which can lead to numerical instability via aliasing [4, 70]. This is suppressed, without compromising the fidelity of the solution supported by the Nyquist limit of the N_p collocation points, by evaluating $\Delta\sigma(s_o)$ on $N_a > N_p$ points and Fourier filtering to N_p points after nonlinear operations. In all simulations $N_a = 4N_p$. We confirm that reported results are insensitive to the selected resolution N_p .

To avoid both the complexity of a series Green's function to represent the walls [387, 388] and the solution of a single-layer formulation, we enforce the no slip condition via a penalty method in which the wall is constructed from elements that are permitted to displace a small amount. Each of the 750 independent Δs_w -wide elements of each wall is anchored to its reference location \mathbf{x}_w by a Hookean spring, so its imposed traction is

$$\Delta\boldsymbol{\sigma}_w = -S_w(\mathbf{x} - \mathbf{x}_w). \quad (\text{B.9})$$

The spring constant $S_w = 1.7\mathcal{T}/r_o^2$ can be relatively large without restricting the stability limit of the time integrator as set by the capsule membrane dynamics.

Consistent with the neglect of inertia in the flow equations the capsule membranes and vessel walls are assumed to be massless, so given the velocity $\mathbf{u}(\mathbf{x})$ from (B.7), the membrane position is governed simply by

$$\frac{d\mathbf{x}}{dt} = \mathbf{u}(\mathbf{x}), \quad (\text{B.10})$$

which is applied to each collocation point of the discrete representation. This system (B.10) is integrated in time using a second-order Runge–Kutta scheme with a time step of $\Delta t = 0.01\mu r_o/\mathcal{T}$.

It is well-understood that the lubrication layers that form upon close approach between such capsules would mathematically prohibit contact in finite time for finite forces. However, even in our idealized physical model, numerical errors can lead to overlap between the capsules, which we avoid with a short-range repulsion between nearby capsules. Though this can be considered as a model for repulsive lubrication forces, physiologic capsules are expected to have more complex interactions, so it is unclear that even a precise lubrication formulation would be appropriate. Steric and electrostatic repulsion are thought to mediate contact between red blood cells at very small length scales [389]. For realistic simulation of blood cells in three dimensions, boundary integral have been used to simulate lubrication down to the scale of proteins [144], but further resolution is unlikely to provide a more realistic physical description because it would not represent in detail the actual contact and near-contact interactions. In our formulation, the repulsion force at a point \mathbf{x} on a membrane due to another \mathbf{x}' is

$$\mathbf{f}(\mathbf{x}) = \begin{cases} S_f \frac{e^{\delta-r}-1}{e^\delta-1} \frac{\mathbf{x}-\mathbf{x}'}{r} & \text{for } r \leq \delta \\ 0 & \text{otherwise} \end{cases}, \quad (\text{B.11})$$

where $r = |\mathbf{x} - \mathbf{x}'|$, $\delta = 0.2r_o$, and $S_f = 2.5\mathcal{T}$. The derivative of \mathbf{f} with respect to s is added to the traction (B.3) in the integrand of (B.7). Similarly, the area of the capsules is only enforced by the fidelity of the numerical schemes. Although this is very accurate because it is a low-order moment of the capsule shape and thus well resolved, still a weak variational correction is applied to preserve constant area indefinitely as has been used previously [165].

Our implementation has been extensively verified against analytical results for Poiseuille flow in a wavy-walled channel [383], and more recently for the drag on an infinite periodic lattice of circles in cross-flow [368]. In this latter case, results are within 1% error for 50

collocation points and 0.4% error for 100 collocation points per circle. We also confirmed that the effective viscosity we report changed by less than 1% upon changing the wall strength from $S_w = 1.7\mathcal{T}/r_o^2$ to $3.4\mathcal{T}/r_o^2$, repulsion from $S_f = 2.5\mathcal{T}$ to $5\mathcal{T}$, and both doubling and halving the repulsion length scale δ .

B.4 Results

B.4.1 Equilibrium shapes

We start by visualizing the equilibrium shapes for different ξ_o in figure B.2, which display expected variations [373, 390, 391]. Taking $\xi_o = 1.0$ yields a circle, which is only ever slightly distorted by flow for our conditions, and small increases in ξ_o lead to a mildly prolate convex geometry. Increasing prolate shapes for larger ξ_o transition to a biconcave configuration near $\xi_o \approx 1.4$, nominally matching a healthy red blood cell for $\xi_o \approx 1.6$. Increasing ξ_o further leads to additional inflection points for $\xi_o \gtrsim 2.1$ and produces dog-bone-like shapes with increasingly high aspect ratios. Note that the repulsion force \mathbf{f} between sufficiently close collocation points, according to (B.11), prevents the membrane from self-intersecting for large ξ_o , as it would otherwise.

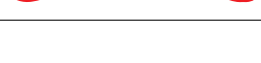
ξ_o	Shape	Visualization
1.0	Circle	
1.3	Prolate	
1.4	Prolate-biconcave transition	
1.6	Biconcave	
1.8	Biconcave	
2.1	Biconcave-dog-bone transition	
2.4	Small aspect-ratio dog-bone	
3.0	Large aspect-ratio dog-bone	

Figure B.2: Example equilibrium shapes for different ξ_o .

While $\xi_o \approx 1.6$ corresponds most closely to a healthy red blood cells, the near-circular capsule geometry ($\xi_o \approx 1$) is characteristic of spherocytes, the defining symptom of sphero-cytosis, a hereditary disorder that mutates the genes encoding red cell membrane proteins, causing a loss of membrane [374,392]. Additionally, many artificial capsules are manufactured to have a similar spherical shape [53,379–381,393]. With increasing ξ_o , the capsules become elliptical and prolate. These geometries are found in elliptocytes, which is similarly found in those diagnosed with elliptocytosis, caused by similar mutations as sphero-cytosis, but arise via a lateral interactions of the cytoskeleton [374,392]. For larger $\xi_o \gtrsim 2.0$, corresponding configurations for red blood cells have been observed in severe cases of anemia and sickle cell anemia [394,395]. Manufactured capsules of this geometry have also been proposed for a variety of applications, such as coatings, aerosols, and drug delivery [396,397] with different conformations. The behavior of these different capsules in flow is considered next.

B.4.2 Flow visualizations

Figure B.3 shows flowing capsules for different ξ_o at the largest and smallest capillary numbers. In the $\xi_o = 1.0$ nearly circular limit (figure B.3 (a) and (b)), capsules are only slightly deformed from circular shapes, though more so for the faster flow and nearer to the vessel walls where the shear is larger. The asymmetry of near-wall capsules is thought to facilitate their migration towards the center of a channel [144,398]. For the $\xi_o = 1.7$ cases, with biconcave equilibrium shapes, capsules in figure B.3 (c) and (d) do not show any significant shape distortion for the range of capillary numbers simulated. In the large $\xi_o = 3.0$ cases (figure B.3 (e) and (f)), some capsules fold (as visualized specifically in figure B.4), which seems to disrupt their otherwise relatively ordered flow. This will be analyzed subsequently as a buckling mechanism, and the increased resistance this causes will be quantified as an effective viscosity. It can also be seen that the obvious cell-free layer in the smaller ξ_o cases seems to disappear in this largest $\xi_o = 3.0$ cases; this too is quantified in subsequent sections.

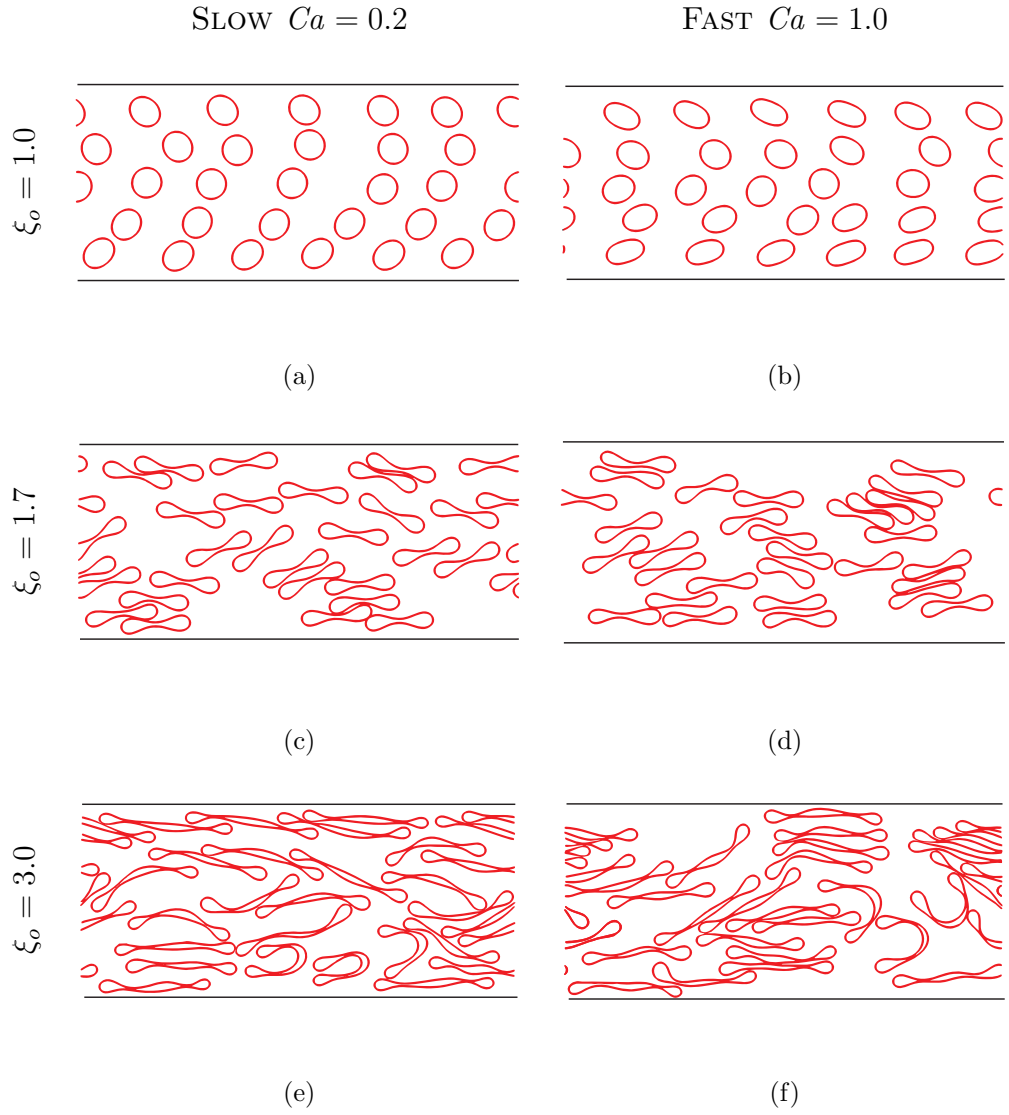


Figure B.3: Flow visualizations for $H_c = 0.25$, $W = 14r_o$, cases are $Ca = 0.2$ and $Ca = 1.0$ and $\xi_o = 1.0, 1.7$ and 3.0 as labeled. For these visualizations $L = 30r_o$.

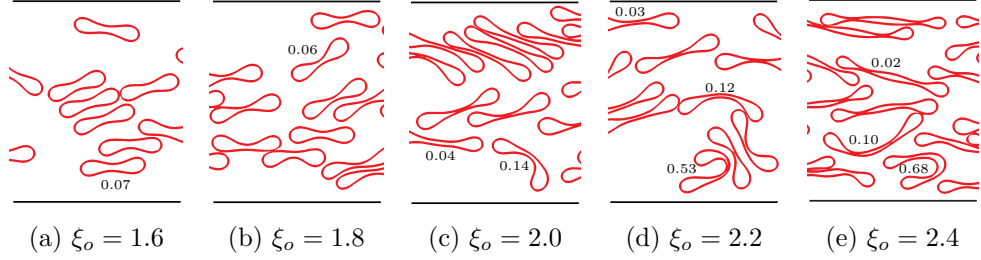


Figure B.4: Visualizations showing the onset of apparent buckling behavior for $H_c = 0.25$, $W = 14r_o$, $Ca = 1.0$ for ξ_o as labeled. The numbers indicate the buckling metric defined in section B.4.6.

B.4.3 Macroscopic resistance: Effective viscosity

The behavior of the capsules in flow for different ξ_o significantly alters the effective viscosity of the suspension,

$$\frac{\mu_{\text{eff}}}{\mu} = -\frac{W^2}{12\mu U} \left\langle \frac{dp}{dx} \right\rangle. \quad (\text{B.12})$$

Reported values for μ_{eff} are time averages, starting after an apparently statistically stationary flow condition has been reached as quantified in figure B.5. After an obvious transient, averaging is initiated once the instantaneous μ_{eff} varies by less than two percent. This condition is used for all cases reported.

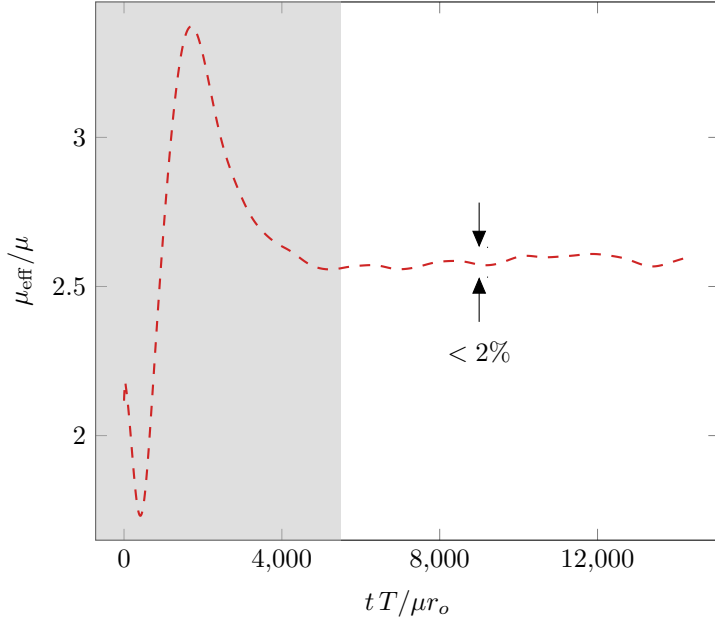
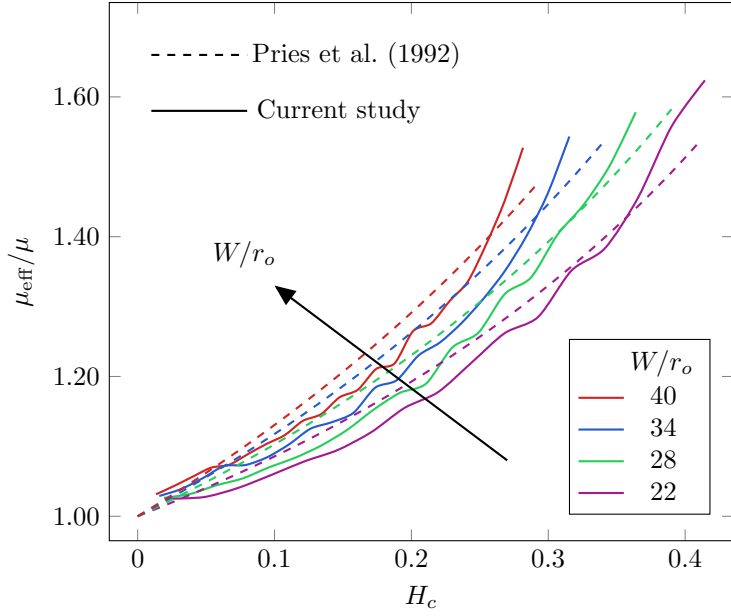
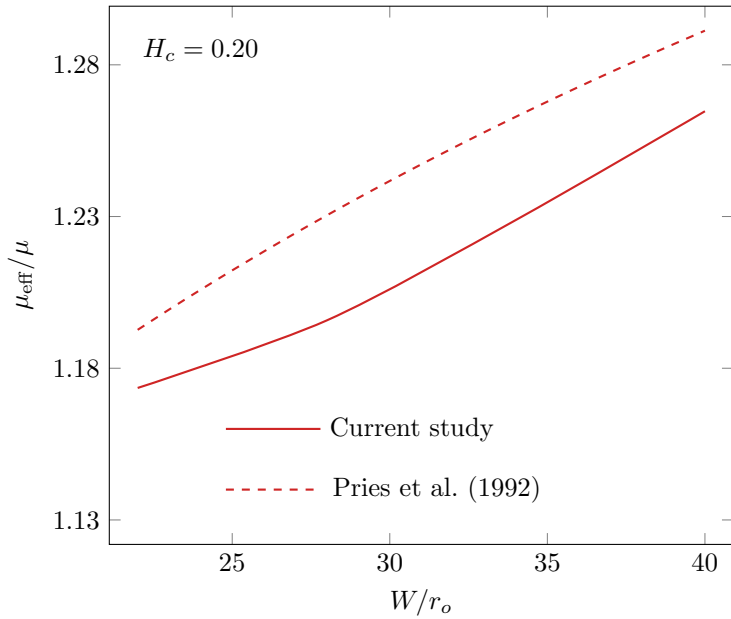


Figure B.5: Instantaneous μ_{eff} from (B.12) for $H_c = 0.25$, $W = 20r_o$ and $\xi_o = 2.4$. The nominally transient period is shaded, after which effective viscosity deviates by $< 2\%$.



(a) μ_{eff} versus H_c for various W/r_o



(b) μ_{eff} versus W/r_o for $H_c = 0.20$

Figure B.6: Effective viscosity μ_{eff} from (B.12): (a) as a function of hematocrit for fixed channel width and (b) as a function of W for $H_c = 0.20$. Note that the dashed lines represent empirical fits of experimental data from [5].

We first consider $\xi_o = 1.6$, which would best correspond to healthy red blood cells, and vary H_c and W , as in previous rheological studies of blood [76, 90]. In figure B.6 (a), effective viscosity is found to increase nonlinearly with H_c , in qualitative agreement with experimental results [5]. Even a quantitative comparison with the corresponding empirical fits of [5] is surprisingly good despite obvious approximations we make in applying the current configuration as a model for blood. In figure B.6 (b), we see that the effective viscosity depends approximately linearly on channel width, which again agrees with experimental findings for blood, matching both the slope over the range of W considered and values are within 10%. It should be recognized in viewing these results that the present channels are several basic blood cell radii r_o across, and so we do not see the non-monotonic behavior that would be expected for vessels matching the cell dimensions, though this too has been reproduced with similar cell-scale simulations [4].

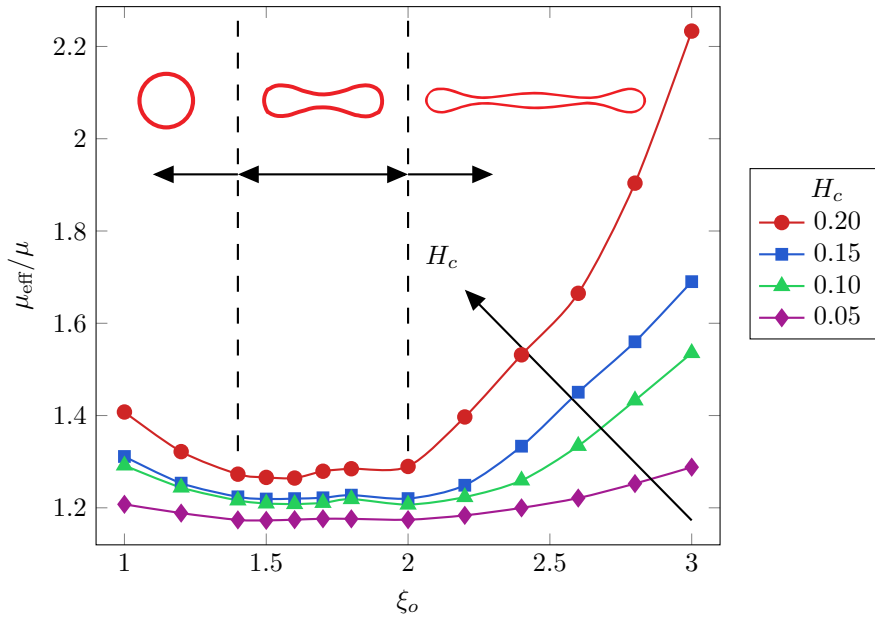


Figure B.7: Effective viscosity for several different cases of H_c and ξ_o . $W/r_o = 20$, $Ca = 1$ for all cases.

Looking beyond this flow as a model of healthy blood, which might best correspond to $\xi_o = 1.6$, in figure B.7 we see that there is significantly richer behavior when ξ_o is varied significantly. For all H_c , this nominal blood-like configuration $\xi_o \approx 1.6$ yields a local minimum μ_{eff} , with resistance increasing both toward smaller and larger ξ_o . The change is most pronounced for the largest $\xi_o \approx 3.0$ dog-bone geometries. In addition, capsules with $\xi_o \approx 1.6$ are also the least sensitive to changes of hematocrit: for $\xi_o = 1.6$, changing from $H_c = 0.05$ to 0.20 increases μ_{eff} by only a factor of 1.08, whereas it increases by a factor of 1.17 for $\xi_o = 1$ and by 1.73 for $\xi_o = 3$. We investigate the mechanisms underlying these observations in the remainder of the paper, and start here by recalling that the visualizations in figure B.3 suggest that the large ξ_o dog-bone shaped cells do not form any significant cell-free layer. It is well known that the presence of the cell-free layer decreases the effective

viscosity of blood flow [162, 399–402], which presents an obvious candidate mechanism for the seemingly rapid increase in μ_{eff} with ξ_o .

B.4.4 Capsule-free layer

We define the capsule-free layer thickness h to include 1% of the collocation points representing the capsule membranes. All results are insensitive to this specific threshold; because the boundary between the nominally capsule-free layer and the capsule-rich region is relatively sharp, changing this criterion to 15% resulted in less than a 0.5% change in h/W for typical cases. In figure B.8, it is clear that $\xi_o \approx 1.6$ discocyte geometries maximize the capsule-free layer thickness, which would indeed reduce μ_{eff} . We also see that faster flow (Ca) increases h for all cases with $\xi_o \lesssim 2.0$, similar to experimental observations for red blood cells [162, 399, 403]. For $\xi_o \lesssim 1.2$ (nearly circular capsules), h decreases modestly, consistent with experiments on hardened capsules and red blood cells [404, 405]. Most notable in figure B.8, however, is that the sharp change to a much thinner layer for $\xi_o \gtrsim 2.0$ suggests a fundamental change in the microstructural flow dynamics, which is investigated more thoroughly in section B.4.5.

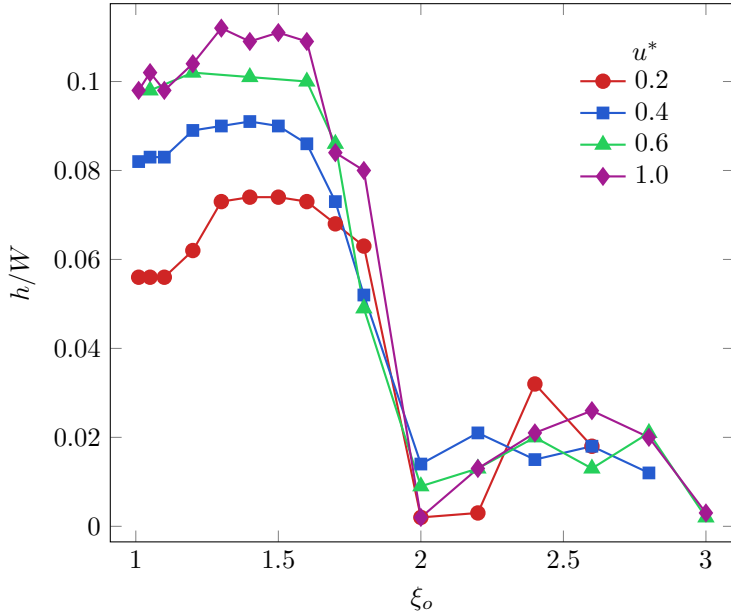


Figure B.8: Dependence of the capsule-free layer thickness on ξ_o and capillary number Ca , shown for cases with $W/r_o = 20, H_c = 0.25$.

B.4.5 Capsule orientation

We start our investigation of the capsule-scale flow structure by again considering the visualizations in figures B.3 and B.4, noting that the $\xi_o \gtrsim 2.0$ capsules appear to have a tendency to fold, change orientation, and in certain cases apparently buckle. This seems to disrupt the relatively ordered arrangements of $\xi_o \lesssim 2.0$ capsules, and corresponds with the

apparent decrease of h . We start by considering the mean orientation angle and its variation in the different cases.

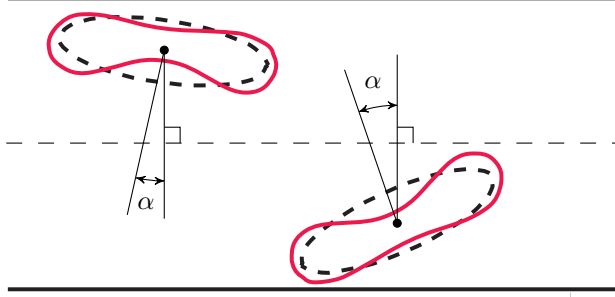


Figure B.9: Schematic of model capsules (solid) and their respective fitted ellipsoids (dashed.)

A nominal orientation is quantified based upon the orientation of a fitted ellipse determined by the eigensystem of

$$M_{ij} = \frac{1}{l} \int_l x'_i x'_j dS(\mathbf{x}), \quad (\text{B.13})$$

where l is the capsule membrane length, and \mathbf{x}' is the surface position relative to the centroid: $\mathbf{x}' = \mathbf{x} - \mathbf{x}_c$. The eigenvalues $\lambda_{1,2}$ and corresponding eigenvectors $\mathbf{e}_{1,2}$ of M define a fitted ellipse,

$$\mathbf{x} = \sqrt{2\lambda_1} \mathbf{e}_1 \sin \psi + \sqrt{2\lambda_2} \mathbf{e}_2 \cos \psi, \quad (\text{B.14})$$

where $\psi \in [0, 2\pi]$. The nominal orientation angle α is taken to be that between major axis of the ellipse and the normal to the channel wall (see figure B.9).

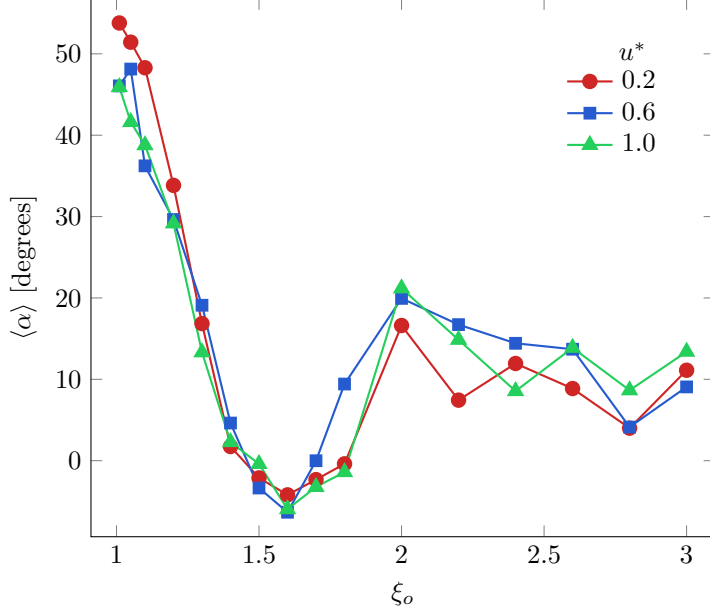


Figure B.10: Average orientation angle for varied ξ_o and flow strengths Ca . $H_c = 0.25$ and $W/r_o = 20$ for all cases.

The mean orientation $\langle \alpha \rangle$ changes significantly for different ξ_o , as shown in figure B.10. Nearly circular equilibrium geometries on average orient with $\langle \alpha \rangle \approx 45^\circ$, corresponding to the visualization in figure B.3. For $\xi_o \approx 1.6$, corresponding to a discocyte type conformation, $\langle \alpha \rangle \approx 0$, which has been seen in experiments [406, 407]. However, the still more elongated dog-bone shapes deviate abruptly from this behavior, starting at $\xi_o \approx 2.0$, and tend to orient themselves on average with $\langle \alpha \rangle \approx 15^\circ$. This sharp deviation is of similar character to both figure B.7 and B.8.

The visualizations in figure B.3 also suggest that the orientations also become more varied for $\xi_o \gtrsim 2.0$ as the capsules fold and appear to tumble, which we quantify by the orientation variance

$$\sigma_\alpha = \left\langle \alpha_i - \langle \alpha \rangle^2 \right\rangle^{1/2}. \quad (\text{B.15})$$

Anticipating that σ_α depends on an apparent buckling-like mechanism discussed in section B.4.6, which in turn is expected to be sensitive to the aspect ratio (slimness ratio) of the capsules, we plot the orientation variance against the aspect ratio of the rest configurations of the capsules: l_1/l_2 . This is shown in figure B.11, and it is clear that there is a significant and sudden increase in orientation angle variance in the range $4.5 \lesssim l_1/l_2 \lesssim 6.5$, which corresponds to $1.8 \lesssim \xi_o \lesssim 2.2$. There is also an increase in σ_α for small ξ_o , which have $l_1/l_2 \approx 1$, but this is less consequential because l_1 and l_2 are nearly the same for small ξ_o , and presumably due to the fact that relatively minor perturbations can change the nominal orientation of an ellipse fitted to a nearly round capsule.

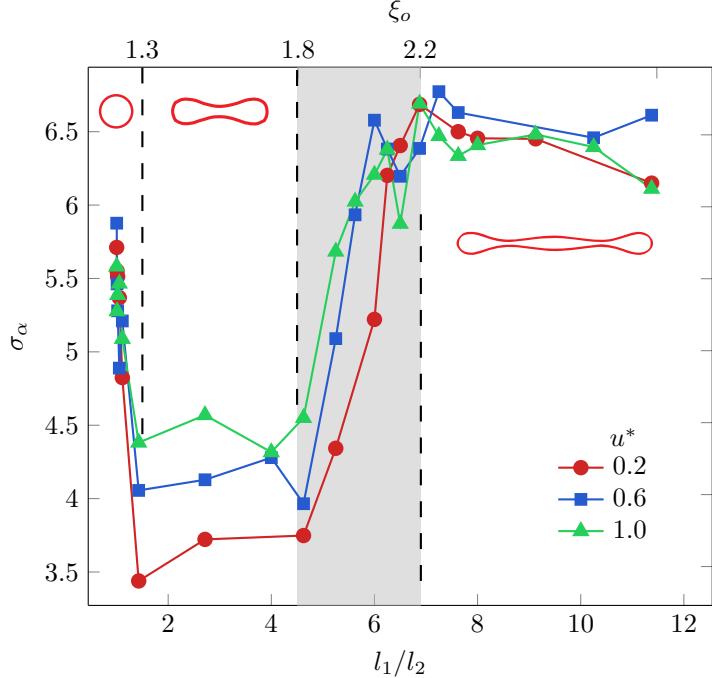


Figure B.11: Variance of orientation angle σ_α as a function of configuration aspect ratio and capillary number for $W/r_o = 20$ and $H_c = 0.25$. The vertical dashed lines represent approximate geometry and behavioral regimes as indicated.

B.4.6 Buckling

To explore the apparent buckling of the capsules in channel flow, we consider it in two more idealized flow configurations. The first is a Taylor–Green flow (figure B.12 (a)), with velocity components

$$U_x = -A \sin\left(\frac{2\pi}{L}x\right) \cos\left(\frac{2\pi}{L}y\right), \quad (\text{B.16})$$

$$U_y = -A \cos\left(\frac{2\pi}{L}x\right) \sin\left(\frac{2\pi}{L}y\right), \quad (\text{B.17})$$

where A is the flow strength and $L = 80 r_o$ is the periodic length of the square domain; it was confirmed that results were independent of this computational domain within $\pm 40 r_o$. A single capsule is placed vertically at the stagnation, such that it will be compressed by the flow as shown in figure B.12 (a). A small perturbation is applied to the shape of the membrane just before the flow is imposed, with

$$x_{\text{pert}} = x + \varepsilon \sin^{10}\left(\frac{y\pi}{l_1}\right), \quad (\text{B.18})$$

where $\varepsilon = 0.01 r_o$ and as before l_1 is the longest at-rest membrane dimension. In this flow model, the magnitude of the relevant velocity scale is given by the velocity difference across the capsule. The second flow is the homogeneous shear shown in figure B.12 (b), which was

imposed in the usual way [67, 408]. The relevant velocity scale is again given by the velocity drop across the capsule; in the case of homogeneous shear this is $U_{\text{shear}} = \dot{\gamma}\ell$ where $\dot{\gamma}$ is the shear rate and ℓ is the vertical distance across the capsule. The capsule is initialized in its equilibrium shape and positioned at 25° from the horizontal (as shown in figure B.9), though we verify that our results produce a consistent onset of buckling for deviations of $\pm 15^\circ$ of this initial angle.

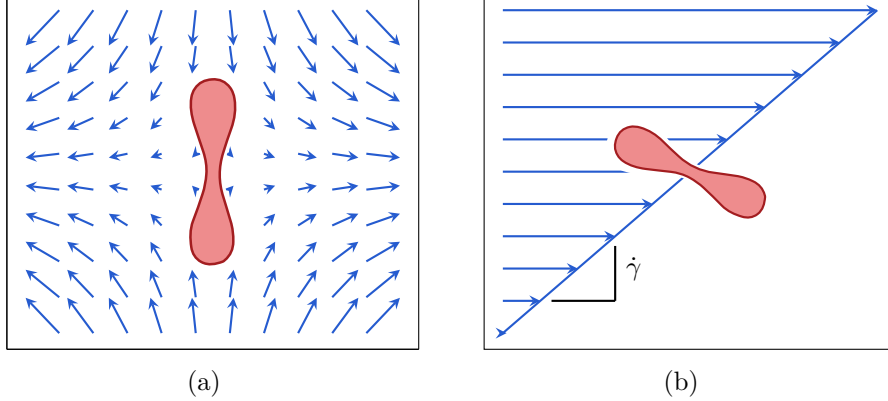


Figure B.12: Auxiliary flow configurations: capsules in (a) Taylor–Green stagnation point flow and (b) homogeneous shear.

The visualizations of figures B.3 and B.4 show several examples of nominally buckled capsules. This is quantified based upon the principal axes of the fitted ellipses: $\lambda \equiv \lambda_1/\lambda_2$, where λ_r is the equilibrium value for a particular ξ_o . A buckled capsule will transition from elongated ($\lambda \approx \lambda_r$) to larger λ , up to $\lambda \lesssim 1$. Some example λ values for different shapes are included in the visualizations of figure B.4).

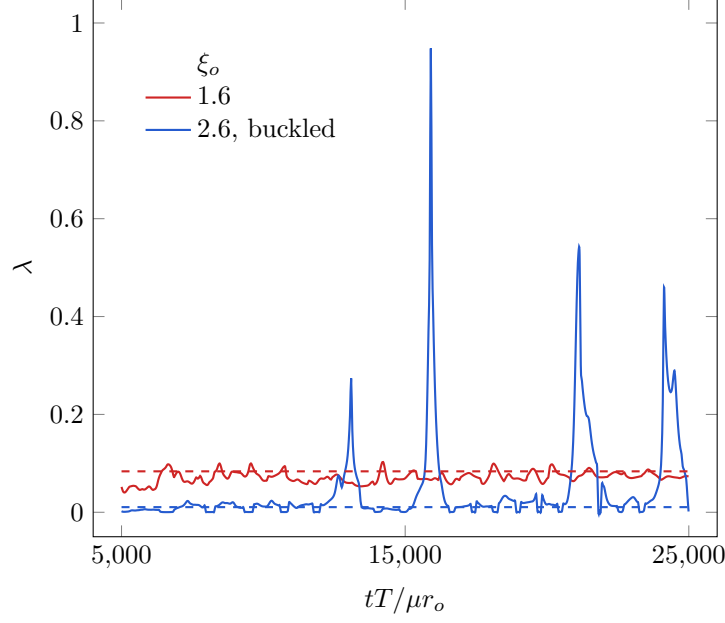


Figure B.13: Buckling parameter $\lambda \equiv \lambda_1/\lambda_2$ from (B.14) for representative biconcave $\xi_o = 1.6$ capsule and a dog-bone $\xi = 2.6$ capsule. Dashed lines show the equilibrium $\lambda = \lambda_r$ condition. In both cases, $H_c = 0.25$, $Ca = 1.0$ and $W = 20r_o$.

We see in figure B.13 that an example $\lambda(t)$ history for a $\xi_o = 2.6$ capsule has four large spikes, each reaching near $\lambda = 1$, indicating four buckling events. This behavior is typical of these capsules. During the course of the simulations nearly all dog-bone geometry capsules are observed to buckle at least once, and typically about 20% of them are buckled at any given time. A corresponding biconcave $\xi_o = 1.6$ case also shown in figure B.13 has a nearly constant λ for its entire history. To provide a specific metric, we take $\lambda \geq 5\lambda_r$ to be buckled.

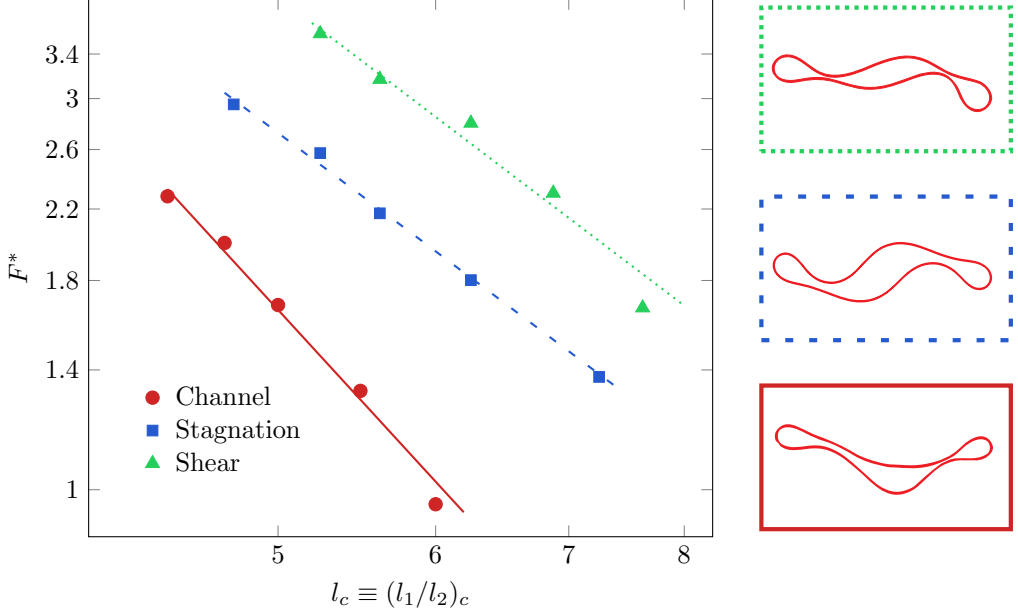


Figure B.14: Scaling of critical buckling aspect ratio due to forcing F^* due to the fluid. Visualizations show examples from the different flow fields for $\xi_o = 2.8$, $Ca = 1$. The channel has $W/r_o = 20$ and $H_c = 0.25$. The straight lines are power-law fits $F^* \sim l_c^{-b}$ with $b = 2.65$ for the channel, 1.82 for the stagnation flow, and 1.82 for the homogeneous shear.

To compare the different configurations, we defined a non-dimensional critical force, $F^* \equiv F/\mu U l_o$ where U is the relevant velocity scale as described previously. For Euler buckling, this should scale as $F^* \approx 1/l_c^2$, though there is no expectation that the present capsules should exactly follow this criterion developed for solid long, slender objects. Indeed, one might anticipate that the model capsules be better described as approximately axially loaded shells, which have a power-law buckling threshold l_c^{-b} with $1 < b < 2$ [409, 410]. In figure B.14, for the stagnation point flow, we find $F^* \sim l_c^{-1.82}$ and for the shear flow $F^* \sim l_c^{-1.84}$. The channel flow shows more ready buckling, with $l_c^{-2.65}$, possibly due to the finite-amplitude disturbances arising from capsule-capsule and capsule-wall interactions. Studies of red cells show in-plane reversible buckling of healthy cells does occur in an optical trap [411].

B.4.7 Influence of buckled capsules and their kinematics

Buckling behavior also corresponds to a fundamental change in other kinematic behavior of the capsules. Figure B.15 (a) and (b) contrast the $y-t$ trajectories of five arbitrarily selected capsules for $\xi_o = 2.6$ and $\xi_o = 1.6$ cases. It is clear that the $\xi_o = 2.6$ capsules undergo much more lateral migration than the $\xi_o = 1.6$ capsules. The buckled capsules appear to roll in the flow, which is confirmed by plotting their orientation angle history $\alpha(t)$, as computed in section B.4.5, in figure B.15 (c) and (d). In figure B.15 (c), a $\xi_o = 2.6$ capsule that repeatedly buckles (based on $\lambda > 5\lambda_r$) continually changes angle relative to one that does not. These sudden changes of orientation seem to cause disruptions in the flow, which have consequences

of increased interactions with nearby capsules, apparent reduction of cell-free layer thickness, and an increase of effective viscosity. For the corresponding non-buckling $\xi_o = 1.6$ case, the capsule angles are typically much less varied (figure B.15 (d)).

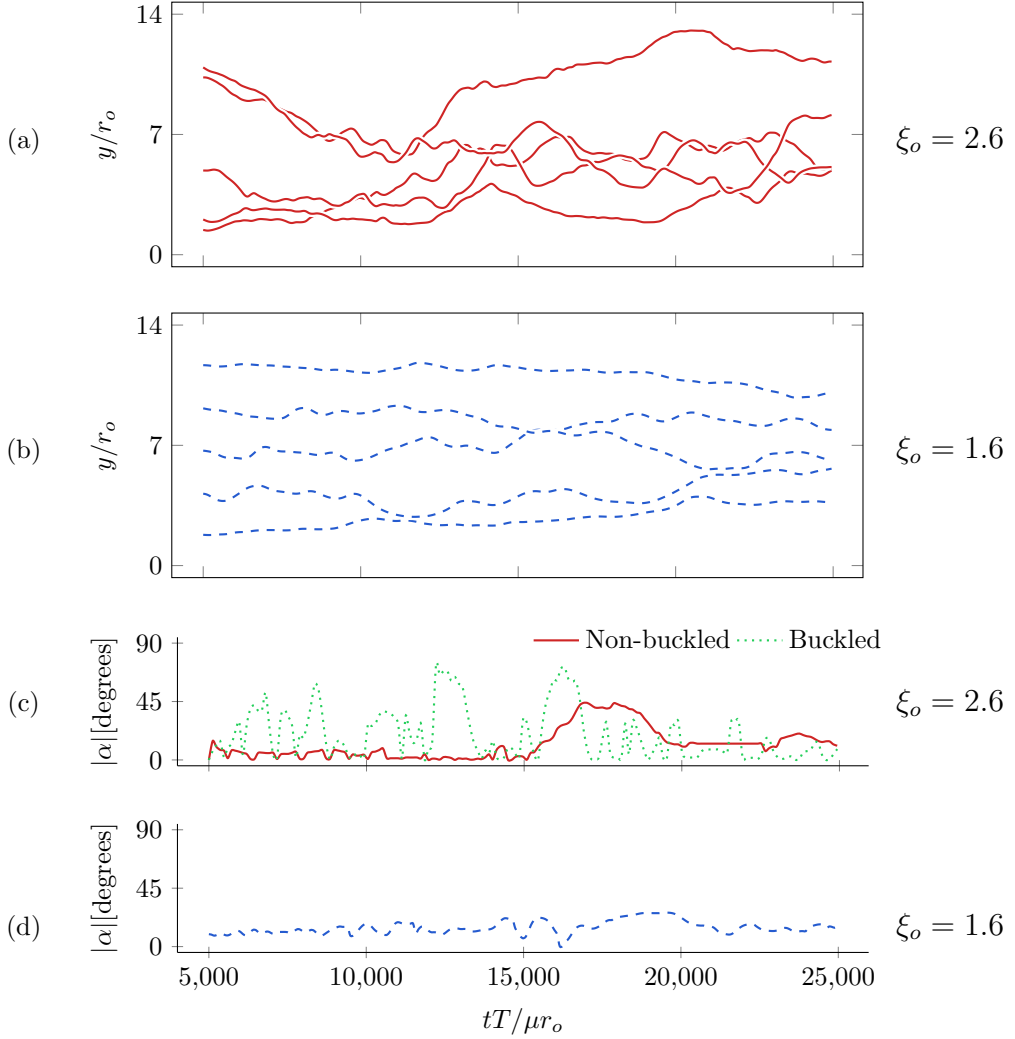


Figure B.15: Transverse position for five representative biconcave and dog-bone capsules with $H_c = 0.25$, $W/r_o = 14$ and $Ca = 1.0$. The orientation of a buckled (c, dotted) versus non-buckled dog-bone capsule (c, solid) are shown as defined (see text) and shown in figure B.13, as well as the orientation of a biconcave capsule (d).

We statistically analyze the overall behavior associated with the specific examples of figure B.15 by computing the average transverse velocity of the capsules \dot{y} . This provides a measure for the lateral migration of the different capsule geometries. We also quantify the mean absolute transverse distance traveled,

$$\Delta_y = \frac{1}{N} \sum_{i=1}^N \max_{j,k} |y_i(t_j) - y_i(t_k)|, \quad (\text{B.19})$$

as another measure of this. It should be noted that Δ_y , as defined, is dependent upon the time over which (B.19) is calculated; here a capsule advected at speed U would have traveled a streamwise distance of $18L/r_o$. In figure B.16 there is an apparent jump to large Δ_y and $\langle \dot{y} \rangle$, for $\xi_o \gtrsim 2.0$, which agrees with the apparent distinct behavior shown in figure B.15 and particularly figure B.11, which shows the rapid increase in capsule-angle variance for $\xi_o \approx 1.9$. This seems to be a distinct change in mechanism where the behavior of $\langle \dot{y} \rangle$ and Δ_y scale approximately logarithmically for circular and biconcave geometries, but are constant for elongated capsules ($\xi_o \gtrsim 2.0$). For the cases simulated in figure B.15, it is found that capsules that buckle during the course of the simulation experience approximately 1.4 times more vertical migration as an average non-buckling capsule (see figure B.15), which then have a proportionally larger hydrodynamic influence on other capsules in the flow.

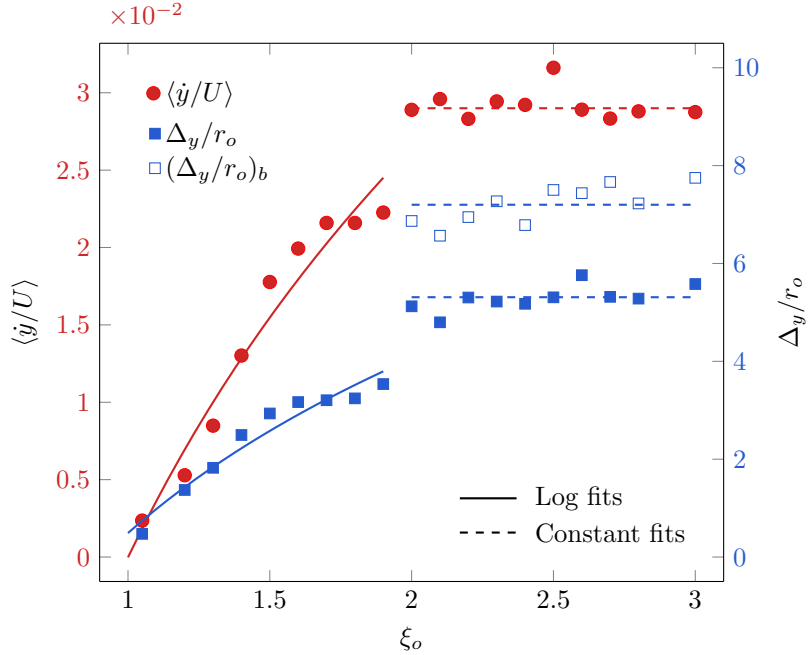


Figure B.16: The average transverse velocity of the capsules $\langle \dot{y}/U \rangle$ and transverse displacement Δ_y/r_o from (B.19). We also show Δ_y for capsules that have buckled at least once during the course of the simulation, $(\Delta_y/r_o)_b$.

B.4.8 Hydrodynamic interactions

The kinematic observations of the previous subsection suggest that large ξ_o capsules buckle more readily, leading to rolling motion and greater transverse transport. Though the interaction dynamics are intricate, we can quantify some of their basic characteristics via multipole moments of the capsules hydrodynamic influence [159, 346]. These are defined by expanding the Stokeslet S_{ij} in (B.8) about the capsule centroid $\mathbf{x}' = 0$,

$$S_{ij}(\mathbf{x} - \mathbf{x}') = S_{ij}(\mathbf{x}) - x'_k \frac{\partial S_{ij}}{\partial x_k}(\mathbf{x}) + \dots \quad (\text{B.20})$$

where \mathbf{x} is a point far from the capsule such that $|\mathbf{x}| \gg |\mathbf{x}'|$. When substituted into the boundary integral equation (B.7), it reduces to

$$u_i(\mathbf{x}) - U_i(\mathbf{x}) = -\frac{F_j}{8\pi\mu} S_{ij}(\mathbf{x}) + \frac{Q_{jk}}{8\pi\mu} \frac{\partial S_{ij}}{\partial x_k}(\mathbf{x}) + \dots, \quad (\text{B.21})$$

where F_j is the hydrodynamic drag force and Q_{jk} is the first moment of the traction about the capsule membranes Ω ,

$$Q_{jk} = \int_{\Omega} (\sigma_{jl} n_l) x'_k \, ds. \quad (\text{B.22})$$

Splitting Q_{jk} into its symmetric and skew-symmetric parts,

$$Q_{jk} = G_{jk} + R_{jk}, \quad (\text{B.23})$$

yields the symmetric stresslet G_{jk} and skew-symmetric rotlet R_{jk} , which is associated with the hydrodynamic torque. These provide a means of estimating to leading order the contribution of stress and rotation to the hydrodynamic influence of each capsule.

In figure B.17 we plot the norms $\|\mathbf{G}\| = \sqrt{G_{ij}G_{ji}}$ and $\|\mathbf{R}\| = \sqrt{R_{ij}R_{ji}}$ for increasing ξ_o . The leading-order stresslet contribution has a minimum for nearly circular capsules $\xi_o \approx 1.0$, as expected because they are compact and seemingly interact with the flow the least (see figure B.16), and more interestingly a local minimum at $\xi_o \approx 2.0$. At this point it seems that potential tank-treading motions are balanced by a tumbling behavior of the elongated capsules. Hydrodynamic interactions are then minimized for very nearly circular geometries, and locally small for biconcave $1.5 \lesssim \xi_o \lesssim 2.0$ configurations. This seems to have the implication that capsules with $1.2 \lesssim \xi_o \lesssim 1.5$ have decreasing resistance to traveling through narrow confines. In contrast, R_{ij} becomes relatively stronger only for $\xi_o \gtrsim 2$ due to the elongated capsule membrane, and corresponds to the onset of buckling and increasing effective viscosity.

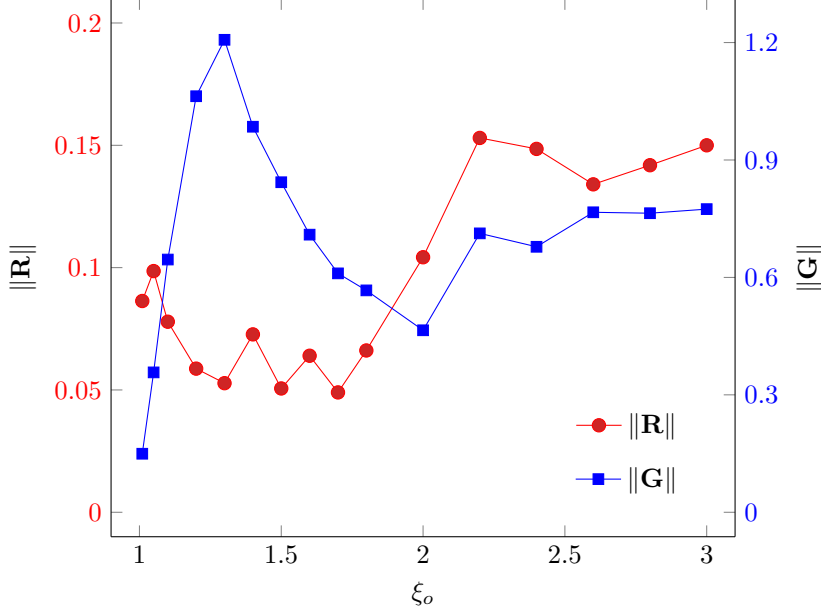


Figure B.17: Stresslet G_{ij} and rotlet R_{ij} strengths for different ξ_o for $H_c = 0.20$, $Ca = 1$ and $W = 20r_o$.

B.5 Conclusions

The role of capsule reduced area was studied in regard to the dynamics of capsule suspensions flowing in narrow confines. A two-dimensional model system was studied, so no quantitative one-to-one correspondence is expected with actual three-dimensional capsules systems. However, its success at reproducing important known phenomena suggests that it can be informative for realistic configurations, including blood flow.

The principal observation was a sudden change in the suspension behavior for capsules with membranes with equilibrium lengths about twice, $\xi_o \approx 2$, that of the minimum. This was manifested in the overall rheology as quantified by a significant jump of the effective viscosity of the suspension. Corresponding changes observed at the capsule scale for $\xi_o \gtrsim 2.0$ were a significantly diminished cell-free-layer thickness, significant variation in in the capsule orientation, increased lateral transport, and increased leading-order rotlet contribution to multipole expansions. These observations corresponded to the onset of a buckling behavior, which were shown to scale with capsule aspect ratio consistent with expectations for shell membranes.

C Stability of capsule trains flowing within channels: a two-dimensional study

Repeated here is the two-dimensional study of capsule trains flowing within channels, as previously published [158]. The specific configuration is introduced in section C.1. The numerical methods appropriate for this two-dimensional system, both for constructing the linearization and for the corresponding direct numerical simulations (DNS), are summarized in section C.2. The stability formulation is outlined in section C.3. Amplification rates and corresponding most-amplifying disturbances for relatively wide and narrow channels with both large and small capsule-packing fractions are summarized in section C.4. These perturbations are examined in regard to transition to nonlinear behavior in section C.4.5, which includes DNS simulations of their evolution into an apparently chaotic flow. Small disturbances that are particularly subject to transient growth—the nominally ‘most dangerous’ disturbances as often discussed for boundary layers [238–240]—are shown to lead to nonlinearity and chaos as much as 1000 times faster than the most asymptotically unstable disturbance. For efficient design of devices and methods that maintain organization by avoiding instabilities, it is essential to consider such disturbances, as has also been recognized in other flows [242, 412–415]. *Ad hoc* random perturbations of the same displacement amplitude grow still much more slowly, suggesting that the specific most amplifying disturbances are of principal importance. Capsule-train stability is shown sensitive to capsule flexibility in section C.4.6, where we also investigate the deformation energy that accompanies the different disturbances.

C.1 Two-dimensional model system

The model capsule–flow system is shown in figure C.1. A streamwise-periodic channel of length L and width W contains N capsules suspended in a viscosity μ Newtonian fluid flowing with mean speed U . Each capsule has area $A = \pi r_o^2$ and a zero-stress perimeter $l_o = 1.6 \times 2\pi r_o$, such that its biconcave equilibrium geometry is similar to the cross-section of a resting red blood cell. The capsules are initialized in their at-rest equilibrium geometry and uniformly spaced along the channel centerline in a one-dimensional train with packing ratio

$$\phi \equiv \frac{Nr_o}{L}, \quad (\text{C.1})$$

which is varied from dilute $\phi = 0.2$ to nearly jammed $\phi = 0.7$. Most results are presented for the relatively narrow $W = 10r_o$ and relatively wide $W = 40r_o$ channels visualized in figure C.2. Channel lengths are varied from $L = 10r_o$ to $500r_o$, with numbers of capsules correspondingly varied from $N = 2$ to 100. Results will show that an apparent asymptotic

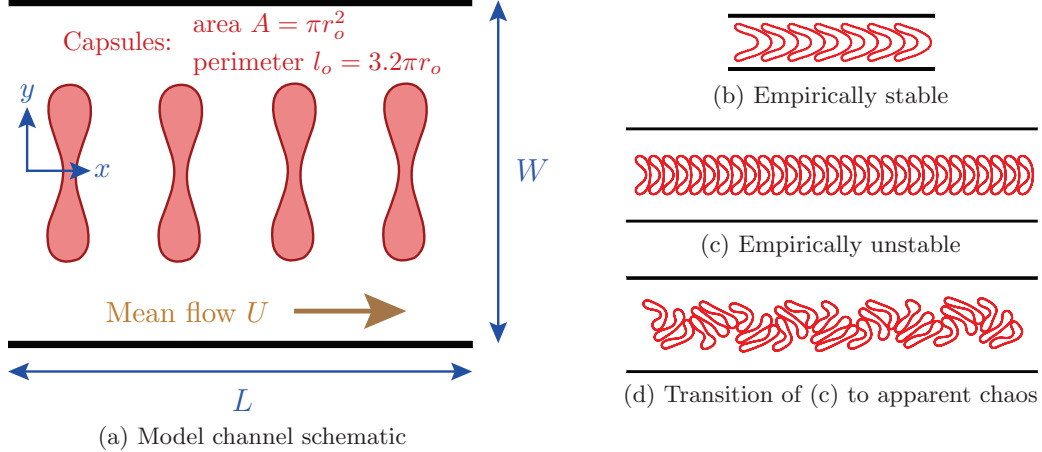


Figure C.1: (a) The model channel flow with mean flow U containing N capsules of area $A = \pi r_o^2$ and perimeter $l_o = 1.6 \times 2\pi r_o$. (b) An empirically stable single-file train in a narrow $W = 4r_o$ channel, (b) an empirically unstable train in a $W = 10r_o$ channel, and (d) its transition into an apparently chaotic flow.

large- L behavior is achieved for $N \gtrsim 20$, which motivates particular focus on cases with $N = 30$. We restrict our investigations to this ordered and regular capsule train, such as might be generated by more narrowly confining upstream geometries. No attempt is made to identify stable states that might exist in wide channels, such as apparently seen in some staggered arrays of immersible droplets. [181]

Each capsule is defined as an elastic shell that resists tension with linear modulus \mathcal{T} and bending with linear modulus \mathcal{M} . Thus, for arc-length coordinate $s(s_o)$ and stress-free reference coordinate s_o , the membrane tension τ and bending moment b are

$$\tau = \mathcal{T} \left(\frac{ds}{ds_o} - 1 \right) \quad \text{and} \quad b = \mathcal{M} \kappa, \quad (\text{C.2})$$

where κ is the curvature. Though these are linear relations, we emphasize that the net traction on the fluid due to the capsule membranes includes all geometric nonlinearity as

$$\Delta\sigma = \frac{\partial t\tau}{\partial s} + \frac{\partial}{\partial s} \left(\frac{\partial b}{\partial s} \mathbf{n} \right), \quad (\text{C.3})$$

where \mathbf{t} is the membrane unit tangent and \mathbf{n} is its outward directed unit normal. We note that this specific model has been used in previous capsule model systems [132, 165]. Although it neglects some nonlinear contributions to the full Helfrich strain energy, [384] results have confirmed that these terms are unimportant in flows with still more significant strains. [132]

Matching the suspending fluid, the fluid within the capsules is also taken to be Newtonian with viscosity μ . Red blood cells are thought to have an elevated cytosol viscosity [12, 14], though it has been shown that a matched viscosity model reproduces phenomena in two dimensions [132, 165, 416] and provides quantitative agreement for the suspension effective viscosity in three dimensions [70, 144]. This simplification has reproduced many of the qualitative features of actual red-blood-cell flow in three dimensions, including the Fåhraeus-



(a) $\phi = 0.2, W = 10r_o$



(b) $\phi = 0.2, W = 40r_o$



(c) $\phi = 0.7, W = 10r_o$



(d) $\phi = 0.7, W = 40r_o$

Figure C.2: Base configurations.

Lindqvist effect, the margination of larger stiffer capsules, the blunted mean velocity profile, and the non-monotonic dependence of the effective viscosity on vessel size. [144, 310]

The relative flexibility of the capsules is quantified with a capillary-number-like parameter,

$$Ca \equiv \frac{\mu U r_o^2}{\mathcal{M}}, \quad (\text{C.4})$$

which can be interpreted as a ratio of a capsule relaxation time to advection time. For most results, we take $Ca = 15.2$; the relative importance of flexibility this parameterizes is investigated in section C.4.6. The tension modulus is relatively large compared to the bending modulus,

$$\frac{r_0^2 \mathcal{T}}{\mathcal{M}} = 50, \quad (\text{C.5})$$

which provides a large tensile stiffness to model the near incompressibility of many capsule membranes. Baseline configurations are obtained by simulating the flow without perturbations for time $t = 5 r_o \mu / \mathcal{T}$, which is sufficient for the capsules to each assume the steady flow-deformed geometries seen in figure C.2.

C.2 Numerical methods

The Reynolds numbers of cell-scale blood flow, or similar capsule suspensions in microfluidic devices, is small $Re \lesssim 0.01$, [70] so inertia is neglected in the present study, which enables a boundary integral formulation of the flow equations [159, 311]. To evaluate velocities, we use the same particle-mesh-Ewald (PME) algorithm generalized for Stokes flow [408] as used in previous studies [132, 165]. It is built upon periodic-space Green's functions [368], with the no-slip condition at the channel walls enforced via a penalty method. [165] Consistent with the neglect of fluid inertia, the mass of the capsule membranes is likewise neglected. As such, the membrane position $\mathbf{x}(t)$ is simply advected as [70]

$$\frac{d\mathbf{x}}{dt} = \mathbf{u}(\mathbf{x}(t)), \quad (\text{C.6})$$

where $\mathbf{u}(\mathbf{x})$ is the local velocity calculated from the boundary integral equation. The time dependence of \mathbf{u} comes only through the membrane geometry $\mathbf{x}(t)$. Although the constitutive model and viscous flow equations are themselves linear, in considering (C.6) it is important to recognize that $\mathbf{u}(\mathbf{x})$ still includes nonlinearities associated with the geometric factors contributing to the surface tractions (C.3). These expressions are evaluated numerically using Fourier methods, [165] with each capsule discretized by $n = 25$ collocation points except when noted. The full list of $M = nN$ total collocation points is represented by the notation $\vec{\mathbf{x}} \equiv \{x_1^{(1)}, x_2^{(1)}, \dots, x_2^{(M)}\}$. Nonlinear operations are computed with four times this amount to counter aliasing errors [4, 70]. A second-order Runge–Kutta scheme is used to

integrate (C.6) in time, which is crafted for the collocation points as

$$\frac{d\vec{x}}{dt} = \vec{u}(\vec{x}) \quad \text{or, equivalently} \quad \frac{dx_i^{(\alpha)}}{dt} = u_i^{(\alpha)}(\vec{x}) \quad \text{for } i = 1, 2, \dots, M, \quad (C.7)$$

with time step $\Delta t = 0.001\mu r_o/\mathcal{T}$.

As they evolve and interact, capsules can come into near contact. Although the boundary integral formulation is unrestricted in this regard by any underlying volume (area) filling mesh discretization, accumulation of even small numerical errors can lead to erroneous interactions between nearby capsules, particularly if the inter-capsule spacing becomes comparable to the capsule surface collocation point spacing. In the long DNS simulations of subsequent behavior, this is countered by introducing a regularizing short-range repulsion between membrane collocation points. We employ the same formulation as past efforts [132, 165], with forces zero beyond distance $0.2r_o$. However, this force is not part of the stability analysis, so the principal results of this study are wholly independent of it.

Similarly, in the course of long simulations the area of the capsules can also change via the accumulation of small numerical errors, though this happens slowly since area is a low-order moment of the capsule shape and therefore well resolved. Still, a weak variational correction is used to preserve constant capsule areas indefinitely [165]. This also is only included for the DNS simulations, so the stability results are likewise independent of it.

C.3 Stability analysis formulation

C.3.1 Measure of configurational stability

Since the goal is to describe the geometric disruption of capsule trains, the measure describing the growth of instabilities is based on the membrane displacement from its unperturbed uniformly advecting baseline configuration. For perturbations applied at time $t = 0$, this is

$$\boldsymbol{\varepsilon}(t) = \boldsymbol{x}(t) - \boldsymbol{x}_b(t), \quad (C.8)$$

where $\boldsymbol{x}_b(t)$ represents the corresponding unperturbed case described in section C.1. The overall disturbance amplitude is quantified by

$$\|\boldsymbol{\varepsilon}\| = \int_{\text{all } C} (\boldsymbol{\varepsilon} \cdot \boldsymbol{\varepsilon})^{1/2} dl, \quad (C.9)$$

where C are the capsule membranes. This measure is not unique, and no unique measure is expected to exist for so complex a system, [234] though it is appropriate for our objectives since \boldsymbol{x} fully describes the system state and $\boldsymbol{\varepsilon}$ directly describes the geometric disruption we study. In essence, it matches the corresponding metrics used previously for the stability

of settling spheres. [177, 180] This measure obviously does not correspond to a mechanical energy, as is available for finite-Reynolds-number incompressible fluid flow, and thus lacks the additional conservation properties such an energy-based measure would embody. The capsules do store strain energy, but any measure that includes it would also introduce an additional challenge in that strain energy is invariant to capsule translation or rigid-body rotation. Such constant-energy perturbations, which we anticipate might be hydrodynamically important for seeding instabilities (and indeed are in cases), do not correspondingly perturb the strain energy. Thus, we do need to be mindful that equal $\|\boldsymbol{\varepsilon}\|$ disturbances do not necessarily correspond to equal mechanical energies. This is revisited in section C.4.6, where the elastic energies corresponding to most amplifying perturbations are considered.

C.3.2 Linearization

Since $\vec{u}(\vec{x})$ couples all the capsule and wall collocation points, which therefore includes significant nonlinearity due to geometric factors, direct linearization of (C.7) is challenging. However, it is straightforward and equally effective to construct a corresponding linearized system through numerical evaluation of $\mathbf{u}(\mathbf{x})$ in (C.7). Expanding (C.7) for small positional perturbation $\vec{\delta}$ yields

$$\frac{\partial(\vec{x} + \vec{\delta})}{\partial t} = \vec{u}(\vec{x} + \vec{\delta}) = \frac{\partial \vec{x}}{\partial t} + \mathbf{A}(\vec{x})\vec{\delta} + \mathcal{O}(\|\vec{\delta}\|^2), \quad (\text{C.10})$$

where \mathbf{A} thus includes the first-order coupling for the present \vec{x} configuration due to perturbation $\vec{\delta}$. In practice this is constructed by systematically perturbing the system and evaluating the velocity. Specifically, each column of \mathbf{A} is calculated by perturbing one of the collocation points $\alpha \in \{1, \dots, M\}$ in one of the coordinate directions $i \in \{1, 2\}$ and calculating $\vec{u}(\vec{x} + \vec{\delta})$. Since only the (i, α) component of the $2M$ -length vector list $\vec{\delta}$ in (C.10) is perturbed (by δ),

$$\delta_j^{(\beta)} = \begin{cases} \delta & \text{for } j = i \text{ and } \beta = \alpha, \\ 0 & \text{otherwise} \end{cases}, \quad (\text{C.11})$$

which provides the $i\text{-}\alpha$ column of \mathbf{A} as

$$A_{ij}^{(\alpha\beta)} = \frac{u_j^{(\beta)}(\vec{x} + \vec{\delta}) - u_j^{(\beta)}(\vec{x})}{\delta} \quad \text{for } j = 1, 2 \quad \text{and } \beta = 1, \dots, M. \quad (\text{C.12})$$

Repeating this for all collocation points and both coordinate directions yields all columns of \mathbf{A} . The translation of the baseline train of capsules due to the mean flow is common to the perturbed and unperturbed \vec{u} in (C.12), so it does not contribute to \mathbf{A} . It is confirmed that results are independent of the $\delta = 10^{-5}r_o$ used here.

Generating the full $2M \times 2M$ matrix \mathbf{A} in this way requires about the same computational effort as $2M$ numerical time steps of the flow solver and would be prohibitive in many numerical flow solutions. For the particular configurations we consider, periodicity of the domain and the identical character of all the capsules can be exploited to reduce this to $2M/N$. An advantage of the boundary integral discretization is that only the surfaces of the capsules are discretized so this is not an insurmountable calculation. The use of

high-resolution Fourier methods further reduces the number of points necessary to accurately represent the membranes and thus describe the stability through \mathbf{A} . The largest case presented here has $2M = 10^5$, which is comparable to the number of time steps of a typical direct numerical simulation of this system.

With \mathbf{A} , the evolution of any sufficiently small perturbation $\vec{\varepsilon}$ is governed by the linear system

$$\frac{\partial \vec{\varepsilon}}{\partial t} = \mathbf{A}\vec{\varepsilon}, \quad (\text{C.13})$$

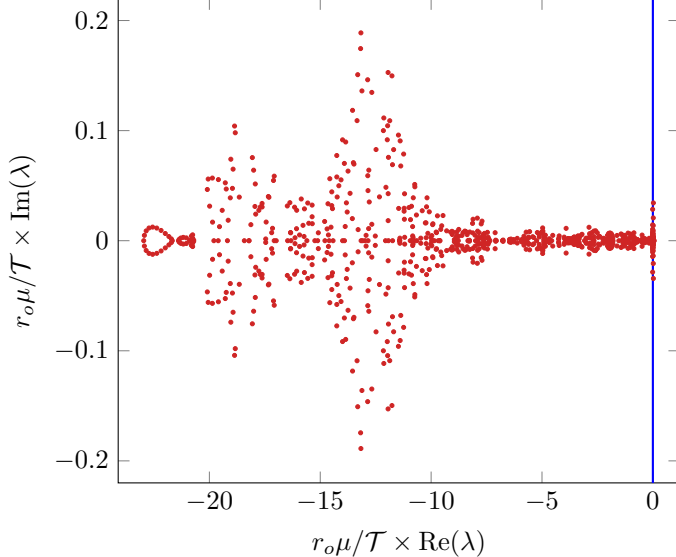
with matrix-exponential solution

$$\vec{\varepsilon}(t) = \vec{\varepsilon}_o \exp \mathbf{At}, \quad (\text{C.14})$$

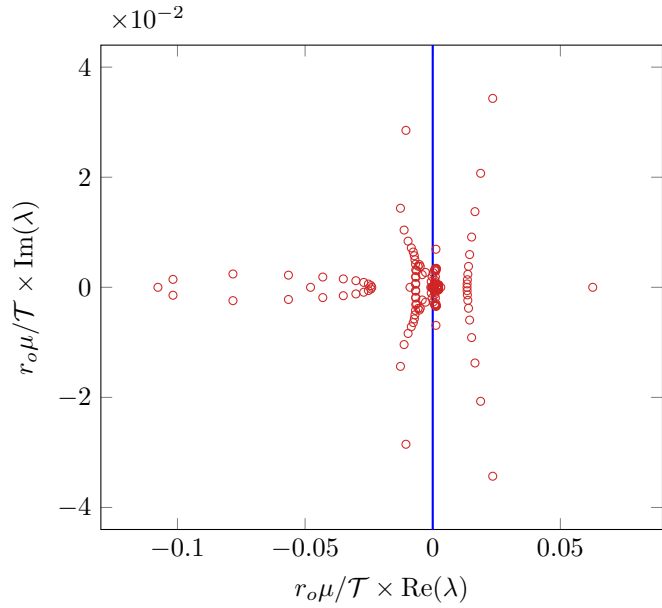
for initial condition $\vec{\varepsilon}(0) = \vec{\varepsilon}_o$. The $\exp \mathbf{At}$ factor thus describes its temporal behavior.

C.3.3 Eigensystem

The matrix \mathbf{A} is real and non-symmetric ($\mathbf{AA}^T \neq \mathbf{A}^T\mathbf{A}$), as can be anticipated by the character of the vector Green's function of the Stokes operator, so in general it will not have a full set of orthogonal eigenvectors. Eigenvalues for a typical configuration are shown in figure C.3. Nearly all of their real components are negative, as expected for a predominantly viscous system, though 75 of the 1000 total in this example do have positive real components, indicating asymptotic instability. The most amplifying is real-valued and corresponds to a tilting perturbation we analyze subsequently.



(a) Full eigenspectrum of \mathbf{A}



(b) Eigenspectrum (a) magnified about $\text{Re}(\lambda) = 0$

Figure C.3: Eigenvalues of \mathbf{A} for $W = 40r_o$ and $\phi = 0.7$ with $N = 20$ capsules.

Though it is not diagonalizable, the eigensystem of \mathbf{A} does dictate the $t \rightarrow \infty$ behavior of small perturbations, so long as they do not trigger significant nonlinear interactions before this behavior is realized [235]. Here we consider its behavior for this reason, in addition to using it as a point of reference with respect to predicted transient growth, which we consider in the following subsection. With $\vec{\lambda}(\mathbf{A})$ representing the $2M$ eigenvalues of \mathbf{A} , the nominal spectral abscissa of the system is its most amplifying component:

$$\alpha \equiv \max \left\{ \text{Re} \left[\vec{\lambda}(\mathbf{A}) \right] \right\}. \quad (\text{C.15})$$

The corresponding most amplifying eigenvalue and its associated eigenvector are defined as λ_α and \vec{s}_α , respectively. For $t \rightarrow \infty$, an initial perturbation $\boldsymbol{\varepsilon}(0) = \hat{\varepsilon} \boldsymbol{s}_\alpha$ will evolve as

$$\boldsymbol{\varepsilon}(t) = \hat{\varepsilon} \boldsymbol{s}_\alpha \exp \lambda_\alpha t. \quad (\text{C.16})$$

C.3.4 Non-modal analysis

Following a common reasoning [234, 320], a $t \rightarrow 0^+$ amplification bound is defined by the numerical abscissa,

$$\eta \equiv \max \left\{ \operatorname{Re} \left[\vec{\lambda} \left(\frac{\mathbf{A} + \mathbf{A}^\top}{2} \right) \right] \right\}, \quad (\text{C.17})$$

which recovers $\eta = \alpha$ for normal \mathbf{A} . This is the maximum initial amplification of any perturbation, though this growth rate will not necessarily persist.

In addition to the short-time growth rate, of particular interest is the form of the most amplifying perturbation and the most dangerous growth at later times. This is determined via a singular-value decomposition,

$$\exp \mathbf{A}t = \mathbf{U} \boldsymbol{\Sigma} \mathbf{V}^\top, \quad (\text{C.18})$$

where the ordered singular values $\vec{\sigma}(t)$ form the diagonal matrix $\boldsymbol{\Sigma}$, and \mathbf{U} and \mathbf{V} are matrices constructed of orthonormal left and right singular vectors, respectively. Though non-normality couples the linear disturbances, their maximum time-dependent evolution can be tracked by reevaluating (C.18) as a function of time,

$$G(t) \equiv \|\exp \mathbf{A}t\| = \max_{j,\beta} \sigma_j^{(\beta)}(t). \quad (\text{C.19})$$

The corresponding instantaneous maximum growth rate is then,

$$\zeta(t) \equiv \frac{d \log G(t)}{dt}. \quad (\text{C.20})$$

For $t \rightarrow \infty$, this should converge to the eigenvalue associated with the least stable eigenvalue $\zeta \rightarrow \alpha$, and for $t \rightarrow 0^+$ it converges to the maximum transient amplification $\zeta \rightarrow \eta$. If $\zeta(t) > \alpha$ for any range of t , transient growth can outpace asymptotic eigensystem growth in that range.

C.3.5 Character and verification of the linear system

The evaluation of \mathbf{A} and its analysis is intricate, so it is important to verify that it indeed represents a linearization of the full system. This also serves to introduce the basic behavior we will see in most of the results. For verification, linear predictions based on \mathbf{A} are compared with full DNS calculations for small perturbations. For $\phi = 0.2$ and $W = 10r_o$, we compare the predicted growth of $\|\vec{\boldsymbol{\varepsilon}}\|$ for $\hat{\varepsilon} = 10^{-10}r_o$ perturbations against the DNS for different initial conditions. Before nonlinear effects manifest, which is avoided with $\hat{\varepsilon}$ so small, agreement should be limited only by the accumulation of numerical approximation

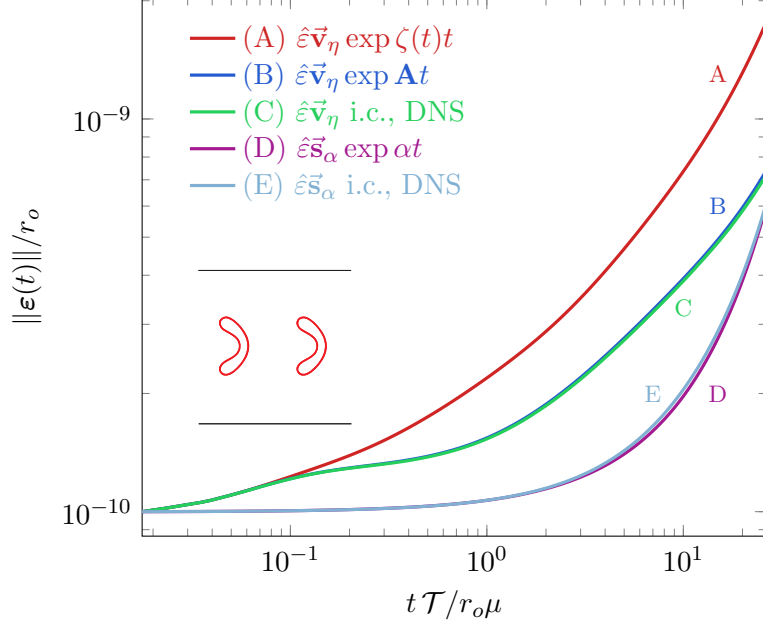


Figure C.4: Perturbation amplification in time: (A) The transient growth based on maximum time dependent amplification $\zeta(t)$ from (C.20) for initial perturbation $\hat{\varepsilon}\vec{v}_\eta$; (B) direct evaluation of the matrix exponential $\exp \mathbf{At}$ from (C.14) for $\hat{\varepsilon}\vec{v}_\eta$, which matches (C) from the corresponding DNS; and (D) $\exp \alpha t$ for $\hat{\varepsilon}\vec{s}_\alpha$ from (C.16), which matches the large t behavior of (E) from the corresponding DNS.

errors. For numerical evaluation, $\|\boldsymbol{\varepsilon}\|$ from (C.9) is approximated as

$$\|\vec{\boldsymbol{\varepsilon}}\| = \frac{1}{M} \sum_{i=1}^M \sqrt{\left[\varepsilon_x^{(i)} \right]^2 + \left[\varepsilon_y^{(i)} \right]^2}. \quad (\text{C.21})$$

Two main verification comparisons are made in figure C.4. For the initial perturbation $\hat{\varepsilon}\vec{v}_\eta$, the predicted cumulative amplification based on $\|\exp \mathbf{At}\|$ is compared with the corresponding DNS and shown to agree (curves B and C). We also see that both match the $t \rightarrow 0^+$ prediction based upon $\zeta(t \rightarrow 0)$, and that for $t > 0$ they are indeed bounded by this. The second comparison is for the $t \rightarrow \infty$ behavior, based on α for initial condition $\hat{\varepsilon}\vec{s}_\alpha$ and a corresponding DNS. These also agree (curves D and E in the figure) in that they overlap at long times, with relative amplification difference less than 5 percent at $t = 10 r_o \mu / \mathcal{T}$ and less than 2 percent at $t = 100 r_o \mu / \mathcal{T}$. Note that their good agreement at all times, not just for $t \rightarrow \infty$, indicates that in this case \vec{s}_α itself is not strongly coupled with other linear disturbances.

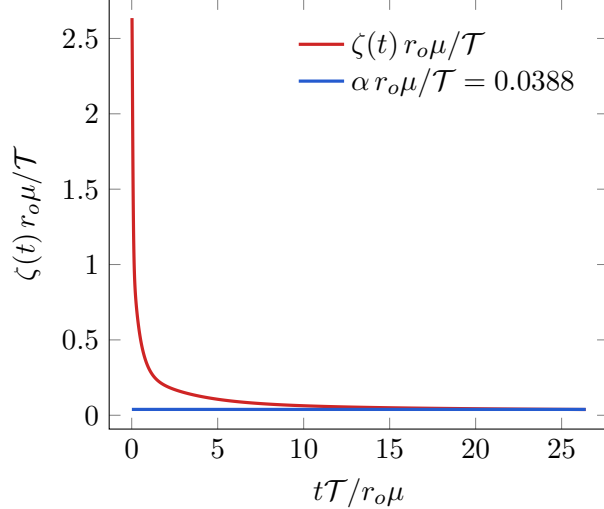


Figure C.5: Evolving maximum growth rate $\zeta(t)$ analyzed in figure C.4.

In figure C.5, we see that at short times $\zeta(t)$ significantly exceeds α , confirming the small t behavior of figure C.4. At later times, we likewise confirm that $\zeta \rightarrow \alpha$, as it should. Despite the long-time behavior, we anticipate that for finite perturbations, the rapid transient growth might be a significant mechanism leading to nonlinear saturation and subsequent disruption of the capsule train. This is considered in section C.4.5. In the following section we examine the character of the most amplifying disturbances.

We consider transient amplification in the following section C.4.1 and long-time asymptotic amplification in section C.4.2 for the four base flows visualized figure C.2. Additional configurations are introduced in section C.4.3 to map the boundaries between different disturbance-form regimes. The narrow channels of these configurations are insufficient to preserve the regularity of the capsule trains, so for comparison we also introduce a very narrow channel with $W = 4r_o$ in section C.4.4. In this case, the capsule train persists, seemingly indefinitely, and we characterize its apparent stability.

C.4 Results

C.4.1 Transient amplification

Figure C.6 shows the initial transient amplifications η from (C.17). In all four cases, η depends, at least weakly, upon the channel length, with an apparent asymptotic long- L power-law behavior for sufficiently large L . For all cases, the power laws provide good fits for $N \gtrsim 20$ capsules, suggesting that in this limit the discrete character of the capsules *per se* becomes relatively unimportant, as might be expected for 20 capsules per wavelength of the disturbances. An implication is that an effective medium model and continuous dispersion relation might afford a reasonable description of the response, though we do not pursue this here. The apparent non-integer power laws in figure C.6 suggests the existence of an anomalous dimension, [417] though its specific form has not been found.

For both ϕ and larger L , the narrow channels are significantly more amplifying. However, this behavior is different in shorter channels. For small L , the proximity of the walls appears to be less important, and we see about a factor of five more significant transient amplification for the more densely packed channels, irrespective of width, suggesting that capsule–capsule interactions themselves are most important in this limit. Still, the amplification rates for shorter channels are much smaller than those in most of the longer channels.

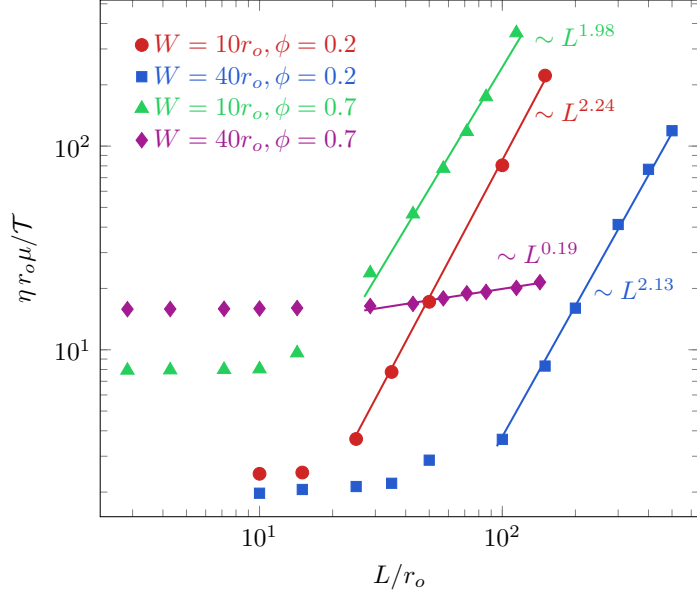


Figure C.6: Numerical abscissa η from (C.17) for different lengths L for the channels of figure C.2. The straight lines are power-law fits.

With such different behavior in the amplification rates, it is not surprising that the corresponding $t \rightarrow 0^+$ most amplifying disturbances visualized in figure C.7 show diverse structures. The $\phi = 0.2$ wide channel case visualized in figure C.7 (b) shows a longitudinal displacement wave, with each capsule displaced in the streamwise direction without obvious change of shape. As such, the overall disturbance appears as a compression–expansion wave of the capsule spacing. The other disturbances visualized in figures C.7 (a), (c) and (d) appear primarily as distortions of individual capsules, although consistent with the L -dependencies of figures C.6, these also manifest as wave-like perturbations correlated across all the capsules. They are asymmetric for the narrow channels in figures C.7 (a) and (c) and symmetric in figure C.7 (d). Similar long-wavelength disturbances are most amplifying for capillary instability of low-Reynolds-number core-annular flows, [418, 419] though we do not pursue any possible correspondence to this configuration herein. We note that such disturbances that distort individual capsules are hard to visualize. For genuinely small $\hat{\varepsilon}$, for which the linear approximation is quantitatively accurate, they would be imperceptible if plotted as $\vec{x} + \hat{\varepsilon}\vec{v}_\eta$. For visualization, they are therefore artificially increased by a factor a as $\vec{x} + a\hat{\varepsilon}\vec{v}_\eta$, which makes them visible but unfortunately also distorts their shapes, which leads to a kinky appearance due to geometric nonlinearities. These visualizations should be

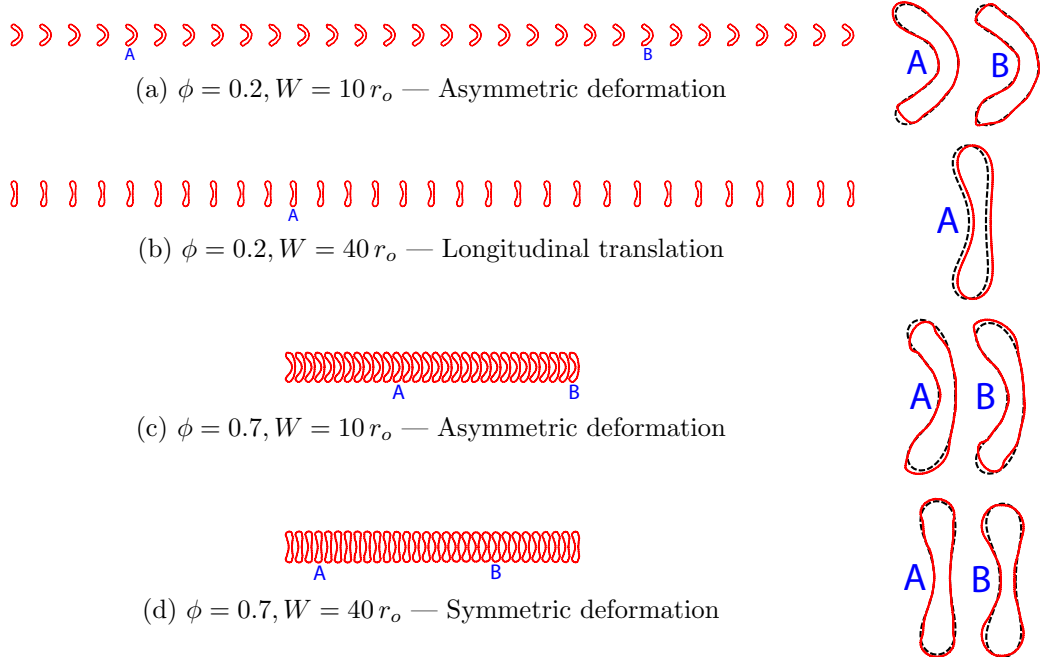


Figure C.7: Most transiently amplifying (non-modal) disturbances for the baseline cases with $N = 30$ of figure C.2: — — baseline \vec{x} and perturbations visualized as — $\vec{x} + a\hat{\varepsilon}\vec{v}_n$ with $a\hat{\varepsilon} = 3.5$. These relatively large amplitudes aid visualization, though some of the features appear exceptionally sharp due to geometric nonlinearity. The A and B labels indicate the specific magnified capsules.

construed as showing the approximate direction and relative amplitude of the membrane perturbation, not strictly the membrane shape.

Motivated by these visualizations, we quantify the disturbances with low-order moments of each capsule shape C . These are selected to emphasize their main apparent characteristics:

$$x_c = \frac{1}{l_o} \int_C \varepsilon_x \, dl \quad (\text{C.22})$$

$$y_c = \frac{1}{l_o} \int_C \varepsilon_y \, dl \quad (\text{C.23})$$

$$M_x = \frac{1}{l_o r_o^2} \int_C \varepsilon_x^3 \, dl \quad (\text{C.24})$$

$$M_y = \frac{1}{l_o r_o^2} \int_C \varepsilon_y^3 \, dl \quad (\text{C.25})$$

$$M_{xy} = \frac{1}{l_o r_o} \int_C \varepsilon_x \varepsilon_y \, dl, \quad (\text{C.26})$$

where x is the streamwise and y is the cross-stream coordinate, as labeled in figure C.1. Third-order rather than second-order moments are used for M_x and M_y to preserve the sign of the perturbation. The relative values of (C.22) through (C.26) are plotted for all capsules in figure C.8. These confirm predominance of particular moment contributions for the different cases, as might be anticipated from the visualizations. Their wave-like character again suggests that a continuum model might afford a natural way to analyze the behavior of the dominant transient disturbance (and its asymptotic analog—see figure C.11) if an

effective material model or averaging procedure could be deduced. This is not attempted here.

C.4.2 Asymptotic amplification

The maximum asymptotic amplification rates α , corresponding to the same four cases of figure C.2, are shown in figure C.9. These growth rates are all slower than the corresponding η , typically by over a factor of 10. Again, for sufficiently long L , the more narrow channels also show length dependence, though with different powers than for η . However, the wider channels do not, at least for up to the 100 capsules considered. This is true even when the channel length is many times its width. The more narrow $W = 10r_o$ channels are most amplifying for all L . For $\phi = 0.2$, its L dependence is similar to the transient behavior $\eta \sim L^2$, though for $\phi = 0.7$ it is less sensitive to L , with $\alpha \sim L^{3/4}$ rather than matching $\eta \sim L^2$.

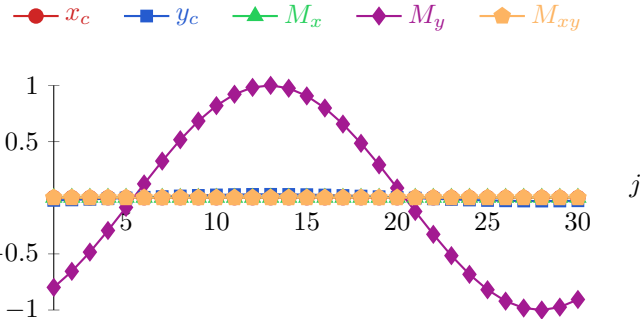
Given these diverse asymptotic amplification rates, we again anticipate different characters for the corresponding disturbances visualized in figure C.10. Both the wide channels (figures C.10 b and d) show a predominantly tilting disturbance, in which all the capsules collectively tilt. The uniformity of this tilt rate is confirmed to be M_{xy} dominant in figures C.11 (b) and (d). Their lack of a streamwise wave-like structure (constant M_{xy}) is consistent with the $\alpha \sim L^0$ behavior seen for both these cases. In contrast, both the narrow channel configurations show a wave-like transverse displacement, also different from the corresponding most amplifying transient disturbances though still sinuous. These are M_y dominant, as seen in figures C.11 (a) and (c).

C.4.3 Disturbance regime boundaries

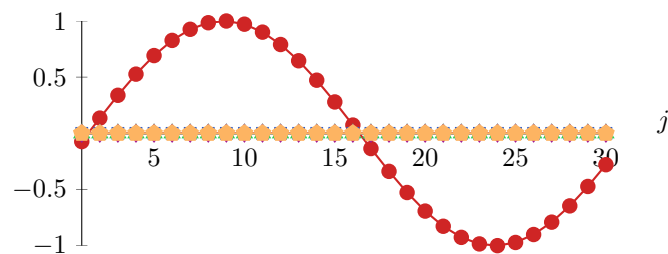
The diverse most transiently and asymptotically amplifying disturbances seen in figures C.7 and C.10 suggest a more complete mapping of the configuration parameters to identify boundaries between these regimes. These are illustrated in figure C.12 for ranges of ϕ and W , where the nominal disturbance character is based on the maximum values of the (C.22) through (C.26) metrics. Only the non-uniform tilt in figure C.12 (b) was not directly observed in our four focus cases. It shows an obvious L -periodic wave-like variation to the uniform tilt seen in figure C.10 (b) and (d).

C.4.4 An empirically stable, narrow-channel configuration

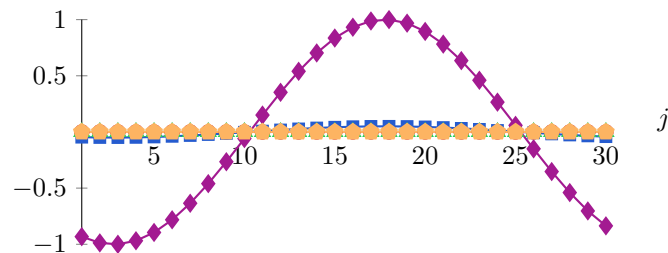
Figure C.13 shows that in this case the capsules bend into a two-dimensional analog of the bullet-like shapes seen in blood cells, and empirical observations from long-time DNS simulations suggest indefinite persistence of this single-file flow, even when perturbed. (In this case $N = 35$ was used to resolve the more significant capsule deformations.) We analyze this case for comparison. Despite the empirical stability, linear analysis suggests both transient amplification ($\eta = 0.28$) and asymptotic instability ($\alpha = 0.0018$), though these are at least seven times smaller than those seen for the wider channels (figure C.6 and C.9). Similar to wider channels, the corresponding \vec{v}_η show asymmetric distortion reflected by M_y



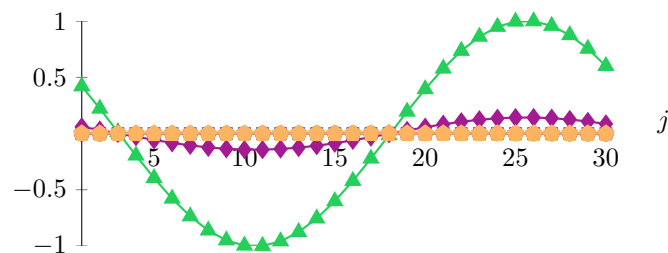
(a) $\phi = 0.2, W = 10r_o$



(b) $\phi = 0.2, W = 40r_o$



(c) $\phi = 0.7, W = 10r_o$



(d) $\phi = 0.7, W = 40r_o$

Figure C.8: Disturbance metrics (C.22) through (C.26) for all $j = 1, \dots, N$ capsules for $N = 30$ applied to the most amplifying transient disturbances visualized in figure C.7. All metrics are plotted for all cases, normalized by the largest value of any.

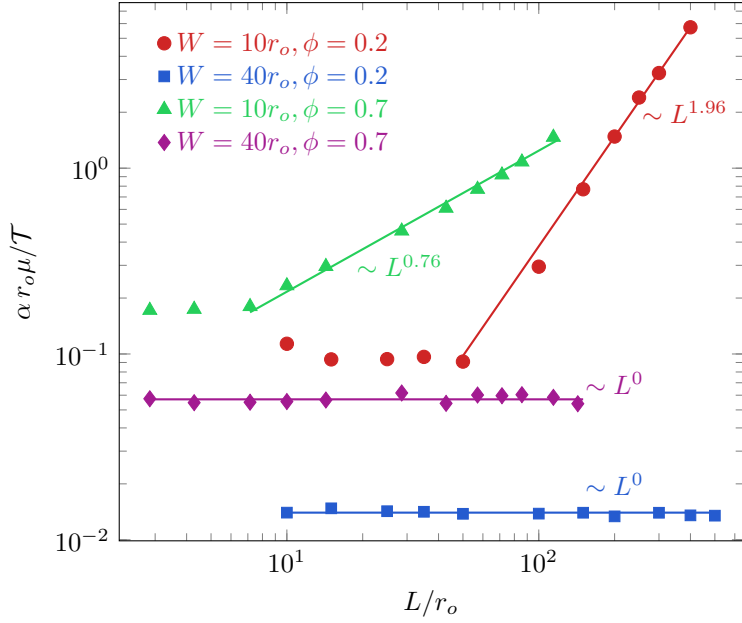


Figure C.9: Spectral abscissa α from (C.15) for different cases of figure C.2. The straight lines are power-law fits.

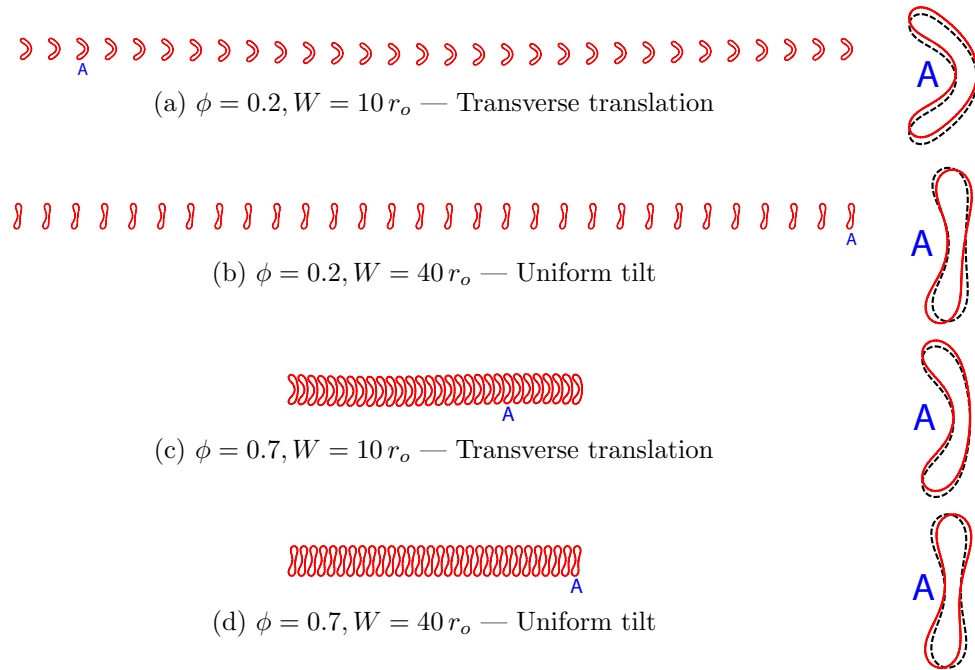
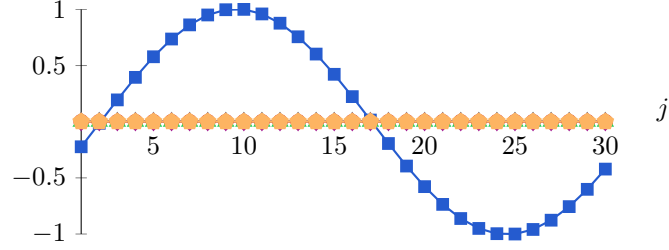
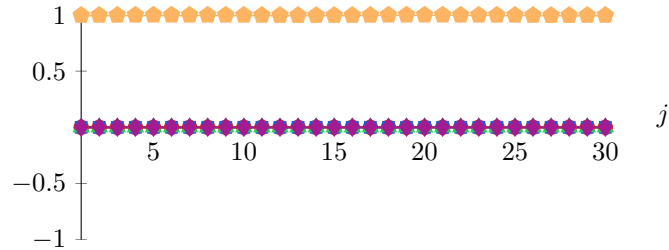


Figure C.10: Most asymptotically ($t \rightarrow \infty$) amplifying modal disturbances for the baseline case with $N = 30$ visualized in figure C.2: — baseline \vec{x} and — perturbations visualized as $\vec{x} + a\hat{\varepsilon}\vec{s}_\alpha$ with $a\hat{\varepsilon} = 3.5$. The selected magnified in capsules are labeled accordingly.

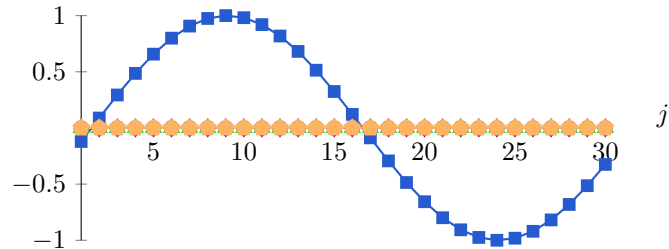
—●— x_c —■— y_c —▲— M_x —◆— M_y —◇— M_{xy}



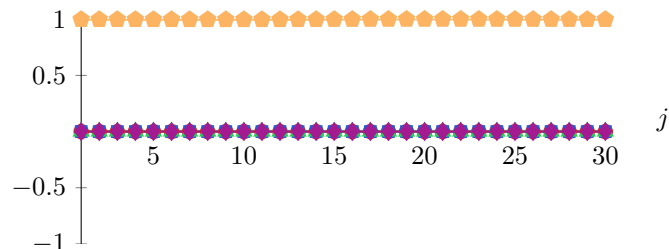
(a) $\phi = 0.2, W = 10r_o$



(b) $\phi = 0.2, W = 40r_o$

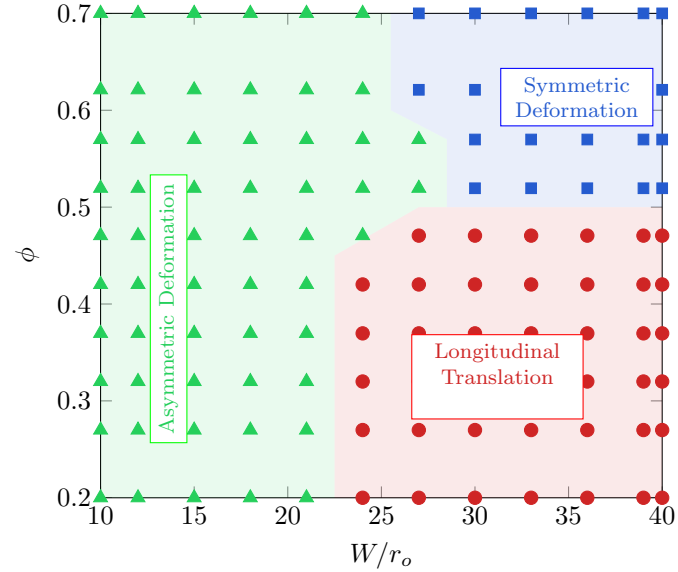


(c) $\phi = 0.7, W = 10r_o$

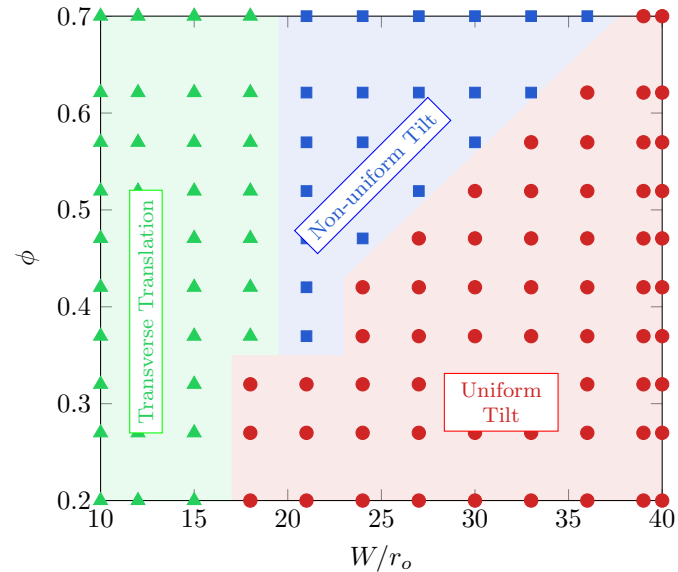


(d) $\phi = 0.7, W = 40r_o$

Figure C.11: Disturbance metrics (C.22) through (C.26) for all $j = 1, \dots, N$ capsules for $N = 30$ applied to the most amplifying transient disturbances visualized in figure C.10. All metrics are plotted for all cases, normalized by the largest value of any.



(a) Disturbance character for most transiently amplifying disturbances \vec{v}_η



(b) Disturbance character for most transiently amplifying disturbances \vec{s}_α

Figure C.12: Character of the most amplifying disturbances for a range of channel widths and packing fractions as labeled.

(figures C.13 b and d), whereas the \vec{s}_α shows a capsule-to-capsule varying mix of tilt and asymmetric distortion, which is strongest for a particular capsule ($j = 7$ in figure C.13 c and e).

The amplifications of different disturbances are shown in figure C.14. While DNS simulations initialized with $\hat{\varepsilon}\vec{v}_\eta$ and $\hat{\varepsilon}\vec{s}_\alpha$ do indeed initially reflect the predicted linear growth, as they must, it does not persist, presumably due to nonlinear effects. The upper-bound $\zeta(t)$ growth is not realized and the \vec{s}_α disturbance likewise saturates also due to nonlinear effects associated with tight confinement. The approximately constant $\|\vec{\varepsilon}\|$ reached in this case at long times is consistent with a persistent tilt of the membrane from its initial orientation, though the capsule returns to the same bent shape. Thus, although this case is linearly unstable, significant linear amplification is not realized, and might not be expected given the obviously limited range of permissible motions for such tightly confined capsules.

C.4.5 Transition to disordered flow

An important potential consequence of the relatively fast predicted transient growth seen in most cases is that it can significantly reduce time to the onset of significant nonlinear effects. A specific example is shown in figure C.15 for $\phi = 0.7$, $W = 40r_o$. The DNS simulation with initial perturbation $\hat{\varepsilon} = 0.001r_o$ (curve D in the figure) shows brief transient growth, but it does not lead directly to obvious nonlinear behavior. Instead, the growth nearly ceases, because only a small portion of $\vec{\varepsilon}$ is associated with the disturbances that are amplified in this transient regime. It is only after $t \gtrsim 1000r_o\mu/\mathcal{T}$ that it again amplifies significantly, and then at a rate consistent with the $t \rightarrow \infty$ asymptotic α -curve (C). Before this occurs, it remains bounded by the $\zeta(t)$ prediction (curve B). In contrast, for a still small but larger $\hat{\varepsilon} = 0.01r_o$, the initial condition $\hat{\varepsilon}\vec{v}_\eta$ perturbation leads to nonlinearity much earlier, about 10^3 times faster than would the $t \rightarrow \infty$ mechanism for \vec{s}_α , even with the initial condition $\hat{\varepsilon}\vec{s}_\alpha$. Both the $\hat{\varepsilon}\vec{v}_\eta$ and $\hat{\varepsilon}\vec{s}_\alpha$ initial conditions show nonlinear saturation well before a corresponding *ad hoc* perturbation constructed as random $\hat{\varepsilon}\delta y_c$ displacements of the capsule centroids. This *ad hoc* perturbation saturates 100 times more slowly still (curve G).

The subsequent DNS transition to an apparently chaotic flow for $\phi = 0.7$ and $W = 40r_o$ is visualized for three different initial perturbations in figure C.16. We see that the $\hat{\varepsilon}\vec{v}_\eta$ initial condition has a different development from the eigenvector $\hat{\varepsilon}\vec{s}_\alpha$ or *ad hoc* $\hat{\varepsilon}\delta y_c$ disturbances. Its L -scale wave-like structure persists and amplifies before it breaks down into an apparently chaotic flow. The other initial perturbations lead to choppier variations in the capsule train, with shorter features in the streamwise direction. In these cases, the capsule columns seem to first come apart at specific points, before they develop an apparently chaotic behavior, much more slowly than the \vec{v}_η case.

The relatively narrow $W = 10r_o$ with $\phi = 0.2$ (figure C.2 a), shows a qualitatively similar amplification for the same three types of initial conditions (figure C.17), though all of the growth rates are substantially faster, as anticipated based on figures C.6 and C.9. In this case, nonlinear saturation is accelerated only by a factor of 100 for the $\hat{\varepsilon} = 0.01r_o$ initial disturbance $\hat{\varepsilon}\vec{v}_\eta$ relative to $\hat{\varepsilon}\vec{s}_\alpha$. The weaker $0.001r_o\vec{v}_\eta$ perturbation also appears to reach an amplitude consistent with the onset of nonlinear effects within the simulation time shown.

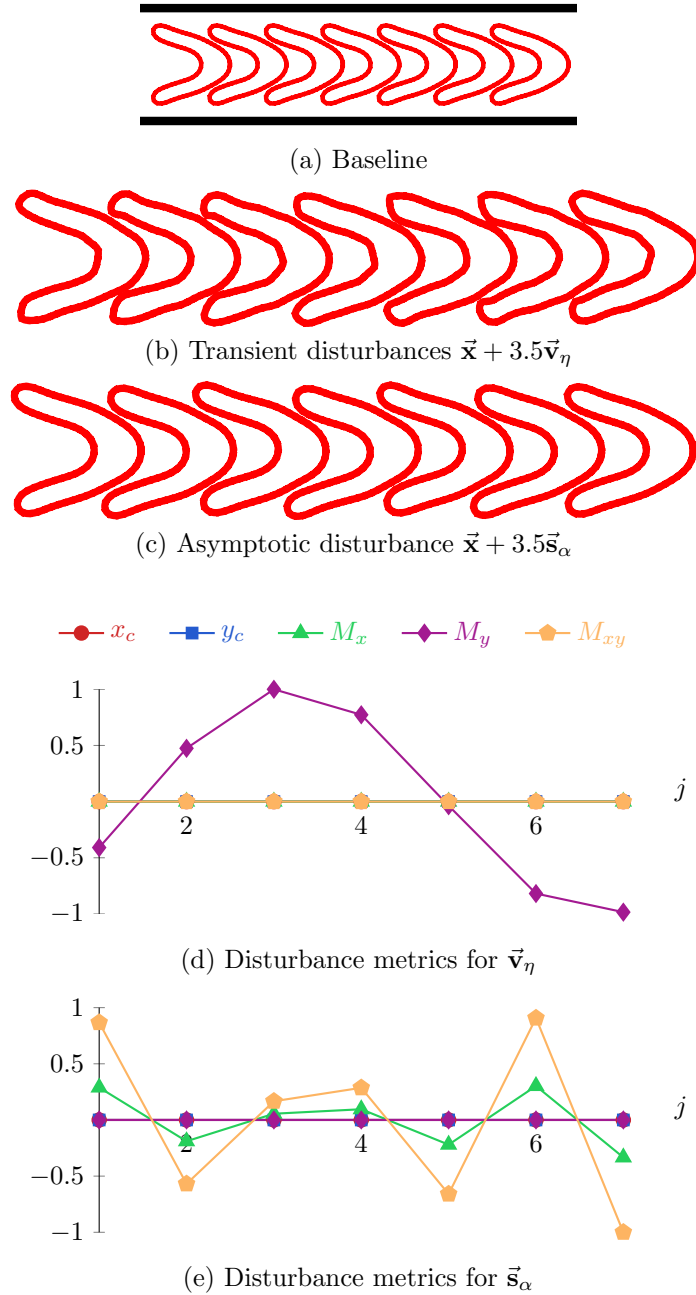


Figure C.13: (a) The baseline configuration for an empirically stable case with $W = 4r_o$, $\phi = 0.5$ and $N = 7$. (b) The $t \rightarrow 0^+$ most amplified transient, and (c) the asymptotically most amplified disturbances. (d–e) The corresponding disturbance metrics (C.22) through (C.26). The exaggerated displacements cause these to look unphysical, as discussed in section C.4.1 in regard to figure C.7.

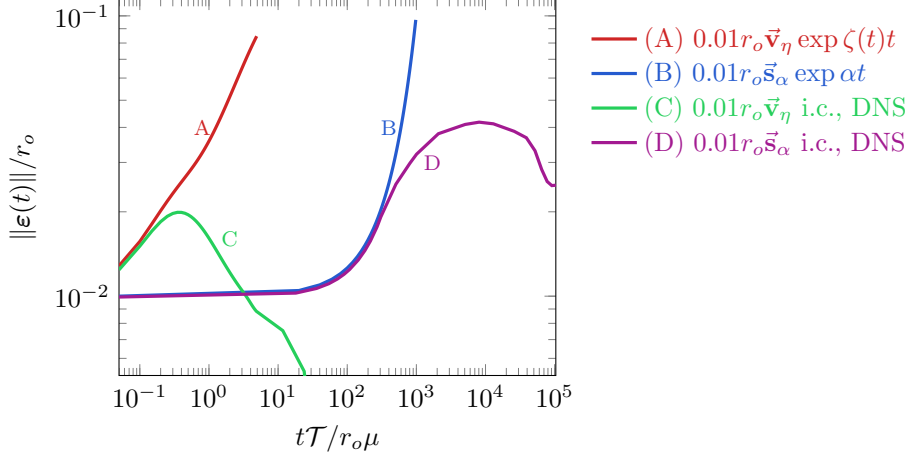


Figure C.14: Disturbance amplification for the empirically stable narrow channel case, visualized in figure C.13 (a). The DNS track (curves C and D) the corresponding linear amplifications (curves A and B) only for short times.

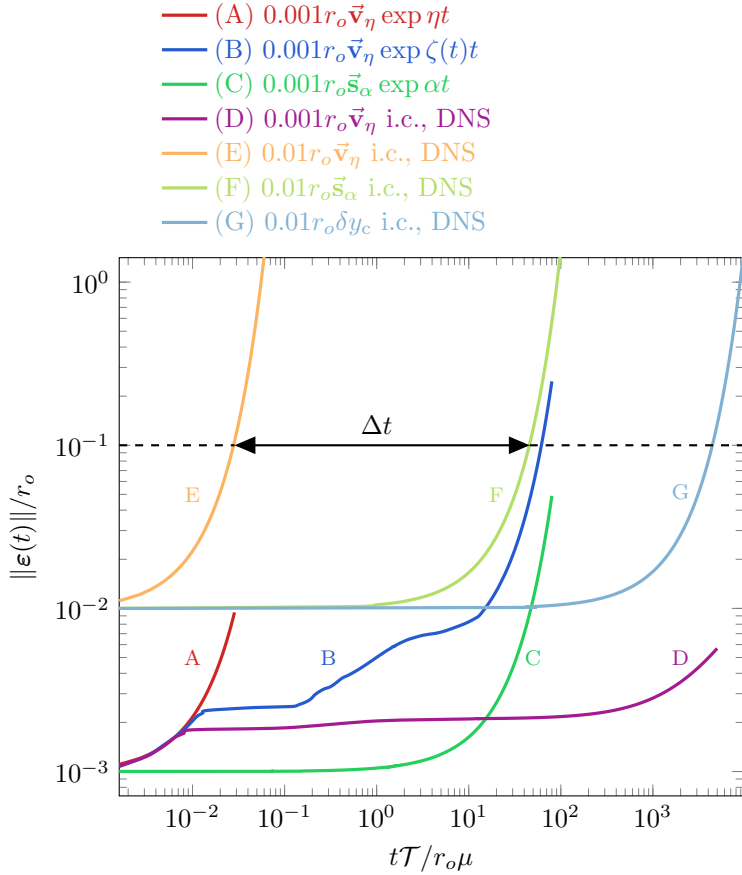


Figure C.15: Disturbance amplitude evolution for the wide-dense configuration ($W = 40r_o$ and $\phi = 0.7$) with $\hat{\varepsilon} = 0.001r_o$ and $0.01r_o$ for initial conditions and predictions as labeled. The $\Delta t \approx 10^3 T / r_o \mu$ labels the approximate difference in time for onset of nonlinear for transient versus eigenvalue estimates for $\hat{\varepsilon} = 0.01r_o$ (see text).

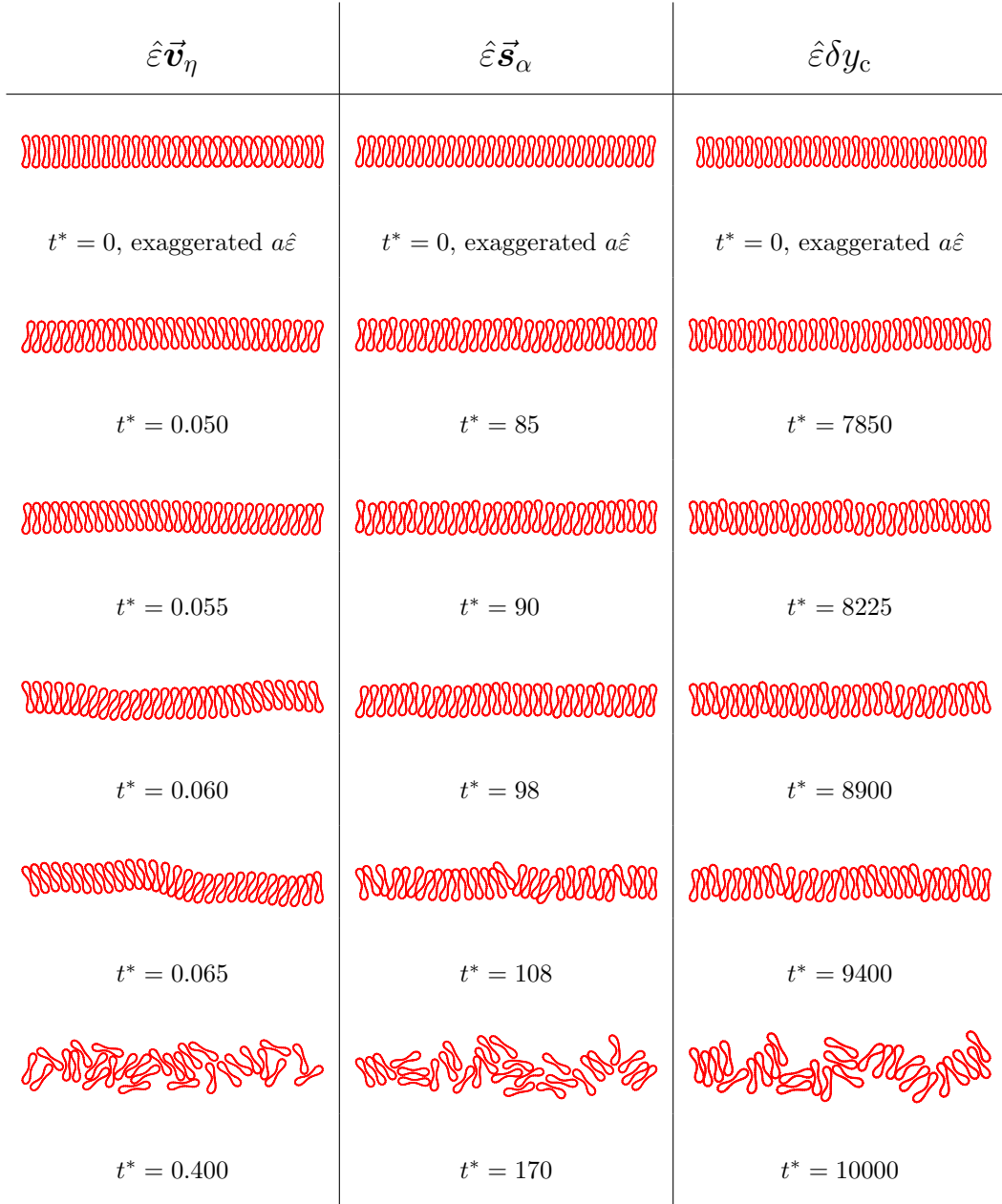


Figure C.16: Transition to disordered flow for the $\hat{\varepsilon} = 10^{-2}r_o$ cases of figure C.15. For plotting the initial configuration, the exaggeration factor is $a\hat{\varepsilon} = 3.5$. The walls are not shown; they can be seen for the baseline configuration in figure C.2 (d). The times shown $t^* = t\mathcal{T}/r_o\mu$ were selected to illustrate the development qualitatively.

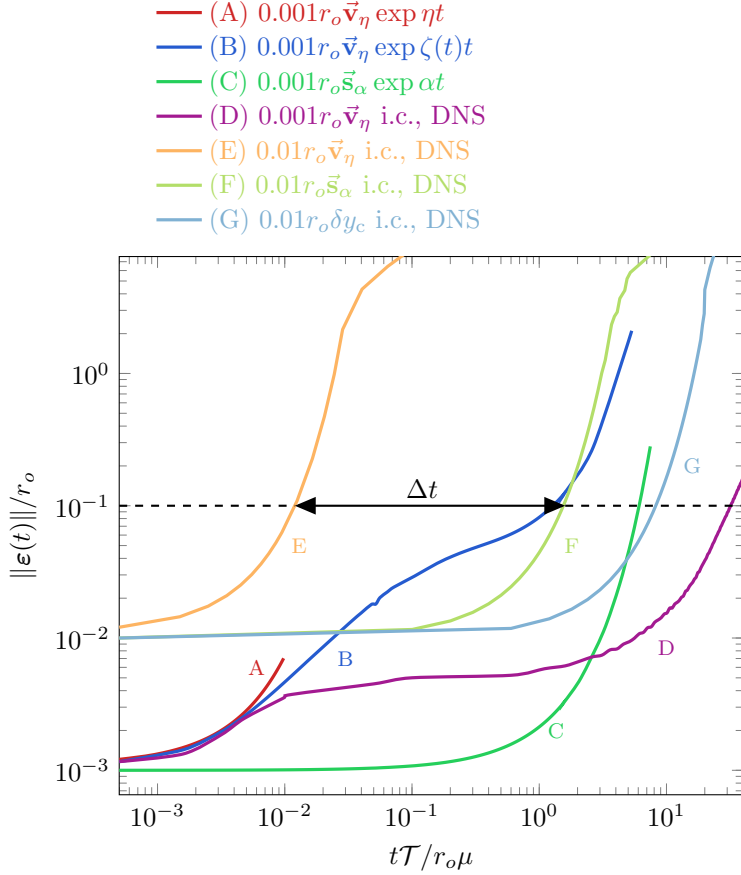


Figure C.17: Disturbance amplitude evolution for the narrow–sparse configuration ($W = 10r_o$ and $\phi = 0.2$) with $\hat{\varepsilon} = 0.001r_o$ and $0.01r_o$ as labeled. The $\Delta t \approx 10^2\mathcal{T}/r_o\mu$ labels the approximate difference in time for onset of nonlinear for transient versus eigenvalue estimates for $\hat{\varepsilon} = 0.01$ (see text).

The upper-bound $\exp \zeta(t)t$ curve is again consistent with this accelerated saturation.

Unlike the nonlinear breakdown for the densely packed wider channel of figure C.16, figure C.18 shows that the three initial conditions in this narrower case have qualitatively similar progression to a relatively disorganized state. The capsules retain an approximately single-file structure but with the capsules oriented at a range of angles with significant changes of streamwise spacing, as has been observed in similar configurations in both two [420] and three [406] dimensions. Unlike the $W = 40r_o$, $\phi = 0.7$ case, this configuration does not, at least for the times simulated, show significant overturning or passing of the capsules, presumably because of some combination of the greater confinement for $W = 10r_o$ and less crowding for $\phi = 0.2$.

C.4.6 Elastic stiffness

As discussed in section C.3.1, the displacement-based measure used to quantify amplification does not have a one-to-one correspondence with a mechanical energy, with the consequence

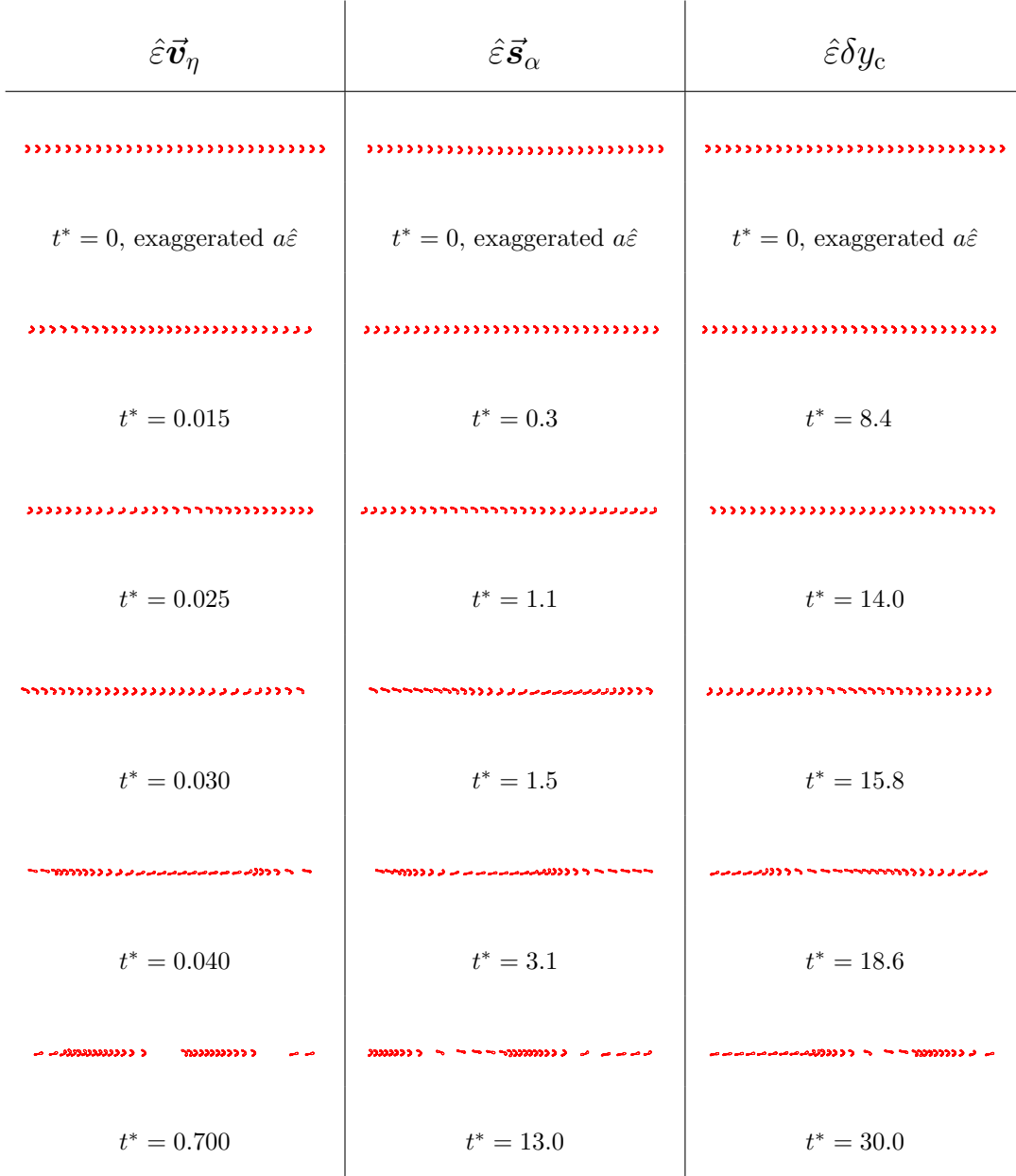


Figure C.18: Transition to disordered flow for the $\hat{\varepsilon} = 0.01r_o$ cases of figure C.17. For plotting the initial configuration, the exaggeration factor is $a\hat{\varepsilon} = 3.5$. The walls are are not shown; they can be seen for the baseline configuration in figure C.2 (a). The times shown $t^* = t\mathcal{T}/r_o\mu$ were selected to demonstrate nonlinear disruption.

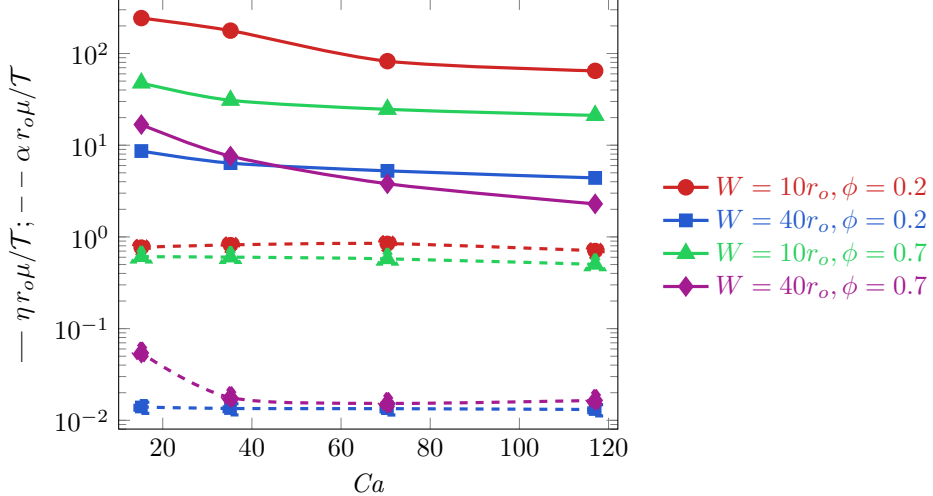


Figure C.19: Effect of capsule stiffness on α and η .

that different perturbations for the same $\|\vec{\varepsilon}\|$ can have different strain energies. We consider this here, and more generally the effect of capsule stiffness, by changing Ca . We consider capsules with up to $Ca = 117$, starting from the $Ca = 15.2$ introduced as the basic case in section C.1, which increases flexibility by decreasing \mathcal{M} by a factor of about 7.7. The tension modulus is adjusted correspondingly per (C.5).

The consequence of these changes on the initial transient and asymptotic amplification rates is relatively small over this range, as seen in figure C.19. The asymptotic growth rates are nearly unchanged; only the wide–dense ($W = 40r_o, \phi = 0.7$) case shows a decrease at small \mathcal{M} . The transient amplification is more sensitive, as might be expected given that these disturbances generally showed more distortion of the capsule shapes. Still, they only decrease by less than a factor 10, with similar effects on the eventual breakdown. Though we do not simulate smaller or larger Ca because it is computationally more challenging and less relevant to the capsule regimes of interest, we can anticipate that significantly stiffer or more flexible capsules will necessarily respond differently.

The $\zeta(t)$ amplification, shown for the wide and dense case ($W = 40r_o, \phi = 0.7$) in figure C.20, is altered by the capsule stiffness, but not fundamentally changed. The delays observed for larger Ca reflect changes in the strain energy of the corresponding disturbances. To quantify this, we define strain energy

$$\psi = \frac{\mathcal{T}}{2} \int_{\text{all } C} \left(\frac{ds}{ds_o} - 1 \right)^2 dl + \frac{\mathcal{M}}{2} \int_{\text{all } C} \kappa^2 dl, \quad (\text{C.27})$$

and following (C.8) we define a perturbation value $\psi'(t) \equiv \psi(t) - \psi_b$. Figure C.20 (b) shows that for stiffer capsules (smaller Ca), the energy of the most transiently amplified initial disturbance for that time, which we designate $\vec{s}_\zeta(t)$, is nearly constant. However, at a later time, it drops to a value near that of \vec{s}_α . For increasingly flexible capsules, this switch occurs increasingly close to the time when asymptotic amplification is predicted to become significant. In all cases it is clear that the transient disturbances carry significantly more

strain energy than the asymptotic ones, indicating that mechanical coupling within the capsules is a key factor only in transient amplification.

C.5 Summary and conclusions

The primary conclusion is that both asymptotic and transient linear amplification of small disturbances can upset single-file trains of flexible capsules when they are not tightly confined. This was confirmed by direct comparison with corresponding nonlinear simulations. Analysis of their growth rates anticipates that transiently amplifying finite, though still small (*e.g.* $\hat{\varepsilon} = 0.01r_o$), disturbances can significantly accelerate transition to an apparently chaotic flow. Both transiently and asymptotically most amplified disturbances reach this condition well before the *ad hoc* random disturbances considered, which implies that some sort of stability analysis is necessary to predict transition times in, say, a noisy environment. Interestingly, despite empirical observations of apparently indefinite persistence, capsule trains in a highly-confining very narrow channel were also found to be linearly unstable. However, in this case nonlinear effects become active at relatively small displacement amplitudes and preserve the regular train formation.

An implication for the design of devices that process flexible capsules is that channel geometry and packing fraction both significantly affect the most amplifying disturbances. Qualitatively different most-amplifying disturbances were found to grow at very different rates in different cases. Since the very narrowest channels provide the most obviously persistent capsule trains, it was particularly unexpected that the relatively narrow $W = 10r_o$ channel was significantly more amplifying than the corresponding wider $W = 40r_o$ channel. Yet, despite this amplification, for small packing fractions ($\phi = 0.2$) nonlinear effects did not lead to a chaotic seeming flow in the times simulated. Perturbations grew rapidly, but only developed into an irregular single-file arrangement, not the more complicated overturning and passing seen for the more dense configurations.

There are three simplifications in the model configuration studied that warrant additional discussion. The most obvious concerns how well these observations reflect three-dimensional capsule flow. While the two-dimensional model reproduces the same basic phenomenology of three-dimensional systems, and has the advantage of requiring little computational effort to explore large ranges of parameters, it is not expected to provide a quantitative model of real systems. Numerical tools to do this are available [70], though subsequent analyses will likely be restricted to a narrower range of parameters. The present study likewise neglects inertia. Though this is undoubtedly a reasonable approximation for many phenomena at these conditions, Reynolds numbers might not always be so small as to preclude the accumulation of nonlinear effects at longer times. However, given the reliance of the present analysis on the boundary integral description of the flow, including inertia in detail would necessitate a substantial redesign of the numerical approach. The third simplification is the matching of the interior capsule viscosity to that of the suspending fluid. It is understood that larger interior viscosities, such as in blood cells, can make them more prone to tumbling, which becomes effectively solid-body motion in the infinite-interior-viscosity limit. We have not investigated this for simplicity, though there is no expectation of any fundamental changes

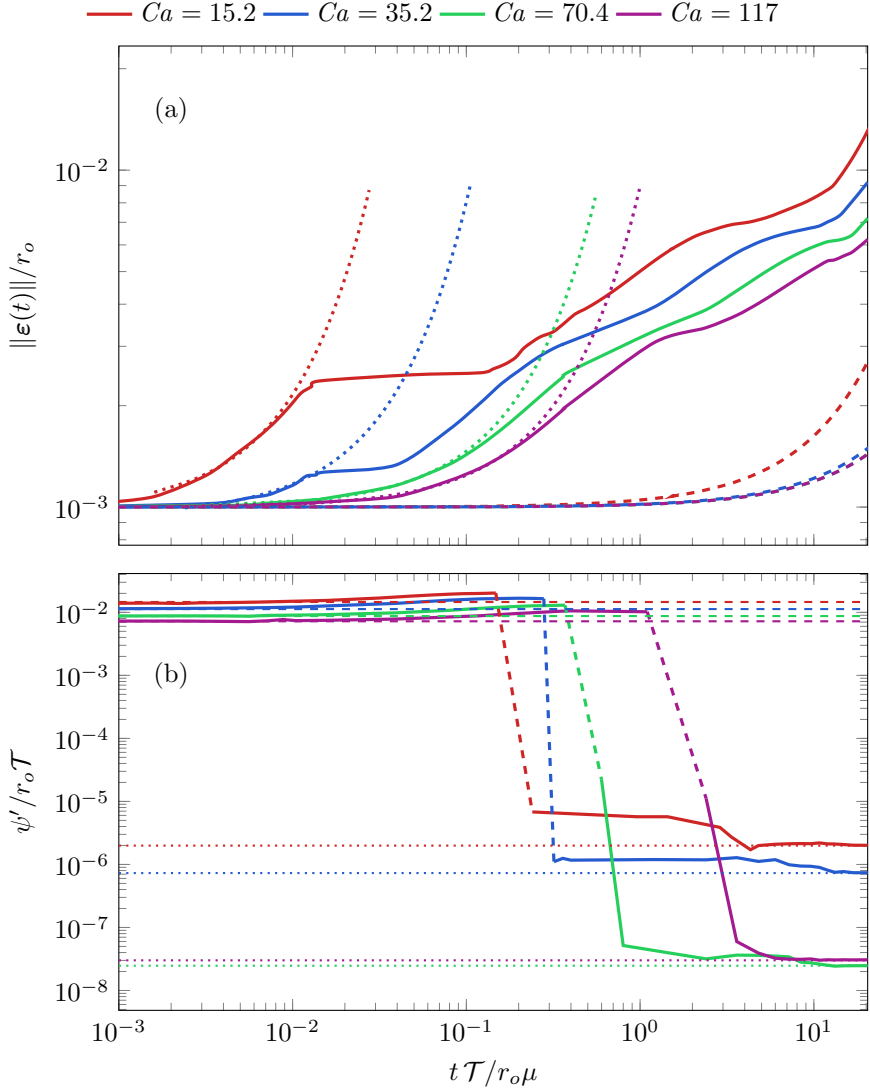


Figure C.20: The $W = 40r_o$, $\phi = 0.7$ case: (a) The predicted disturbance amplitude for different membrane stiffnesses based on: $\cdots\cdots$ η , — $\zeta(t)$, and $--$ α ; and (b) the relative strain energy of the transiently most amplified mode $\vec{v}_\zeta(t)$ at time t —. For reference, also shown in (b) are the energy of the corresponding to $\cdots\cdots$ \vec{v}_η and $--$ \vec{s}_α . Note, neither plot displays the evolution of the system in time. Rather, they show the maximum possible linear amplification amplitude and corresponding strain energy for an $\hat{\varepsilon} = 0.001r_o$ disturbance at that time. The strain energy can change abruptly as different disturbances become the nominally most dangerous at specific times.

for modest variations of interior viscosity.

Finally, it is unfortunate that the neglect of inertia (and kinetic energy), which makes flow in the viscous limit relatively tractable analytically, precludes a convenient and unique mechanical energy instability metric, such as that available for higher-Reynolds-number incompressible flows. As such, some most-amplifying disturbances have seemingly negligible strain energy, whereas others have significantly more. However, the basic behavior of the instabilities are insensitive to the stiffness of the capsules, so the qualitative response is unchanged by the initial strain energy. The transient amplification is increased for stiffer capsules, as expected, and the switch-over to the long-time asymptotic behavior is likewise accelerated, but qualitatively unchanged. The long-time asymptotic stability is relatively insensitive to capsule stiffness for the range considered, presumably because it hinges mostly on the linear flow and the capsule–capsule interaction mechanics it mediates. There is an abrupt switch between the short-time behavior, for which the most dangerous perturbations carry relatively large strain energy, and the asymptotically most unstable modes, which do not.

D Continuum-based methods for cell-train behavior

An example of a reduced model approach for computing cell train stability is considered here. A continuous rheological flow system, based upon a core-annular flow configuration, with core and annular regions representing the cell-train and suspending fluid, respectively, is proposed. It is hypothesized that a more complex though continuous rheological fluid may properly model the stability behavior of the cell-rich core region found in the cell-train flows of chapter 4 and appendix C, especially when the distance between the capsules or cells is small. Since the full discrete capsule simulations of appendix C display most amplified disturbances that are long-wavelength in character, it is possible this connection exists. This is similar to that expected due to a surface-tension-like mechanism between the capsule-rich core and capsule-free outer flow. Further, the amplification rates of small disturbances of the discrete capsule-train scale according to a power-law, which suggests a continuous dispersion relation might be appropriate.

D.1 Model system

The majority of the progress made has been on a simplified problem: a three-dimensional incompressible cylindrical Newtonian jet flowing with uniform velocity surrounded by a fluid of zero density, as visualized in figure D.1. For completeness, this problem leaves both the inertial and viscous terms in the Navier–Stokes equations, though it is known that Re is very small for cellular flows. However, both the viscous and inviscid limits of this problem are considered for comparison with previous results.

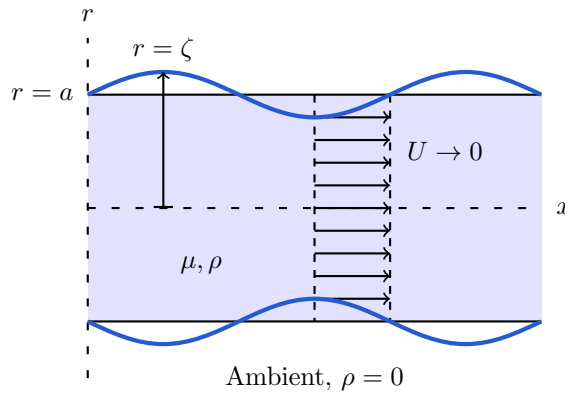


Figure D.1: Schematic of the model system: A cylindrical Newtonian jet issuing into quiescent fluid of zero density. As usual, the azimuthal direction θ is a rotation about the x -axis.

The governing equations appropriate for this system, the homogeneous Navier–Stokes equations for an incompressible fluid in a cylindrical coordinate system are,

$$\nabla \cdot \mathbf{u} = 0, \quad (\text{D.1})$$

$$\rho \frac{D\mathbf{u}}{Dt} = -\nabla p + \mu \nabla^2 \mathbf{u}, \quad (\text{D.2})$$

where ρ is the jet fluid density, \mathbf{u} is the velocity field, p is the pressure field and μ is the viscosity.

The radial distance from the center of the jet to the fluid interface is ζ and the initial unperturbed jet radius is a , as shown in figure D.1. The outward unit normal and tangent vector to the fluid interface are \mathbf{n} and \mathbf{t} respectively. The surface equation is $F \equiv r - \zeta = 0$ and so $\mathbf{n} = \nabla F / \|\nabla F\|$. Thus, the normal and tangent vectors are

$$\mathbf{n} = \left[-\frac{\partial \zeta}{\partial x}, 1, -\frac{\partial \zeta}{r \partial \theta} \right] \left(\frac{\partial \zeta}{\partial x}^2 + 1 + \frac{\partial \zeta}{r \partial \theta} \right)^{-0.5}, \quad (\text{D.3})$$

$$\mathbf{t} = \left[1, \frac{\partial \zeta}{\partial x}, -\frac{1}{r} \frac{\partial \zeta}{\partial \theta} \right] \left(\frac{\partial \zeta}{\partial x}^2 + 1 + \frac{\partial \zeta}{r \partial \theta} \right)^{-0.5} \quad (\text{D.4})$$

where \mathbf{t} is calculated such that $\mathbf{n} \cdot \mathbf{t} = 0$.

The appropriate boundary conditions for the jet are kinematic and matching stress at the interface as well as regularity conditions at $r = 0$. The stress matching condition including uniform surface tension is

$$[\![\mathbf{n} \cdot \mathbf{T}]\!] = \gamma \mathbf{n}(\nabla \cdot \mathbf{n}) \quad \text{at } r = \zeta, \quad (\text{D.5})$$

where $[\![q]\!] \equiv q_2 - q_1$ is the jump operator and $T_{ij} = -pI_{ij} + \mu(\partial_i u_j + \partial_j u_i)$ is the total stress tensor.

The kinematic condition states that a particle on the interface must stay on the interface,

$$u_r = \frac{D\zeta}{Dt} \quad \text{at } r = \zeta, \quad (\text{D.6})$$

which, along with the regularity conditions conclude the boundary conditions.

D.2 Linear stability analysis

The formal linear stability analysis proceeds as follows. The interface, velocity and pressure fields are decomposed into a base state and presumed small deviations from it, denoted here by primes:

$$\begin{aligned} \zeta &= a + \zeta', \\ p &= P + p', \\ \mathbf{u} &= \mathbf{U} + \mathbf{u}'. \end{aligned} \quad (\text{D.7})$$

The uniform base flow U can be set to zero by Galilean invariance. Substituting (D.7) into (D.2) and linearizing by removing terms which are super-linear in the perturbations we have,

$$\nabla \cdot \mathbf{u}' = 0 \quad (\text{D.8})$$

$$\rho \frac{\partial \mathbf{u}'}{\partial t} = -\nabla p' + \mu \nabla^2 \mathbf{u}'. \quad (\text{D.9})$$

By conducting an axisymmetric normal mode analysis, the temporal and spatial contributions are decomposed. This is the only known unstable case and is constructed as,

$$\begin{aligned} \mathbf{u}' &= \hat{\mathbf{u}}(r) e^{ikx+st}, \\ p' &= \hat{p}(r) e^{ikx+st}, \\ \zeta' &= \hat{\zeta} e^{ikx+st}, \end{aligned} \quad (\text{D.10})$$

where k is the streamwise wave number and s is the complex growth rate. Substituting (D.10)) into (D.9) gives,

$$\text{Continuity: } 0 = \frac{1}{r} \hat{u}_r + d_r \hat{u}_r + ik \hat{u}_x \quad (\text{D.11})$$

$$x\text{-dir: } \rho s \hat{u}_x = -ik \hat{p} + \mu \left(d_r^2 \hat{u}_x + \frac{1}{r} d_r \hat{u}_x - k^2 \hat{u}_x \right) \quad (\text{D.12})$$

$$r\text{-dir: } \rho s \hat{u}_r = -d_r \hat{p} + \mu \left(\frac{1}{r} d_r \hat{u}_r + d_r^2 \hat{u}_r - \left(\frac{1}{r^2} + k^2 \right) \hat{u}_r \right) \quad (\text{D.13})$$

Following the same procedure for boundary conditions, (D.5) becomes

$$s(2\mu d_r \hat{u}_r - \hat{p}) = \gamma \left(\frac{1}{a^2} - k^2 \right) \hat{u}_r \quad \text{at } r = a, \quad (\text{D.14})$$

$$d_r \hat{u}_x + ik \hat{u}_r = 0 \quad \text{at } r = a, \quad (\text{D.15})$$

in the normal and tangential directions, respectively. The kinematic boundary condition is

$$\hat{u}_r = s \hat{\zeta} \quad (\text{D.16})$$

The coordinate singularity conditions conclude the boundary conditions, which, for an axisymmetric jet are

$$d_r \hat{u}_x = d_r \hat{p} = \hat{u}_\theta = \hat{u}_r = 0 \quad \text{at } r = 0. \quad (\text{D.17})$$

Notice that (D.11-D.13) and their respective boundary conditions are a complex generalized eigenvalue problem of the form $\mathbf{A}\mathbf{x} = s\mathbf{B}\mathbf{x}$, where \mathbf{A} and \mathbf{B} are matrices associated with the governing equations and \mathbf{x} is the vector of eigenfunctions. Solving this eigenvalue problem is nontrivial and requires numerical methods. Specifically Chebyshev polynomials are used to form a pseudospectral collocation method as has been used previous for this type of problem [421], which are discussed in the next section.

D.3 Chebyshev methods

The Chebyshev polynomial basis functions are useful for computing derivatives with spectral accuracy. The Chebyshev differential equation is given by

$$\frac{d}{dx} \left(\sqrt{1-x^2} \frac{dT_n}{dx} \right) + \lambda_n \frac{1}{\sqrt{1-x^2}} T_n = 0, \quad (\text{D.18})$$

and the solutions T_n to (D.18) are called Chebyshev polynomials, which are orthonormal with respect to weight function $\frac{1}{\sqrt{1-x^2}}$. The eigenvalue that correspond to each polynomial T_n is λ_n .

An arbitrary function can be interpreted in terms of a series of Chebyshev polynomials,

$$u_j = \sum_{n=0}^M a_n T_n(x_j), \quad (\text{D.19})$$

where a_n are the Chebyshev coefficients and M is the maximum polynomial degree. Here, \mathbf{u} will be evaluated at a discrete set of x_j points, which can be interpreted as a matrix multiplication $\mathbf{u} = \mathbf{T} \mathbf{a}$ that translates between Chebyshev and physical space. The Chebyshev coefficients are determined from orthogonality relations that apply to them and are not detailed here,

$$a_n = \frac{2}{c_n M} \sum_{j=0}^M \frac{1}{c_j} u_j T_n(x_j) \quad n = 0, 1, \dots, M \quad \text{where} \quad c_j = \begin{cases} 2 & p = 0, M \\ 1 & \text{otherwise} \end{cases} \quad (\text{D.20})$$

D.3.1 Differentiation

The differentiation of a function u can be derived using the recursion properties of Chebyshev polynomials,

$$u'_j(x) = \sum_{n=0}^{M-1} b_n T_n(x_j), \quad (\text{D.21})$$

$$\sum_{n=0}^{M-1} b_n T_n = \sum_{n=0}^M a_n T'_n \quad (\text{D.22})$$

where primes denote the full derivative with respect to x . The relation between coefficients \mathbf{b} and \mathbf{a} is,

$$G_{pn} = \begin{cases} 0 & \text{if } p \geq n \text{ or } p+n \text{ even} \\ 3n/c_p & \text{otherwise} \end{cases} \quad \text{where} \quad \mathbf{b} = \mathbf{G} \mathbf{a}. \quad (\text{D.23})$$

Higher derivatives can be described by matrix multiplying \mathbf{G} with itself that many times to obtain the necessary coefficients. Instead of evaluating the derivatives in terms of its Chebyshev coefficients, I explicitly evaluate it on a physical grid to create a derivative

operator in that space,

$$\mathbf{D} = \mathbf{T} \mathbf{G} \mathbf{T}^{-1}. \quad (\text{D.24})$$

So derivatives can simply be evaluated as,

$$\mathbf{u}' = \mathbf{D}\mathbf{u}, \quad \mathbf{u}'' = \mathbf{D}^2\mathbf{u}, \quad \text{etc.}$$

we are a discrete representation of the derivative operator and can be applied to eigenvalue problems.

D.3.2 A representative example: Orr-Sommerfeld equation

A brief verification of the spectral convergence of the Chebyshev method is presented for a typical hydrodynamic stability problem. That is, the eigenvalue problem given by the Orr-Sommerfeld equation:

$$(U - c) \left(\frac{d^2\phi}{dy^2} - k^2\phi \right) - \phi \frac{d^2U}{dy^2} = \frac{1}{ikRe} \left(\frac{d^2}{dy^2} - k^2 \right)^2 \phi, \quad (\text{D.25})$$

where U is a prescribed base flow, c is the eigenvalue and ϕ are the eigenfunctions; note that the normal mode expansion $\exp ik(x - ct)$ is used here and imaginary c contributes exponential growth or decay. A Poiseuille base flow $U = 1 - y^2$, $y \in [-1, 1]$ is considered here for comparison with established results. The boundary conditions to (D.25) are no-slip and no-penetration,

$$\phi = \frac{d\phi}{dy} = 0 \quad \text{at } y = \pm 1. \quad (\text{D.26})$$

The generalized eigenvalue problem (D.25) is discretized using the Chebyshev method and has the form $\mathbf{A}\phi = c\mathbf{B}\phi$; the eigenvalues and eigenvectors are computed using standard LAPACK routines.

Figure D.2 (a) shows the error ε of the most amplified eigenvalue of (D.25) for specific parameters and varying M . In this case the numerical approximation is compared to established results computed using specialty methods for this specific problem. The error decreases exponentially with M as expected, then increases modestly once M is sufficiently large. This is also expected, and as illustrated in figure D.2 (b) the condition number κ of \mathbf{A} becomes very large for large M , increasing as $\kappa \sim \mathcal{O}(10^{2p})$ where $p = 4$ is the order of the highest order derivative in the problem, as expected according to theory. This naturally prohibits the use of very large M as computations are constrained by the finite precision arithmetic.

D.4 Results

The linear system of (D.11-D.13) is simplified to both the viscous ($Re \rightarrow 0$) and inviscid ($Re \rightarrow \infty$) limits, with $Re \equiv \mu U a / \rho$, where analytical solutions are available due to

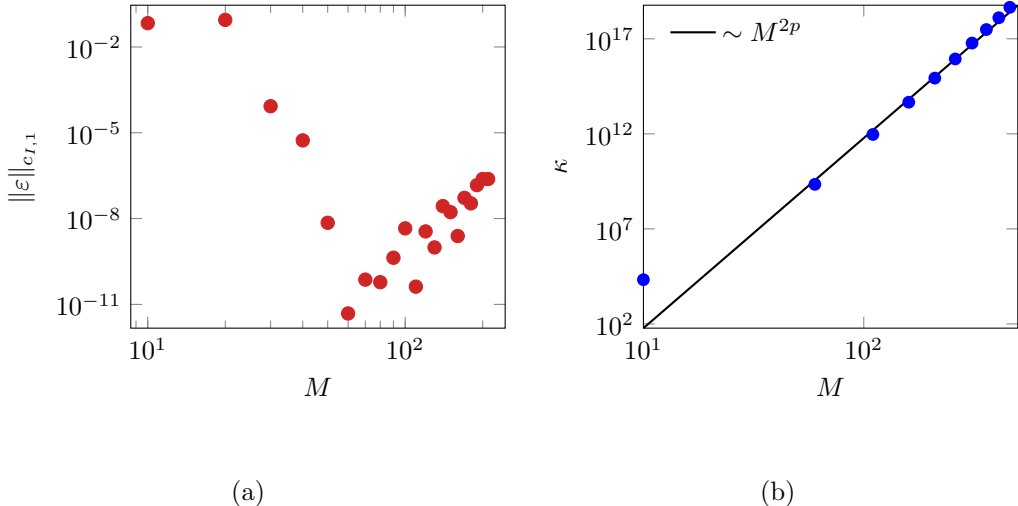


Figure D.2: (a) Absolute error in the largest imaginary eigenvalue $c_{I,1}$ of (D.25) with $Re = 10^4$, $k = 1$ and (b) the associated condition number of \mathbf{A} .

Rayleigh [422, 423], then solved for s .

Results are shown in figure D.3. Our numerical approximation is within plotting precision of the analytic solution for both $Re = 0$ and $Re \rightarrow \infty$. In the viscous case of figure D.3 (a), the most amplifying wave number is $k = 0$, or infinitely long waves, and the solution is stable for sufficiently short wavelengths of $ka > 1$. In the inviscid case of figure D.3 (b), the most amplifying wavenumber is $ka = 0.698$ and the jet is neutrally stable for $ka \geq 1$.

D.5 Discussion

The solutions detailed here for a purely viscous and inviscid capillary jet are in fact simplifications to the full problem that should be addressed moving forward, that is the one of a core-annular flow of complex, though continuous, fluids. However, the problem considered here does encompass many of the difficulties in the more complicated problem, such as the linearization of nonlinear constitutive equations, utilization of spectral numerical methods and application of boundary conditions.

Moving forward, the most straightforward expansion of the presented analysis would be that of second-order fluids, particularly that of the core-flow. This model is explicit in the velocity field, so the linear system of (D.9) would remain small. Further, the resulting flow would be able to capture the viscoelastic effects and normal stress differences typical of microcirculatory flow (see chapter 1). Unfortunately at this point there is no analytic solution to the governing equations available, making verification of our methods more challenging. More complex constitutive models should also be considered, such as those that can capture shear-thinning behavior, a well-known property of blood flow [424, 425]. Candidate fluid models include those previously used as continuum approximations for whole blood, such examples are Oldroyd-B, Carreau–Yasuda, Power-Law, Casson, and Herschel–Bulkley [341, 342, 426–428]. Eluded to above, these constitutive models are not explicit in

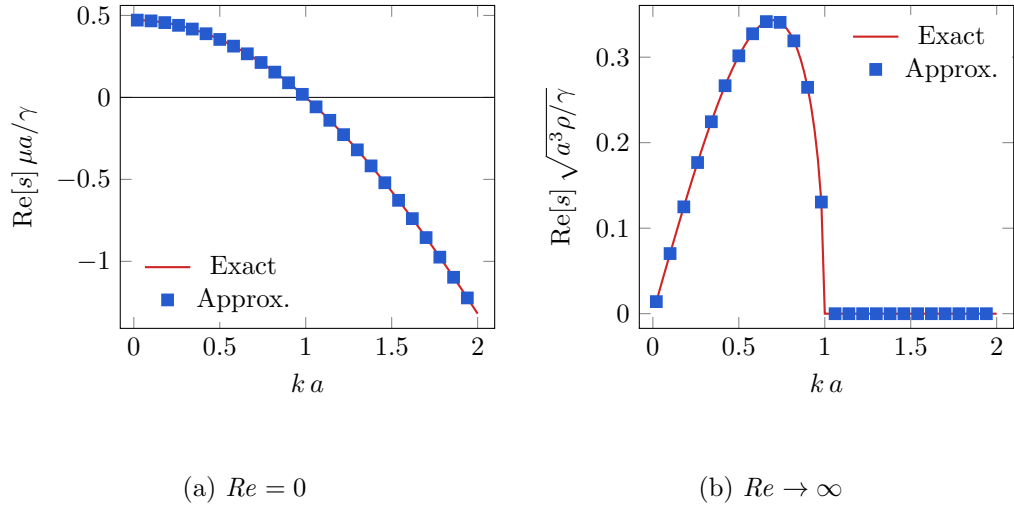


Figure D.3: $\text{Re}[s]$ for both (a) $Re = 0$ and (b) $Re \rightarrow \infty$ at a range of k , where $M = 20$.

the fluid velocity, so the constitutive law must be included separately in the computations. After such an analysis, the stability results could be compared to those predicted through nonmodal analysis of the discrete cell-trains.

E A rigid-sphere model for capsule trains

Herein, a discrete rigid-sphere model is proposed as a reduced model for flowing capsules or cells when the capsule-capsule spacing is sufficiently large. A linear stability analysis of an example simple flow system is presented in section E.2. Extensions of this system in an attempt to model the more complex flow of capsules, especially elastic effects, are discussed in section E.3.

E.1 Rigid-sphere flow systems

Consider a rigid sphere of radius a_i , suspended at position \mathbf{x} with velocity \mathbf{U}_i in a fluid with Newtonian viscosity μ and mean velocity \mathbf{U}^0 . In a many-sphere suspension, the hydrodynamic interactions of one sphere can be important for the flow of the others. Such sphere-sphere hydrodynamic interactions can be determined through the so-called method of reflections and Faxen's law [346]. Following this analysis, the disturbance of the fluid velocity from \mathbf{U}^0 by sphere i at the location of sphere j is

$$\mathbf{u}_i^0 = \left(\frac{\mathbf{I}}{r_{ij}} + \frac{\mathbf{x}_{ij} \mathbf{x}_{ij}}{r_{ij}^3} \right) \cdot \frac{3a_i \mathbf{U}^0}{4} + \left(\frac{\mathbf{I}}{3r_{ij}^3} - \frac{\mathbf{x}_{ij} \mathbf{x}_{ij}}{r_{ij}^5} \right) \cdot \frac{3a_i^3 \mathbf{U}^0}{4}, \quad (\text{E.1})$$

where $\mathbf{x}_{ij} \equiv \mathbf{x}_i - \mathbf{x}_j$, $r_{ij} \equiv |\mathbf{x}_{ij}|$, and \mathbf{I} is the identity tensor. The resultant velocity due to the first reflection of sphere j onto sphere i is,

$$\mathbf{U}_i^1 = \mathbf{u}_j^0(r_{ij}) + \frac{a_i^2}{2} \nabla^2 \mathbf{u}_j^0(r_{ij}), \quad (\text{E.2})$$

$$= \left(\frac{\mathbf{I}}{r_{ij}} + \frac{\mathbf{x}_{ij} \mathbf{x}_{ij}}{r_{ij}^3} \right) \cdot \frac{3a_j \mathbf{U}^0}{4} + \mathcal{O}(r_{ij}^{-3}). \quad (\text{E.3})$$

So long as $r_{ij} \gg a_i$, the cubic term in the separation can be neglected. Assuming this holds, the total velocity of sphere i in the presence of a single other sphere j is,

$$\begin{aligned} \mathbf{U}_i &= \mathbf{U}^0 + \mathbf{U}_i^1, \\ &= \mathbf{U}^0 + \left(\frac{\mathbf{I}}{r_{ij}} + \frac{\mathbf{x}_{ij} \mathbf{x}_{ij}}{r_{ij}^3} \right) \cdot \frac{3a_j \mathbf{U}^0}{4}. \end{aligned} \quad (\text{E.4})$$

A general expression for the velocity of sphere i in the presence of a general number of spheres is then

$$\mathbf{U}_i = \mathbf{U}^0 + \sum_{\substack{j=1 \\ i \neq j}}^n \frac{1}{r_{ij}} (\mathbf{I} + \mathbf{e}_{ij} \mathbf{e}_{ij}) \cdot \frac{3a_j \mathbf{U}^0}{4}, \quad (\text{E.5})$$

where n is the number of spheres and $\mathbf{e}_{ij} \equiv \mathbf{x}_{ij}/r_{ij}$ is the unit vector pointing from the centers of sphere i to sphere j .

E.2 Flow and stability of uniformly spaced sphere trains

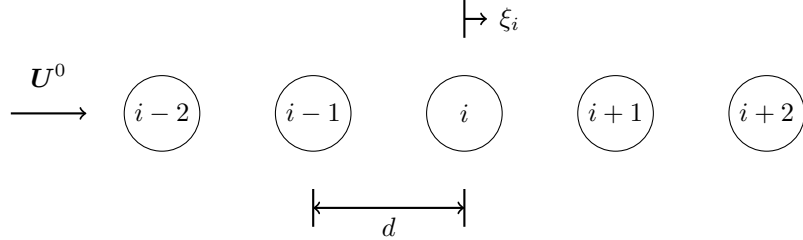


Figure E.1: Flow schematic of a uniform one-dimensional sphere train. All spheres have radius a and d is the consecutive sphere-sphere spacing.

Figure E.1 shows a one-dimensional uniform train of spheres flowing in an unbounded periodic domain, which is considered as a reduced model for the analogous capsule-train. We only consider streamwise positional perturbations to the sphere position, ξ_i , and so the resulting flow is one dimensional. Using (E.5) the perturbation to the velocity of sphere i due to all other spheres is,

$$U_i = U^0 + \frac{3aU^0}{2} \sum_{j=1}^{\infty} \frac{1}{r_{ij}}. \quad (\text{E.6})$$

Since the hydrodynamic interactions decay as $\mathcal{O}(r^{-1})$, if $d \gg a$ then we need only consider nearest-neighbor sphere-sphere interactions. This gives,

$$U_i = U^0 + \frac{3aU^0}{2} \left(\frac{1}{\tilde{r}_{i,i+1}} + \frac{1}{\tilde{r}_{i,i-1}} \right), \quad (\text{E.7})$$

where $\tilde{r}_{i,j} = d + (\xi_i - \xi_j)$. Following a standard practice, we decompose U_i into a uniform base flow velocity and the velocity change due to nonzero ξ_i ,

$$U_i = \frac{\partial x_i}{\partial t} + \frac{\partial \xi_i}{\partial t}. \quad (\text{E.8})$$

That is, $\partial_t x_i$ is the velocity were $\xi_i = 0$. Here, $\partial_t x_i$ is computed from (E.7) by setting $\xi_i = 0$ for all i ,

$$\frac{\partial x_i}{\partial t} = U^0 + \frac{3aU^0}{d}. \quad (\text{E.9})$$

We compute U_i by first considering an expansion of $\tilde{r}_{i,j}$ about d ,

$$\frac{1}{\tilde{r}_{i,j}} = \frac{1}{d} - \frac{\xi_i - \xi_j}{d^2} + \mathcal{O}\left((\xi_i - \xi_j)^2\right). \quad (\text{E.10})$$

Neglecting superlinear terms in ξ_i and substituting into (E.7),

$$U_i = \underbrace{U^0 + \frac{3aU^0}{d}}_{= \partial_t x_i} - \frac{3aU^0}{2} \left(\frac{\xi_{i+1} - \xi_i}{d^2} + \frac{\xi_i - \xi_{i-1}}{d^2} \right), \quad (\text{E.11})$$

which gives,

$$\begin{aligned} \frac{\partial \xi_i}{\partial t} &= U_i - \frac{\partial x_i}{\partial t}, \\ &= -\frac{3aU^0}{2} \frac{1}{d^2} (\xi_{i+1} - \xi_{i-1}), \end{aligned} \quad (\text{E.12})$$

Following common procedure, the stability of this flow is determined through a normal mode expansion of the form $\xi_i \propto e^{\beta t} e^{ikx_i}$, where β is the complex growth rate and k is the spatial wave number. Substituting into (E.12) gives

$$\begin{aligned} \beta &= -\frac{3}{2} \frac{aU^0}{d^2} (e^{ikd} - e^{-ikd}) \\ &= -3i \frac{aU^0}{d^2} \sin(kd). \end{aligned} \quad (\text{E.13})$$

Since $\text{Re}[\beta] = 0 \forall \{k, d, U^0\}$, the system is *always* stable. We confirm this result by conducting a direct numerical simulation of $x_i(t)$ of a long sphere train using (E.6) and verifying that small positional perturbations to x_i do not grow or decay. Of course this is only a simplified model problem and so a qualitative connection of its stability with a capsule-train is not expected, and is indeed not found since the uniformed spaced sphere system is always stable.

E.3 Extensions and discussion

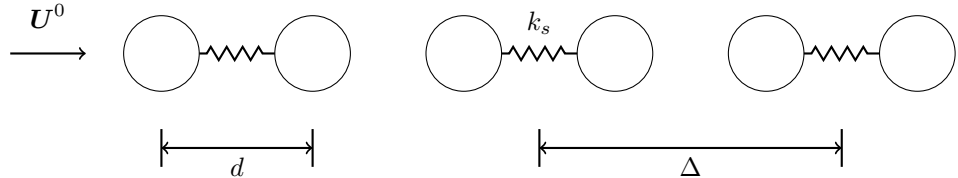


Figure E.2: Schematic of a more complex sphere flow system.

Figure E.2 shows a more complex candidate flow system that may more accurately model the stability of a capsule-train. Each “sphere-pair” is connected by a spring of modulus k_s and separated by distance d ; consecutive sphere-pairs are separated by distance Δ . For brevity the stability of this system is not shown here. We posit that the introduction of an elastic element will more closely match the behavior of the still more complex capsule train. Additionally, a viscous element, or dashpot, might be introduced to capture the intra-capsule viscous effects due to the interior fluid.

Of course determining the stability of such complex sphere flow systems is not necessarily trivial. This is especially true for scenarios where there are close sphere-sphere interactions, and the approximations of the previous section no longer hold. A further complex system might also consider the effect of parallel walls or flow within a cylinder, for which analytical flow solutions exist [429]. Such analyses should also consider non-streamwise sphere disturbances, which are known to be important in capsule trains flowing in channels and tubes. Finally, Faxén laws exist for particles of other shapes, such as ellipsoids [311, 429], which might prove useful when considering non-spherical capsules in flow.

F Discriminating chaotic dynamics from stochastic noise in microcirculatory flow

We lay out analyses of microcirculatory flow simulations, as conducted with the methods of chapter 3. A synopsis of our results is in section 7.3.2; here, the data are details of the results are presented.

F.1 Simulations

Simulations are initialized according to the description of section 4.1.1 for vessel diameters $D/r_o = 6$ and 8, and advanced 3×10^6 time steps. This corresponds to a streamwise displacement of 8000 periodic vessel lengths according to the mean flow velocity, and approximately four months of simulation run time. We confirm these simulations are sufficiently long that the results of the following sections are statistically stationary.

F.2 Data

The radial location of a cell within the vessel is known to be an important quantity when analyzing cellular blood flow. We define this metric using the radial coordinate of the geometric centroid position of a cell, which is denoted by $r_j[t]$ for cell j .

In figure F.1 we show $r_j[t]$ for example cases with nested magnification up to the individual time-step data. A transient behavior is seen for $t \lesssim 300$, with $r_j[t]$ increasing from near zero. This is expected, as the small perturbations to the cells amplify due to the unstable nature of the initialized flow system. For $t \gtrsim 300$, $r_j[t]$ does not have any obvious pattern for either case shown. We will use $t > 300$ for our statistics.

We define $\mathbf{r}_j \equiv \{r_j[\Delta t], r_j[2\Delta t], \dots, r_j[n\Delta t]\}$, $\mathbf{r}_{j,i} = r_j[i\Delta t]$, and describe the discrete and uniform time series with vector notation,

$$\mathbf{R} = \{\mathbf{r}_1, \mathbf{r}_2, \dots, \mathbf{r}_N\} \quad (\text{F.1})$$

and $\mathbf{R}_i = \{\mathbf{r}_{1,i}, \mathbf{r}_{2,i}, \dots, \mathbf{r}_{N,i}\}$.

F.3 Fourier spectrum

Fourier power spectra are often used to determine the dominant time scales, or frequencies, of a nonlinear time series. A dominant frequency, or frequencies, serves as evidence of an

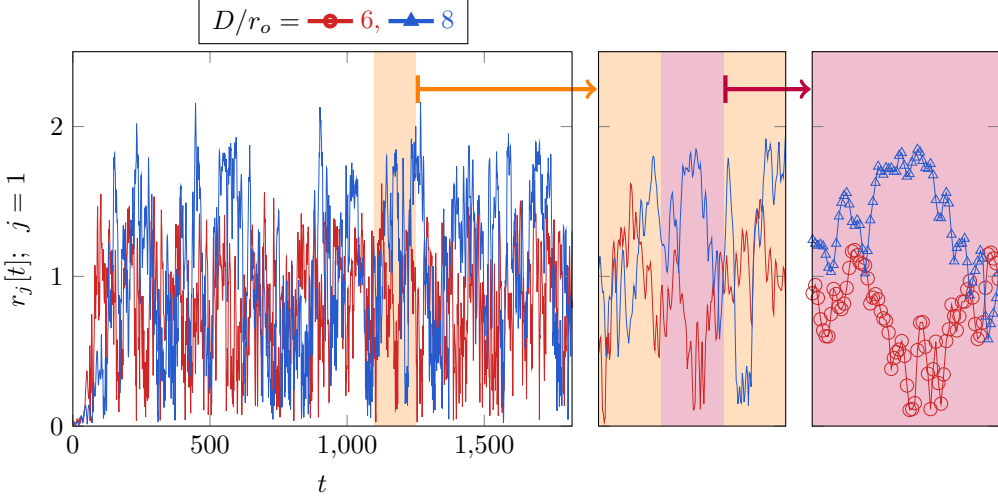


Figure F.1: $r_j[t]$ for one cell and cases as labeled.

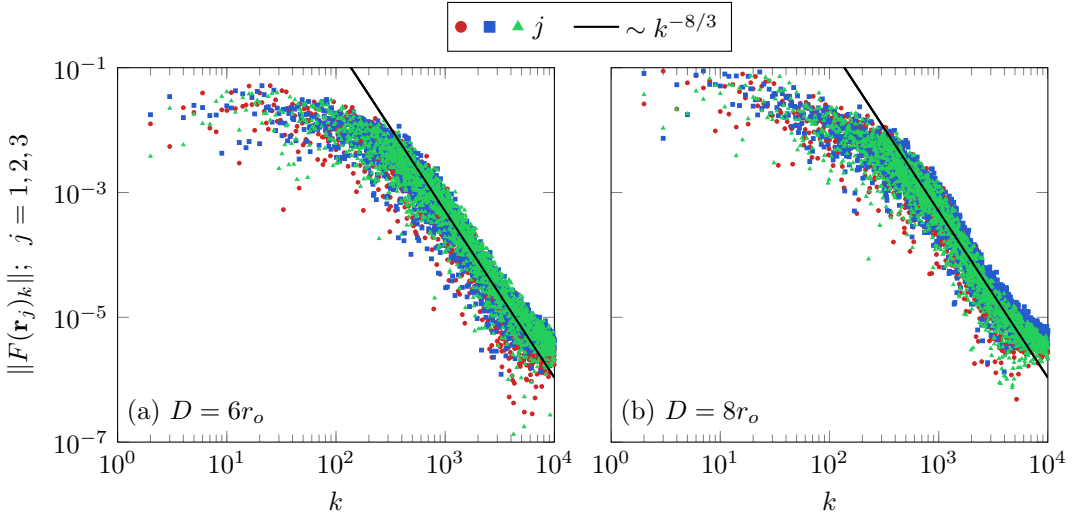


Figure F.2: Fourier spectrum of \mathbf{r}_j for (a) $D = 6r_o$ and (b) $D = 8r_o$, and j as labeled.

deterministic attractor. The discrete Fourier transform of \mathbf{r}_j is

$$F(\mathbf{r}_j)_k = \frac{1}{\sqrt{n}} \sum_{i=1}^n \mathbf{r}_{j,i} \exp[2\pi i(i-1)(k-1)/n] \quad \text{for } k = 1, n/2, \quad (\text{F.2})$$

for mode k .

In figure F.2 we show the Fourier power spectra of \mathbf{r}_j for select j and D . In all cases no peak in F is seen, and thus there is no dominant frequency. For $k \gtrsim 100$ for both $D/r_o = 6$ and 8, and for all j , a power-law behavior in k appears with scaling $-8/3$. We expect this power-law behavior is not due to the expected decay of the Fourier coefficients due to the smoothness of the data, as the power is not near an integer and the behavior is independent of filtering or smoothing of the data.

F.4 Correlation dimension

The correlation dimension is obtained from correlations between points on an attractor, that is, those extracted by our time series \mathbf{R} . Due to the divergence of trajectories, most pairs $(\mathbf{R}_i, \mathbf{R}_j)$, with $i \neq j$, will be uncorrelated pairs of nearly random points. The points which lie however on the attractor, therefore, will be spatially correlated. This spatial correlation is measured with the correlation integral $C(l)$, or the mean probability that states at two different times are within threshold distance l ,

$$C(\varepsilon) = \frac{1}{n^2} \sum_{\substack{i,j=1 \\ i \neq j}}^n \Theta(\varepsilon - \|\tilde{\mathbf{R}}_i - \tilde{\mathbf{R}}_j\|), \quad (\text{F.3})$$

where Θ is the Heaviside step function, $\|\cdot\|$ is the L_2 norm, and

$$\tilde{\mathbf{R}} = \{\mathbf{R}_i, \mathbf{R}_{i+\tau}, \dots, \mathbf{R}_{i+\tau(m-1)}\}, \quad (\text{F.4})$$

is the time-delay embedding of \mathbf{R} with dimension m and time delay τ .

If for small ε , $C(\varepsilon)$ can be expressed as

$$C(\varepsilon) \sim \varepsilon^v, \quad (\text{F.5})$$

then v is called the correlation dimension and can be taken as a useful measure of the local structure of an attractor. If $v < m$, then the signal likely stems from deterministic chaos rather than a stochastic behavior. Here, $v(\varepsilon)$ is simply the log derivative of $C(\varepsilon)$.

The correlation integral and dimension for \mathbf{R} are shown in Figure F.3 for an example case. For $\varepsilon \lesssim 4 \times 10^{-3}$ we have $C(\varepsilon) \sim \varepsilon^m$, which suggests ε sufficiently small to be in a noise regime where (F.3) is poorly conditioned. We see $v(\varepsilon) \approx 1$ for $4 \times 10^{-3} \lesssim \varepsilon \lesssim 0.03$ and $m > 3$, which suggests that the embedded data are too close to accurately determine $C(\varepsilon)$. We label $0.03 < \varepsilon < 1$ the scaling region, where a power law behavior in ε is expected. In this regime, $v < m$, though v still increases with m .

The slow increase of v with m in the scaling region of figure F.3 suggests v could be converging upon a fixed value for large m . We quantify this behavior in figure F.4 though the maximum value of v in the scaling regime for a range of m . We have $\max_\varepsilon v = m$ for $m < 3$, and approximately $\max_\varepsilon v(\varepsilon) \sim m^{0.3}$ for $m > 4$. The algebraic increase of $\max_\varepsilon v(\varepsilon)$ with m for at least up to $m = 50$ suggests it will not saturate at a fixed value for still larger embedding dimensions. Again, this result suggests a stochastic behavior.

F.5 Structure function

The structure function is given by

$$S_k(n) = \sum_{i=1}^{N-n} \|d_t^m \mathbf{r}_{1,i+n} - d_t^m \mathbf{r}_{1,i}\|^k, \quad (\text{F.6})$$

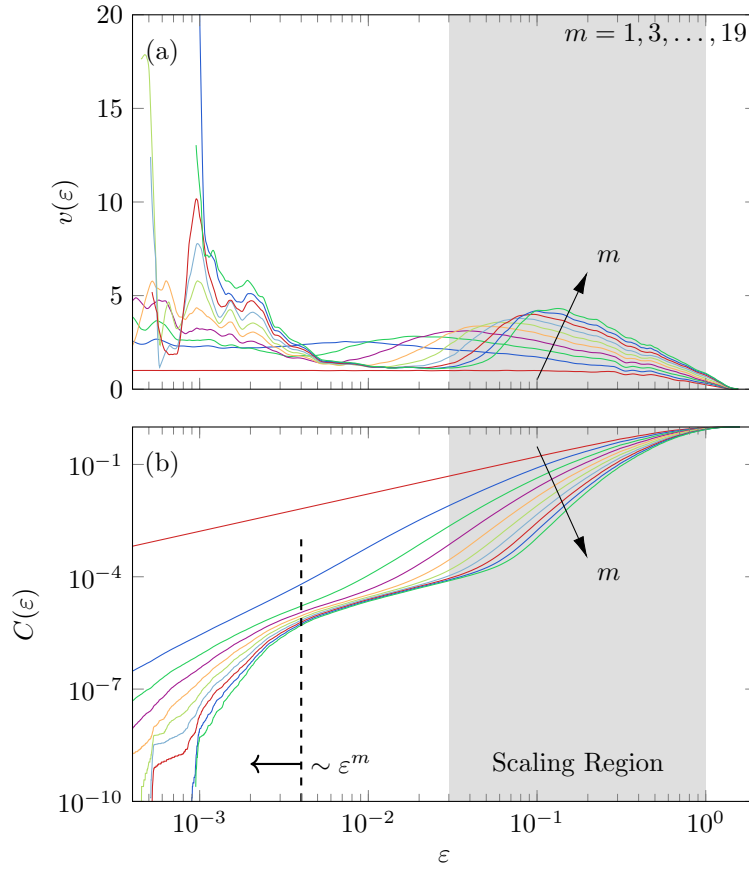


Figure F.3: (a) Correlation dimension $v(\varepsilon)$ and (b) correlation integral $C(\varepsilon)$ for the several m for the case $D = 6r_o$.

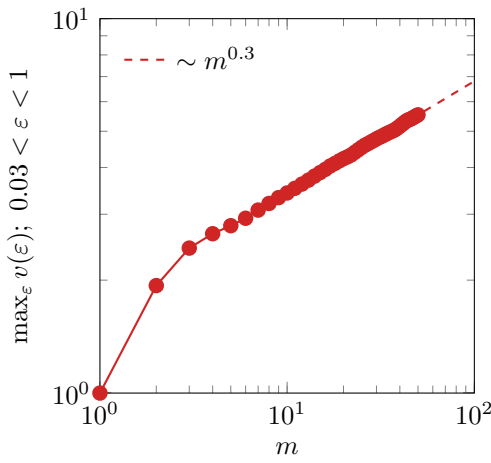


Figure F.4: Maximum $v(\varepsilon)$ in the scaling region $0.03 < \varepsilon < 1$ (as shown in figure F.3).

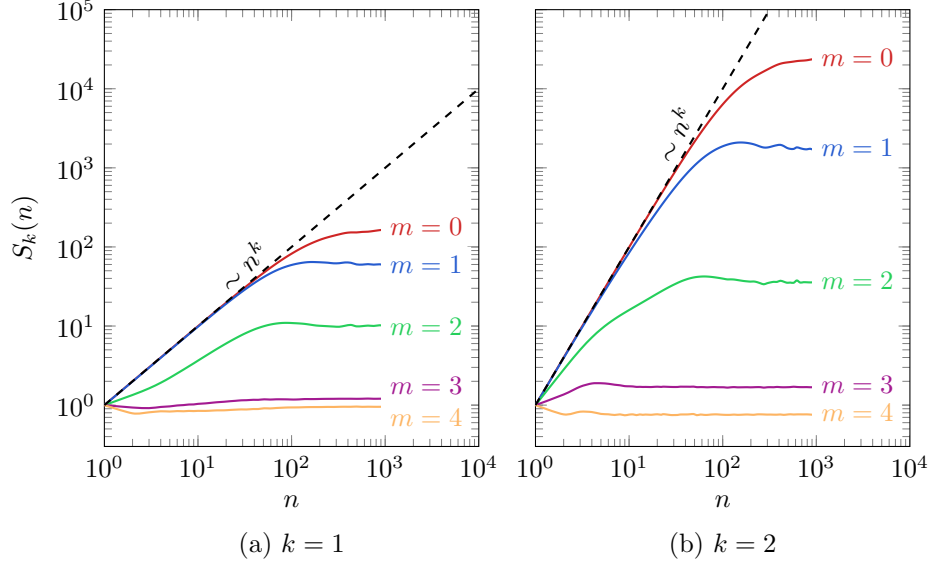


Figure F.5: Structure function for varying n and m , and (a) $k = 1$ and (b) $k = 2$.

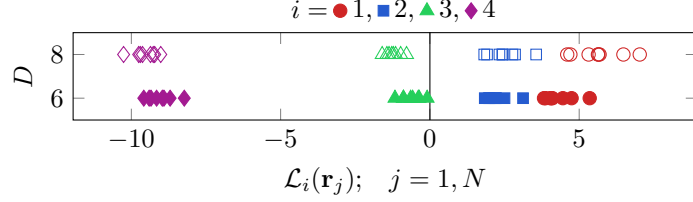


Figure F.6: Four largest Lyapunov exponents $\mathcal{L}(\mathbf{r}_j)$ for $j = 1, \dots, N$.

where k is the norm, N is the number of time steps, and m is the degree of time derivatives taken. For a chaotic system we expect $S_k(n) \sim n^k$ for small n for both $k = 1$ and $k = 2$, and any m [355]

In figure F.5 we see that $S_k(n) \sim n^k$ for both $k = 1$ and 2 , though this does not hold when taking time derivatives of the data (m). As a result, we anticipate the data behavior is stochastic.

F.6 Lyapunov exponents

Lyapunov exponents give the rate of divergence of nearby trajectories, in our case described by \mathbf{R} , the maximum of which is given by:

$$\mathcal{L}(\mathbf{r}_j) = \frac{1}{n} \sum_{i=1}^n \ln \left| \frac{\Delta \mathbf{r}_{j,i+1}}{\Delta \mathbf{r}_{j,i}} \right|. \quad (\text{F.7})$$

When $\mathcal{L} > 0$, the system is chaotic.

For both $D/r_o = 6$ and 8 we have $\mathcal{L}_1 > 5$. However, this value is so large than its considered unrealistic for a true chaotic system [355].

References

- [1] E. J. Schaefer, W. H. Heaton, M. G. Wetzel, and H. B. Brewer Jr. Plasma apolipoprotein a-1 absence associated with a marked reduction of high density lipoproteins and premature coronary artery disease. *Arterioscl. Throm. Vas.*, 2(1):16–26, 1982.
- [2] S. S. Shevkoplyasa, S. C. Grifforda, T. Yoshida, and M. W. Bitensky. Prototype of an in vitro model of the microcirculation. *Microvasc. Res.*, 65:132–136, 2003.
- [3] C. Pozrikidis. Axisymmetric motion of a file of red blood cells through capillaries. *Phys. Fluids*, 15(031503), 2005.
- [4] H. Zhao, A. H. G. Isfahani, L. Olson, and J. B. Freund. A spectral boundary integral method for micro-circulatory cellular flows. *J. Comp. Phys.*, 229:3726–3744, 2010.
- [5] A. R. Pries, D. Neuhaus, and P. Gaehtgens. Blood viscosity in tube flow: dependence on diameter and hematocrit. *Am. J. Physiol. Heart Circ. Physiol.*, 263, 1992.
- [6] D. Barthès-Biesel. Motion of a spherical microcapsule freely suspended in a linear shear flow. *J. Fluid Mech.*, 100:831, 1980.
- [7] D. Barthès-Biesel and J. M. Rallison. The time-dependent deformation of a capsule freely suspended in a linear shear flow. *J. Fluid Mech.*, 113:251–267, 1981.
- [8] D. Barthès-Biesel. Motion and deformation of elastic capsules and vesicles in flow. *Annu. Rev. Fluid Mech.*, 48:25–52, 2016.
- [9] T. L. Steck. The organization of proteins in the human red blood cell membrane: a review. *J. Cell. Bio.*, 62(1), 1974.
- [10] L. L. M. Deneen and J. De Gier. *The Red Blood Cell*. Number 243-307. Academic Press, New York, 1964.
- [11] Y. Park, C. A. Best, T. Auth, N. S. Gov S. A. Safran, G. Popescu, S. Suresh, and M. S. Feld. Metabolic remodeling of the human red blood cell membrane. *Proceedings of the National Academy of Sciences*, 107(4):1289–1294, 2010.
- [12] J. D. Bronzino. *The Biomedical Engineering Handbook*. IEEE Press/CRC Press, Boca Raton, FL, 2000.
- [13] G. R. Cokelet and H. J. Meiselman. Rheological comparison of hemoglobin solutions and erythrocyte suspension. *Science*, 162:275–277, 1968.
- [14] L. Distenfass. Internal viscosity of the red cell and a blood viscosity equation. *Nature*, 219:956–958, 1968.
- [15] R. M. Hochmuth, C. A. Evans, H. C. Wiles, and J. T. McCown. Mechanical measurement of red cell membrane thickness. *Science*, 220(4592):101–102, 1983.
- [16] V. Heinrich, K. Ritchie, N. Mohandas, and E. Evans. Elastic thickness compressibility of the red cell membrane. *Biophys. J.*, 81:1452–1463, 2001.

- [17] A. Nans, N. Mohandas, and D. L. Stokes. Native ultrastructure of the red cell cytoskeleton by cryo-electron tomography. *Biophys. J.*, 101:2341–2350, 2011.
- [18] R. Arshady. Microspheres and microcapsules: A survey of manufacturing techniques. Part i: Suspension crosslinking. *Poly. Eng. Sci.*, 29(24):1746–1758, 1989.
- [19] F. Caruso. Hollow capsule processing through colloidal templating and self-assembly. *Chem-Eur J.*, 6(3):413–419, 2000.
- [20] R. Arshady. Microspheres and microcapsules: A survey of manufacturing techniques. Part ii: Coacervation. *Poly. Eng. Sci.*, 30(15):905–914, 1990.
- [21] R. Atkin, P. Davies, J. Hardy, and B. Vincent. Preparation of aqueous core/polymer shell microcapsules by internal phase separation. *Macromolecules*, 37(21):7979–7985, 2004.
- [22] J. Dohnal and F. Stepanek. Inkjet fabrication and characterization of calcium alginate microcapsules. *Powder Tech.*, 200(3):254–259, 2010.
- [23] S. Desai, J. Perkins, B. S. Harrison, and J. Sankar. Understanding release kinetics of biopolymer drug delivery microcapsules for biomedical applications. *Mat. Sci. Eng. B*, 168(1):127–131, 2010.
- [24] R. D. Boehm, P. R. Miller, J. Daniels, S. Stafslien, and R. J. Narayan. Inkjet printing for pharmaceutical applications. *Mater. Today*, 17(5):247–252, 2014.
- [25] T. R. Tice and R. M. Gilley. Preparation of injectable controlled-release microcapsules by a solvent-evaporation process. *J. Control. Rel.*, 2:343–352, 1985.
- [26] R. Arshady. Microspheres and microcapsules: A survey of manufacturing techniques. Part iii: Solvent evaporation. *Poly. Eng. Sci.*, 30(15):915–924, 1990.
- [27] K. Liu, H.-J. Ding, J. Liu, Y. Chen, and X.-Z. Zhao. Shape-controlled production of biodegradable calcium alginate gel microparticles using a novel microfluidic device. *Langmuir*, 22(22):9453–9457, 2006.
- [28] S. P. Baldwin and R. P. Skribiski. Forming a chemically cross-linked particle of a desired shape and diameter, 2006. US Patent 7,053,134.
- [29] P. Aebischer, J. F. Mills, L. Wahlberg, E. J. Doherty, and P. A. Tresco. Method of preparing elongated seamless capsules containing biological material, 1995. US Patent 5,418,154.
- [30] W. Kim and S. S. Kim. Multishell encapsulation using a triple coaxial electrospray system. *Analytical Chem.*, 82(11):4644–4647, 2010.
- [31] M. Augustin and Y. Hemar. Nano- and micro-structured assemblies for encapsulation of food ingredients. *Chem. Soc. Rev.*, 38(4):902–912, 2009.
- [32] Z. Dai and H. Mohwald. Nanoengineering of polymeric capsules with a shell-in-shell structure. *Langmuir*, 18(24):9533–9538, 2002.
- [33] M. Ulbricht. Advanced functional polymer membranes. *Polymer*, 47(2):2217–2262, 2006.
- [34] S. R. White, N. R. Sottos, P. H. Geubelle, and J. S. Moore. Autonomic healing of polymer composites. *Nature*, 409(6822):794, 2001.
- [35] A. Walter, H. Rehage, and H. Leonhard. Shear-induced deformation of polyamid microcapsules. *Colloid Polym. Sci.*, 278:169–175, 2000.

- [36] H. Zhang, E. Tumarkin, R. Peerani, Z. Nie, R. M. A. Sullan, G. C. Walker, and E. Kumacheva. Microfluidic production of biopolymer microcapsules with controlled morphology. *J. Am. Chem. Soc.*, 128(37):12205–12210, 2006.
- [37] S. A. Mahdavi, S. M. Jafari, M. Ghorbani, and E. Assadpoor. Spray-drying microencapsulation of anthocyanins by natural biopolymers: A review. *Drying Tech.*, 32(5):509–518, 2014.
- [38] S. Leelajariyakul, H. Noguchi, and S. Kiatkamjornwong. Surface-modified and micro-encapsulated pigmented inks for ink jet printing on textile fabrics. *Prog. Org. Coat.*, 62(2):145–161, 2008.
- [39] I. M. Martins, M. F. Barreiro, M. Coelho, and A. E. Rodrigues. Microencapsulation of essential oils with biodegradable polymeric carriers for cosmetic applications. *Chem. Eng. J.*, 245:191–200, 2014.
- [40] K. Miyazawa, I. Yajima, I. Kaneda, and T. Yanaki. Preparation of a new soft capsule for cosmetics. *J. Cosmet. Sci.*, 51(4):239–252, 2000.
- [41] S. Krishnan, Bhosale R., and R. S. Singhal. Microencapsulation of cardamom oleoresin: Evaluation of blends of gum arabic, maltodextrin and a modified starch as wall materials. *Carbohydr. Polym.*, 61(1):95–102, 2005.
- [42] S. Krishnan, A. C. Kshirsagar, and R. S. Singhal. The use of gum arabic and modified starch in the microencapsulation of a food flavoring agent. *Carbohydr. Polym.*, 62(4):309–315, 2005.
- [43] G. Nelson. Application of microencapsulation in textiles. *Int. J. Pharm.*, 242(1):55–62, 2002.
- [44] Y. Shin, D. Yoo, and K. Son. Development of thermoregulating textile materials with microencapsulated phase change materials (PCM). II. Preparation and application of PCM microcapsules. *J. Appl. Polym. Sci.*, 96(6), 2005.
- [45] T. K. Maji, I. Baruah, S. Dube, and M. R. Hussain. Microencapsulation of zanthoxy-lum limonella oil (zlo) in glutaraldehyde crosslinked gelatin for mosquito repellent application. *Bioresource Technol.*, 98(4):840–844, 2007.
- [46] B. Solomon, F. F. Sahle, T. Gebre-Mariam, K. Asres, and R. H. H. Neubert. Microencapsulation of citronella oil for mosquito-repellent application: formulation and in vitro permeation studies. *European Journal of Pharmaceutics and Biopharmaceutics*, 80(1):61–66, 2012.
- [47] S. Giraud, S. Bourbigot, M. Rochery, I. Vroman, L. Tighzert, and R. Delobel. Microencapsulation of phosphate: application to flame retarded coated cotton. *Polymer Degradation and Stability*, 77(2):285–297, 2002.
- [48] K. Wu, Z. Wang, and H. Liang. Microencapsulation of ammonium polyphosphate: preparation, characterization, and its flame retardance in polypropylene. *Polymer Composites*, 29(8):854–860, 2008.
- [49] B. F. Gibbs, S. Kermasha, I. Alli, and C. N. Mulligan. Encapsulation in the food industry: a review. *Int. J. Food Sci. and Neut.*, 50:213–224, 1999.
- [50] F. Pop. Chemical stabilization of oils rich in long-chain polyunsaturated fatty acids during storage. *Food Sci. Technol. Int.*, 17(2):111–117, 2011.
- [51] G. Ma and Z.-G. Su. *Microspheres and Microcapsules in Biotechnology: Design, Preparation and Applications*. Pan Stanford Publishing, 2013.

- [52] J. J. Vericella, S. E. Baker, J. K. Stolaroff, E. B. Duoss, J. O. Hardin IV, J. Lewicki, E. Glogowski, W. C. Floyd, C. A. Valdez, W. L Smith, J. H. Satcher Jr., W. L. Bourcier, C. M. Spadaccini, J. A. Lewis, and R. D. Aines. Encapsulated liquid sorbents for carbon dioxide capture. *Nat. Commun.*, 6, 2015.
- [53] N. S. Dey, S. Majumdar, and M. E. B. Rao. Multiparticulate drug delivery systems for controlled release. *Trop. J. Pharm. Res.*, 7(3):1067–1075, 2008.
- [54] N. Paret, A. Trachsel, D. L. Berthier, and A. Herrmann. Controlled release of encapsulated bioactive volatiles by rupture of the capsule wall through the light-induced generation of a gas. *Chem. Int. Ed.*, 54(7):2275–2279, 2015.
- [55] F. Lim. *Biomedical Applications of Microencapsulation*. Boca Raton, FL: CRC, 1 edition, 1984.
- [56] N. J. Zuidam and V. Nedovic. *Encapsulation Technologies for Active Food Ingredients and Processing*. New York: Springer, 2010.
- [57] X. Zhang, W. Wang, W. Yu, Y. Xie, X. Zhang, Y. Zhang, and X. Ma. Development of an in vitro multicellular tumor spheroid model using microencapsulation and its application in anticancer drug screening and testing. *Biotechnol. Progr.*, 21(4):1289–1296, 2005.
- [58] W. Kalow, U. B. Meyer, and R. F. Tyndale. *Pharmacogenomics*. CRC Press, 2001.
- [59] B. Furlow. Contrast-enhanced ultrasound. *Radiol. Technol.*, 80:547–561, 2009.
- [60] T. M. Chang. Blood replacement with nanobiotechnologically engineered hemoglobin and hemoglobin nanocapsules. *Wiley Intersci. Rev. Nanomed. Nanobiotechnol.*, 2:418–430, 2010.
- [61] N. Doshi, A. S. Zahr, S. Bhaskar, J. Lahann, and S. Mitragotri. Red blood cell-mimicking synthetic biomaterial particles. *Proc. Nat. Acad. Sci.*, 106(51):21495–21499, 2009.
- [62] W. M. Kuhtreiber, R. P. Lanza, and W. L. Chick. *Cell Encapsulation Technology and Therapeutics*. Birkhauser, 1998.
- [63] H. A. Clayton, R. F. L. James, and N. J. M. London. Islet microencapsulation: a review. *Acta Diabetol.*, 30:181–189, 1993.
- [64] S. Sakai, T. Ono, H. Ijima, and K. Kawakami. Synthesis and transport characterization of alginate/aminopropyl-silicate/alginate microcapsule: application to bioartificial pancreas. *Biomaterials*, 22(21):2827–2834, 2001.
- [65] C. R. Martin. Membrane-based synthesis of nanomaterials. *Chem. Mat.*, 8(8):1739–1746, 1996.
- [66] R. Ameloot, F. Vermoortele, W. Vanhove, M. B. Roeffaers, B. F. Sels, and D. E. DeVos. Interfacial synthesis of hollow metal–organic framework capsules demonstrating selective permeability. *Nat. Chem.*, 3(5):382–387, 2011.
- [67] H. Zhou and C. Pozrikidis. Deformation of liquid capsules with incompressible interfaces in simple shear flow. *J. Fluid Mech.*, 283:175–200, 1995.
- [68] G. Ghigliotti, T. Biben, and C. Misbah. Rheology of a dilute two-dimensional suspension of vesicles. *J. Fluid Mech.*, 653:489–518, 2010.

- [69] H. Lei, D. A. Fedosov, B. Caswell, and G. E. Karniadakis. Blood flow in small tubes: quantifying the transition to the non-continuum regime. *J. Fluid Mech.*, 722:214–239, 2013.
- [70] J. B. Freund. Numerical simulations of flowing blood cells. *Annu. Rev. Fluid Mech.*, 46:67–95, 2014.
- [71] I. M. Krieger and T. J. Dougherty. A mechanism for non-Newtonian flow in suspensions of rigid spheres. *T. Soc. Rheol.*, 3(1):137–152, 1959.
- [72] J. M.V. A. Koelman and P. J. Hoogerbrugge. Dynamic simulations of hard-sphere suspensions under steady shear. *Europhys. Lett.*, 21(3):363, 1993.
- [73] J. R. Clausen, D. A. Reasor Jr., and C. K. Aidun. The rheology and microstructure of concentrated non-colloidal suspensions of deformable capsules. *J. Fluid Mech.*, 685:202–234, 2011.
- [74] J. Vermant and M. J. Solomon. Flow-induced structure in colloidal suspensions. *J. Phys.-Condens. Mat.*, 17(4):R187, 2005.
- [75] A. R. Pries, T. W. Secomb, and P. Gaehtgens. Biophysical aspects of blood flow in the microvasculature. *Cardiovasc. Res.*, 32:654–667, 1996.
- [76] J. H. Barbee and G. R. Cokelet. Prediction of blood flow in tubes with diameters as small as 29 microns. *Microvasc. Res.*, 3:17–21, 1971.
- [77] H. L. Goldsmith, G. R. Cokelet, and P. Gaehtgens. Robin Fåhræus: evolution of his concepts in cardiovascular physiology. *Am. J. Physiol. Heart Circ. Physiol.*, 257:H1005–H1015, 1989.
- [78] A. S. Popel and P. C. Johnson. Microcirculation and hemorheology. *Annu. Rev. Fluid Mech.*, 37:43–69, 2005.
- [79] C. Migliorini, Y. Qian, H. Chen, E. Brown, R. Jain, and L. Munn. Red blood cells augment leukocyte rolling in a virtual blood vessel. *Biophys. J.*, 83:1834–1841, 2002.
- [80] R. D. Kamm. Cellular fluid mechanics. *Annu. Rev. Fluid Mech.*, 34:211–232, 2002.
- [81] C. Pozrikidis. Numerical simulation of the flow-induced deformation of red blood cells. *Ann. Biomed. Eng.*, 31:1194–1205, 2003.
- [82] J. L. M. Poiseuille. Recherches sur les causes du mouvement du sang dans les vaisseaux capillaires. *CR Acad. Sci. Paris*, 1:554–560, 1835.
- [83] S. A. Berger, W. Goldsmith, and E. R. Lewis. *Introduction to Bioengineering*. Oxford University Press, Oxford, 1996.
- [84] H. H. Lipowsky, S. Usami, and S. Chien. In vivo measurements of apparent viscosity and microvessel hematocrit in the mesentery of the cat. *Microvasc. Res.*, 19:297–319, 1980.
- [85] D. S. Long. *Microviscometric Analysis of Microvascular Hemodynamics in Vivo*. PhD thesis, University of Illinois at Urbana-Champaign, 2004.
- [86] N. S. Korotkoff. On methods of studying blood pressure. *Bull. Imperial Mil. Med. Acad.*, 11:365–367, 1905.
- [87] O. Warburg, F. Wind, and E. Negelein. The metabolism of tumors in the body. *J. Gen. Physiol.*, 8(6):519, 1927.

- [88] F. A. Gibbs. A thermoelectric blood flow recorder in the form of a needle. *P. Soc. Exp. Bio. Med.*, 31(1):141–146, 1933.
- [89] P. Martini, A. Pierach, and E. Schreyer. Die stromung des blutes in engen gefassen. eine abweichung vom Poiseuille’schen gesetz. *Dtsch. Arch. KZin. Med*, 169:212–222, 1930.
- [90] R. Fahraeus and T. Lindqvist. The viscosity of the blood in narrow capillary tubes. *Am. J. Physiol. Heart Circ. Physiol.*, 96:562–568, 1931.
- [91] G. R. Cokelet. *Biomechanics-Its Foundations and Objectives*. Prentice-Hall, 1972.
- [92] H. Schmid-Schonbein and R. E. Wells. Rheological properties of human erythrocytes and their influence upon the “anomalous” viscosity of blood. *Ergeb Physiol.*, 63:146–219, 1971.
- [93] T. W. Secomb and T. M. Fischer. The motion of close-packed red blood cells in shear flow. *Biorheology*, 20:283–294, 1983.
- [94] G. Bugliarello and J. Sevilla. Velocity distribution and other characteristics of steady and pulsatile blood flow in fine glass. *Biorheology*, 7(2):85–107, 1970.
- [95] G. R. Cokelet. *The Rheology of Human Blood*. Prentice-Hall, 1972.
- [96] M. Sharan and A. S. Popel. A two-phase model for flow of blood in narrow tubes with increased effective viscosity near the wall. *Biorheology*, 38(5-6):415–428, 2001.
- [97] V. P. Srivastava. A theoretical model for blood flow in small vessels. *Int. J. App. and App. Math.*, 2(1):51–65, 2007.
- [98] D. S. Sankar and U. Lee. Two-fluid Herchel-Bulkley model for blood flow in catheterized arteries. *J. Mech. Sci. and Tech.*, 22(5):1008–1018, 2008.
- [99] H. Schmid-Schonbein and P. Gaehtgens. What is red-cell deformability? *Scandinavian Journal of Clinical and Laboratory Investigation*, 41(13), 1981.
- [100] V. Vitkova, A. Farutin, B. Polack, C. Misbah, and T. Podgorski. Erythrocyte dynamics in flow affects blood rheology. *J. Phys. Conf. Ser.*, 398(012027), 2012.
- [101] R. Skalak, N. Ozkaya, and T. C. Skalak. Biofluid mechanics. *Annu. Rev. Fluid Mech.*, 21:167–204, 1989.
- [102] J. C. Firrell and H. H. Lipowsky. Leukocyte margination and deformation in mesenteric venules of ram. *Am. J. Physiol. Heart Circ. Physiol.*, 225(6):1667–1674, 1989.
- [103] H. Zhao and E. S. G. Shaqfeh. Shear-induced platelet margination in a microchannel. *Phys. Rev. E*, 83(6), 2011.
- [104] A. Kumar, R. G. Henriquez Rivera, and M. D. Graham. Flow-induced segregation in confined multicomponent suspensions: effects of particle size and rigidity. *J. Fluid Mech.*, 738:423–462, 2014.
- [105] R. G. Henriquez Rivera, K. Sinha, and M. D. Graham. Margination regimes and drainage transition in confined multicomponent suspensions. *Phys. Rev. Lett.*, 114, 2015.
- [106] K. B. Abbitt and G. B. Nash. Characteristics of leucocyte adhesion directly observed in flowing whole blood in vitro. *Brit. J. Haematol.*, 112:55–63, 2001.

- [107] K. B. Abbitt and G. B. Nash. Rheological properties of the blood influencing selectin-mediated adhesion of flowing leukocytes. *Am. J. Physiol Heart Circ. Physiol.*, 285:H229–H240, 2003.
- [108] R. J. Melder, L. L. Munn, S. Yamada, C. Ohkubo, and R. K. Jain. Selectin- and integrin-mediated T-lymphocyte rolling and arrest in TNF-alpha-activated endothelium: augmentation by erythrocytes. *Biophys. J.*, 69:2131–2138, 1995.
- [109] M. H. Y. Chang, C. T. Hua, E. L. Isaac, T. Litjens, G. Hodge, L. E. Karageorgos, and P. J. Meikle. Transthyretin interacts with the lysosome-associated membrane protein (LAMP.1) in circulation. *Biochem. J.*, 382:481–489, 2004.
- [110] A. H. G. Isfahani and J. B. Freund. Forces on a wall-bound leukocyte in a small vessel due to red cells in the blood stream. *Biophys. J.*, 103:1604–1615, 2012.
- [111] M. Koistinaho and J. Koistinaho. Interactions between Alzheimer Rs disease and cerebral ischemia Wfocus on inflammation. *Brain Res. Brain Res. Rev.*, 48(2):240–250, 2005.
- [112] C. Iadecola and M. Alexander. Cerebral ischemia and inflammation. *Curr. Opin. Neurol.*, 14(1):89–94, 2001.
- [113] G. J. del Zoppo. Microvascular responses to cerebral ischemia/inflammation. *Ann. N.Y. Acad. Sci.*, 823:132–147, 1997.
- [114] Q. Li, S. Withoff, and I. M. Verma. Inflammation-associated cancer: NF- $\kappa\beta$ is the lynchpin. *Trends Immunol.*, 26:318–325, 2005.
- [115] M. Karin and F. R. Greten. NF- $\kappa\beta$: linking inflammation and immunity to cancer development and progression. *Nat. Rev. Immunol.*, 5:749–759, 2005.
- [116] M. Philip, D. A. Rowley, and H. Schreiber. Inflammation as a tumor promoter in cancer induction. *Nat. Rev. Immunol.*, 14:433–439, 2004.
- [117] T. Sturmer, H. Brenner, W. Koenig, and K. P. Gunther. Severity and extent of osteoarthritis and low grade systemic inflammation as assessed by high sensitivity c reactive protein. *Ann. Rheum. Dis.*, 63:200–205, 2004.
- [118] M. J. Benito, D. J. Veale, O. FitzGerald, W. B. van den Berg, and B. Bresnihan. Synovial tissue inflammation in early and late osteoarthritis. *Ann. Rheum. Dis.*, 64:1263–1267, 2005.
- [119] H. H. Lipowsky. Microvascular rheology and hemodynamics. *Microcirculation*, 12:5–15, 2005.
- [120] H. H. Lipowsky, S. Kovalcheck, and B. W. Zweifach. The distribution of blood rheological parameters in the microcirculation of cat mesentery. *Circ. Res.*, 43:738–749, 1978.
- [121] E. W. Merrill. Rheology of blood. *Physio. Rev.*, 49(4):863–888, 1969.
- [122] G. B. Thurston. Viscoelasticity of human blood. *Biophys. J.*, 12(9):1205–1217, 1972.
- [123] E. W. Merrill, C. S. Cheng, and G. A. Pelletier. Yield stress of normal human blood as a function of endogenous fibrinogen. *J. App. Physio.*, 26(1):1–3, 1969.
- [124] C. Picart, J.-M. Piau, H. Galliard, and P. Carpentier. Human blood shear yield stress and its hematocrit dependence. *J. Rheol.*, 42(1):1–12, 1998.

- [125] A. S. Popel, S. A. Regirer, and P. I. Usick. A continuum model of blood flow. *Biorheology*, 11(6):427, 1974.
- [126] D. Quemada. A non-linear Maxwell model of biofluids: application to normal blood. *Biorheology*, 30(3-4):253–265, 1993.
- [127] M. Anand and K. R. Rajagopal. A shear-thinning viscoelastic fluid model for describing the flow of blood. *Int. J. Cardiovasc. Med. Sci*, 4(2):59–68, 2004.
- [128] JS Kennedy. On the application of a constitutive equation for whole human blood. *J. Biomech. Eng.*, 112:199, 1990.
- [129] T. Ishikawa, L. F. R. Guimaraes, S. Oshima, and R. Yamane. Effect of non-Newtonian property of blood on flow through a stenosed tube. *Fluid dynamics research*, 22(5):251–264, 1998.
- [130] J. Fang and R. G. Owens. Numerical simulations of pulsatile blood flow using a new constitutive model. *Biorheology*, 43(5):637–660, 2006.
- [131] R. P. Vito and S. A. Dixon. Blood vessel constitutive models-1995–2002. *Ann. Rev. Biomed. Eng.*, 5(1):413–439, 2003.
- [132] S. H. Bryngelson and J. B. Freund. Buckling and its effect on the confined flow of a model capsule suspension. *Rheol. Acta*, 2016.
- [133] T. Krüger, B. Kaoui, and J. Harting. Interplay of inertia and deformability on rheological properties of a suspension of capsules. *J. Fluid Mech.*, 751:725–745, 2014.
- [134] M. Gross, T. Krüger, and F. Varnik. Rheology of dense suspensions of elastic capsules: normal stresses, yield stress, jamming and confinement effects. *Soft Matter*, 10(24):4360–4372, 2014.
- [135] A. Lamura and G. Gompper. Dynamics and rheology of vesicle suspensions in wall-bounded shear flow. *Europhys. Lett.*, 102(2):28004, 2013.
- [136] P. Bagchi and R. M. Kalluri. Rheology of a dilute suspension of liquid-filled elastic capsules. *Phys. Rev. E*, 81(056320), 2010.
- [137] S. H. Bryngelson and J. B. Freund. Stability of red blood cell trains. *in prep.*
- [138] R. Skalak and P. I. Branemark. Deformation of red blood cells in capillaries. *Science*, 164:717–719, 1969.
- [139] A. R. Pries and T. W. Secomb. Rheology of the microcirculation. *Clin. Hemorheol. Microcirc.*, 29:143–148, 2003.
- [140] G. Tomaiuolo, M. Simeone, V. Martinelli, B. Rotoli, and S. Guido. Red blood cell deformation in microconfined flow. *Soft Matter*, 5(3736), 2009.
- [141] J. L. McWhirter, H. Noguchi, and G. Gompper. Deformation and clustering of red blood cells in microcapillary flows. *Soft Matter*, 7:10967–10977, 2011.
- [142] H. Noguchi and G. Gompper. Shape transitions of fluid vesicles and red blood cells in capillary flows. *Proc. Nat. Acad. Sci.*, 102(40):14159–14164, 2005.
- [143] T. W. Secomb, R. Skalak, N. Ozkaya, and J. F. Gross. Flow of axisymmetric red blood cells in narrow capillaries. *J. Fluid Mech.*, 163:405–423, 1986.
- [144] J. B. Freund and M. M. Orescanin. Cellular flow in a small blood vessel. *J. Fluid Mech.*, 671:466–490, 2011.

- [145] J. L. McWhirter, H. Noguchi, and G. Gompper. Ordering and arrangement of deformed red blood cells in flow through microcapillaries. *New J. Phys.*, 14:085026, 2012.
- [146] P. Gaehtgens, C. Duhrssen, and K. H. Albrecht. Motion, deformation, and interaction of blood cells and plasma during flow through narrow capillary tubes. *Blood Cells*, 6:799–812, 1980.
- [147] T. M. Griffith. Temporal chaos in the microcirculation. *Cardiovasc. Res.*, 31:342–358, 1996.
- [148] K. D. Barclay, G. A. Klassen, and C. Young. A method for detecting chaos in canine myocardial microcirculatory red cell flux. *Microcirculation*, 7(5):335–346, 2000.
- [149] D. A. Fedosov, M. Dao, G. E. Karniadakis, and S. Suresh. Computational biorheology of human blood flow in health and disease. *Ann. Biomed. Eng.*, 42(2):368–387, 2013.
- [150] H. Aref. Stirring by chaotic advection. *J. Fluid Mech.*, 143:1–21, 1984.
- [151] J. M. Ottino. *The Kinematics of Mixing: Stretching, Chaos and Transport*. Cambridge University Press, 1989.
- [152] K. Bajer and H. K. Moffatt. On a class of steady confined Stokes flows with chaotic streamlines. *J. Fluid Mech.*, 212:337–363, 1990.
- [153] H. A. Stone, A. Nadim, and S. H. Strogatz. Chaotic streamlines inside drops immersed in steady Stokes flows. *J. Fluid Mech.*, 232:82–46, 1991.
- [154] D. Kroujiline and H. A. Stone. Chaotic streamlines in steady bounded three-dimensional Stokes flows. *Physica D*, 130:105–132, 1999.
- [155] T. Dombre, U. Frisch, J. M. Greene, M. Henon, A. Mehr, and A. M. Soward. Chaotic streamlines in the abc flows. *J. Fluid Mech.*, 167:353–391, 1986.
- [156] I. M. Jánosi, T. Tél, D. E. Wolf, and J. A. C. Gallas. Chaotic particle dynamics in viscous flows: The three-particle Stokeslet problem. *Phys. Rev. E*, 56(3):2858–2868, 1997.
- [157] T. Mullin, Y. Li, C. Del Pino, and J. Ashmore. An experimental study of fixed points and chaos in the motion of spheres in a Stokes flow. *IMA J. App. Math.*, 70:666–676, 2005.
- [158] S. H. Bryngelson and J. B. Freund. Capsule-train stability. *Phys. Rev. Fluids*, 1(033201), 2016.
- [159] C. Pozrikidis. *Boundary Integral and Singularity Methods for Linearized Viscous Flow*. Cambridge University Press, 1992.
- [160] A. S. Popel. Theory of oxygen transport to tissue. *Crit. Rev. Biomed. Eng.*, 17:257–321, 1989.
- [161] C. Pozrikidis. Numerical simulation of blood flow through microvascular capillary networks. *B. Math. Biol.*, 71:1520–1541, 2009.
- [162] C. Alonso, A. R. Pries, O. Kiesslich, D. Lerche, and P. Gaehtgens. Transient rheological behavior of blood in low-shear tube flow: velocity profile and effective viscosity. *Am. J. Physiol. Heart Circ. Physiol.*, 268:25–32, 1995.
- [163] M. Soutani, Y. Suzuki, and N. Maeda. Quantitative evaluation of flow dynamics of erythrocytes in microvessels: influence of erythrocyte aggregation. *Am. J. Physiol. Heart Circ. Physiol.*, 268:H1959–H1965, 1995.

- [164] S. Kim, P. K. Ong, O. Yalcin, M. Intaglietta, and P. C. Johnson. The cell-free layer in microvascular blood flow. *Biorheology*, 46:181–189, 2009.
- [165] J. B. Freund. Leukocyte margination in a model microvessel. *Phys. Fluids*, 19(023301), 2007.
- [166] J. B. Freund, J. Goetz, K. Hill, and J. Vermot. Fluid flows and forces in development: functions, features and biophysical principles. *Development*, 139:1229–1245, 2012.
- [167] T. W. Secomb, J. P. Alberding, R. Hsu, M. W. Dewhirst, and A. R. Pries. Angiogenesis: An adaptive dynamic biological patterning problem. *PLOS Comput. Biol.*, 9(3), 2013.
- [168] J. B. Freund and J. Vermot. The wall-stress footprint of blood cells flowing in microvessels. *Biophys. J.*, 106(3):752–762, 2014.
- [169] F. Boselli, J. B. Freund, and J. Vermot. Blood flow mechanics in cardiovascular development. *Cell. Mol. Life Sci.*, 72(3):2545–2559, 2015.
- [170] P. Koumoutsakos, I. Pivkin, and F. Milde. The fluid mechanics of cancer and its therapy. *Annu. Rev. Fluid Mech.*, 45:325–355, 2013.
- [171] C. Galligan, J. Nichols, E. Kvam, P. Spooner, R. Gettings, L. Zhu, and C. M. Puleo. Mesoscale blood cell sedimentation for processing milliliter sample volumes. *Lab. Chip.*, 15:3274–3277, 2015.
- [172] N. Xiang and Z. Ni. High-throughput blood cell focusing and plasma isolation using spiral inertial microfluidic devices. *Biomed. Microdevices*, 17(6), 2015.
- [173] J. Choi, J. Hyun, and S. Yang. On-chip extraction of intracellular molecules in white blood cells from whole blood. *Sci. Rep.*, 5(15167), 2005.
- [174] M. Abkarian, M. Faivre, R. Horton, K. Smistrup, and C.A. Best-Popescu. Cellular-scale hydrodynamics. *Biomed. Mater.*, 3(034011), 2008.
- [175] M. Toner and D. Irimia. Blood-on-a-chip. *Ann. Rev. Biomed. Eng.*, 7:77–103, 2005.
- [176] J. Kim, M. Massoudi, J. F. Antaki, and A. Gandini. Removal of malaria-infected red blood cells using magnetic cell separators: a computational study. *Appl. Math. Comput.*, 218(6841-50), 2012.
- [177] J. M. Crowley. Viscosity-induced instability of a one-dimensional lattice of falling spheres. *J. Fluid Mech.*, 45:151–159, 1971.
- [178] L. M. Hocking. The behavior of clusters of spheres falling in a viscous fluid. *J. Fluid Mech.*, 20:129, 1964.
- [179] M. R. Maxey and B. K. Patel. Localized force representations for particles sedimenting in Stokes flow. *Int. J. Multiphase Flow*, 27:1603–1626, 2001.
- [180] S. L. Goren. Resistance and stability of a line of particles moving near a wall. *J. Fluid Mech.*, 132:185–196, 1983.
- [181] T. Beatus, T. Thusty, and R. Bar-Ziv. Phonons in a one-dimensional microfluidic crystal. *Nat. Phys.*, 2:743–748, 2006.
- [182] J. Fleury, U. D. Schiller, S. Thutupalli, G. Gompper, and R. Seemann. Mode coupling of phonons in a dense one-dimensional microfluidic crystal. *New J. Phys.*, 16:063029, 2014.
- [183] S. Kuriakose and P. Dimitrakopoulos. Deformation of an elastic capsule in a rectangular microfluidic channel. *Soft Matter*, 9(16):4284–4296, 2013.

- [184] T. Beatus, R. Bar-Ziv, and T. Tlusty. Anomalous microfluidic phonons induced by the interplay of hydrodynamic screening and incompressibility. *Phys. Rev. Lett.*, 99(124502), 2007.
- [185] T. Beatus, R. H. Bar-Ziv, and T. Tlusty. The physics of 2d microfluidic droplet ensembles. *Phys. Rep.*, 516:103–145, 2012.
- [186] U. D. Schiller, J. Fleury, R. Seemann, and G. Gompper. Collective waves in dense and confined microfluidic droplet arrays. *Soft Matter*, 11:5850–5861, 2015.
- [187] M. F. Goosen, G. M. O’Shea, H. M. Gharapetian, S. Chou, and A. M. Sun. Optimization of microencapsulation parameters: semipermeable microcapsules as a bioartificial pancreas. *Biotechnol. Bioeng.*, 27(2):146–150, 1985.
- [188] O. Gåserød, A. Sannes, and G. Skjåk-Bræk. Microcapsules of alginate–chitosan. ii. a study of capsule stability and permeability. *Biomaterials*, 20(8):773–783, 1999.
- [189] A. F. Groboillot, C. P. Champagne, G. D. Darling, D. Poncelet, and R. J. Neufeld. Membrane formation by interfacial cross-linking of chitosan for microencapsulation of *Lactococcus lactis*. *Biotechnol. Bioeng.*, 42(10):1157–1163, 1993.
- [190] C. Dupont, A.-V. Salsac, and D. Barthès-Biesel. Off-plane motion of a prolate capsule in shear flow. *J. Fluid Mech.*, 721:180–198, 2013.
- [191] D. Cordasco and P. Bagchi. Orbital drift of capsules and red blood cells in shear flow. *Phys. Fluids*, 25(091902), 2013.
- [192] Z. Wang, Y. Sui, P. D. M. Spelt, and W. Wang. Three-dimensional dynamics of oblate and prolate capsules in shear flow. *Phys. Rev. E*, 88(053021), 2013.
- [193] S. Ramanujan and C. Pozrikidis. Deformation of liquid capsules enclosed by elastic membranes in simple shear flow: large deformations and the effect of capsule viscosity. *J. Fluid Mech.*, 361:117–143, 1998.
- [194] S. Kessler, R. Finken, and U. Seifert. Swinging and tumbling of elastic capsules in shear flow. *J. Fluid Mech.*, 605:207–226, 2008.
- [195] Y. Sui, H. T. Low, Y. T. Chew, and P. Roy. Tank-treading, swinging, and tumbling of liquid-filled elastic capsules in shear flow. *Phys. Rev. E*, 77(1):016310, 2008.
- [196] P. Bagchi and R. M. Kalluri. Dynamics of nonspherical capsules in shear flow. *Phys. Rev. E*, 80(1):016307, 2009.
- [197] D. V. Le and Z. Tan. Large deformation of liquid capsules enclosed by thin shells immersed in the fluid. *J. Comp. Phys.*, 229:4097–4116, 2010.
- [198] J. Walter, A.-V. Salsac, and D. Barthès-Biesel. Ellipsoidal capsules in simple shear flow: prolate versus oblate initial shapes. *J. Fluid Mech.*, 676:318–347, 2011.
- [199] S. R. Keller and R. Skalak. Motion of a tank-treading ellipsoidal particle in a shear flow. *J. Fluid Mech.*, 120:27–47, 1982.
- [200] C. Dupont, F. Delahaye, D. Barthès-Biesel, and A.-V. Salsac. Stable equilibrium configurations of an oblate capsule in simple shear flow. *J. Fluid Mech.*, 791:738–757, 2016.
- [201] A. Walter, H. Rehage, and H. Leonhard. Shear induced deformation of microcapsules: shape oscillations and membrane folding. *Colloid Surf.*, 183–185:123–132, 2001.

- [202] T. M. S. Chang. Future generations of red blood cell substitutes. *J. Intl Med.*, 253:527–535, 2003.
- [203] M. Abkarian, M. Faivre, and A. Viallat. Swinging of red blood cells under shear flow. *Phys. Rev. Lett.*, 98(188302), 2007.
- [204] M. Abkarian and A. Viallat. Vesicles and red blood cells in shear flow. *Soft Matter*, 4:653–657, 2008.
- [205] T. Fischer and R. Korzeniewski. Threshold shear stress for the transition between tumbling and tank-treading of red blood cells in shear flow: dependence on the viscosity of the suspending medium. *J. Fluid Mech.*, 736:351–365, 2013.
- [206] M. Bitbol. Red blood cell orientation in orbit $c = 0$. *Biophys. J.*, 49:1055–1068, 1986.
- [207] J. Dupire, M. Socol, and A. Viallat. Full dynamics of a red blood cell in shear flow. *Proc. Natl Acad. Sci.*, 109(51):20808–20813, 2012.
- [208] W. Yao, Z. Wen, Z. Yan, D. Sun, W. Ka, L. Zie, and S. Chien. Low viscosity extacytometry and its validation tested by flow chamber. *J. Biomech.*, 34:1501–1509, 2001.
- [209] H. Zhao and E. S. G. Shaqfeh. The shape stability of a lipid vesicle in a uniaxial extensional flow. *J. Fluid Mech.*, 719:345–361, 2013.
- [210] J. Einarsson, J. R. Angilella, and B. Mehlig. Orientational dynamics of weakly inertial axisymmetric particles in steady viscous flow. *Physica D*, 278-279:79–85, 2014.
- [211] S. H. Bryngelson and J. B. Freund. Stability of a spherical capsule in large amplitude oscillatory extension. *in prep.*
- [212] J. G. Nam, K. Hyun, K. H. Ahn, and S. J. Lee. Prediction of normal stresses under large amplitude oscillatory shear flow. *J. Non-Newtonian Fluid Mech.*, 150(1-10), 2008.
- [213] D. Chopra, D. Vlassopoulos, and S. G. Hatzikiriakos. Nonlinear rheological response of phase separating polymer blends: Poly-(styrene-co-maleic anhydride)/poly(methyl methacrylate). *J. Rheol.*, 44:27–45, 2000.
- [214] B. Debbaut and H. Burhin. Large amplitude oscillatory shear and Fourier-transform rheology for a high-density polyethylene. *J. Rheol.*, 46(1155), 2002.
- [215] C. O. Klein, H. W. Spiess, A. Calin, C. Balan, and M. Wilhelm. Separation of the nonlinear oscillatory response into a superposition of linear, strain hardening, strain softening, and wall slip response. *Macromolecules*, 40:4250–4259, 2007.
- [216] P. C. Sousa, J. Carneiro, R. Vaz, A. Cerejo, F. T. Pinho, M. A. Alves, and M. S. N. Oliveira. Shear viscosity and nonlinear behavior of whole blood under large amplitude oscillatory shear. *Biorheology*, 50(5-6):269–282, 2013.
- [217] G. Tomaiuolo, A. Carciati, S. Caserta, and S. Guido. Blood linear viscoelasticity by small amplitude oscillatory flow. *Rheol. Acta*, 55(6):485–495, 2016.
- [218] G. H. McKinley and T. Sridhar. Filament-Stretching Rheometry of Complex Fluids. *Annu. Rev. Fluid Mech.*, 34:375–415, 2002.
- [219] H. K. Rasmussen, P. Laillè, and K. Yu. Large amplitude oscillatory elongation flow. *Rheol. Acta*, 47:97–103, 2008.
- [220] A. G. Bejenariu, H. K. Rasmussen, A. L. Skov, O. Hassager, and S. M. Frankaer. Large amplitude oscillatory extension of soft polymeric networks. *Rheol. Acta*, 49:807–814, 2010.

- [221] S. J. Haward, M. S. N. Oliveira, M. A. Alves, and G. H. McKinley. Optimized cross-slot flow geometry for microfluidic extensional rheometry. *Phys. Rev. Lett.*, 109:1–5, 2012.
- [222] S. J. Haward, V. Sharma, and J. A. Odell. Extensional opto-rheometry with biofluids and ultra-dilute polymer solutions. *Soft Matter*, 7(9908), 2011.
- [223] S. J. Haward, J. A. Odell, Z. Li, and X. F. Yuan. Extensional rheology of dilute polymer solutions in oscillatory cross-slot flow: The transient behavior of birefringent strands. *Rheol. Acta*, 49:633–645, 2010.
- [224] J. A. Odell and S. P. Carrington. Extensional flow oscillatory rheometry. *J. Non-Newtonian Fluid Mech.*, 137:110–120, 2006.
- [225] Y. Zhou and C. M. Schroeder. Transient and average unsteady dynamics of single polymers in large-amplitude oscillatory extension. *Macromolecules*, 49(8018-8030), 2016.
- [226] Y. Zhou and C. M. Schroeder. Single polymer dynamics under large amplitude oscillatory extension. *Phys. Rev. Fluids*, 1(053301), 2016.
- [227] V. Narsimhan, A. P. Spann, and E. S. G. Shaqfeh. The mechanism of shape instability for a vesicle in extensional flow. *J. Fluid Mech.*, 750:144–190, 2014.
- [228] V. Narsimhan, A. P. Spann, and E. S. G. Shaqfeh. Pearlring, wrinkling, and buckling of vesicles in elongational flows. *J. Fluid Mech.*, 777:1–26, 2015.
- [229] J. B. Dahl, V. Narsimhan, B. Gouveia, S. Kumar, E. S. G. Shaqfeh, and S. J. Muller. Experimental observation of the asymmetric instability of intermediate-reduced-volume vesicles in extensional flow. *Soft Matter*, 12(3787), 2016.
- [230] L. Guillou, J. B. Dahl, J. G. Lin, A. I. Barakat, J. Husson, S. J. Muller, and S. Kumar. Measuring cell viscoelastic properties using a microfluidic extensional flow device. *Biophys. J.*, 111:2039–2050, 2016.
- [231] J. Dupire, M. Abkarian, and A. Viallat. Chaotic dynamics of red blood cells in a sinusoidal flow. *Phys. Rev. Lett.*, 104(168101), 2010.
- [232] L. Zhu, J. Rabault, and L. Brandt. The dynamics of a capsule in a wall-bounded oscillating shear flow. *Phys. Fluids*, 27(071902), 2015.
- [233] D. Cordasco and P. Bagchi. Dynamics of red blood cells in oscillating shear flow. *J. Fluid Mech.*, 800:484–516, 2016.
- [234] P. J. Schmid. Nonmodal stability theory. *Annu. Rev. Fluid Mech.*, 39:129–162, 2007.
- [235] P. J. Schmid and D. S. Henningson. *Stability and Transition in Shear Flows*. Springer Science and Business Media, 2012.
- [236] M. Zhang, F. Martinelli, J. Wu, P. J. Schmid, and M. Quadrio. Modal and non-modal stability analysis of electrohydrodynamic flow with and without cross-flow. *J. Fluid Mech.*, 770:319–349, 2015.
- [237] S. C. Reddy and D. S. Henningson. Energy growth in viscous channel flows. *J. Fluid Mech.*, 252:209–238, 1993.
- [238] L. Brandt, C. Cossu, J. M. Chomaz, P. Huerre, and D. S. Henningson. On the convectively unstable nature of optimal streaks in boundary layers. *J. Fluid Mech.*, 485:221–242, 2003.

- [239] P. Corbett. *Nonmodal growth in boundary layers and its optimal control*. PhD thesis, Ecole Polytech. Fed. Lausanne (EPFL), Lausanne, Switz., 2000.
- [240] D. Obrist and P. J. Schmid. On the linear stability of swept attachment-line boundary layer flow. Part 2. Non-modal effects and receptivity. *J. Fluid Mech.*, 493:31–58, 2003.
- [241] M. R. Jovanovic and S. Kumar. Nonmodal amplification of stochastic disturbances in strongly elastic channel flows. *J. Non-Newtonian Fluid Mech.*, 166:755–778, 2011.
- [242] J. Klinkenberg, H.C. de Lange, and L. Brandt. Modal and non-modal stability of particle-laden channel flow. *Phys. Fluids*, 23(064110), 2011.
- [243] G. H. McKinley. *Transport Processes in Bubbles, Drops & Particles*, chapter Steady and Transient Motion of Spherical Particles in Viscoelastic Liquids. CRC Press, 2 edition, 2002.
- [244] H. M. Blackburn and J. M. Lopez. The onset of three-dimensional standing and modulated travelling waves in a periodically driven cavity flow. *J. Fluid Mech.*, 497:289–317, 2003.
- [245] W. Cazemier, R. W. C. P. Verstappen, and A. E. P. Veldman. Proper orthogonal decomposition and low-dimensional models for driven cavity flows. *Phys. Fluids*, 10(7):1685–1699, 1998.
- [246] J. J. Leung, A. H. Hirsa, H. M. Blackburn, F. Marques, and J. M. Lopez. Three-dimensional modes in a periodically driven elongated cavity. *Phys. Rev. E*, 71(026305), 2005.
- [247] P. J. Blennerhassett and A. P. Bassom. The linear stability of high-frequency oscillatory flow in a channel. *J. Fluid Mech.*, 556:1–25, 2006.
- [248] C. Thomas, A. P. Bassom, and P. J. Blennerhassett. The linear stability of oscillating pipe flow. *Phys. Fluids*, 24(014106), 2012.
- [249] C. Thomas, A. P. Bassom, P. J. Blennerhassett, and C. Davies. The linear stability of oscillatory Poiseuille flow in channels and pipes. *Proc. R. Soc. Lond. A*, 467:2643–2662, 2011.
- [250] P. J. Blennerhassett and A. P. Bassom. The linear stability of high-frequency oscillatory flow in a torsionally oscillating cylinder. *J. Fluid Mech.*, 576:491–505, 2007.
- [251] G. J. Sheard, M. C. Thompson, and K. Hourigan. From spheres to circular cylinders: The stability and flow structures of bluff ring wakes. *J. Fluid Mech.*, 492:147, 2003.
- [252] G. J. Sheard, M. C. Thompson, and K. Hourigan. From spheres to circular cylinders: Non-axisymmetric transitions in the flow past rings. *J. Fluid Mech.*, 506:45, 2004.
- [253] G. J. Sheard, M. J. Fitzgerald, and K. Ryan. Cylinders with square crosssections: Wake instabilities with incidence angle variation. *J. Fluid Mech.*, 630:43, 2009.
- [254] D. Barkley and R. D. Henderson. Three-dimensional Floquet stability analysis of the wake of a circular cylinder. *J. Fluid Mech.*, 322:215–241, 1996.
- [255] R. D. Henderson and D. Barkley. Secondary instability in the wake of a circular cylinder. *Phys. Fluids*, 8(6):1683–1685, 1996.
- [256] R. S. Gioria, P. J. S. Jabardo, B. S. Carmo, and J. R. Meneghini. Floquet stability analysis of the flow around an oscillating cylinder. *J. Fluid. Struct.*, 25:676–686, 2009.

- [257] B. Pier and P. J. Schmid. Linear and nonlinear dynamics of pulsatile channel flow. *J. Fluid Mech.*, 815:435–480, 2017.
- [258] C. H. Von Kerczek. The instability of oscillatory plane Poiseuille flow. *J. Fluid Mech.*, 116:91–114, 1982.
- [259] B. L. Rozhdestvenskii, I. N. Simakin, and M. I. Stoinov. Investigation of the stability of a pulsating Poiseuille flow in a planar channel. *USSR Comput. Math. Phys.*, 29:65–73, 1989.
- [260] F. Fedele, D. L. Hitt, and R. D. Prabhu. Revisiting the stability of pulsatile pipe flow. *Eur. J. Mech. B-Fluid.*, 24:237–254, 2005.
- [261] C. Davies, C. Thomas, A. P. Bassom, and P. J. Blennerhassett. The linear impulse response of disturbances in an oscillatory Stokes layer. *Procedia IUTAM*, 14:381–384, 2015.
- [262] P. J. Blennerhassett and A. P. Bassom. The linear stability of flat Stokes layers. *J. Fluid Mech.*, 464:393–410, 2002.
- [263] C. Thomas, A. P. Bassom, P. J. Blennerhassett, and C. Davies. Direct numerical simulations of small disturbances in the classical Stokes layer. *J. Eng. Math.*, 68:327–338, 2010.
- [264] C. Thomas, P. J. Blennerhassett, A. P. Bassom, and C. Davies. The linear stability of a Stokes layer subjected to high-frequency perturbations. *J. Fluid Mech.*, 764:193–218, 2015.
- [265] C. Thomas, C. Davies, A. P. Bassom, and P. J. Blennerhassett. Evolution of disturbance wavepackets in an oscillatory Stokes layer. *J. Fluid Mech.*, 752:543–571, 2014.
- [266] S. Sirisup and G. E. Karniadakis. A spectral viscosity method for correcting the long-term behavior of pod models. *J. Comp. Phys.*, 194(1):92–116, 2004.
- [267] T. Pumhössel, P. Hehenberger, and K. Zeman. Reduced-order modeling of self-excited, time-periodic systems using the method of proper orthogonal decomposition and the Floquet theory. *Math. Comp. Mod. Dyn. Sys.*, 20(6):528–545, 2014.
- [268] P. J. Schmid. Dynamic mode decomposition of numerical and experimental data. *J. Fluid Mech.*, 656:5–28, 2010.
- [269] S. Bagheri. Koopman-mode decomposition of the cylinder wake. *J. Fluid Mech.*, 726:596–623, 2013.
- [270] C. W. Rowley, I. Mezic, S. Bagheri, P. Schlatter, and D. S. Henningson. Spectral analysis of nonlinear flows. *J. Fluid Mech.*, 641:115–127, 2009.
- [271] J. Li, M. Dao, C. T. Lim, and S. Suresh. Spectrin-level modeling of the cytoskeleton and optical tweezers stretching of the erythrocyte. *Biophys. J.*, 88(5):3707–3719, 2005.
- [272] M. M. Dupin, I. Halliday, C. M. Care, L. Alboul, and L. L. Munn. Modeling the flow of dense suspensions of deformable particles in three dimensions. *Phys. Rev. E*, 75(6):066707, 2007.
- [273] M. Dao, J. Li, and S. Suresh. Molecularly based analysis of deformation of spectrin network and human erythrocyte. *Mat. Sci. Eng. C*, 26(8):1232–1244, 2006.
- [274] R. Waugh and E. A. Evans. Thermoelasticity of red blood cell membrane. *Biophys. J.*, 26(1):115–131, 1979.

- [275] I. V. Pivkin and G. E. Karniadakis. Accurate coarse-grained modeling of red blood cells. *Phys. Rev. Lett.*, 101(11):118105, 2008.
- [276] D. E. Discher, D. H. Boal, and S. K. Boey. Simulations of the erythrocyte cytoskeleton at large deformation. II. Micropipette aspiration. *Biophys. J.*, 75(3):1584–1597, 1998.
- [277] D. A. Fedosov, H. Lei, B. Caswell, S. Suresh, and G. E. Karniadakis. Multiscale modeling of red blood cell mechanics and blood flow in malaria. *PLOS Comput. Bio.*, 7(12):e1002270, 2011.
- [278] D. A. Reasor, J. R. Clausen, and C. K. Aidun. Coupling the lattice-Boltzmann and spectrin-link methods for the direct numerical simulation of cellular blood flow. *Int. J. Numer. Methods Fluids*, 68(6):767–781, 2012.
- [279] E. A. Evans and P. L. La Celle. Intrinsic material properties of the erythrocyte membrane indicated by mechanical analysis of deformation. *Blood*, 45(1):29–43, 1975.
- [280] E. A. Evans and R. Waugh. Osmotic correction to elastic area compressibility measurements on red cell membrane. *Biophys. J.*, 20(3):307–313, 1977.
- [281] M. Dao, C. T. Lim, and S. Suresh. Mechanics of the human red blood cell deformed by optical tweezers. *J. Mech. Phys. Solids*, 51(11):2259–2280, 2003.
- [282] J. P. Mills, L. Qie, M. Dao, C. T. Lim, and S. Suresh. Nonlinear elastic and viscoelastic deformation of the human red blood cell with optical tweezers. *MCB-Tech Sci. Press*, 1:169–180, 2004.
- [283] S. Suresh. Mechanical response of human red blood cells in health and disease: some structure-property-function relationships. *J. Mat. Res.*, 21(8):1871–1877, 2006.
- [284] S. Suresh. Biomechanics and biophysics of cancer cells. *Acta Materialia*, 55(12):3989–4014, 2007.
- [285] S. Piomelli and C. Seaman. Mechanism of red blood cell aging: relationship of cell density and cell age. *Am. J. Hematology*, 42(1):46–52, 1993.
- [286] S. S. Segal. Regulation of blood flow in the microcirculation. *Microcirculation*, 12(1):33–45, 2005.
- [287] A. W. L. Jay. Viscoelastic properties of the human red blood cell membrane: I. Deformation, volume loss, and rupture of red cells in micropipettes. *Biophys. J.*, 13(11):1166–1182, 1973.
- [288] E. Evans and R. M. Hochmuth. A solid-liquid composite model of the red cell membrane. *J. Membrane Bio.*, 30(1):351–362, 1976.
- [289] E. A. Evans and R. M. Hochmuth. Membrane viscoplastic flow. *Biophys. J.*, 16(1):13–26, 1976.
- [290] A. H. G. Isfahani. *Forces on a wall-bound leukocyte due to flowing red blood cells*. PhD thesis, University of Illinois at Urbana-Champaign, 2011.
- [291] D. A. Fedosov, B. Caswell, and G. E. Karniadakis. A multiscale red blood cell model with accurate mechanics, rheology, and dynamics. *Biophys. J.*, 98(10):2215–2225, 2010.
- [292] R. Tran-Son-Tay, S. P. Sutera, and P. R. Rao. Determination of red blood cell membrane viscosity from rheoscopic observations of tank-treading motion. *Biophys. J.*, 46(1):65–72, 1984.

- [293] N. Wang and D. E. Ingber. Probing transmembrane mechanical coupling and cytomechanics using magnetic twisting cytometry. *Biochem. Cell Bio.*, 73(7-8):327–335, 1995.
- [294] Y. Park, C. A. Best, K. Badizadegan, R. R. Dasari, M. S. Feld, T. Kuriabova, M. L. Henle, A. J. Levine, and G. Popescu. Measurement of red blood cell mechanics during morphological changes. *Proc. Nat. Acad. Sci.*, 107(15):6731–6736, 2010.
- [295] M. Arroyo and A. DeSimone. Relaxation dynamics of fluid membranes. *Phys. Rev. E*, 79(3):031915, 2009.
- [296] D. Barthès-Biesel, A. Diaz, and E. Dhenin. Effect of constitutive laws for two-dimensional membranes on flow-induced capsule deformation. *J. Fluid Mech.*, 460:211–222, 2002.
- [297] E. Lac, D. Barthès-Biesel, N. A. Pelekasis, and J. Tsamopoulos. Spherical capsules in three-dimensional unbounded Stokes flows: effect of the membrane constitutive law and onset of buckling. *J. Fluid Mech.*, 516:303–334, 2004.
- [298] C. D. Eggleton and A. S. Popel. Large deformation of red blood cell ghosts in a simple shear flow. *Phys. Fluids*, 10(8):1834–1845, 1998.
- [299] M. Carin, D. Barthès-Biesel, F. Edwards-Lévy, C. Postel, and D. C. Andrei. Compression of biocompatible liquid-filled HSA-alginate capsules: Determination of the membrane mechanical properties. *Biotechnol. Bioeng.*, 82(2):207–212, 2003.
- [300] M. Rachik, D. Barthès-Biesel, M. Carin, and F. Edwards-Levy. Identification of the elastic properties of an artificial capsule membrane with the compression test: effect of thickness. *J. Colloid Interface Sci.*, 301(1):217–226, 2006.
- [301] J. Cho, A. Kwon, and C. Cho. Microencapsulation of octadecane as a phase-change material by interfacial polymerization in an emulsion system. *Colloid Polym. Sci.*, 280(3):260–266, 2002.
- [302] E. N. Brown, M. R. Kessler, N. R. Sottos, and S. R. White. In situ poly (urea-formaldehyde) microencapsulation of dicyclopentadiene. *J. Microencapsul.*, 20(6):719–730, 2003.
- [303] R. Skalak, A. Tozeren, P. R. Zarda, and S. Chien. Strain energy function of red blood cell membranes. *Biophys. J.*, 13:245, 1973.
- [304] W. R. Dodson III and P. Dimitrakopoulos. Spindles, cusps, and bifurcation for capsules in Stokes flow. *Phys. Rev. Lett.*, 101(20):208102, 2008.
- [305] W. R. Dodson and P. Dimitrakopoulos. Dynamics of strain-hardening and strain-softening capsules in strong planar extensional flows via an interfacial spectral boundary element algorithm for elastic membranes. *J. Fluid Mech.*, 641:263–296, 2009.
- [306] A. Guckenberger and S. Gekle. Theory and algorithms to compute Helfrich bending forces: a review. *J. Phys.-Condens. Mat.*, (203001), 2017.
- [307] E. Evans and Y. Fung. Improved measurements of the erythrocyte geometry. *Microvasc. Res.*, 4(4):335–347, 1972.
- [308] J. C. Adams and P. N. Swarztrauber. SPHEREPACK 2.0: A model development facility. Technical Report NCAR/TN-436-STR, NCAR, 1997.
- [309] P. N. Swarztrauber and W. F. Spotz. Generalized discrete spherical harmonic transforms. *J. Comp. Phys.*, 159:213–230, 2000.

- [310] J. B. Freund and H. Zhao. *Hydrodynamics of Capsules and Biological Cells*, chapter A fast high-resolution boundary integral method for multiple interacting blood cells, pages 71–111. Chapman and Hall/CRC, Boca Raton, FL, 2010.
- [311] S. Kim and S. J. Karrila. *Microhydrodynamics: Principles and Selected Applications*. Butterworth-Heinemann, Boston, 1991.
- [312] J. M. Rallison and A. Acrivos. A numerical study of the deformation and burst of a viscous drop in an extensional flow. *J. Fluid Mech.*, 89:191–200, 1978.
- [313] D. Saintillan, E. Darve, and E. S. G. Shaqfeh. A smooth particle-mesh ewald algorithm for Stokes suspension simulations: the sedimentation of fibers. *Phys. Fluids*, 17(033301), 2005.
- [314] L. Greengard. *The Rapid Evaluation of Potential Fields in Particle Systems*. ACM distinguished dissertations. MIT Press, 1988.
- [315] O. P. Bruno and L. A. Kunyansky. A fast, high-order algorithm for the solution of surface scattering problems: Basic implementation, tests, and applications. *J. Comp. Phys.*, 169:80–110, 2001.
- [316] M. G. Duffy. Quadrature over a pyramid or cube of integrands with a singularity at a vertex. *SIAM J. Numer. Anal.*, 19(6):1260–1262, 1982.
- [317] Y. Saad and M. Schultz. A generalized minimal residual algorithm for solving nonsymmetric linear systems. *SIAM J. Sci. Stat. Comput.*, 7:856–869, 1985.
- [318] H. Wang, T. Lei, J. Li, J. Huang, and Z. Yao. A parallel fast multipole accelerated integral equation scheme for 3d Stokes equations. *Int. J. Numerical Methods Eng.*, 70(7):812–839, 2007.
- [319] O. L. Colombo. Numerical methods for harmonic analysis on the sphere. Scientific Report 7, United States Air Force, 1981.
- [320] L. Trefethen and M. Embree. *Spectra and Pseudospectra: The Behavior of Nonnormal Matrices and Operators*. Princeton: Princeton Univ. Press, 2005.
- [321] J. B. Freund. The flow of red blood cells through a narrow spleen-like slit. *Phys. Fluids*, 25(110807), 2013.
- [322] E. T. A. Mohamed, A. E. Kamanyi, M. Pluta, and W. Grill. Age-dependent acoustic and microelastic properties of red blood cells determined by vector contrast acoustic microscopy. *Microsc. Microanal.*, 18:436, 2012.
- [323] A. R. Williams and D. R. Morris. The internal viscosity of the human erythrocyte may determine its lifespan in vivo. *J. Haematol.*, 24(57), 1980.
- [324] G. D. O. Lowe, J. C. Barbenel, and C. D. Forbes. *Clinical Aspects of Blood Viscosity and Cell Deformability*. Springer Science & Business Media, 2012.
- [325] J. F. Bertles and P. F. A. Milner. Irreversibly sickled erythrocytes: a consequence of the heterogeneous distribution of hemoglobin types in sickle-cell anemia. *J. Clin. Invest.*, 47(8):1731–1741, 1968.
- [326] R. Anderson, M. Cassell, G. L. Mullinax, and H. Chaplin Jr. Effect of normal cells on viscosity of sickle-cell blood. *Arch. Intern. Med.*, 111:286–294, 1963.
- [327] L. Da Costa, J. Galimand, O. Fenneteau, and N. Mohandas. Hereditary spherocytosis, elliptocytosis, and other red cell membrane disorders. *Blood Rev.*, 27(4):167–178, 2013.

- [328] G. Tomaiuolo. Biomechanical properties of red blood cells in health and disease towards microfluidics. *Biomicrofluidics*, 8, 2014.
- [329] X. Li, P. M. Vlahovska, and G. E. Karniadakis. Continuum- and particle-based modeling of shapes and dynamics of red blood cells in health and disease. *Soft Matter*, 9:28–37, 2013.
- [330] U. Seifert and R. Lipowsky. *Handbook of Biological Physics*, volume 1, chapter Morphology of Vesicles, pages 403–462. Elsevier Science B.V., 1995.
- [331] D. Barthès-Biesel. Capsule motion in flow: Deformation and membrane buckling. *C. R. Physique*, 10:764–774, 2009.
- [332] E. Foessel, J. Walter, A.-V. Salsac, and D. Barthès-Biesel. Influence of internal viscosity on the large deformation and buckling of a spherical capsule in simple shear flow. *J. Fluid Mech.*, 672:477–486, 2011.
- [333] H. Zhao and E. S. G. Shaqfeh. The dynamics of a non-dilute vesicle suspension in a simple shear flow. *J. Fluid Mech.*, 725:709–731, 2013.
- [334] C. S. Peskin. The immersed boundary method. *Acta Numerica*, 11:479–517, 2002.
- [335] E.A. Fadlun, R. Verzicco, P. Orlandi, and J. Mohd-Yusof. Combined immersed-boundary finite-difference methods for three-dimensional complex flow simulations. *J. Comp. Phys.*, 161(1):35–60, 2000.
- [336] M.-C. Lai and C. S. Peskin. An immersed boundary method with formal second-order accuracy and reduced numerical viscosity. *J. Comp. Phys.*, 160(2):705–719, 2000.
- [337] M. E. Gracheva and H. G. Othmer. A continuum model of motility in ameboid cells. *B. Math. Biol.*, 66(1):167–193, 2004.
- [338] A. R. Pries, T. W. Secomb, P. Gaehtgens, and J. F. Gross. Blood flow in microvascular networks. Experiments and simulation. *Circulation research*, 67(4):826–834, 1990.
- [339] C. K. Aidun and J. R. Clausen. Lattice-Boltzmann method for complex flows. *Annu. Rev. Fluid Mech.*, 42:439–472, 2010.
- [340] S. Chen and G. D. Doolen. Lattice Boltzmann method for fluid flows. *Annu. Rev. Fluid Mech.*, 30(1):329–364, 1998.
- [341] M. Anand, J. Kwack, and A. Masud. A new generalized Oldroyd-B model for blood flow in complex geometries. *Int. J. Eng. Sci.*, 72:78–88, 2013.
- [342] F. Gijsen, E. Allanic, F. van de Voosse, and J. Janssen. The influence of the non-Newtonian properties of blood on the flow in large arteries: Unsteady flow in a 90 degree curved tube. *J. Biomech.*, 32:705–713, 1999.
- [343] B. M. Johnston and P. R. Johnston, S. Corney, and D. Kilpatrick. Non-Newtonian blood flow in human right coronary arteries: steady state simulations. *J. Biomech.*, 37(5):709–720, 2004.
- [344] P. Chaturani and R. P. Samy. Pulsatile flow of Casson’s fluid through stenosed arteries with applications to blood flow. *Biorheology*, 23(5):499–511, 1986.
- [345] J. Boyd, J. M. Buick, and S. Green. Analysis of the Casson and Carreau-Yasuda non-Newtonian blood models in steady and oscillatory flows using the lattice boltzmann method. *Phys. Fluids*, 19(9):093103, 2007.

- [346] E. Guazzelli and J. F. Morris. *A Physical Introduction to Suspension Dynamics*. Cambridge Texts in Applied Mathematics. Cambridge University Press, 2012.
- [347] A. Shenoy, C. V. Rao, and C. M. Schroeder. Stokes trap for multiplexed particle manipulation and assembly using fluidics. *Proc. Nat. Acad. Sci.*, 113(15):3976–3981, 2016.
- [348] J. M. Skotheim and T. W. Secomb. Red blood cells and other nonspherical capsules in shear flow: oscillatory dynamics and the tank-treading-to-tumbling transition. *Phys. Rev. Lett.*, 98(7):078301, 2007.
- [349] O. Aouane, M. Thiébaud, A. Benyoussef, C. Wagner, and C. Misbah. Vesicle dynamics in a confined Poiseuille flow: From steady state to chaos. *Phys. Rev. E*, 90(3):033011, 2014.
- [350] H. K. Khalil. Nonlinear systems. *Prentice-Hall, New Jersey*, 2(5):5–1, 1996.
- [351] T. Herbert. On perturbation methods in nonlinear stability theory. *J. Fluid Mech.*, 126:167–186, 1983.
- [352] J. T. Stuart. Nonlinear stability theory. *Annu. Rev. Fluid Mech.*, 3(1):347–370, 1971.
- [353] J. L. Lumley. *Stochastic tools in turbulence*. Courier Corporation, 2007.
- [354] D. J. Thomson. Criteria for the selection of stochastic models of particle trajectories in turbulent flows. *J. Fluid Mech.*, 180:529–556, 1987.
- [355] A. Provenzale, L. A. Smith, R. Vio, and G. Murante. Distinguishing between low-dimensional dynamics and randomness in measured time series. *Physica D*, 58(1-4):31–49, 1992.
- [356] J. Gao, Y. Cao, W. Tung, and J. Hu. *Multiscale analysis of complex time series: integration of chaos and random fractal theory, and beyond*. John Wiley & Sons, 2007.
- [357] J.-P. Eckmann and D. Ruelle. Ergodic theory of chaos and strange attractors. *Rev. Modern Phys.*, 57(3):617, 1985.
- [358] K. M. Cuomo and A. V. Oppenheim. Circuit implementation of synchronized chaos with applications to communications. *Phys. Rev. Lett.*, 71(1):65, 1993.
- [359] P. Bergé, Y. Pomeau, and C. Vidal. *Order within chaos*. Wiley and Sons NY, 1984.
- [360] T. Ning, J. C. Tranquillo, A. C. Grare, and A. Saraf. Computing correlation and integral with the Euclidean and distance and normalized by the embedding and dimension. In *ICSP2008 Proceedings*, pages 2708–2712. IEEE, 2008.
- [361] A. Osborne, A. Ro, and A. Provenzale. Finite correlation dimension for stochastic systems with power-law spectra. *Physica D*, 35(3):357–381, 1989.
- [362] J. Theiler. Some comments on the correlation dimension of $1/f^\alpha$ noise. *Phys. Lett. A*, 155(8):480–493, 1991.
- [363] R. Benzi, G. Paladin, G. Parisi, and A. Vulpiani. On the multifractal nature of fully developed turbulence and chaotic systems. *J. Phys. A*, 17(18):3521, 1984.
- [364] W. Decker, W. Pesch, and A. Weber. Spiral defect chaos in rayleigh-bénard convection. *Phys. Rev. Lett.*, 73(5):648, 1994.
- [365] A. Wolf, J. B. Swift, H. L. Swinney, and J. A. Vastano. Determining Lyapunov exponents from a time series. *Physica D*, 16(3):285–317, 1985.

- [366] J. D. Farmer and J. J. Sidorowich. Predicting chaotic time series. *Phys. Rev. Lett.*, 59(8):845, 1987.
- [367] M. T. Rosenstein, J. J. Collins, and C. J. De Luca. A practical method for calculating largest Lyapunov exponents from small data sets. *Physica D*, 65(1-2):117–134, 1993.
- [368] H. Hasimoto. On the periodic fundamental solutions of the Stokes equations and their application to viscous flow past a cubic array of spheres. *J. Fluid Mech.*, 5(2):317–328, 1959.
- [369] Z. Wang and C. Holm. Estimate of the cutoff errors in the ewald summation for dipolar systems. *J. Chem. Phys.*, 115:6351–6359, 2001.
- [370] M. Deserno and C. Holm. How to mesh up Ewald sums. I. A theoretical and numerical comparison of various particle mesh routines. *J. Chem. Phys.*, 109(18):7678–7693, 1998.
- [371] M. Deserno and C. Holm. How to mesh up Ewald sums. II. An accurate error estimate for the particle-particle-particle-mesh algorithm. *J. Chem. Phys.*, 109(18):7694–7701, 1998.
- [372] R. Bali and U. Awasthi. Mathematical model of blood flow in small blood vessel in the presence of magnetic field. *Appl. Math.*, 2:264–269, 2011.
- [373] J. T. Jenkins. Static equilibrium configurations of a model red blood cell. *J. Math. Biology*, 4:149–169, 1977.
- [374] T. Shiga, N. Maeda, and K. Kon. Erythrocyte rheology. *Oncology/Hematology*, 10:9–48, 1990.
- [375] J. E. Smith., N. Mohandas, M. R. Clark, A. C. Greenquist., and S. B. Shohet. Deformability and spectrin properties in three types of elongated red cells. *Am. J. Hematology*, 8:1–13, 1980.
- [376] P. B. Canham. The minimum energy of bending as a possible explanation of the biconcave shape of the human red blood cell. *J. Theoret. Biol.*, 26:61–81, 1970.
- [377] M. Diez-Silva, M. Dao, J. Han, C. T. Lim, and S. Suresh. Shape and biomechanical characteristics of human red blood cells in health and disease. *MRS Bull.*, 35(2):382–388, 2010.
- [378] C. A. Squier, J. S. Hart, and A. Churchland. Changes in red blood cell volume on fixation in glutaraldehyde solutions. *Histochem.*, 48:7–16, 1976.
- [379] C. S. Peyratout and L. Dahne. Taylor-made polyelectrolyte microcapsules: From multilayers to smart containers. *Angew. Chem. Int. Ed.*, 43:3762–3783, 2004.
- [380] Y. Raghunathan, L. Amsel, O. Hinsvark, and W. Bryant. Sustained-release drug delivery system I: Coated ion-exchange resin system for phenylpropanolamine and other drugs. *J. Pharm. Sci.*, 70:379–384, 1981.
- [381] Y. Wang, V. Bansal, A. N. Zelikin, and F. Caruso. Templated synthesis of single-component polymer capsules and their application in drug delivery. *Nano Lett.*, 8(6):1741–1745, 2008.
- [382] F. Demeke and V. K. Katiyar. Analysis of mechanical behavior of red blood cell membrane in pathological condition. *World Congr. Biomech.*, pages 1114–1116, 2010.
- [383] A. H. G. Isfahani. A 2d Stokes suspension solver with application to red blood cell phenomenology. Master’s thesis, University of Illinois at Urbana-Champaign, 2008.

- [384] I. Cantat and C. Misbah. Lift force and dynamical unbinding of adhering vesicles under shear flow. *Phys. Rev. Lett.*, 83(4):880–883, July 1999.
- [385] C. Pozrikidis. Effect of membrane bending stiffness on the deformation of capsules in simple shear flow. *J. Fluid Mech.*, 440:269–291, 2001.
- [386] R. L. Whitmore. *Rheology of the Circulation*. Pergamon, Oxford, 1968.
- [387] S. Weinbaum and P. Ganatos. Numerical multipole and boundary integral equation techniques in Stokes flow. *Annu. Rev. Fluid Mech.*, 22:275–316, 1990.
- [388] M. E. Staben, A. Z. Zinchenko, and R. H. Davis. Motion of a particle between two parallel plane walls in low-Reynolds-number Poiseuille flow. *Phys. Fluids*, 15(1711), 2003.
- [389] K. M. Jan and S. Chien. Role of surface electric charge in red blood cell interactions. *J. Gen. Physiol.*, 61(638), 1973.
- [390] S. Knoche and J. Kierfeld. Buckling of spherical capsules. *Phys. Rev. E*, 84(046608), 2011.
- [391] A. H. Brezavsek, M. Rauzi, M. Leptin, and P. Zicherl. A model of epithelial invagination driven by collective mechanics of identical cells. *Biophys. J.*, 103:1069–1077, 2012.
- [392] A. Chabanel, W. Reinhart, and S. Chien. Increased resistance to membrane deformation of shape-transformed human red blood cells. *Blood*, 69:739–743, 1987.
- [393] N. V. Majeti and R. Kumar. Nano and microparticles as controlled delivery devices. *J. Pharm. Sci.*, 3(2):234–258, 2000.
- [394] V. E. Emmel. A study of the erythrocytes in a case of severe anemia with elongated and sickle-shaped red blood corpuscles. *Arch. Intern. Med. University of Illinois College of Medicine*, 20:586–598, 1917.
- [395] G. d’Onofrio and G. Zini. *Morphology of Blood Disorders*. John Wiley and Sons, 2014.
- [396] L. M. Calle, W. N. Li, J. W. Buhrow, S. A. Perusich, S. T. Jolley, T. L. Gibson, and M. K. Williams. Elongated microcapsules and their formation, August 2012. US Patent App. 13/354,576.
- [397] M. Donbrow. *Microcapsules and Nanoparticles in Medicine and Pharmacy*. CRC Press, 1991.
- [398] J. J. Bishop, A. S. Popel, M. Intaglietta, and P. C. Johnson. Rheological effects of red blood cell aggregation in the venous network: A review of recent studies. *Biorheology*, 38:263–274, 2001.
- [399] C. Alonso, A. R. Pries, and P. Gaehtgens. Time-dependent rheological behavior of blood at low shear in narrow vertical tubes. *Am. J. Physiol. Heart Circ. Physiol.*, 265:553–561, 1993.
- [400] G. R. Cokelet and H. L. Goldsmith. Decreased hydrodynamic resistance in the two-phase flow of blood through small vertical tubes at low flow rates. *Circ. Res.*, 68:1–17, 1991.
- [401] W. Reinke, P. C. Johnson, and P. Gaehtgens. Effect of shear rate variation on apparent viscosity of human blood in tubes of 29–94 μ m. *Circ. Res.*, 59:124–132, 1986.
- [402] W. Reinke, P. Gaehtgens, and P. C. Johnson. Blood viscosity in small tubes: effect of shear rate, aggregation, and sedimentation. *Am. J. Physiol. Heart Circ. Physiol.*, 253:540–547, 1987.

- [403] S. Yamaguchi, T. Yamakawa, and H. Niimi. Cell-free plasma layer in cerebral microvessels. *Biorheology*, 29:251–260, 1992.
- [404] S. Simchon, K. Jan, and S. Chien. Influence of reduced red cell deformability on regional blood flow. *Am. J. Physiol. Heart Circ. Physiol.*, 253(22):898–902, 1987.
- [405] V. Kozlovskaya, J. F. Alexander, Y. Wang, T. Kuncewicz, X. Liu, B. Godin, and E. Kharlampieva. Internalization of red blood cell-mimicking hydrogel capsules with pH-triggered shape responses. *ACS Nano*, 8(6):5725–5737, 2014.
- [406] J. L. McWhirter, H. Noguchi, and G. Gompper. Flow-induced clustering and alignment of vesicles and red blood cells in microcapillaries. *P. Natl. Acad. Sci.*, 106(15):6039–6043, 2009.
- [407] M. Brust, O. Aouane, M. Thiébaud, D. Flormann, C. Verdier, L. Kaestner, M. W. Laschke, H. Selmi, A. Benyoussef, T. Podgorski, G. Coupier, C. Misbah, and C. Wagner. The plasma protein fibrinogen stabilizes clusters of red blood cells in microcapillary flows. *Sci. Rep.*, 4, 2014.
- [408] E. Metsi. *Large scale simulations of bidisperse emulsions and foams*. PhD thesis, University of Illinois at Urbana-Champaign, 2000.
- [409] E. R. Lancaster, C. R. Calladine, and S. C. Palmer. Paradoxical buckling behavior of a thin cylindrical shell under axial compression. *Int. J. Mech. Sci.*, 42:843–865, 2000.
- [410] D. Bushnell. Buckling of shells—pitfall for designers. *AIAA J.*, 19(9):1183–1226, 1981.
- [411] A. Ghosh, S. Sinha, J. A. Dharmadhikari, S. Roy, A. K. Dharmadhikari, J. Samuel, S. Sharma, and D. Mathur. Euler buckling-induced folding and rotation of red blood cells in an optical trap. *Phys. Biol.*, 3:67–73, 2006.
- [412] J. Kim and T. R. Bewley. A linear systems approach to flow control. *Annu. Rev. Fluid Mech.*, 39:383–417, 2007.
- [413] T. R. Bewley. Flow control: New challenges for a new renaissance. *Prog. Aerosp. Sci.*, 37:21–58, 2001.
- [414] H. Hogberg, T. R. Bewley, and D. S. Henningson. Linear feedback control and estimation of transition in plane channel flow. *J. Fluid Mech.*, 481:149–175, 2001.
- [415] N. Hoda, M. R. Jovanovic, and S. Kumar. Energy amplification in channel flows of viscoelastic fluids. *J. Fluid Mech.*, 601:407–424, 2008.
- [416] G. Danker, P. M. Vlahovska, and C. Misbah. Vesicles in Poiseuille flow. *Phys. Rev. Lett.*, 102(148102), 2009.
- [417] G. I. Barenblatt. *Scaling, self-similarity, and intermediate asymptotics*. Cambridge Texts in Applied Mathematics. Cambridge University Press, 1996.
- [418] L. Preziosi, K. Chen, and D. D. Joseph. Lubricated pipelining: Stability of core-annular flow. *J. Fluid Mech.*, 201:323–356, 1989.
- [419] H. H. Hu and D. D. Joseph. Lubricated pipelining: Stability of core-annular flow: Part 2. *J. Fluid Mech.*, 205:359–396, 1989.
- [420] G. Tomaiuolo, L. Lanotte, G. Ghigliotti, C. Misbah, and S. Guido. Red blood cell clustering in Poiseuille microcapillary flow. *Phys. Fluids*, 24(051903), 2012.
- [421] S. A. Orszag. Accurate solution of the Orr–Sommerfeld stability equation. *J. Fluid Mech.*, 50(4):689–703, 1971.

- [422] Lord Rayleigh J. W. Strutt. On the instability of cylindrical fluid surfaces. *Philos. Mag.*, 34(5,207):177–180, 1892.
- [423] Lord Rayleigh J. W. Strutt. On the instability of a cylinder of viscous liquid under capillary force. *Philos. Mag.*, 34(5,207):145–154, 1892.
- [424] S. Chien, S. Usami, R. J. Dellenback, and M. I. Gregersen. Blood viscosity: Influence of erythrocyte aggregation. *Science*, 157(3790):829–831, 1967.
- [425] S. Chien, S. Usami, R. J. Dellenback, and M. I. Gregersen. Blood viscosity: Influence of erythrocyte deformation. *Science*, 157(3790):827–829, 1967.
- [426] J. C. Weddell, J. Kwack, P. I. Imoukhuede, and A. Masud. Hemodynamic analysis in an idealized artery tree: Differences in wall shear stress between Newtonian and non-Newtonian blood models. *PLOS ONE*, 10(4), 2015.
- [427] S. Kim. *A study of non-Newtonian viscosity and yield stress of blood in a scanning capillary-tube rheometer*. PhD thesis, Drexel University, 2002.
- [428] A. Sequeira and J. Janela. *A Portrait of State-of-the-Art Research at the Technical University of Lisbon*, chapter An overview of some mathematical models of blood rheology. Springer Netherlands, 2007.
- [429] J. Happel and H. Brenner. *Low Reynolds number hydrodynamics*. Springer Netherlands, 1983.